# NLO QCD Corrections to the Production of Two Lepton Pairs via Vector-Boson Fusion at the LHC

---

**Dissertation**

zur

Erlangung der naturwissenschaftlichen Doktorwürde
(Dr. sc. nat.)

vorgelegt der

Mathematisch-naturwissenschaftlichen Fakultät

der

Universität Zürich

von

**Lucia Hošeková**

aus der

Slowakei

**Promotionskomitee**

Prof. Dr. Thomas Gehrmann (Vorsitz)
Prof. Dr. Ansgar Denner (Leiter der Dissertation)
Prof. Dr. Daniel Wyler
Prof. Dr. Ulrich Straumann

Zürich, 2012

# Zusammenfassung

Die über Eichboson-Fusion vermittelte Produktion von Higgs-Bosonen gehört aufgrund ihrer äußerst charakteristischen Signatur mit zwei Tagging-Jets in Vorwärts- und Rückwärtsrichtung des Detektors zu den wichtigsten Kanälen zur Entdeckung des Higgs-Bosons wie auch zur Erforschung seiner Eigenschaften. Da der Großteil des irreduziblen Untergrundes von anderen Eichboson-Fusionsprozessen stammt, die dieselben kinematischen Charakteristika aufweisen, ist es erforderlich, auch diese Prozesse mit über die führende Ordnung hinausgehender Genauigkeit zu analysieren und zu verstehen.

Diese Arbeit stellt eine Methode zur Berechnung der naechst-führenden Korrekturen in der starken Wechselwirkung vor, die sowohl resonante wie auch nicht-resonante Vektorboson-Fusionsprozesse umfasst. Hierbei werden mit Hilfe des Weyl–van-der-Waerden Helizitätsformalismus und Polarisations-Summen komplizierte Feynman-Diagramme in einfachere Baublöcke zerlegt. Die gegenseitige Aufhebung von Singularitäten, die in den virtuellen Korrekturen sowie in der reellen Abstrahlung auftreten, wird über den Dipolsubtraktions- Formalismus nach Catani und Seymour vermittelt. Exemplarisch werden für den Prozess $pp \to jje^+\nu_e\mu^+\nu_\mu$ integrierte Wirkungsquerschnitte sowie eine Auswahl an kinematischen Verteilungen diskutiert. Die von der Nichtberücksichtigung höherer störungstheoretischer Ordnungen herrührende theoretische Unsicherheit hinsichtlich der betrachteten Observablen wird durch die in dieser Arbeit präsentierten Berechnungen gegenüber der führenden Ordnung signifikant reduziert.

# Abstract

Higgs production via gauge boson fusion, due to its unique signature formed by two tagging jets in the forward and backward region of the detector, is one of the most important channels for discovery of the Higgs boson at the LHC and for exploring its properties. As most of the irreducible background originates from other gauge boson fusion processes sharing the same kinematical characteristics, it is desirable to analyze and understand these processes with accuracy that goes beyond the leading order. This thesis presents a method for calculating the next-to-leading-order QCD corrections to both resonant and non-resonant contributions to the vector boson fusion processes, implementing the Weyl van der Waerden helicity formalism and polarization sums to divide complex Feynman diagrams into blocks. Singularities arising from the virtual and radiative corrections are controlled using the Catani-Seymour dipole subtraction technique. Total cross section and selected kinematic distributions are presented for the process $pp \to jje^+\nu_e\mu^+\nu_\mu$. In comparison to the leading order, the results of this calculation show a significant reduction in the estimated uncertainties caused by higher perturbative orders.

# Contents

Chapter 1

# Introduction and motivation

The particle physics has taken it upon itself to study and determine the fundamental laws that guide the interactions between basic elements of matter in the universe. The Standard Model of Elementary Particles constitutes a summary of our knowledge about three out of four forces of nature, accumulated and tested for over 50 years with an immense amount of supporting data from independent experiments around the world. It establishes that the material in the visible universe is made up of fermions that interact through fields associated with gauge bosons.

First pieces of the puzzle appeared in the 1950's when particle accelators entered new energy domains and unveiled a large number of new particles that could not be predicted nor theoretically explained. Over the next years, many ideas and models began to form in an attempt to classify these particles, recognize patterns and form a deeper and more fundamental view on the laws they are ruled by. In 1957, the idea of intermediate vector bosons $W^{\pm}$ was proposed as carriers for the weak interactions [1, 2], later expanded by introducing a neutral weak boson Z [3], leading to a Lagrangian for the electroweak synthesis and estimation of W and Z mass [4, 5]. In 1964, the first concept of quarks emerged as a mathematical model of hadrons, which were first evidenced in 1968-1969 at the Stanford Linear Accelerator and the need of existence of a fourth quark arose to fit in the pattern [6]. Concurrently, the idea of colour charge as a property of quarks was introduced, which finally led to invention of the QCD Lagrangian in 1973 [7, 8, 9]. The gauge symmetry as a guiding principle for constructing quantum field theories was brought about in 1961 [10], together with the idea of spontaneous symmetry breaking, which gives an explanation to why some conservation laws are not exact, and the Goldstone theorem [11, 12] which proposes a new massless scalar particle for each broken symmetry generator. As there was no experimental evidence of these particles, a new theory was proposed, introducing the so-called Higgs mechanism [13, 14, 15] which, when applied to the electroweak Lagrangian, gives rise to a massive scalar particle called the Higgs boson. These and many more other pieces, followed by successful experimental confirmations of the theoretical predictions, led to establishing a view of physics now called the Standard Model. It encouraged construction of new powerful accelators which managed to observe the first evidence of the W and Z bosons [16, 17] in 1983, masses of which were in very good agreement with the Standard Model predictions. Later, in 1995, after years of searching at many accelerators, the CDF and D0 detectors at Fermilab

observed top-quark production [18, 19], completing the series of experiments that set out to observe the third generation of fermions and confirming the existence of the entire particle content of the Standard Model, with the exception of the Higgs boson.

To address this task, a new particle accelator named Large Hadron Collider (LHC) has been constructed at CERN, designed to collide proton beams at up to 7 TeV each, an energy that was deemed sufficient to measure the Higgs boson of any mass compatible with the Standard Model in a variety of observation channels. In July 2012, a dramatic progress was made when two LHC experiments, CMS and ATLAS, independently announced a discovery of a new Higgs-like boson with the mass of approximately 125 GeV, which appears to be consistent with the Standard Model. The next challenge for the high-energy physics for the following months and years will be to measure properties and couplings of this particle to both fermions and gauge bosons and compare them with the predicted properties of the Higgs boson as well as explore the possibility of physics beyond the Standard Model.

Signatures for new physical states such as the Higgs boson consist of production and decay modes, both contributing specific kinematic properties that can be used for distinguishing signal from background. Although the Higgs boson is expected to couple to most of the Standard Model particles, not all modes are observable in a hadron collider environment. At the LHC, there are four relevant Higgs production modes: gluon fusion which dominates inclusive production; top quark associated production; weak-boson-associated production and the vector-boson fusion (VBF) which is the focus of this work. Despite the fact that the gluon fusion provides the largest production rate, Higgs production via VBF (qq→qqH) offers a unique signature formed by two easily identifiable outgoing jets. This channel has a potential to provide valuable insight not only while confirming the existence of the Standard Model Higgs boson, but also into many of its characteristics, including decay width, CP properties [20] and its couplings to both fermions and gauge bosons, in particular HWW coupling which can identify the observed resonance as the scalar responsible for the spontaneous symmetry breaking in the electroweak sector [21, 22].

Vector-boson-fusion processes in general constitute an irreducible background to the Higgs boson production mode in association with two jets, in particular in combination with $H \to ZZ/W^+W^- \to 4l$ decay modes as they share the same kinematic characteristics. It is therefore desirable to obtain highly accurate theoretical predictions and error estimates for these background processes. They are also seen as an important probe of the electroweak symmetry breaking itself, especially in relation to perturbative unitarity of the Standard Model at very high energy scales [23] which is, without the presence of the Higgs boson, violated in the processes involving $W^+W^- \to W^+W^-$ scattering unless some other mechanism beyond that described by the Standard Model controls the unphysical behaviour (see e.g. [24]).

The cross section estimates of the VBF processes at the leading perturbative order carry a large uncertainty, as evidenced by its large dependence on the factorization scale, which calls for a calculation at the next-to-leading (NLO) order in the strong coupling constant to obtain a more reliable control over the irreducible background at the LHC. For a long time, complexity of these processes presented a limitation that has only been overcome in the recent years when the first calculations of this kind started to emerge. In most cases, the

next-to-leading order calculations were presented for a resonant production of two gauge bosons associated with two jets, while the leptonic decays were included subsequently while accounting for the spin correlations [25, 26, 27]. Calculations including both resonant and non-resonant contributions that give rise to four final-state leptons and two jets have been published over several years in [28, 29, 30] and [31], last of which has recently been combined with a parton shower [32] using POWHEG box [33, 34].

The work presented in this thesis represents an independent calculation of the NLO QCD corrections to the VBF processes, taking into account the non-resonant contributions. In Chapter 2, we provide a brief overview of some of the aspects of the Standard Model that bear a relevance to the calculation. Chapter 3 presents a list of all subprocesses that contribute to the cross section, categorized according to the intermediate gauge boson involved in the vector boson fusion. Chapter 4 explains some of the technical aspects of the evaluation of matrix elements that are common to both leading- and next-to-leading order. Construction of the leading-order amplitudes is the primary focus of Chapter 5, while the virtual and radiative corrections are discussed in more detail in Chapter 6. Finally, Chapter 7 presents a numerical discussion and analysis of one of the considered processes, and Chapter 8 offers a brief summary. The Appendix section contains an overview of the Weyl van der Waerden helicity formalism (Appendix A) and a list of the polarization sums used to construct the matrix elements for all considered subprocesses (Appendix B).

Chapter 2

# Initial considerations

The calculations in this thesis are completed in the frame of the Standard Model (SM) of elementary particles. SM is a non-Abelian local gauge theory invariant under transformations of the gauge group $SU(3)\times SU(2)\times U(1)$. It is formed by two underlying models: the Glashow-Weinberg-Salam Model which is based on the spontaneously broken group $SU(2)_L \times U(1)_Y$ and provides a description of the electroweak interactions and quantum chromodynamics (QCD) which is generated by the unbroken gauge group $SU(3)_C$ and describes strong interactions of coloured quarks and gluons. A detailed explanation of the SM can be found e.g. in [35, 36].

At present, the Standard Model is not analytically solvable and in order to use it as a predictive tool, one needs to resort to approximative methods. Perturbative expansions in the coupling deliver very accurate predictions, particularly for processes dominated by electroweak interactions since the fine structure constant $\alpha_{\text{EW}} \approx 10^{-2}$ provides strong suppression in the higher orders of the expansion. In QCD however, the perturbative techniques cannot be applied universally as the strong coupling constant is highly energy-dependent and only becomes small for short-distance interactions. The renormalization group equation (RGE) [37, 38] yields in the first- and second-order approximation the following formula for the running of the strong coupling constant

$$\alpha_S(Q^2)_{\text{1-loop}} = \frac{12\pi}{(11N_C - 2N_f)\ln\frac{Q^2}{\Lambda^2_{\text{QCD}}}}, \tag{2.1}$$

$$\alpha_S(Q^2)_{\text{2-loop}} = \alpha_S(Q^2)_{\text{1-loop}}\left(1 - \frac{6(51N_C - 19N_f)}{(11N_C - 2N_f)^2}\frac{\ln\left(\ln\frac{Q^2}{\Lambda^2_{\text{QCD}}}\right)}{\ln\frac{Q^2}{\Lambda^2_{\text{QCD}}}}\right) \tag{2.2}$$

where $Q^2$ denotes the momentum transfer of the process, $N_C$ stands for the number of colours, $N_f$ for the number of active flavours and $\lambda_{\text{QCD}}$ represents the QCD scale parameter which sets the scale for renormalization. If $Q^2 \gg \Lambda^2_{\text{QCD}}$, the strong coupling is small enough for the perturbative expansion to be applicable. Energy-dependent behaviour of $\alpha_S(Q)$ (see e.g. [39]) suggests that for energies relevant to the collider physics, the value of $\alpha_S$ is of the order of $0.1$ and thus suitable for perturbative theory. For lower energies and longer distances (where $Q^2$ is of order $\Lambda^2_{\text{QCD}}$), the non-perturbative effects become dominant due to

confinement, as the partons become bound in hadrons. More details on the running of the strong coupling constant and factorization can be found in [39].

While asymptotic freedom allows us to calculate the cross sections involving partons, their bound states, hadrons, are not accessible perturbatively. For hadronic scattering experiments, such as those conducted at the LHC, it is necessary to decouple the non-perturbative long-range effects from the perturbative high-energy effects. Studies of the deep inelastic scattering processes show that the hadronic scattering cross sections can in general be written as a convolution of two factors: the partonic cross section of the hard process $\hat{\sigma}$ and the parton distribution functions (PDF) which are used to describe distribution of the quarks and gluons inside hadrons

$$\sigma(k_1, k_2) = \sum_{a,b} \int_0^1 \mathrm{d}x_1 \int_0^1 \mathrm{d}x_2 f_a(x_1, \mu_F) f_b(x_2, \mu_F) \hat{\sigma}_{ab}(x_1 k_1, x_2 k_2, \mu_F), \tag{2.3}$$

where $f_a$ and $f_b$ correspond to the PDF's of the scattering hadrons, values of which need to be acquired experimentally and the sum represents summing over all possible partonic initial states. This factorization implies that the contributions from long distance scales only appear in the PDF's, while the contributions from short distance scales only show up in the hard scattering functions. An artifact of this splitting is an artificial dependence on the factorization scale $\mu_F$ which decreases as one takes into account higher perturbative orders.

A traditional approach to treating the perturbation theory in QCD, which is also used in this calculation, is the matrix-element method that relies on computing Feynman diagrams, order by order. In the class of processes referred to as vector-boson fusion at hadron colliders, two initial-state protons scatter and produce two final-state jets and two gauge bosons which subsequently decay into four final-state leptons. At partonic level, the leading order of the perturbative expansion corresponds to $\alpha_{\mathrm{EW}}^6$ in the case of the electroweak (EW) production mode or $\alpha_{\mathrm{EW}}^4 \alpha_S^2$ for the QCD production mode in which the exchange between two quark lines is mediated by gluons rather than vector bosons. Since the jets in the gluon-mediated production mode show a preference to being closer in rapidity than in EW production mode, a cut requiring a large rapidity separation $\Delta y_{\mathrm{jj}}$ together with other VBF cuts results in suppressing the QCD production mode by two orders of magnitude as demonstrated in [32, 24]. In this thesis, we focus only on the class of processes in which both initial partons are quarks as it can be isolated by a convenient selection of cuts. The next-to-leading QCD order of the perturbative expansion is therefore $\alpha_{\mathrm{EW}}^6 \alpha_S$.

Due to the fact that the detection of the quarks and leptons at the LHC experiments requires relativistic energies, the fermion mass effects are suppressed and have been neglected in this calculation. At the same time, only the two lighter generations of quarks (u, d, c and s) and leptons have been taken into consideration. Under these circumstances, it can be demonstrated [30] that the Cabibbo-Kobayashi-Maskawa matrix which contains information on the quark flavour mixing in weak interactions can be approximated by a diagonal matrix provided the interferences between different kinematic channels are negligible which is verified in Section 7.4.

To treat the propagators of the unstable massive intermediate particles (W, Z and Higgs

boson), two different width schemes have been implemented in the calculation. One is the fixed-width scheme, which sees all massive propagators $P(k)$ receive a constant width $\Gamma_V$ so that

$$P_{\mathrm{FMS}}(k) = \frac{1}{(k^2 - M_V^2 + \mathrm{i}M_V\Gamma_V)}. \tag{2.4}$$

Its main drawback is that it violates the $SU(2)$ gauge invariance. The second scheme is the complex-mass scheme [40, 41, 42], in which the $SU(2)$ gauge invariance is restored by globally replacing the masses and keeping the propagator the same as in the fixed mass scheme

$$M_{V\,\mathrm{CMS}} = \sqrt{M_V^2 - \mathrm{i}M_V\Gamma_V}, \qquad P_{\mathrm{CMS}}(k) = \frac{1}{(k^2 - M_V^2 + \mathrm{i}M_V\Gamma_V)}. \tag{2.5}$$

Complex masses are then introduced in the Feynman rules, including the weak mixing angle

$$\cos^2\Theta_W \mapsto \frac{M_{\mathrm{W}}^2 - \mathrm{i}M_{\mathrm{W}}\Gamma_{\mathrm{W}}}{M_{\mathrm{Z}}^2 - \mathrm{i}M_{\mathrm{Z}}\Gamma_{\mathrm{Z}}}, \tag{2.6}$$

rendering the couplings complex. This scheme thus respects all relations and transformations that do not involve complex conjugation, such as the Ward identity and independence from the gauge parameter.

Chapter 3

# List of the contributing subprocesses

This section provides an overview of all subprocesses considered in our calculation. The subject of this study is an NLO-QCD calculation of processes involving the fusion of a gauge boson pair with the subsequent leptonic decay relevant to the precision measurements at the LHC. These are characterized by the typical *t*-channel and *u*-channel Feynman diagrams with two vector bosons radiated from two incoming quark lines, fusing in the center and subsequently decaying into four leptons.

From the phenomenological, as well as practical point of view, it is useful to categorize the processes with respect to the intermediate vector bosons produced in the vector-boson fusion diagrams

$$\begin{aligned} \mathrm{qq} &\to \mathrm{jj}W^{\pm}\mathrm{W}^{\pm} \to \mathrm{jj4l} \\ \mathrm{qq} &\to \mathrm{jj}W^{\pm}\mathrm{Z}/\gamma \to \mathrm{jj4l} \\ \mathrm{qq} &\to \mathrm{jj}W^{\pm}\mathrm{W}^{\mp} \to \mathrm{jj4l} \\ \mathrm{qq} &\to \mathrm{jjZ}/\gamma\mathrm{Z}/\gamma \to \mathrm{jj4l}. \end{aligned}$$

Charges of the produced gauge bosons determine the charge and helicity configurations of the external quarks and leptons. Table 3.1 displays a list of generic subprocesses for each category at the leading order. All of the listed subprocesses correspond to *t*-channel diagrams (shown schematically in Figure 3.1a) with two quarks in the initial state and two quarks and four leptons in the final state. Of the four fermionic pairs, each belongs to a different generation, to prevent interferences from channel mixing.

In general, all remaining channels contributing to each process can be derived from the $t$-channel subprocesses displayed in Table 3.1. This is achieved either by applying the crossing symmetry to reverse the flow of either one or both quark currents (Figure 3.1b) and to construct the *s*-channel diagrams (Figure 3.1c), or by exchanging the outgoing lines to obtain *u*-channel diagrams (Figure 3.1d) and diagrams with swapped quark legs.

For a process with incoming partonic momenta $k_1$ and $k_2$, and outgoing partonic momenta $k_3$ and $k_4$, a $t$-channel subprocesses with external antiquarks can be obtained from the generic $t$-channel matrix element $\mathcal{M}_{\mathrm{gen},QQ\to QQ}$ by crossing the momenta in a following

| | | | |
|---|---|---|---|
| $pp \to jjW^+W^+$ | $uc \to dse^+\nu_e\mu^+\nu_\mu$ | | |
| $pp \to jjW^-W^-$ | $ds \to uce^-\bar{\nu}_e\mu^-\bar{\nu}_\mu$ | $pp \to jjZZ/\gamma\gamma/Z\gamma$ | $ds \to dse^+e^-\mu^+\mu^-$ |
| $pp \to jjW^+Z/\gamma$ | $uc \to dce^+\nu_e\mu^+\mu^-$ | | $uc \to uce^+e^-\mu^+\mu^-$ |
| | $us \to dse^+\nu_e\mu^+\mu^-$ | | $us \to use^+e^-\mu^+\mu^-$ |
| $pp \to jjW^-Z/\gamma$ | $dc \to uce^-\bar{\nu}_e\mu^+\mu^-$ | | $us \to dce^+e^-\mu^+\mu^-$ |
| | $ds \to use^-\bar{\nu}_e\mu^+\mu^-$ | | $ds \to dse^+e^-\nu_\mu\bar{\nu}_\mu$ |
| $pp \to jjW^+W^-$ | $ds \to dse^+\nu_e\mu^-\bar{\nu}_\mu$ | | $uc \to uce^+e^-\nu_\mu\bar{\nu}_\mu$ |
| | $uc \to uce^+\nu_e\mu^-\bar{\nu}_\mu$ | | $us \to use^+e^-\nu_\mu\bar{\nu}_\mu$ |
| | $us \to use^+\nu_e\mu^-\bar{\nu}_\mu$ | | $us \to dce^+e^-\nu_\mu\bar{\nu}_\mu$ |
| | $us \to dce^+\nu_e\mu^-\bar{\nu}_\mu$ | | |

**Table 3.1:** List of generic $t$-channel subprocesses corresponding to the intermediate gauge bosons produced in the fusion diagrams. All remaining subprocesses contributing to the total cross section can be obtained from these matrix elements.

way:

$$\begin{aligned}
\mathcal{M}_{t,Q\bar{Q}\to Q\bar{Q}}(k_1,k_2,k_3,k_4,...) &= \mathcal{M}_{\text{gen},QQ\to QQ}(k_1,-k_4,k_3,-k_2,...)\\
\mathcal{M}_{t,\bar{Q}Q\to \bar{Q}Q}(k_1,k_2,k_3,k_4,...) &= \mathcal{M}_{\text{gen},QQ\to QQ}(-k_3,k_2,-k_1,k_4,...)\\
\mathcal{M}_{t,\bar{Q}\bar{Q}\to \bar{Q}\bar{Q}}(k_1,k_2,k_3,k_4,...) &= \mathcal{M}_{\text{gen},QQ\to QQ}(-k_3,-k_4,-k_1,-k_2,...). \qquad (3.1)
\end{aligned}$$

The $u$-channel subprocesses listed further in this chapter can be obtained by applying the replacements:

$$\begin{aligned}
\mathcal{M}_{u,QQ\to QQ}(k_1,k_2,k_3,k_4,...) &= \mathcal{M}_{\text{gen},QQ\to QQ}(k_2,k_1,k_3,k_4,...)\\
\mathcal{M}_{u,\bar{Q}Q\to Q\bar{Q}}(k_1,k_2,k_3,k_4,...) &= \mathcal{M}_{\text{gen},QQ\to QQ}(-k_4,k_1,k_3,-k_2,...)\\
\mathcal{M}_{u,Q\bar{Q}\to \bar{Q}Q}(k_1,k_2,k_3,k_4,...) &= \mathcal{M}_{\text{gen},QQ\to QQ}(k_2,-k_3,-k_1,k_4,...)\\
\mathcal{M}_{u,\bar{Q}\bar{Q}\to \bar{Q}\bar{Q}}(k_1,k_2,k_3,k_4,...) &= \mathcal{M}_{\text{gen},QQ\to QQ}(-k_4,-k_3,-k_1,-k_2,...). \qquad (3.2)
\end{aligned}$$

Finally, in order to obtain the $s$-channel subprocesses, one does the following replacements:

$$\begin{aligned}
\mathcal{M}_{s,\bar{Q}Q\to \bar{Q}Q}(k_1,k_2,k_3,k_4,...) &= \mathcal{M}_{\text{gen},QQ\to QQ}(-k_3,k_1,-k_2,k_4,...)\\
\mathcal{M}_{s,Q\bar{Q}\to Q\bar{Q}}(k_1,k_2,k_3,k_4,...) &= \mathcal{M}_{\text{gen},QQ\to QQ}(-k_1,k_3,k_4,-k_2,...)\\
\mathcal{M}_{s,\bar{Q}Q\to Q\bar{Q}}(k_1,k_2,k_3,k_4,...) &= \mathcal{M}_{\text{gen},QQ\to QQ}(-k_3,k_1,k_4,-k_2,...)\\
\mathcal{M}_{s,Q\bar{Q}\to \bar{Q}Q}(k_1,k_2,k_3,k_4,...) &= \mathcal{M}_{\text{gen},QQ\to QQ}(-k_1,k_3,-k_2,k_4,...) \qquad (3.3)
\end{aligned}$$

In some cases, an additional reversal of the momenta of the upper and lower quark lines ($k_1 \leftrightarrow k_2$, $k_3 \leftrightarrow k_4$) needs to be applied before the above replacements to obtain some of

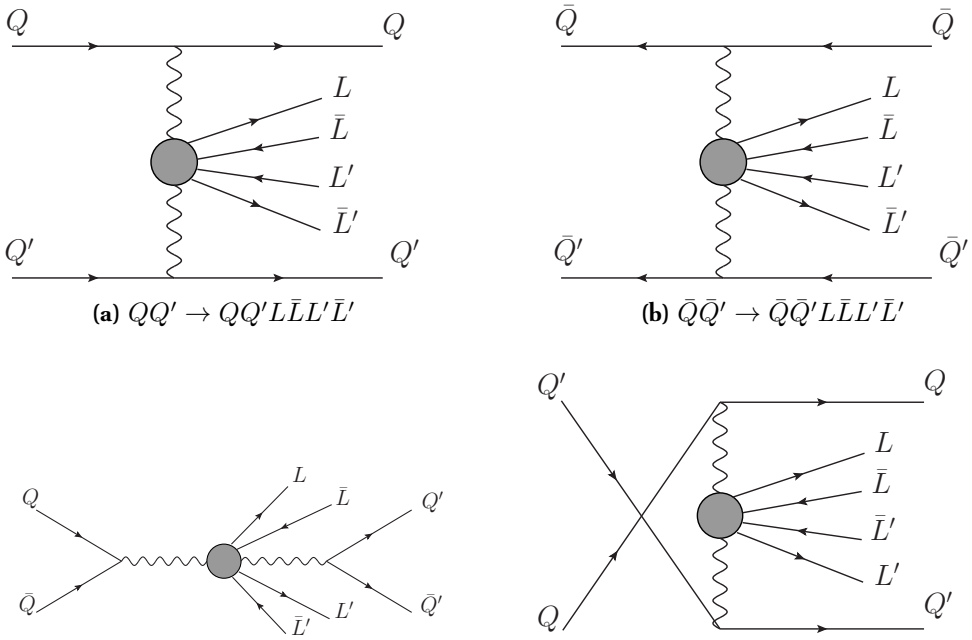


**(a)** $QQ' \to QQ'L\bar{L}L'\bar{L}'$ **(b)** $\bar{Q}\bar{Q}' \to \bar{Q}\bar{Q}'L\bar{L}L'\bar{L}'$

**(c)** $Q\bar{Q} \to Q'\bar{Q}'L\bar{L}L'\bar{L}'$ **(d)** $QQ' \to Q'QL\bar{L}L'\bar{L}'$

**Figure 3.1:** Examples of Feynman diagrams corresponding to the $t$-channel (3.1a and 3.1b), $s$-channel (3.1c) and $u$-channel (3.1d) subprocesses.

the subprocesses, for instance the $s$-channel subprocess $c\bar{c} \to d\bar{u}e^+\nu_e\mu^+\mu^-$ from the generic subprocess $uc \to dce^+\nu_e\mu^+\mu^-$.

Further details on how the crossing symmetry is applied are covered in Sections 4.2 and 5.5.

The subprocesses with quark lines of the same flavour get contributions from two of the three Mandelstam channels, depending on the configuration of quarks and antiquarks. These can be constructed by combining two single-channel subprocesses and adding interferences between the two channels. For instance, the squared amplitude for the process $uu \to uue^+e^-\mu^+\mu^-$ receives contributions from both $t$-channel diagrams $\mathcal{M}_t$ (corresponding to a purely $t$-channel subprocess $uc \to uce^+e^-\mu^+\mu^-$) and $u$-channel diagrams $\mathcal{M}_u$ (corresponding to a $u$-channel subprocess $uc \to cue^+e^-\mu^+\mu^-$) in the following way:

$$|\mathcal{M}|^2 = |\mathcal{M}_t|^2 + |\mathcal{M}_u|^2 - \mathcal{M}_t^*\mathcal{M}_u - \mathcal{M}_t\mathcal{M}_u^*. \tag{3.4}$$

An argument can be made ([31, 30, 28, 29]) that by applying suitable kinematical cuts, all interferences between channels (e.c. $\mathcal{M}_t^*\mathcal{M}_u + \mathcal{M}_t\mathcal{M}_u^*$), along with the contributions from the $s$-channel diagrams have only negligible impact on the final cross section, and therefore it is not necessary to include them in the NLO calculations. To verify this reasoning, we have evaluated the Born-level amplitudes using both setups: 1. without $s$-channel or interferences and 2. including $s$-channel and all interferences.

As all considered processes involve production of two intermediate gauge bosons, all final states contain two leptonic pairs. Due to the fact that all leptons are considered massless, subprocesses with different combination of leptonic flavours can be obtained from the generic amplitudes listed in Table 3.1. For instance, supposing the momenta of the outgoing leptons are $k_1, ...k_4$, the matrix element $\mathcal{M}'$ for us $\to$ use$^+$e$^-$e$^+$e$^-$ can be obtained from the matrix element $\mathcal{M}$ of the generic subprocess us $\to$ use$^+$e$^-\mu^+\mu^-$ by combining momenta flowing into identical particles:

$$\mathcal{M}'(k_1,k_2,k_3,k_4) \;=\; [\mathcal{M}(k_1,k_2,k_3,k_4) - \mathcal{M}(k_3,k_2,k_1,k_4)]\,. \tag{3.5}$$

The only exception is the leptonic final state $QQ \to QQ\mathrm{e}^+\nu_\mathrm{e}\mathrm{e}^-\bar{\nu}_\mathrm{e}$ which gets contributions from both $QQ \to QQ\mathrm{e}^+\nu_\mathrm{e}\mu^-\bar{\nu}_\mu$ and $QQ \to QQ\mathrm{e}^+\mathrm{e}^-\nu_\mu\bar{\nu}_\mu$ and an additional interference term.

In the following sections, we provide a list and a brief overview of the subprocesses we have taken into account in our calculation for each of the combinations of intermediate gauge bosons.

## 3.1 qq $\to$ jjW$^\pm$W$^\pm$ $\to$ jj4l

This process is the least complex as it yields a single configuration for the charges and polarizations of the external fermions and only one generic $t$-channel subprocess (Figure 3.1). In order to produce W$^+$W$^+$ (W$^-$W$^-$), both quarks in the initial state must have positive (negative) charge and the quarks in the final state have negative (positive) charge. The W bosons produced in the vector-boson scattering decay into two lepton pairs with a positive (negative) charge, i.e. $\mathrm{e}^\pm\nu_\mathrm{e}\mu^\pm\nu_\mu$, $\mathrm{e}^\pm\nu_\mathrm{e}\mathrm{e}^\pm\nu_\mathrm{e}$ or $\mu^\pm\nu_\mu\mu^\pm\nu_\mu$. Table 3.2 shows a list of all leading-order partonic subprocesses that correspond to this setup.

All subprocesses listed in Table 3.2 can be obtained from the generic subprocess uc $\to$ dse$^+\nu_\mathrm{e}\mu^+\nu_\mu$ according to Table 3.1. The list is obtained by generating all possible final states and fixing the order of final-state particles while finding every possible combination of initial-state quarks for each incoming proton. For instance, if final state is formed by d and s quark, the subprocesses included in the cross section are uc $\to$ dse$^+\nu_\mathrm{e}\mu^+\nu_\mu$ and cu $\to$ dse$^+\nu_\mathrm{e}\mu^+\nu_\mu$, while considering also uc $\to$ sde$^+\nu_\mathrm{e}\mu^+\nu_\mu$ and cu $\to$ sde$^+\nu_\mathrm{e}\mu^+\nu_\mu$ would result in double-counting as they have the same matrix elements and PDF's.

For each single channel subprocess (quark lines and lepton pairs not sharing the same flavour), the leading order yields 93 Feynman diagrams. As we do not take into account the quark masses, the matrix elements of the subprocesses which can be obtained simply by exchanging generations of the quarks (or antiquarks), for instance uu $\to$ ddW$^+$W$^+$ and cc $\to$ ssW$^+$W$^+$, are identical. As outlined in the previous section, if the quarks (antiquarks) belong to the same generation, the subprocess receives contribution from two channels. Additionaly, if the quarks in the final state are identical, the resulting cross section needs to be multiplied with a symmetry factor $1/2$. In the table, this is indicated in the 'channels' column.

| $\mathbf{pp \to jjW^+W^+}$ | channel | $\mathbf{pp \to jjW^-W^-}$ | channel |
|---|---|---|---|
| $QQ \to QQ\mathrm{e}^{\pm}\nu_{\mathrm{e}}\mu^{\pm}\nu_{\mu}$ | | | |
| $\mathrm{uc} \to \mathrm{dse}^{+}\nu_{\mathrm{e}}\mu^{+}\nu_{\mu}$ | $t$ | $\mathrm{ds} \to \mathrm{uce}^{-}\bar{\nu}_{\mathrm{e}}\mu^{-}\bar{\nu}_{\mu}$ | $t$ |
| $\mathrm{cu} \to \mathrm{dse}^{+}\nu_{\mathrm{e}}\mu^{+}\nu_{\mu}$ | $u$ | $\mathrm{sd} \to \mathrm{uce}^{-}\bar{\nu}_{\mathrm{e}}\mu^{-}\bar{\nu}_{\mu}$ | $u$ |
| $\mathrm{uu} \to \mathrm{dde}^{+}\nu_{\mathrm{e}}\mu^{+}\nu_{\mu}$ | $\frac{t+u}{2}$ | $\mathrm{dd} \to \mathrm{dde}^{-}\bar{\nu}_{\mathrm{e}}\mu^{-}\bar{\nu}_{\mu}$ | $\frac{t+u}{2}$ |
| $\mathrm{cc} \to \mathrm{sse}^{+}\nu_{\mathrm{e}}\mu^{+}\nu_{\mu}$ | $\frac{t+u}{2}$ | $\mathrm{ss} \to \mathrm{cce}^{-}\bar{\nu}_{\mathrm{e}}\mu^{-}\bar{\nu}_{\mu}$ | $\frac{t+u}{2}$ |
| $\bar{Q}\bar{Q} \to \bar{Q}\bar{Q}\mathrm{e}^{\pm}\nu_{\mathrm{e}}\mu^{\pm}\nu_{\mu}$ | | | |
| $\bar{\mathrm{d}}\bar{\mathrm{s}} \to \bar{\mathrm{u}}\bar{\mathrm{c}}\mathrm{e}^{+}\nu_{\mathrm{e}}\mu^{+}\nu_{\mu}$ | $t$ | $\bar{\mathrm{u}}\bar{\mathrm{c}} \to \bar{\mathrm{d}}\bar{\mathrm{s}}\mathrm{e}^{-}\bar{\nu}_{\mathrm{e}}\mu^{-}\bar{\nu}_{\mu}$ | $t$ |
| $\bar{\mathrm{s}}\bar{\mathrm{d}} \to \bar{\mathrm{u}}\bar{\mathrm{c}}\mathrm{e}^{+}\nu_{\mathrm{e}}\mu^{+}\nu_{\mu}$ | $u$ | $\bar{\mathrm{c}}\bar{\mathrm{u}} \to \bar{\mathrm{d}}\bar{\mathrm{s}}\mathrm{e}^{-}\bar{\nu}_{\mathrm{e}}\mu^{-}\bar{\nu}_{\mu}$ | $u$ |
| $\bar{\mathrm{d}}\bar{\mathrm{d}} \to \bar{\mathrm{u}}\bar{\mathrm{u}}\mathrm{e}^{+}\nu_{\mathrm{e}}\mu^{+}\nu_{\mu}$ | $\frac{t+u}{2}$ | $\bar{\mathrm{u}}\bar{\mathrm{u}} \to \bar{\mathrm{d}}\bar{\mathrm{d}}\mathrm{e}^{-}\bar{\nu}_{\mathrm{e}}\mu^{-}\bar{\nu}_{\mu}$ | $\frac{t+u}{2}$ |
| $\bar{\mathrm{s}}\bar{\mathrm{s}} \to \bar{\mathrm{c}}\bar{\mathrm{c}}\mathrm{e}^{+}\nu_{\mathrm{e}}\mu^{+}\nu_{\mu}$ | $\frac{t+u}{2}$ | $\bar{\mathrm{c}}\bar{\mathrm{c}} \to \bar{\mathrm{s}}\bar{\mathrm{s}}\mathrm{e}^{-}\bar{\nu}_{\mathrm{e}}\mu^{-}\bar{\nu}_{\mu}$ | $\frac{t+u}{2}$ |
| $\bar{Q}Q \to \bar{Q}Q\mathrm{e}^{\pm}\nu_{\mathrm{e}}\mu^{\pm}\nu_{\mu}$ | | | |
| $\bar{\mathrm{d}}\mathrm{c} \to \bar{\mathrm{u}}\mathrm{se}^{+}\nu_{\mathrm{e}}\mu^{+}\nu_{\mu}$ | $t$ | $\bar{\mathrm{u}}\mathrm{s} \to \bar{\mathrm{d}}\mathrm{ce}^{-}\bar{\nu}_{\mathrm{e}}\mu^{-}\bar{\nu}_{\mu}$ | $t$ |
| $\mathrm{c}\bar{\mathrm{d}} \to \bar{\mathrm{u}}\mathrm{se}^{+}\nu_{\mathrm{e}}\mu^{+}\nu_{\mu}$ | $u$ | $\mathrm{s}\bar{\mathrm{u}} \to \bar{\mathrm{d}}\mathrm{ce}^{-}\bar{\nu}_{\mathrm{e}}\mu^{-}\bar{\nu}_{\mu}$ | $u$ |
| $\bar{\mathrm{s}}\mathrm{u} \to \bar{\mathrm{c}}\mathrm{de}^{+}\nu_{\mathrm{e}}\mu^{+}\nu_{\mu}$ | $t$ | $\bar{\mathrm{c}}\mathrm{d} \to \bar{\mathrm{s}}\mathrm{ue}^{-}\bar{\nu}_{\mathrm{e}}\mu^{-}\bar{\nu}_{\mu}$ | $t$ |
| $\mathrm{u}\bar{\mathrm{s}} \to \bar{\mathrm{c}}\mathrm{de}^{+}\nu_{\mathrm{e}}\mu^{+}\nu_{\mu}$ | $u$ | $\mathrm{d}\bar{\mathrm{c}} \to \bar{\mathrm{s}}\mathrm{ue}^{-}\bar{\nu}_{\mathrm{e}}\mu^{-}\bar{\nu}_{\mu}$ | $u$ |
| $\bar{\mathrm{d}}\mathrm{u} \to \bar{\mathrm{u}}\mathrm{de}^{+}\nu_{\mathrm{e}}\mu^{+}\nu_{\mu}$ | $t+s$ | $\bar{\mathrm{u}}\mathrm{d} \to \bar{\mathrm{d}}\mathrm{ue}^{-}\bar{\nu}_{\mathrm{e}}\mu^{-}\bar{\nu}_{\mu}$ | $t+s$ |
| $\mathrm{u}\bar{\mathrm{d}} \to \bar{\mathrm{u}}\mathrm{de}^{+}\nu_{\mathrm{e}}\mu^{+}\nu_{\mu}$ | $u+s$ | $\mathrm{d}\bar{\mathrm{u}} \to \bar{\mathrm{d}}\mathrm{ue}^{-}\bar{\nu}_{\mathrm{e}}\mu^{-}\bar{\nu}_{\mu}$ | $u+s$ |
| $\bar{\mathrm{s}}\mathrm{c} \to \bar{\mathrm{c}}\mathrm{se}^{+}\nu_{\mathrm{e}}\mu^{+}\nu_{\mu}$ | $t+s$ | $\bar{\mathrm{c}}\mathrm{s} \to \bar{\mathrm{s}}\mathrm{ce}^{-}\bar{\nu}_{\mathrm{e}}\mu^{-}\bar{\nu}_{\mu}$ | $t+s$ |
| $\mathrm{c}\bar{\mathrm{s}} \to \bar{\mathrm{c}}\mathrm{se}^{+}\nu_{\mathrm{e}}\mu^{+}\nu_{\mu}$ | $u+s$ | $\mathrm{s}\bar{\mathrm{c}} \to \bar{\mathrm{s}}\mathrm{ce}^{-}\bar{\nu}_{\mathrm{e}}\mu^{-}\bar{\nu}_{\mu}$ | $u+s$ |
| $\bar{\mathrm{d}}\mathrm{u} \to \bar{\mathrm{c}}\mathrm{se}^{+}\nu_{\mathrm{e}}\mu^{+}\nu_{\mu}$ | $s$ | $\bar{\mathrm{u}}\mathrm{d} \to \bar{\mathrm{s}}c\mathrm{e}^{-}\bar{\nu}_{\mathrm{e}}\mu^{-}\bar{\nu}_{\mu}$ | $s$ |
| $\mathrm{u}\bar{\mathrm{d}} \to \bar{\mathrm{c}}\mathrm{se}^{+}\nu_{\mathrm{e}}\mu^{+}\nu_{\mu}$ | $s$ | $\mathrm{d}\bar{\mathrm{u}} \to \bar{\mathrm{s}}c\mathrm{e}^{-}\bar{\nu}_{\mathrm{e}}\mu^{-}\bar{\nu}_{\mu}$ | $s$ |
| $\bar{\mathrm{s}}\mathrm{c} \to \bar{\mathrm{u}}\mathrm{de}^{+}\nu_{\mathrm{e}}\mu^{+}\nu_{\mu}$ | $s$ | $\bar{\mathrm{c}}\mathrm{s} \to \bar{\mathrm{d}}u\mathrm{e}^{-}\bar{\nu}_{\mathrm{e}}\mu^{-}\bar{\nu}_{\mu}$ | $s$ |
| $\mathrm{c}\bar{\mathrm{s}} \to \bar{\mathrm{u}}\mathrm{de}^{+}\nu_{\mathrm{e}}\mu^{+}\nu_{\mu}$ | $s$ | $\mathrm{s}\bar{\mathrm{c}} \to \bar{\mathrm{d}}u\mathrm{e}^{-}\bar{\nu}_{\mathrm{e}}\mu^{-}\bar{\nu}_{\mu}$ | $s$ |

**Table 3.2:** List of partonic subprocesses contributing to intermediate $\mathrm{W}^+\mathrm{W}^+$ and $\mathrm{W}^-\mathrm{W}^-$ processes at the leading order. The subprocesses $\mathrm{uc} \to \mathrm{dse}^{+}\nu_{\mathrm{e}}\mu^{+}\nu_{\mu}$ and $\mathrm{ds} \to \mathrm{uce}^{-}\bar{\nu}_{\mathrm{e}}\mu^{-}\bar{\nu}_{\mu}$ correspond to generic subprocesses from Table 3.1.

Table 3.2 contains subprocesses with only one leptonic final state, $\mathrm{e}^{\pm}\nu_{\mathrm{e}}\mu^{\pm}\nu_{\mu}$, where both leptonic pairs are of different flavours. Since the leptons are considered to be massless throughout this calculation, the matrix elements for different generations of leptons can be obtained trivially.

Three different groups of diagrams contribute to the NLO QCD subprocesses. One of

| $\mathbf{pp \to jjW^+W^+}$ | | $\mathbf{pp \to jjW^-W^-}$ | |
|---|---|---|---|
| $GQ \to \bar{Q}QQ\mathrm{e}^{\pm}\nu_\mathrm{e}\mu^{\pm}\nu_\mu$ | | | |
| $\mathrm{gc} \to \bar{\mathrm{u}}\mathrm{ds}\,\mathrm{e}^+\nu_\mathrm{e}\mu^+\nu_\mu$ | $\mathrm{gu} \to \bar{\mathrm{u}}\mathrm{dd}\,\mathrm{e}^+\nu_\mathrm{e}\mu^+\nu_\mu$ | $\mathrm{gs} \to \bar{\mathrm{d}}\mathrm{uc}\,\mathrm{e}^-\bar{\nu}_\mathrm{e}\mu^-\bar{\nu}_\mu$ | $\mathrm{gd} \to \bar{\mathrm{d}}\mathrm{uu}\,\mathrm{e}^-\bar{\nu}_\mathrm{e}\mu^-\bar{\nu}_\mu$ |
| $\mathrm{gu} \to \bar{\mathrm{c}}\mathrm{ds}\,\mathrm{e}^+\nu_\mathrm{e}\mu^+\nu_\mu$ | $\mathrm{gc} \to \bar{\mathrm{c}}\mathrm{ss}\,\mathrm{e}^+\nu_\mathrm{e}\mu^+\nu_\mu$ | $\mathrm{gd} \to \bar{\mathrm{s}}\mathrm{uc}\,\mathrm{e}^-\bar{\nu}_\mathrm{e}\mu^-\bar{\nu}_\mu$ | $\mathrm{gs} \to \bar{\mathrm{s}}\mathrm{cc}\,\mathrm{e}^-\bar{\nu}_\mathrm{e}\mu^-\bar{\nu}_\mu$ |
| $G\bar{Q} \to Q\bar{Q}\bar{Q}\mathrm{e}^{\pm}\nu_\mathrm{e}\mu^{\pm}\nu_\mu$ | | | |
| $\mathrm{g}\bar{\mathrm{s}} \to \mathrm{d}\bar{\mathrm{u}}\bar{\mathrm{c}}\,\mathrm{e}^+\nu_\mathrm{e}\mu^+\nu_\mu$ | $\mathrm{g}\bar{\mathrm{d}} \to \mathrm{s}\bar{\mathrm{u}}\bar{\mathrm{c}}\,\mathrm{e}^+\nu_\mathrm{e}\mu^+\nu_\mu$ | $\mathrm{g}\bar{\mathrm{c}} \to \mathrm{u}\bar{\mathrm{d}}\bar{\mathrm{s}}\,\mathrm{e}^-\bar{\nu}_\mathrm{e}\mu^-\bar{\nu}_\mu$ | $\mathrm{g}\bar{\mathrm{u}} \to \mathrm{c}\bar{\mathrm{d}}\bar{\mathrm{s}}\,\mathrm{e}^-\bar{\nu}_\mathrm{e}\mu^-\bar{\nu}_\mu$ |
| $\mathrm{g}\bar{\mathrm{d}} \to \mathrm{d}\bar{\mathrm{u}}\bar{\mathrm{u}}\,\mathrm{e}^+\nu_\mathrm{e}\mu^+\nu_\mu$ | $\mathrm{g}\bar{\mathrm{s}} \to \mathrm{s}\bar{\mathrm{c}}\bar{\mathrm{c}}\,\mathrm{e}^+\nu_\mathrm{e}\mu^+\nu_\mu$ | $\mathrm{g}\bar{\mathrm{u}} \to \mathrm{u}\bar{\mathrm{d}}\bar{\mathrm{d}}\,\mathrm{e}^-\bar{\nu}_\mathrm{e}\mu^-\bar{\nu}_\mu$ | $\mathrm{g}\bar{\mathrm{c}} \to \mathrm{c}\bar{\mathrm{s}}\bar{\mathrm{s}}\,\mathrm{e}^-\bar{\nu}_\mathrm{e}\mu^-\bar{\nu}_\mu$ |

**Table 3.3:** List of subprocesses with a gluon in the initial state contributing to intermediate $\mathrm{W^+W^+}$ and $\mathrm{W^-W^-}$ production at the next-to-leading order. The subprocesses where the initial-state gluon originates from the second incoming parton can be obtained from this list simply by exchanging the order of the incoming partons.

them are the virtual subprocesses, initial and final states of which are identical to the leading order subprocesses listed in Table 3.2.

Further, the next-to-leading order receives contributions from two types of real radiation subprocesses. The first type features an external gluon in the final state, and has a structure similar to the leading-order (Table 3.2) with an exception of an additional external gluon in the final state (e.c. $\mathrm{uc} \to \mathrm{gdse}^+\nu_\mathrm{e}\mu^+\nu_\mu$). The external gluon is radiated off one of the quark legs. The other type of contributions comes from subprocesses with a gluon in the initial state, splitting into a quark and an antiquark, one of which enters the hard process. As discussed in Section 6.3, this group of subprocesses can be obtained from the ones with a final-state gluon using the crossing symmetry. The list of the gluon-splitting partonic subprocesses can be found in Table 3.3.

## 3.2 $\mathbf{qq \to jjW^{\pm}Z/\gamma \to jj4l}$

In this process we consider the production of one charged and one neutral vector boson in the intermediate state. The quark leg radiating a W boson changes charge while the other one does not due to the electrical neutrality of the Z boson and $\gamma$. The W boson decays into a charged lepton and a neutrino, while $\gamma$ and Z decay either into two opposite-charged leptons or a neutrino-antineutrino pair.

This setup leaves us with two possibilities for each charge of W, where the quark leg emitting a neutral vector boson is either up-type (u, c) or down-type (d, s). A list of all leading-order partonic subprocesses for a positively-charged W boson in the intermediate state and the up-type quark leg is shown in Table 3.4, while the down-type subprocesses are listed in Table 3.5. Equivalent lists for a negatively-charged W boson can be obtained by charge-conjugating all subprocesses in Tables 3.4 and 3.5.

It should be noted that a final state with three neutrinos can also be considered; we

| $\mathbf{pp \to jjW^+Z/\gamma}$**: uc** $\to$ **dce**$^+\nu_e\mu^+\mu^-$ | | | |
|---|---|---|---|
| $QQ \to QQe^+\nu_e\mu^+\mu^-$ | | | |
| $uc \to dce^+\nu_e\mu^+\mu^-$ | $t$ | $cu \to sue^+\nu_e\mu^+\mu^-$ | $t$ |
| $cu \to dce^+\nu_e\mu^+\mu^-$ | $u$ | $uc \to sue^+\nu_e\mu^+\mu^-$ | $u$ |
| $uu \to due^+\nu_e\mu^+\mu^-$ | $t+u$ | $cc \to sce^+\nu_e\mu^+\mu^-$ | $t+u$ |
| $\bar{Q}\bar{Q} \to \bar{Q}\bar{Q}e^+\nu_e\mu^+\mu^-$ | | | |
| $\bar{d}\bar{c} \to \bar{u}\bar{c}e^+\nu_e\mu^+\mu^-$ | $t$ | $\bar{u}\bar{s} \to \bar{u}\bar{c}e^+\nu_e\mu^+\mu^-$ | $t$ |
| $\bar{c}\bar{d} \to \bar{u}\bar{c}e^+\nu_e\mu^+\mu^-$ | $u$ | $\bar{s}\bar{u} \to \bar{u}\bar{c}e^+\nu_e\mu^+\mu^-$ | $u$ |
| $\bar{d}\bar{u} \to \bar{u}\bar{u}e^+\nu_e\mu^+\mu^-$ | $\frac{t+u}{2}$ | $\bar{s}\bar{c} \to \bar{c}\bar{c}e^+\nu_e\mu^+\mu^-$ | $\frac{t+u}{2}$ |
| $\bar{u}\bar{d} \to \bar{u}\bar{u}e^+\nu_e\mu^+\mu^-$ | $\frac{t+u}{2}$ | $\bar{c}\bar{s} \to \bar{c}\bar{c}e^+\nu_e\mu^+\mu^-$ | $\frac{t+u}{2}$ |
| $\bar{Q}Q \to \bar{Q}Qe^+\nu_e\mu^+\mu^-$ | | | |
| $\bar{d}c \to \bar{u}ce^+\nu_e\mu^+\mu^-$ | $t$ | $\bar{s}u \to \bar{c}ue^+\nu_e\mu^+\mu^-$ | $t$ |
| $c\bar{d} \to \bar{u}ce^+\nu_e\mu^+\mu^-$ | $u$ | $u\bar{s} \to \bar{c}ue^+\nu_e\mu^+\mu^-$ | $u$ |
| $u\bar{c} \to d\bar{c}e^+\nu_e\mu^+\mu^-$ | $t$ | $c\bar{u} \to s\bar{u}e^+\nu_e\mu^+\mu^-$ | $t$ |
| $\bar{u}c \to s\bar{u}e^+\nu_e\mu^+\mu^-$ | $u$ | $\bar{c}u \to d\bar{c}e^+\nu_e\mu^+\mu^-$ | $u$ |
| $\bar{s}c \to \bar{c}ce^+\nu_e\mu^+\mu^-$ | $t+s$ | $u\bar{d} \to \bar{u}ue^+\nu_e\mu^+\mu^-$ | $u+s$ |
| $u\bar{u} \to d\bar{u}e^+\nu_e\mu^+\mu^-$ | $t+s$ | $c\bar{c} \to s\bar{c}e^+\nu_e\mu^+\mu^-$ | $t+s$ |
| $\bar{u}u \to d\bar{u}e^+\nu_e\mu^+\mu^-$ | $u+s$ | $\bar{c}c \to s\bar{c}e^+\nu_e\mu^+\mu^-$ | $u+s$ |
| $\bar{d}u \to \bar{u}ue^+\nu_e\mu^+\mu^-$ | $t+s$ | $c\bar{s} \to \bar{c}ce^+\nu_e\mu^+\mu^-$ | $u+s$ |
| $u\bar{d} \to \bar{c}ce^+\nu_e\mu^+\mu^-$ | $s$ | $\bar{s}c \to \bar{u}ue^+\nu_e\mu^+\mu^-$ | $s$ |
| $\bar{d}u \to \bar{c}ce^+\nu_e\mu^+\mu^-$ | $s$ | $c\bar{s} \to \bar{u}ue^+\nu_e\mu^+\mu^-$ | $s$ |
| $u\bar{u} \to s\bar{c}e^+\nu_e\mu^+\mu^-$ | $s$ | $c\bar{c} \to d\bar{u}e^+\nu_e\mu^+\mu^-$ | $s$ |
| $\bar{u}u \to s\bar{c}e^+\nu_e\mu^+\mu^-$ | $s$ | $\bar{c}c \to d\bar{u}e^+\nu_e\mu^+\mu^-$ | $s$ |

**Table 3.4:** List of subprocesses contributing to intermediate $W^+Z/\gamma$ processes with one up-type quark line at the leading order. The subprocesses corresponding to $W^-Z/\gamma$ production can be obtained by applying charge conjugation (similarly as in the second column in Table 3.2).

have, however, chosen to omit it as its experimental detection is problematic.

The next-to-leading-order involves a similar type of subprocesses as was described in the $W^+W^+$ case in the previous section: they include virtual QCD corrections obtained by appending a gluon loop to the quark lines and real radiation corrections with gluon either in final or in initial state. The subprocesses for the latter case are listed in Table 3.6.

| $\mathbf{pp \to jjW^+Z}/\gamma$**: us** $\to$ **dse**$^+\nu_e\mu^+\mu^-$ | | | |
|---|---|---|---|
| $QQ \to QQ\mathrm{e}^+\nu_\mathrm{e}\mu^+\mu^-$ | | | |
| $\mathrm{us} \to \mathrm{dse}^+\nu_\mathrm{e}\mu^+\mu^-$ | $t$ | $\mathrm{dc} \to \mathrm{dse}^+\nu_\mathrm{e}\mu^+\mu^-$ | $t$ |
| $\mathrm{su} \to \mathrm{dse}^+\nu_\mathrm{e}\mu^+\mu^-$ | $u$ | $\mathrm{cd} \to \mathrm{dse}^+\nu_\mathrm{e}\mu^+\mu^-$ | $u$ |
| $\mathrm{du} \to \mathrm{dde}^+\nu_\mathrm{e}\mu^+\mu^-$ | $\frac{t+u}{2}$ | $\mathrm{sc} \to \mathrm{sse}^+\nu_\mathrm{e}\mu^+\mu^-$ | $\frac{t+u}{2}$ |
| $\mathrm{ud} \to \mathrm{dde}^+\nu_\mathrm{e}\mu^+\mu^-$ | $\frac{t+u}{2}$ | $\mathrm{cs} \to \mathrm{sse}^+\nu_\mathrm{e}\mu^+\mu^-$ | $\frac{t+u}{2}$ |
| $\bar{Q}\bar{Q} \to \bar{Q}\bar{Q}\mathrm{e}^+\nu_\mathrm{e}\mu^+\mu^-$ | | | |
| $\bar{\mathrm{d}}\bar{\mathrm{s}} \to \bar{\mathrm{u}}\bar{\mathrm{s}}\mathrm{e}^+\nu_\mathrm{e}\mu^+\mu^-$ | $t$ | $\bar{\mathrm{s}}\bar{\mathrm{d}} \to \bar{\mathrm{c}}\bar{\mathrm{d}}\mathrm{e}^+\nu_\mathrm{e}\mu^+\mu^-$ | $t$ |
| $\bar{\mathrm{s}}\bar{\mathrm{d}} \to \bar{\mathrm{u}}\bar{\mathrm{s}}\mathrm{e}^+\nu_\mathrm{e}\mu^+\mu^-$ | $u$ | $\bar{\mathrm{d}}\bar{\mathrm{s}} \to \bar{\mathrm{c}}\bar{\mathrm{d}}\mathrm{e}^+\nu_\mathrm{e}\mu^+\mu^-$ | $u$ |
| $\bar{\mathrm{d}}\bar{\mathrm{d}} \to \bar{\mathrm{u}}\bar{\mathrm{d}}\mathrm{e}^+\nu_\mathrm{e}\mu^+\mu^-$ | $t+u$ | $\bar{\mathrm{s}}\bar{\mathrm{s}} \to \bar{\mathrm{c}}\bar{\mathrm{s}}\mathrm{e}^+\nu_\mathrm{e}\mu^+\mu^-$ | $t+u$ |
| $\bar{Q}Q \to \bar{Q}Q\mathrm{e}^+\nu_\mathrm{e}\mu^+\mu^-$ | | | |
| $\bar{\mathrm{d}}\mathrm{s} \to \bar{\mathrm{u}}\mathrm{se}^+\nu_\mathrm{e}\mu^+\mu^-$ | $t$ | $\bar{\mathrm{s}}\mathrm{d} \to \bar{\mathrm{c}}\mathrm{de}^+\nu_\mathrm{e}\mu^+\mu^-$ | $t$ |
| $\mathrm{s}\bar{\mathrm{d}} \to \bar{\mathrm{u}}\mathrm{se}^+\nu_\mathrm{e}\mu^+\mu^-$ | $u$ | $\mathrm{d}\bar{\mathrm{s}} \to \bar{\mathrm{c}}\mathrm{de}^+\nu_\mathrm{e}\mu^+\mu^-$ | $u$ |
| $\mathrm{u}\bar{\mathrm{s}} \to \mathrm{d}\bar{\mathrm{s}}\mathrm{e}^+\nu_\mathrm{e}\mu^+\mu^-$ | $t$ | $\mathrm{c}\bar{\mathrm{d}} \to \mathrm{s}\bar{\mathrm{d}}\mathrm{e}^+\nu_\mathrm{e}\mu^+\mu^-$ | $t$ |
| $\bar{\mathrm{d}}\mathrm{c} \to \mathrm{s}\bar{\mathrm{d}}\mathrm{e}^+\nu_\mathrm{e}\mu^+\mu^-$ | $u$ | $\bar{\mathrm{s}}\mathrm{u} \to \mathrm{d}\bar{\mathrm{s}}\mathrm{e}^+\nu_\mathrm{e}\mu^+\mu^-$ | $u$ |
| $\bar{\mathrm{s}}\mathrm{s} \to \bar{\mathrm{c}}\mathrm{se}^+\nu_\mathrm{e}\mu^+\mu^-$ | $t+s$ | $\mathrm{d}\bar{\mathrm{d}} \to \bar{\mathrm{u}}\mathrm{de}^+\nu_\mathrm{e}\mu^+\mu^-$ | $u+s$ |
| $\mathrm{u}\bar{\mathrm{d}} \to \mathrm{d}\bar{\mathrm{d}}\mathrm{e}^+\nu_\mathrm{e}\mu^+\mu^-$ | $t+s$ | $\mathrm{c}\bar{\mathrm{s}} \to \mathrm{s}\bar{\mathrm{s}}\mathrm{e}^+\nu_\mathrm{e}\mu^+\mu^-$ | $t+s$ |
| $\bar{\mathrm{d}}\mathrm{u} \to \mathrm{d}\bar{\mathrm{d}}\mathrm{e}^+\nu_\mathrm{e}\mu^+\mu^-$ | $u+s$ | $\bar{\mathrm{s}}\mathrm{c} \to \mathrm{s}\bar{\mathrm{s}}\mathrm{e}^+\nu_\mathrm{e}\mu^+\mu^-$ | $u+s$ |
| $\bar{\mathrm{d}}\mathrm{d} \to \bar{\mathrm{u}}\mathrm{de}^+\nu_\mathrm{e}\mu^+\mu^-$ | $t+s$ | $\mathrm{s}\bar{\mathrm{s}} \to \bar{\mathrm{c}}\mathrm{se}^+\nu_\mathrm{e}\mu^+\mu^-$ | $u+s$ |
| $\mathrm{d}\bar{\mathrm{d}} \to \bar{\mathrm{c}}\mathrm{se}^+\nu_\mathrm{e}\mu^+\mu^-$ | $s$ | $\bar{\mathrm{s}}\mathrm{s} \to \bar{\mathrm{u}}\mathrm{de}^+\nu_\mathrm{e}\mu^+\mu^-$ | $s$ |
| $\mathrm{u}\bar{\mathrm{d}} \to \mathrm{s}\bar{\mathrm{s}}\mathrm{e}^+\nu_\mathrm{e}\mu^+\mu^-$ | $s$ | $\mathrm{s}\bar{\mathrm{s}} \to \bar{\mathrm{u}}\mathrm{de}^+\nu_\mathrm{e}\mu^+\mu^-$ | $s$ |
| $\mathrm{d}\bar{\mathrm{d}} \to \mathrm{c}\bar{\mathrm{s}}\mathrm{e}^+\nu_\mathrm{e}\mu^+\mu^-$ | $s$ | $\mathrm{c}\bar{\mathrm{s}} \to \mathrm{d}\bar{\mathrm{d}}\mathrm{e}^+\nu_\mathrm{e}\mu^+\mu^-$ | $s$ |
| $\bar{\mathrm{d}}\mathrm{u} \to \mathrm{s}\bar{\mathrm{s}}\mathrm{e}^+\nu_\mathrm{e}\mu^+\mu^-$ | $s$ | $\bar{\mathrm{s}}\mathrm{c} \to \mathrm{d}\bar{\mathrm{d}}\mathrm{e}^+\nu_\mathrm{e}\mu^+\mu^-$ | $s$ |

**Table 3.5:** List of subprocesses contributing to intermediate $\mathrm{W^+Z}/\gamma$ with one down-type quark line processes at the leading order. The subprocesses corresponding to $\mathrm{W^-Z}/\gamma$ can be obtained by applying charge conjugation (similarly as in the second column in Table 3.2).

## 3.3 qq $\to$ jjW$^+$W$^-$ $\to$ jj4l

In this process, one positively and one negatively-charged W boson are radiated from the quark lines. In the vector-boson fusion diagrams, they scatter and subsequently decay into two lepton pairs formed by a positively and negatively charged lepton and neutrino (or antineutrino). A generic subprocess can be written as $\mathrm{qq} \to \mathrm{jj}\ \mathrm{e}^+\nu_\mathrm{e}\mu^-\bar{\nu}_\mu$.

| $\mathbf{pp \to jjW^+Z/\gamma{:}uc \to dc\ e^+\nu_e\mu^+\mu^-}$ | | $\mathbf{pp \to jjW^+Z/\gamma{:}us \to ds\ e^+\nu_e\mu^+\mu^-}$ | |
|---|---|---|---|
| $GQ \to \bar{Q}QQ\ \mathrm{e}^+\nu_\mathrm{e}\mu^+\mu^-$ | | | |
| $\mathrm{gc} \to \bar{\mathrm{u}}\mathrm{dc}\ \mathrm{e}^+\nu_\mathrm{e}\mu^+\mu^-$ | $\mathrm{gu} \to \bar{\mathrm{c}}\mathrm{su}\ \mathrm{e}^+\nu_\mathrm{e}\mu^+\mu^-$ | $\mathrm{gs} \to \bar{\mathrm{u}}\mathrm{ds}\ \mathrm{e}^+\nu_\mathrm{e}\mu^+\mu^-$ | $\mathrm{gd} \to \bar{\mathrm{c}}\mathrm{ds}\ \mathrm{e}^+\nu_\mathrm{e}\mu^+\mu^-$ |
| $\mathrm{gu} \to \bar{\mathrm{c}}\mathrm{dc}\ \mathrm{e}^+\nu_\mathrm{e}\mu^+\mu^-$ | $\mathrm{gc} \to \bar{\mathrm{u}}\mathrm{su}\ \mathrm{e}^+\nu_\mathrm{e}\mu^+\mu^-$ | $\mathrm{gu} \to \bar{\mathrm{s}}\mathrm{ds}\ \mathrm{e}^+\nu_\mathrm{e}\mu^+\mu^-$ | $\mathrm{gc} \to \bar{\mathrm{d}}\mathrm{ds}\ \mathrm{e}^+\nu_\mathrm{e}\mu^+\mu^-$ |
| $\mathrm{gu} \to \bar{\mathrm{u}}\mathrm{du}\ \mathrm{e}^+\nu_\mathrm{e}\mu^+\mu^-$ | $\mathrm{gc} \to \bar{\mathrm{c}}\mathrm{sc}\ \mathrm{e}^+\nu_\mathrm{e}\mu^+\mu^-$ | $\mathrm{gu} \to \bar{\mathrm{d}}\mathrm{dd}\ \mathrm{e}^+\nu_\mathrm{e}\mu^+\mu^-$ | $\mathrm{gs} \to \bar{\mathrm{c}}\mathrm{ss}\ \mathrm{e}^+\nu_\mathrm{e}\mu^+\mu^-$ |
| | | $\mathrm{gd} \to \bar{\mathrm{u}}\mathrm{dd}\ \mathrm{e}^+\nu_\mathrm{e}\mu^+\mu^-$ | $\mathrm{gc} \to \bar{\mathrm{s}}\mathrm{ss}\ \mathrm{e}^+\nu_\mathrm{e}\mu^+\mu^-$ |
| $G\bar{Q} \to Q\bar{Q}\bar{Q}\ \mathrm{e}^+\nu_\mathrm{e}\mu^+\mu^-$ | | | |
| $\mathrm{g}\bar{\mathrm{c}} \to \mathrm{d}\bar{\mathrm{u}}\bar{\mathrm{c}}\ \mathrm{e}^+\nu_\mathrm{e}\mu^+\mu^-$ | $\mathrm{g}\bar{\mathrm{s}} \to \mathrm{u}\bar{\mathrm{u}}\bar{\mathrm{c}}\ \mathrm{e}^+\nu_\mathrm{e}\mu^+\mu^-$ | $\mathrm{g}\bar{\mathrm{s}} \to \mathrm{d}\bar{\mathrm{u}}\bar{\mathrm{s}}\ \mathrm{e}^+\nu_\mathrm{e}\mu^+\mu^-$ | $\mathrm{g}\bar{\mathrm{d}} \to \mathrm{s}\bar{\mathrm{c}}\bar{\mathrm{d}}\ \mathrm{e}^+\nu_\mathrm{e}\mu^+\mu^-$ |
| $\mathrm{g}\bar{\mathrm{d}} \to \mathrm{c}\bar{\mathrm{u}}\bar{\mathrm{c}}\ \mathrm{e}^+\nu_\mathrm{e}\mu^+\mu^-$ | $\mathrm{g}\bar{\mathrm{u}} \to \mathrm{s}\bar{\mathrm{u}}\bar{\mathrm{c}}\ \mathrm{e}^+\nu_\mathrm{e}\mu^+\mu^-$ | $\mathrm{g}\bar{\mathrm{d}} \to \mathrm{s}\bar{\mathrm{u}}\bar{\mathrm{s}}\ \mathrm{e}^+\nu_\mathrm{e}\mu^+\mu^-$ | $\mathrm{g}\bar{\mathrm{s}} \to \mathrm{d}\bar{\mathrm{c}}\bar{\mathrm{d}}\ \mathrm{e}^+\nu_\mathrm{e}\mu^+\mu^-$ |
| $\mathrm{g}\bar{\mathrm{u}} \to \mathrm{d}\bar{\mathrm{u}}\bar{\mathrm{u}}\ \mathrm{e}^+\nu_\mathrm{e}\mu^+\mu^-$ | $\mathrm{g}\bar{\mathrm{c}} \to \mathrm{s}\bar{\mathrm{c}}\bar{\mathrm{c}}\ \mathrm{e}^+\nu_\mathrm{e}\mu^+\mu^-$ | $\mathrm{g}\bar{\mathrm{d}} \to \mathrm{d}\bar{\mathrm{u}}\bar{\mathrm{d}}\ \mathrm{e}^+\nu_\mathrm{e}\mu^+\mu^-$ | $\mathrm{g}\bar{\mathrm{s}} \to \mathrm{s}\bar{\mathrm{c}}\bar{\mathrm{s}}\ \mathrm{e}^+\nu_\mathrm{e}\mu^+\mu^-$ |
| $\mathrm{g}\bar{\mathrm{d}} \to \mathrm{u}\bar{\mathrm{u}}\bar{\mathrm{u}}\ \mathrm{e}^+\nu_\mathrm{e}\mu^+\mu^-$ | $\mathrm{g}\bar{\mathrm{s}} \to \mathrm{c}\bar{\mathrm{c}}\bar{\mathrm{c}}\ \mathrm{e}^+\nu_\mathrm{e}\mu^+\mu^-$ | | |

**Table 3.6:** List subprocesses a gluon in the initial state contributing to intermediate $W^+\mathrm{Z}$ processes at the next-to-leading order, obtained from the generic process $\mathrm{uc} \to \mathrm{dc}\ \mathrm{e}^+\nu_\mathrm{e}\mu^+\mu^-$ and $\mathrm{us} \to \mathrm{ds}\ \mathrm{e}^+\nu_\mathrm{e}\mu^+\mu^-$ (on the right). The subprocesses corresponding to $\mathrm{W}^-\mathrm{Z}/\gamma$ can be obtained by applying charge conjugation (similarly as in the second column in Table 3.3).

Since the sum of all electric charges of leptons in the final state is zero, the overall charge of the initial-state quarks is the same as that of the final-state quarks. One possibility for constructing this configuration is if all initial- and final-state quarks are up-type (Table 3.7, left column) or down-type (Table 3.7, right column). Another possibility is for one quark leg to be up-type and the other down-type (e.g. $\mathrm{us} \to \mathrm{us}\ \mathrm{e}^+\nu_\mathrm{e}\mu^-\bar{\nu}_\mu$). A fourth possibility is one that contains W boson-scattering diagrams: one up-type quark and one down-type quark in both initial- and final- state, with each quark line changing its electric charge after radiating a W boson (e.g. $\mathrm{us} \to \mathrm{dc}\ \mathrm{e}^+\nu_\mathrm{e}\mu^-\bar{\nu}_\mu$). The subprocesses belonging to the last two cases are listed together in Table 3.8 since they interfere with each other in case the flavours of both quark lines are identical. For instance, the process $\mathrm{ud} \to \mathrm{ud}\ \mathrm{e}^+\nu_\mathrm{e}\mu^-\bar{\nu}_\mu$ receives $t$-channel contribution corresponding to the generic subprocess $\mathrm{us} \to \mathrm{us}\ \mathrm{e}^+\nu_\mathrm{e}\mu^-\bar{\nu}_\mu$, and $u$-channel contribution obtained from $\mathrm{us} \to \mathrm{dc}\ \mathrm{e}^+\nu_\mathrm{e}\mu^-\bar{\nu}_\mu$.

The subprocesses involving virtual QCD corrections and final-state-gluon radiation can be derived from these in the same way as described previously. Initial-state-gluon subprocesses are listed in Table 3.9.

## 3.4 $\mathbf{qq \to jjZZ/Z\gamma/\gamma\gamma \to jj4l}$

This VBF process involves a production of two gauge bosons with neutral charge (two Z bosons, two photons or one of each). The gauge bosons subsequently decay either into

| $\mathbf{pp \to jjW^+W^-}$ | | | |
|---|---|---|---|
| $\mathbf{uc \to uce^+\nu_e\mu^-\bar{\nu}_\mu}$ | | $\mathbf{ds \to dse^+\nu_e\mu^-\bar{\nu}_\mu}$ | |
| $QQ \to QQe^+\nu_e\mu^-\bar{\nu}_\mu$ | | | |
| $uc \to uce^+\nu_e\mu^-\bar{\nu}_\mu$ | $t$ | $ds \to dse^+\nu_e\mu^-\bar{\nu}_\mu$ | $t$ |
| $cu \to uce^+\nu_e\mu^-\bar{\nu}_\mu$ | $u$ | $sd \to dse^+\nu_e\mu^-\bar{\nu}_\mu$ | $u$ |
| $uu \to uue^+\nu_e\mu^-\bar{\nu}_\mu$ | $\frac{t+u}{2}$ | $dd \to dde^+\nu_e\mu^-\bar{\nu}_\mu$ | $\frac{t+u}{2}$ |
| $cc \to cce^+\nu_e\mu^-\bar{\nu}_\mu$ | $\frac{t+u}{2}$ | $ss \to sse^+\nu_e\mu^-\bar{\nu}_\mu$ | $\frac{t+u}{2}$ |
| $\bar{Q}\bar{Q} \to \bar{Q}\bar{Q}e^+\nu_e\mu^-\bar{\nu}_\mu$ | | | |
| $\bar{u}\bar{c} \to \bar{u}\bar{c}e^+\nu_e\mu^-\bar{\nu}_\mu$ | $t$ | $\bar{d}\bar{s} \to \bar{d}\bar{s}e^+\nu_e\mu^-\bar{\nu}_\mu$ | $t$ |
| $\bar{c}\bar{u} \to \bar{u}\bar{c}e^+\nu_e\mu^-\bar{\nu}_\mu$ | $u$ | $\bar{s}\bar{d} \to \bar{d}\bar{s}e^+\nu_e\mu^-\bar{\nu}_\mu$ | $u$ |
| $\bar{u}\bar{u} \to \bar{u}\bar{u}e^+\nu_e\mu^-\bar{\nu}_\mu$ | $\frac{t+u}{2}$ | $\bar{d}\bar{d} \to \bar{d}\bar{d}e^+\nu_e\mu^-\bar{\nu}_\mu$ | $\frac{t+u}{2}$ |
| $\bar{c}\bar{c} \to \bar{u}\bar{u}e^+\nu_e\mu^-\bar{\nu}_\mu$ | $\frac{t+u}{2}$ | $\bar{s}\bar{s} \to \bar{d}\bar{d}e^+\nu_e\mu^-\bar{\nu}_\mu$ | $\frac{t+u}{2}$ |
| $\bar{Q}Q \to \bar{Q}Qe^+\nu_e\mu^-\bar{\nu}_\mu$ | | | |
| $\bar{u}c \to \bar{u}ce^+\nu_e\mu^-\bar{\nu}_\mu$ | $t$ | $\bar{s}d \to \bar{s}de^+\nu_e\mu^-\bar{\nu}_\mu$ | $t$ |
| $\bar{c}u \to \bar{c}ue^+\nu_e\mu^-\bar{\nu}_\mu$ | $t$ | $\bar{d}s \to \bar{d}se^+\nu_e\mu^-\bar{\nu}_\mu$ | $t$ |
| $c\bar{u} \to \bar{u}ce^+\nu_e\mu^-\bar{\nu}_\mu$ | $u$ | $d\bar{s} \to \bar{s}de^+\nu_e\mu^-\bar{\nu}_\mu$ | $u$ |
| $u\bar{c} \to \bar{c}ue^+\nu_e\mu^-\bar{\nu}_\mu$ | $u$ | $s\bar{d} \to \bar{d}se^+\nu_e\mu^-\bar{\nu}_\mu$ | $u$ |
| $\bar{u}u \to \bar{c}ce^+\nu_e\mu^-\bar{\nu}_\mu$ | $s$ | $\bar{d}d \to \bar{s}se^+\nu_e\mu^-\bar{\nu}_\mu$ | $s$ |
| $\bar{c}c \to \bar{u}ue^+\nu_e\mu^-\bar{\nu}_\mu$ | $s$ | $\bar{s}s \to \bar{d}de^+\nu_e\mu^-\bar{\nu}_\mu$ | $s$ |
| $u\bar{u} \to \bar{c}ce^+\nu_e\mu^-\bar{\nu}_\mu$ | $s$ | $d\bar{d} \to \bar{s}se^+\nu_e\mu^-\bar{\nu}_\mu$ | $s$ |
| $c\bar{c} \to \bar{u}ue^+\nu_e\mu^-\bar{\nu}_\mu$ | $s$ | $s\bar{s} \to \bar{d}de^+\nu_e\mu^-\bar{\nu}_\mu$ | $s$ |
| $\bar{u}u \to \bar{u}ue^+\nu_e\mu^-\bar{\nu}_\mu$ | $s+t$ | $\bar{d}d \to \bar{d}de^+\nu_e\mu^-\bar{\nu}_\mu$ | $s+t$ |
| $\bar{c}c \to \bar{c}ce^+\nu_e\mu^-\bar{\nu}_\mu$ | $s+t$ | $\bar{s}s \to \bar{s}se^+\nu_e\mu^-\bar{\nu}_\mu$ | $s+t$ |
| $u\bar{u} \to \bar{u}ue^+\nu_e\mu^-\bar{\nu}_\mu$ | $s+u$ | $d\bar{d} \to \bar{d}de^+\nu_e\mu^-\bar{\nu}_\mu$ | $s+u$ |
| $c\bar{c} \to \bar{c}ce^+\nu_e\mu^-\bar{\nu}_\mu$ | $s+u$ | $s\bar{s} \to \bar{s}se^+\nu_e\mu^-\bar{\nu}_\mu$ | $s+u$ |

**Table 3.7:** List of subprocesses contributing to intermediate $W^+W^-$ processes at leading order with both quark lines formed either by up-type quarks (left column) or down-type quarks (right column).

an electron-positron (or muon-antimuon) or neutrino-antineutrino pair. Since we do not consider processes with more than 2 neutrinos in the final state, we encounter only two types of subprocesses: $pp \to jje^+e^-\mu^+\mu^-$ and $pp \to jje^+e^-\bar{\nu}_\mu\nu_\mu$.

The overall electric charge of the final-state leptons is 0, similarly as in the case of $W^+W^-$ described in the previous section. As a consequence, the same considerations for the initial- and final-state quarks apply and result in the same four charge configurations

| $\mathbf{pp \to jjW^+W^-}$ | | | |
|---|---|---|---|
| $QQ \to QQ\mathrm{e}^+\nu_\mathrm{e}\mu^-\bar{\nu}_\mu$ | | | |
| $\mathrm{dc} \to \mathrm{dc}\ \mathrm{e}^+\nu_\mathrm{e}\mu^-\bar{\nu}_\mu$ | $t$ | $\mathrm{us} \to \mathrm{dc}\ \mathrm{e}^+\nu_\mathrm{e}\mu^-\bar{\nu}_\mu$ | $t$ |
| $\mathrm{su} \to \mathrm{su}\ \mathrm{e}^+\nu_\mathrm{e}\mu^-\bar{\nu}_\mu$ | $t$ | $\mathrm{cd} \to \mathrm{su}\ \mathrm{e}^+\nu_\mathrm{e}\mu^-\bar{\nu}_\mu$ | $t$ |
| $\mathrm{cd} \to \mathrm{dc}\ \mathrm{e}^+\nu_\mathrm{e}\mu^-\bar{\nu}_\mu$ | $u$ | $\mathrm{su} \to \mathrm{dc}\ \mathrm{e}^+\nu_\mathrm{e}\mu^-\bar{\nu}_\mu$ | $u$ |
| $\mathrm{us} \to \mathrm{su}\ \mathrm{e}^+\nu_\mathrm{e}\mu^-\bar{\nu}_\mu$ | $u$ | $\mathrm{dc} \to \mathrm{su}\ \mathrm{e}^+\nu_\mathrm{e}\mu^-\bar{\nu}_\mu$ | $u$ |
| $\mathrm{ud} \to \mathrm{du}\ \mathrm{e}^+\nu_\mathrm{e}\mu^-\bar{\nu}_\mu$ | $t+u$ | $\mathrm{du} \to \mathrm{du}\ \mathrm{e}^+\nu_\mathrm{e}\mu^-\bar{\nu}_\mu$ | $t+u$ |
| $\mathrm{cs} \to \mathrm{sc}\ \mathrm{e}^+\nu_\mathrm{e}\mu^-\bar{\nu}_\mu$ | $t+u$ | $\mathrm{sc} \to \mathrm{sc}\ \mathrm{e}^+\nu_\mathrm{e}\mu^-\bar{\nu}_\mu$ | $t+u$ |
| $\bar{Q}\bar{Q} \to \bar{Q}\bar{Q}\mathrm{e}^+\nu_\mathrm{e}\mu^-\bar{\nu}_\mu$ | | | |
| $\bar{\mathrm{d}}\bar{\mathrm{c}} \to \bar{\mathrm{u}}\bar{\mathrm{s}}\ \mathrm{e}^+\nu_\mathrm{e}\mu^-\bar{\nu}_\mu$ | $t$ | $\bar{\mathrm{u}}\bar{\mathrm{s}} \to \bar{\mathrm{u}}\bar{\mathrm{s}}\ \mathrm{e}^+\nu_\mathrm{e}\mu^-\bar{\nu}_\mu$ | $t$ |
| $\bar{\mathrm{s}}\bar{\mathrm{u}} \to \bar{\mathrm{c}}\bar{\mathrm{d}}\ \mathrm{e}^+\nu_\mathrm{e}\mu^-\bar{\nu}_\mu$ | $t$ | $\bar{\mathrm{c}}\bar{\mathrm{d}} \to \bar{\mathrm{c}}\bar{\mathrm{d}}\ \mathrm{e}^+\nu_\mathrm{e}\mu^-\bar{\nu}_\mu$ | $t$ |
| $\bar{\mathrm{c}}\bar{\mathrm{d}} \to \bar{\mathrm{u}}\bar{\mathrm{s}}\ \mathrm{e}^+\nu_\mathrm{e}\mu^-\bar{\nu}_\mu$ | $u$ | $\bar{\mathrm{s}}\bar{\mathrm{u}} \to \bar{\mathrm{u}}\bar{\mathrm{s}}\ \mathrm{e}^+\nu_\mathrm{e}\mu^-\bar{\nu}_\mu$ | $u$ |
| $\bar{\mathrm{u}}\bar{\mathrm{s}} \to \bar{\mathrm{c}}\bar{\mathrm{d}}\ \mathrm{e}^+\nu_\mathrm{e}\mu^-\bar{\nu}_\mu$ | $u$ | $\bar{\mathrm{d}}\bar{\mathrm{c}} \to \bar{\mathrm{c}}\bar{\mathrm{d}}\ \mathrm{e}^+\nu_\mathrm{e}\mu^-\bar{\nu}_\mu$ | $u$ |
| $\bar{\mathrm{d}}\bar{\mathrm{u}} \to \bar{\mathrm{u}}\bar{\mathrm{d}}\ \mathrm{e}^+\nu_\mathrm{e}\mu^-\bar{\nu}_\mu$ | $t+u$ | $\bar{\mathrm{u}}\bar{\mathrm{d}} \to \bar{\mathrm{u}}\bar{\mathrm{d}}\ \mathrm{e}^+\nu_\mathrm{e}\mu^-\bar{\nu}_\mu$ | $t+u$ |
| $\bar{\mathrm{s}}\bar{\mathrm{c}} \to \bar{\mathrm{c}}\bar{\mathrm{s}}\ \mathrm{e}^+\nu_\mathrm{e}\mu^-\bar{\nu}_\mu$ | $t+u$ | $\bar{\mathrm{c}}\bar{\mathrm{s}} \to \bar{\mathrm{c}}\bar{\mathrm{s}}\ \mathrm{e}^+\nu_\mathrm{e}\mu^-\bar{\nu}_\mu$ | $t+u$ |
| $\bar{Q}Q \to \bar{Q}Q\mathrm{e}^+\nu_\mathrm{e}\mu^-\bar{\nu}_\mu$ | | | |
| $\bar{\mathrm{d}}\mathrm{s} \to \bar{\mathrm{u}}\mathrm{c}\ \mathrm{e}^+\nu_\mathrm{e}\mu^-\bar{\nu}_\mu$ | $t$ | $\mathrm{s}\bar{\mathrm{d}} \to \bar{\mathrm{u}}\mathrm{c}\ \mathrm{e}^+\nu_\mathrm{e}\mu^-\bar{\nu}_\mu$ | $u$ |
| $\bar{\mathrm{s}}\mathrm{d} \to \bar{\mathrm{c}}\mathrm{u}\ \mathrm{e}^+\nu_\mathrm{e}\mu^-\bar{\nu}_\mu$ | $t$ | $\mathrm{d}\bar{\mathrm{s}} \to \bar{\mathrm{c}}\mathrm{u}\ \mathrm{e}^+\nu_\mathrm{e}\mu^-\bar{\nu}_\mu$ | $u$ |
| $\bar{\mathrm{d}}\mathrm{d} \to \bar{\mathrm{c}}\mathrm{c}\ \mathrm{e}^+\nu_\mathrm{e}\mu^-\bar{\nu}_\mu$ | $s$ | $\mathrm{d}\bar{\mathrm{d}} \to \bar{\mathrm{c}}\mathrm{c}\ \mathrm{e}^+\nu_\mathrm{e}\mu^-\bar{\nu}_\mu$ | $s$ |
| $\bar{\mathrm{s}}\mathrm{s} \to \bar{\mathrm{u}}\mathrm{u}\ \mathrm{e}^+\nu_\mathrm{e}\mu^-\bar{\nu}_\mu$ | $s$ | $\mathrm{s}\bar{\mathrm{s}} \to \bar{\mathrm{u}}\mathrm{u}\ \mathrm{e}^+\nu_\mathrm{e}\mu^-\bar{\nu}_\mu$ | $s$ |
| $\bar{\mathrm{d}}\mathrm{d} \to \bar{\mathrm{u}}\mathrm{u}\ \mathrm{e}^+\nu_\mathrm{e}\mu^-\bar{\nu}_\mu$ | $t+s$ | $\mathrm{d}\bar{\mathrm{d}} \to \bar{\mathrm{u}}\mathrm{u}\ \mathrm{e}^+\nu_\mathrm{e}\mu^-\bar{\nu}_\mu$ | $u+s$ |
| $\bar{\mathrm{s}}\mathrm{s} \to \bar{\mathrm{c}}\mathrm{c}\ \mathrm{e}^+\nu_\mathrm{e}\mu^-\bar{\nu}_\mu$ | $t+s$ | $\mathrm{s}\bar{\mathrm{s}} \to \bar{\mathrm{c}}\mathrm{c}\ \mathrm{e}^+\nu_\mathrm{e}\mu^-\bar{\nu}_\mu$ | $u+s$ |
| $\bar{\mathrm{u}}\mathrm{c} \to \bar{\mathrm{d}}\mathrm{s}\ \mathrm{e}^+\nu_\mathrm{e}\mu^-\bar{\nu}_\mu$ | $t$ | $\mathrm{c}\bar{\mathrm{u}} \to \bar{\mathrm{d}}\mathrm{s}\ \mathrm{e}^+\nu_\mathrm{e}\mu^-\bar{\nu}_\mu$ | $u$ |
| $\bar{\mathrm{c}}\mathrm{u} \to \bar{\mathrm{s}}\mathrm{d}\ \mathrm{e}^+\nu_\mathrm{e}\mu^-\bar{\nu}_\mu$ | $t$ | $\mathrm{u}\bar{\mathrm{c}} \to \bar{\mathrm{s}}\mathrm{d}\ \mathrm{e}^+\nu_\mathrm{e}\mu^-\bar{\nu}_\mu$ | $u$ |
| $\bar{\mathrm{u}}\mathrm{u} \to \bar{\mathrm{s}}\mathrm{s}\ \mathrm{e}^+\nu_\mathrm{e}\mu^-\bar{\nu}_\mu$ | $s$ | $\mathrm{u}\bar{\mathrm{u}} \to \bar{\mathrm{s}}\mathrm{s}\ \mathrm{e}^+\nu_\mathrm{e}\mu^-\bar{\nu}_\mu$ | $s$ |
| $\bar{\mathrm{c}}\mathrm{c} \to \bar{\mathrm{d}}\mathrm{d}\ \mathrm{e}^+\nu_\mathrm{e}\mu^-\bar{\nu}_\mu$ | $s$ | $\mathrm{c}\bar{\mathrm{c}} \to \bar{\mathrm{d}}\mathrm{d}\ \mathrm{e}^+\nu_\mathrm{e}\mu^-\bar{\nu}_\mu$ | $s$ |
| $\bar{\mathrm{u}}\mathrm{u} \to \bar{\mathrm{d}}\mathrm{d}\ \mathrm{e}^+\nu_\mathrm{e}\mu^-\bar{\nu}_\mu$ | $t+s$ | $\mathrm{u}\bar{\mathrm{u}} \to \bar{\mathrm{d}}\mathrm{d}\ \mathrm{e}^+\nu_\mathrm{e}\mu^-\bar{\nu}_\mu$ | $u+s$ |
| $\bar{\mathrm{c}}\mathrm{c} \to \bar{\mathrm{s}}\mathrm{s}\ \mathrm{e}^+\nu_\mathrm{e}\mu^-\bar{\nu}_\mu$ | $t+s$ | $\mathrm{c}\bar{\mathrm{c}} \to \bar{\mathrm{s}}\mathrm{s}\ \mathrm{e}^+\nu_\mathrm{e}\mu^-\bar{\nu}_\mu$ | $u+s$ |

of the quark legs. The relevant subprocesses are thus identical to the ones listed in Table 3.7 and Table 3.8 save for the leptonic final state which should be replaced $\mathrm{e}^+\mathrm{e}^-\mu^+\mu^-$ and $\mathrm{e}^+\mathrm{e}^-\bar{\nu}_\mu\nu_\mu$. In a similar manner, the list of the initial-state-gluon subprocesses in Table 3.9 is also applicable.

In the case where both leptonic pairs in the final state involving the neutrino-antineutrino pair are of the same flavour, ($\mathrm{e}^+\mathrm{e}^-\bar{\nu}_\mathrm{e}\nu_\mathrm{e}$), the interference with the subprocesses in Table 3.7 and 3.8 should be taken into account.

| $\bar{Q}Q \to \bar{Q}Q\mathrm{e}^+\nu_\mathrm{e}\mu^-\bar{\nu}_\mu$ | | | |
|---|---|---|---|
| $\bar{\mathrm{u}}\mathrm{s} \to \bar{\mathrm{u}}\mathrm{s}\ \mathrm{e}^+\nu_\mathrm{e}\mu^-\bar{\nu}_\mu$ | $t$ | $\mathrm{s}\bar{\mathrm{u}} \to \bar{\mathrm{u}}\mathrm{s}\ \mathrm{e}^+\nu_\mathrm{e}\mu^-\bar{\nu}_\mu$ | $u$ |
| $\bar{\mathrm{c}}\mathrm{d} \to \bar{\mathrm{c}}\mathrm{d}\ \mathrm{e}^+\nu_\mathrm{e}\mu^-\bar{\nu}_\mu$ | $t$ | $\mathrm{d}\bar{\mathrm{c}} \to \bar{\mathrm{c}}\mathrm{d}\ \mathrm{e}^+\nu_\mathrm{e}\mu^-\bar{\nu}_\mu$ | $u$ |
| $\bar{\mathrm{u}}\mathrm{d} \to \bar{\mathrm{c}}\mathrm{s}\ \mathrm{e}^+\nu_\mathrm{e}\mu^-\bar{\nu}_\mu$ | $s$ | $\mathrm{d}\bar{\mathrm{u}} \to \bar{\mathrm{c}}\mathrm{s}\ \mathrm{e}^+\nu_\mathrm{e}\mu^-\bar{\nu}_\mu$ | $s$ |
| $\bar{\mathrm{c}}\mathrm{s} \to \bar{\mathrm{u}}\mathrm{d}\ \mathrm{e}^+\nu_\mathrm{e}\mu^-\bar{\nu}_\mu$ | $s$ | $\mathrm{s}\bar{\mathrm{c}} \to \bar{\mathrm{u}}\mathrm{d}\ \mathrm{e}^+\nu_\mathrm{e}\mu^-\bar{\nu}_\mu$ | $s$ |
| $\bar{\mathrm{u}}\mathrm{d} \to \bar{\mathrm{u}}\mathrm{d}\ \mathrm{e}^+\nu_\mathrm{e}\mu^-\bar{\nu}_\mu$ | $t+s$ | $\mathrm{d}\bar{\mathrm{u}} \to \bar{\mathrm{u}}\mathrm{d}\ \mathrm{e}^+\nu_\mathrm{e}\mu^-\bar{\nu}_\mu$ | $u+s$ |
| $\bar{\mathrm{c}}\mathrm{s} \to \bar{\mathrm{c}}\mathrm{s}\ \mathrm{e}^+\nu_\mathrm{e}\mu^-\bar{\nu}_\mu$ | $t+s$ | $\mathrm{s}\bar{\mathrm{c}} \to \bar{\mathrm{c}}\mathrm{s}\ \mathrm{e}^+\nu_\mathrm{e}\mu^-\bar{\nu}_\mu$ | $u+s$ |
| $\bar{\mathrm{d}}\mathrm{c} \to \bar{\mathrm{d}}\mathrm{c}\ \mathrm{e}^+\nu_\mathrm{e}\mu^-\bar{\nu}_\mu$ | $t$ | $\mathrm{c}\bar{\mathrm{d}} \to \bar{\mathrm{d}}\mathrm{c}\ \mathrm{e}^+\nu_\mathrm{e}\mu^-\bar{\nu}_\mu$ | $u$ |
| $\bar{\mathrm{s}}\mathrm{u} \to \bar{\mathrm{s}}\mathrm{u}\ \mathrm{e}^+\nu_\mathrm{e}\mu^-\bar{\nu}_\mu$ | $t$ | $\mathrm{u}\bar{\mathrm{s}} \to \bar{\mathrm{s}}\mathrm{u}\ \mathrm{e}^+\nu_\mathrm{e}\mu^-\bar{\nu}_\mu$ | $u$ |
| $\bar{\mathrm{d}}\mathrm{u} \to \bar{\mathrm{s}}\mathrm{c}\ \mathrm{e}^+\nu_\mathrm{e}\mu^-\bar{\nu}_\mu$ | $s$ | $\mathrm{u}\bar{\mathrm{d}} \to \bar{\mathrm{s}}\mathrm{c}\ \mathrm{e}^+\nu_\mathrm{e}\mu^-\bar{\nu}_\mu$ | $s$ |
| $\bar{\mathrm{s}}\mathrm{c} \to \bar{\mathrm{d}}\mathrm{u}\ \mathrm{e}^+\nu_\mathrm{e}\mu^-\bar{\nu}_\mu$ | $s$ | $\mathrm{c}\bar{\mathrm{s}} \to \bar{\mathrm{d}}\mathrm{u}\ \mathrm{e}^+\nu_\mathrm{e}\mu^-\bar{\nu}_\mu$ | $s$ |
| $\bar{\mathrm{d}}\mathrm{u} \to \bar{\mathrm{d}}\mathrm{u}\ \mathrm{e}^+\nu_\mathrm{e}\mu^-\bar{\nu}_\mu$ | $t+s$ | $\mathrm{u}\bar{\mathrm{d}} \to \bar{\mathrm{d}}\mathrm{u}\ \mathrm{e}^+\nu_\mathrm{e}\mu^-\bar{\nu}_\mu$ | $u+s$ |
| $\bar{\mathrm{s}}\mathrm{c} \to \bar{\mathrm{s}}\mathrm{c}\ \mathrm{e}^+\nu_\mathrm{e}\mu^-\bar{\nu}_\mu$ | $t+s$ | $\mathrm{c}\bar{\mathrm{s}} \to \bar{\mathrm{s}}\mathrm{c}\ \mathrm{e}^+\nu_\mathrm{e}\mu^-\bar{\nu}_\mu$ | $u+s$ |

**Table 3.8:** List of subprocesses contributing to intermediate $\mathrm{W}^+\mathrm{W}^-$ processes at the leading order with the quark lines formed by a combination of up-type and down-type quarks.

| $\mathbf{pp \to jjW^+W^-}$ | | | |
|---|---|---|---|
| $GQ \to \bar{Q}QQ\ \mathrm{e}^+\nu_\mathrm{e}\mu^-\bar{\nu}_\mu$ | | | |
| $\mathrm{gc} \to \bar{\mathrm{d}}\mathrm{dc}\ \mathrm{e}^+\nu_\mathrm{e}\mu^-\bar{\nu}_\mu$ | $\mathrm{gd} \to \bar{\mathrm{c}}\mathrm{dc}\ \mathrm{e}^+\nu_\mathrm{e}\mu^-\bar{\nu}_\mu$ | $\mathrm{gu} \to \bar{\mathrm{s}}\mathrm{su}\ \mathrm{e}^+\nu_\mathrm{e}\mu^-\bar{\nu}_\mu$ | $\mathrm{gs} \to \bar{\mathrm{u}}\mathrm{su}\ \mathrm{e}^+\nu_\mathrm{e}\mu^-\bar{\nu}_\mu$ |
| $\mathrm{gd} \to \bar{\mathrm{u}}\mathrm{du}\ \mathrm{e}^+\nu_\mathrm{e}\mu^-\bar{\nu}_\mu$ | $\mathrm{gu} \to \bar{\mathrm{d}}\mathrm{du}\ \mathrm{e}^+\nu_\mathrm{e}\mu^-\bar{\nu}_\mu$ | $\mathrm{gs} \to \bar{\mathrm{c}}\mathrm{sc}\ \mathrm{e}^+\nu_\mathrm{e}\mu^-\bar{\nu}_\mu$ | $\mathrm{gc} \to \bar{\mathrm{s}}\mathrm{sc}\ \mathrm{e}^+\nu_\mathrm{e}\mu^-\bar{\nu}_\mu$ |
| $\mathrm{gs} \to \bar{\mathrm{u}}\mathrm{dc}\ \mathrm{e}^+\nu_\mathrm{e}\mu^-\bar{\nu}_\mu$ | $\mathrm{gu} \to \bar{\mathrm{s}}\mathrm{dc}\ \mathrm{e}^+\nu_\mathrm{e}\mu^-\bar{\nu}_\mu$ | $\mathrm{gd} \to \bar{\mathrm{c}}\mathrm{sc}\ \mathrm{e}^+\nu_\mathrm{e}\mu^-\bar{\nu}_\mu$ | $\mathrm{gc} \to \bar{\mathrm{d}}\mathrm{su}\ \mathrm{e}^+\nu_\mathrm{e}\mu^-\bar{\nu}_\mu$ |
| $G\bar{Q} \to Q\bar{Q}\bar{Q}\ \mathrm{e}^+\nu_\mathrm{e}\mu^-\bar{\nu}_\mu$ | | | |
| $\mathrm{g}\bar{\mathrm{c}} \to \mathrm{d}\bar{\mathrm{u}}\bar{\mathrm{s}}\ \mathrm{e}^+\nu_\mathrm{e}\mu^-\bar{\nu}_\mu$ | $\mathrm{g}\bar{\mathrm{d}} \to \mathrm{c}\bar{\mathrm{u}}\bar{\mathrm{s}}\ \mathrm{e}^+\nu_\mathrm{e}\mu^-\bar{\nu}_\mu$ | $\mathrm{g}\bar{\mathrm{u}} \to \mathrm{s}\bar{\mathrm{c}}\bar{\mathrm{d}}\ \mathrm{e}^+\nu_\mathrm{e}\mu^-\bar{\nu}_\mu$ | $\mathrm{g}\bar{\mathrm{s}} \to \mathrm{u}\bar{\mathrm{c}}\bar{\mathrm{d}}\ \mathrm{e}^+\nu_\mathrm{e}\mu^-\bar{\nu}_\mu$ |
| $\mathrm{g}\bar{\mathrm{s}} \to \mathrm{u}\bar{\mathrm{u}}\bar{\mathrm{s}}\ \mathrm{e}^+\nu_\mathrm{e}\mu^-\bar{\nu}_\mu$ | $\mathrm{g}\bar{\mathrm{u}} \to \mathrm{s}\bar{\mathrm{u}}\bar{\mathrm{s}}\ \mathrm{e}^+\nu_\mathrm{e}\mu^-\bar{\nu}_\mu$ | $\mathrm{g}\bar{\mathrm{c}} \to \mathrm{c}\bar{\mathrm{c}}\bar{\mathrm{d}}\ \mathrm{e}^+\nu_\mathrm{e}\mu^-\bar{\nu}_\mu$ | $\mathrm{g}\bar{\mathrm{c}} \to \mathrm{d}\bar{\mathrm{c}}\bar{\mathrm{d}}\ \mathrm{e}^+\nu_\mathrm{e}\mu^-\bar{\nu}_\mu$ |
| $\mathrm{g}\bar{\mathrm{u}} \to \mathrm{d}\bar{\mathrm{u}}\bar{\mathrm{d}}\ \mathrm{e}^+\nu_\mathrm{e}\mu^-\bar{\nu}_\mu$ | $\mathrm{g}\bar{\mathrm{d}} \to \mathrm{u}\bar{\mathrm{u}}\bar{\mathrm{d}}\ \mathrm{e}^+\nu_\mathrm{e}\mu^-\bar{\nu}_\mu$ | $\mathrm{g}\bar{\mathrm{c}} \to \mathrm{s}\bar{\mathrm{c}}\bar{\mathrm{s}}\ \mathrm{e}^+\nu_\mathrm{e}\mu^-\bar{\nu}_\mu$ | $\mathrm{g}\bar{\mathrm{s}} \to \mathrm{c}\bar{\mathrm{c}}\bar{\mathrm{s}}\ \mathrm{e}^+\nu_\mathrm{e}\mu^-\bar{\nu}_\mu$ |

**Table 3.9:** List of subprocesses contributing to intermediate $\mathrm{W}^+\mathrm{W}^-$ processes at the leading order with quark lines formed by both up-type and down-type quarks.

Chapter 4

# Helicity formalism

The traditional approach to the task of obtaining squared matrix elements in order to compute the desired cross section lies in calculating squares of spinor chains and evaluating traces of products of Dirac gamma matrices. This method can lead to very complex analytical expressions for processes involving a large amount of external particles (and by extension a large number of Feynman diagrams), since the number of contributing terms grows with the square. Moreover, if one wants to preserve the spin information and calculate a polarized cross section, the size of expressions grows even further.

One way to overcome this problem lies in using the so-called spinor-helicity techniques that provide a way to obtain numerical values for the matrix element for each helicity configuration of external fields. This method delivers relatively simple analytical expressions very convenient for use in computer algebra since they can be easily automatized and evaluated numerically without the necessity of squaring them. In addition, as we show in Section 4.3, it allows us to effectively cut amplitudes into independent blocks each of which is represented by a complex number depending only on momenta and helicities of the external lines.

The Weyl van der Waerden method, as presented in [43], is an example of a helicity formalism that provides an advantage of expressing all kinematical objects, be it wave functions, polarization vectors or momenta, using only a single mathematical construct called Weyl van der Waerden (WvdW) spinor [44, 45]. Ir is a two-component object that forms the simplest non-trivial representation of the Lorentz group. In Appendix A, we give a short overview of how these objects are constructed. A more detailed introduction to the WvdW formalism can be found in [43].

## 4.1 Example $u \to d\, W^+$

Appendix A provides a recipe on how to construct any helicity amplitude containing massless fermions. In this section, we demonstrate the WvdW formalism on a simple vertex diagram $u \to d\, W^+$ that, occurs frequently in the calculation of several considered subprocesses.

At tree level, this process has a single vertex diagram shown in Figure 4.1.

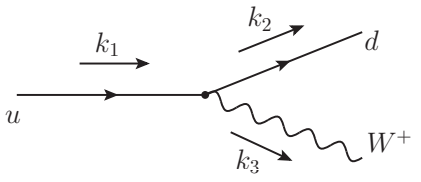


**Figure 4.1:** u $\to$ d $W^+$

The corresponding matrix element in the standard Dirac formalism, using notation for the momenta from Figure 4.1, reads

$$\mathcal{M} \sim \mathrm{i}\frac{e}{\sqrt{2}\sin\theta_W}\bar{\Psi}_L(k_2)\gamma_\mu\varepsilon_i^{*\mu}(k_3)\Psi_L(k_1). \tag{4.1}$$

In this expression, and several others in this chapter we have omitted additional factors that arise from the colour structure of the diagrams as they do not play role in present considerations. A more detailed discussion about these factors can be found in Sections 5.9 and 6.4.

Translated to the Weyl van der Waerden formalism, this reads

$$\mathcal{M} \sim \mathrm{i}\frac{e}{\sqrt{2}\sin\theta_W}n_{1\dot{A}}(k_2)\varepsilon_i^{*\dot{A}B}(k_3)n_{1B}(k_1). \tag{4.2}$$

Decomposing all objects into their respective eigenvectors $n_i$, we obtain the following expressions for the three helicities of the W boson:

$$\begin{aligned}
\varepsilon_+^{*\mu}(k_3): \quad \mathcal{M} &\sim \mathrm{i}\frac{e}{\sqrt{2}\sin\theta_W}2\sqrt{2k_{01}k_{02}}\langle n_1(k_2)n_1(k_3)\rangle^*\langle n_1(k_1)n_2(k_3)\rangle \\
\varepsilon_-^{*\mu}(k_3): \quad \mathcal{M} &\sim \mathrm{i}\frac{e}{\sqrt{2}\sin\theta_W}2\sqrt{2k_{01}k_{02}}\langle n_1(k_2)n_2(k_3)\rangle^*\langle n_1(k_1)n_1(k_3)\rangle \\
\varepsilon_0^{*\mu}(k_3): \quad \mathcal{M} &\sim \mathrm{i}\frac{e}{\sqrt{2}\sin\theta_W}\frac{2}{M_\mathrm{W}}\sqrt{k_{01}k_{02}} \\
&\quad (\lambda_1(k_3)\langle n_1(k_2)n_1(k_3)\rangle^*\langle n_1(k_1)n_1(k_3)\rangle \\
&\quad -\lambda_2(k_3)\langle n_1(k_2)n_2(k_3)\rangle^*\langle n_1(k_1)n_2(k_3)\rangle)
\end{aligned} \tag{4.3}$$

Since we are dealing with massless quarks, the scalar products in (4.3) can further be written out in terms of components of $k^\mu$ according to ($A.20$).

## 4.2 Crossing Symmetry

Discrete symmetries provide a convenient way to relate amplitudes of different processes with certain common attributes and are often used both for verification and to simplify the calculation. The crossing symmetry is a manifestation of the fact that the *S*-matrix is identical for the process involving a particle with momentum $k^\mu$ and for the same process involving an antiparticle with momentum $-k^\mu$, i.e.

$$\mathcal{M}(...\psi(k)... \to ...) = \mathcal{M}(... \to ...\bar{\psi}(-k)...). \tag{4.4}$$

In Weyl van der Waerden formalism, the 4-momentum $k^\mu$ is expressed as $K_{\dot{A}B} = \sum_i \kappa_{i,\dot{A}}\kappa_{i,B}$. In order to consistently reverse the momentum, we need to change the sign of one of the WvdW spinors while keeping the other unchanged, such as:

$$\kappa_{i,\dot{A}} \to -\kappa_{i,\dot{A}} \qquad\qquad \kappa_{i,A} \to \kappa_{i,A} \tag{4.5}$$

One should keep in mind that applying the crossing symmetry also reverses the helicity of the crossed fermion and changes the global sign (factor $\pm\text{sign}(\lambda)$ for each crossed fermion and $-1$ for each crossed vector field.

In the example $\text{u} \to \text{d}\ \text{W}^+$ from the previous section, the only non-zero combination of helicities for the quarks is $\lambda_1 = -1$ and $\lambda_2 = -1$. In order to find the amplitude for a process $\bar{\text{d}} \to \bar{\text{u}}\ \text{W}^+$ (Figure 4.2a) with antiquark helicities $\lambda_1 = 1$ and $\lambda_2 = 1$, all we need to do is take the expressions in (4.3) and change the signs of the scalar products involving dotted spinors:

$$\begin{aligned}
\varepsilon_+^{*\mu}(k_3): \qquad \mathcal{M} &\sim \mathrm{i}\frac{e}{\sqrt{2}\sin\theta_W} 2\sqrt{2k_{01}k_{02}}\langle(-n_1(k_1))n_1(k_3)\rangle^*\langle n_1(k_2)n_2(k_3)\rangle \\
\varepsilon_-^{*\mu}(k_3): \qquad \mathcal{M} &\sim \mathrm{i}\frac{e}{\sqrt{2}\sin\theta_W} 2\sqrt{2k_{01}k_{02}}\langle(-n_1(k_1))n_2(k_3)\rangle^*\langle n_1(k_2)n_1(k_3)\rangle \\
\varepsilon_0^{*\mu}(k_3): \qquad \mathcal{M} &\sim \mathrm{i}\frac{e}{\sqrt{2}\sin\theta_W}\frac{2}{M_\mathrm{W}}\sqrt{k_{01}k_{02}} \\
&\quad (\lambda_1(k_3)\langle(-n_1(k_1))n_1(k_3)\rangle^*\langle n_1(k_2)n_1(k_3)\rangle \\
&\quad -\lambda_2(k_3)\langle(-n_1(k_1))n_2(k_3)\rangle^*\langle n_1(k_2)n_2(k_3)\rangle)
\end{aligned} \tag{4.6}$$

Similarly, the amplitude for the process $\text{u}\bar{\text{d}} \to \text{W}^+$ (Figure 4.2b) with quark helicities $\lambda_1 = -1$ and $\lambda_2 = 1$ can be obtained by crossing the eigenvector $n_{i\dot{A}}(k_2)$, which, since we only have left-handed quarks in this particular vertex, results only in the change of the overall sign.

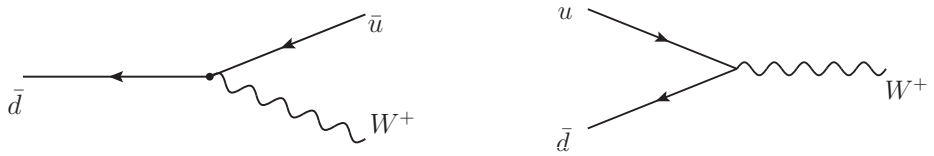


**(a)** $\bar{\mathrm{d}} \to \bar{\mathrm{u}}\mathrm{W}^+$ **(b)** $\mathrm{u}\bar{\mathrm{d}} \to \mathrm{W}^+$

**Figure 4.2:** Two examples of diagrams that can be obtained from the diagram in Figure 4.1 via crossing symmetry.

## 4.3 Structure of the diagrams, polarization sums

Computation of the vector-boson fusion processes with leptonic decay at NLO provides a fair amount of technical challenge, mainly due to the large number of external particles and thus number of Feynman diagrams involved. The internal structure of the diagrams offers, however, some space for exploitation, since the electroweak and QCD sections of the diagrams are largely independent of one another. Figure 4.3 demonstrates four generic types into which all *t*-channel diagrams involved in our calculation can be categorized. This categorization is similar to that in [28].

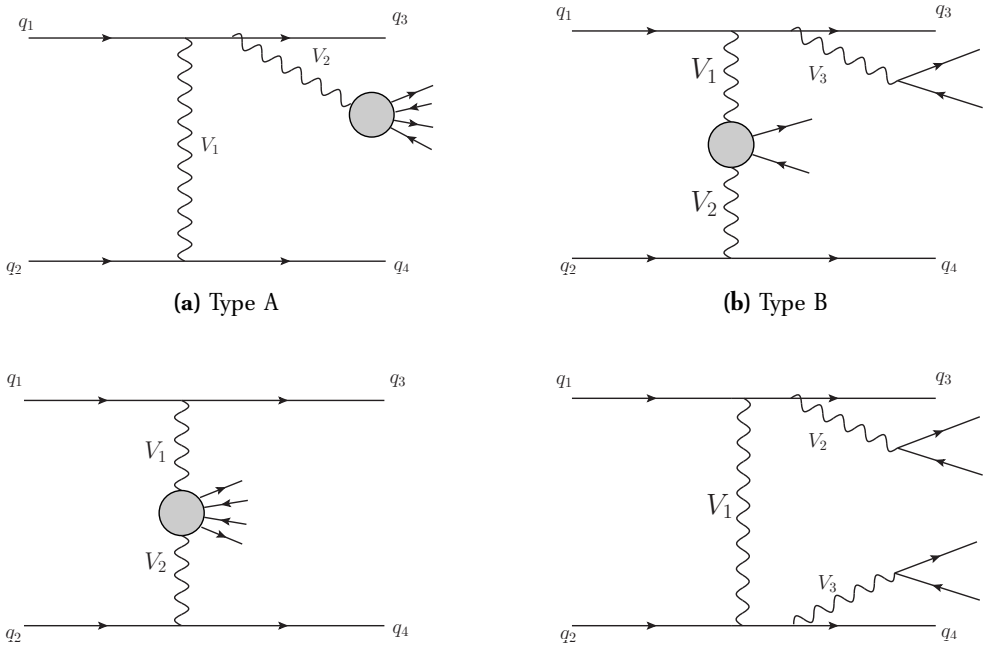


**(a)** Type A **(b)** Type B

**(c)** Type C **(d)** Type D

**Figure 4.3:** Generic types of *t*-channel diagrams

Type A (Figure 4.3a) contains two quark legs connected with a gauge boson and another gauge boson radiated off one of the quark legs which decays via electroweak interactions into four final-state leptons.

Type B (Figure 4.3b) has a gauge boson radiated off one of the quark legs, decaying into two leptons and two more gauge bosons fusing in the central region to produce a second pair of leptons.

Type C (Figure 4.3c) represents the pure vector-boson fusion diagram, with two gauge bosons radiated off the quark legs fusing in the center to produce four leptons in the final state.

Finally, type D (Figure 4.3d) sees one gauge boson connecting the quark legs, and two more radiated off the quark legs decaying into two lepton pairs.

Since all LO diagrams for all four processes fall into one of these types, this classification provides a very convenient way to organize the diagrams and will be referred to on a number of occasions.

One can notice that changes to either QCD or electroweak sector that do not change the momenta of the internal gauge bosons have no effect on the rest of the diagram. For instance, should one apply the crossing symmetry to the upper quark leg and change quarks into antiquarks, the lower quark leg and all leptonic parts would remain unchanged. Similar argument holds for adding a gluon loop to either of the quark legs, which essentially amounts to calculating virtual NLO QCD corrections to the entire diagram. Since the leptonic sector of the diagram in itself can be quite complicated, there is little point in recalculating this block for each gluon loop if one has the option to calculate each part independently.

Factorization of sections of the diagrams can be achieved by inserting the polarization sums for massive gauge bosons [35]

$$g^{\mu\nu} = -\sum_{i=\{+,-,0\}} \varepsilon_i^{\mu}(k)\varepsilon_i^{*\nu}(k) + \frac{k^{\mu}k^{\nu}}{k^2} \tag{4.7}$$

in place of each internal vector boson, effectively thus cutting the diagram into blocks that can be evaluated on their own and only related by the internal momenta. The polarization vectors $\varepsilon_i^{\mu}(k)$ and $\varepsilon_i^{*\nu}(k)$ for off-shell particles are obtained by replacing the masses $m$ by $\sqrt{k^2}$ in formulas A.22 and A.23, respectively.

Calculation of the QCD NLO corrections requires evaluation of diagrams with one gluon loop, or an external gluon attached to either of the two quark lines. Both possibilities involve applying changes to a single quark leg while leaving the leptonic sector and the other quark leg unchanged. Implementing the block structure by cutting all internal gauge bosons that couple to the quark lines in the diagrams in Figure 4.3 allows us to not only save time by evaluating each required block only once, but also to keep the number of required blocks relatively small by reusing them in multiple instances throughout all diagrams and even subprocesses (i.e. in the subprocess $\mathrm{uu} \to \mathrm{uue}^{+}\nu_{\mathrm{e}}\mu^{-}\bar{\nu}_{\mu}$, the analytical expressions for the lower and upper quark legs are identical and the electroweak blocks are the exactly same as in the subprocess $\mathrm{d\bar{d}} \to \mathrm{d\bar{d}e}^{+}\nu_{\mathrm{e}}\mu^{-}\bar{\nu}_{\mu}$).

## 4.4 Example us $\to$ dc

In this section, we use a simple example to demonstrate how the polarization sums (4.7) can be incorporated into the Weyl van der Waerden helicity formalism.

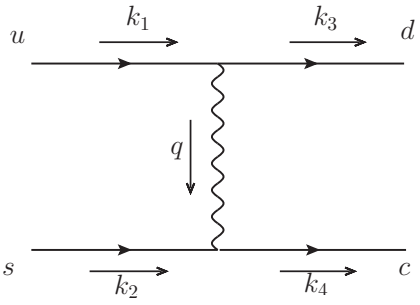


**Figure 4.4:** us $\to$ dc

Let us consider the process us $\to$ dc. At tree level, there is only one $t$-channel diagram (Figure 4.4) involving two quark legs with a W boson running between them. Its kinematic structure can be considered a simplified version of the vector-boson fusion diagrams (4.3), without the purely electroweak section. In Dirac formalism, its matrix element can be written as

$$\mathcal{M} = \left(\frac{\mathrm{i}e}{\sqrt{2}\sin\theta_W}\right)^2 \bar{u}(k_3)\gamma_\mu P_- \, u(k_1)\frac{-\mathrm{i}g^{\mu\nu}}{(k_4-k_2)^2 - M_\mathrm{W}^2}\bar{u}(k_2)\gamma_\nu P_- \, u(k_4). \tag{4.8}$$

In order to cut this diagram into two blocks using polarization sum, we replace $g^{\mu\nu}$ in the nominator of the propagator with the expression from (4.7). This leaves us with a sum of four terms, each of which can be interpreted as a product of two independent matrix elements $\mathcal{M}_{1,\,i}$ and $\mathcal{M}_{2,\,i}$

$$\mathcal{M} \sim -\mathcal{M}_{1,\,+}\mathcal{M}_{2,\,+} - \mathcal{M}_{1,\,-}\,\mathcal{M}_{2,\,-} - \mathcal{M}_{1,\,0}\mathcal{M}_{2,\,0} + \frac{\mathcal{M}_{1,\,q}\mathcal{M}_{2,\,q}}{q^2}, \tag{4.9}$$

where $q = (k_4 - k_2)$ is the momentum of the W boson and $\mathcal{M}_{1,\,i}$ and $\mathcal{M}_{2,\,i}$ correspond to the following subdiagrams

$\mathcal{M}_{1,\,i}$ :

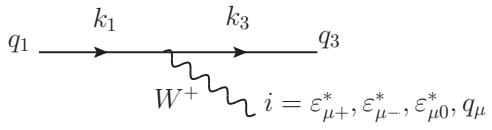


$\mathcal{M}_{2,\,i}$ :

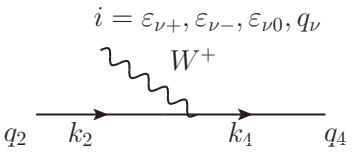

The elements where $i = q_\mu, q_\nu$, $\mathcal{M}_{1,\,q}$ and $\mathcal{M}_{2,\,q}$, are obtained by replacing $\varepsilon^*_{\mu\,i}$ and $\varepsilon_{\nu\,i}$ with $q_\mu$ and $q_\nu$.

To write the array representing the first block, $\mathcal{M}_{1,i}$, we can use the result we obtained in (4.3) while replacing the momenta $k_2 \mapsto k_3$ and $k_3 \mapsto q$ and adding the fourth term:

$$\begin{aligned}
\mathcal{M}'_{1,\,+} = \quad & \mathrm{i}\frac{e}{\sqrt{2}\sin\theta_W} 2\sqrt{2k_{01}k_{0\,3}}\langle n_1(k_3)n_1(q)\rangle^*\langle n_1(k_1)n_2(q)\rangle \\
\mathcal{M}'_{1,\,-} = \quad & \mathrm{i}\frac{e}{\sqrt{2}\sin\theta_W} 2\sqrt{2k_{01}k_{0\,3}}\langle n_1(k_3)n_2(q)\rangle^*\langle n_1(k_1)n_1(q)\rangle \\
\mathcal{M}'_{1,\,0} = \quad & \mathrm{i}\frac{e}{\sqrt{2}\sin\theta_W}\frac{2}{M_{\mathrm{W}}}\sqrt{k_{01}k_{0\,3}} \\
& (\lambda_1(q)\langle n_1(k_3)n_1(q)\rangle^*\langle n_1(k_1)n_1(q)\rangle - \lambda_2(q)\langle n_1(k_3)n_2(q)\rangle^*\langle n_1(k_1)n_2(q)\rangle) \\
\mathcal{M}'_{1,\,q} = \quad & \mathrm{i}\frac{e}{\sqrt{2}\sin\theta_W} 2\sqrt{2k_{01}k_{0\,3}}(\lambda_1(q)\langle n_1(k_3)n_1(q)\rangle^*\langle n_1(k_1)n_1(q)\rangle \\
& +\lambda_2(q)\rangle n_1(k_3)n_2(q)\rangle^*\rangle n_1(k_1)n_2(q)\rangle).
\end{aligned} \tag{4.10}$$

The matrix element for $\mathcal{M}_{2,i}$ has a very similar structure, except the W boson is now considered to be an incoming particle. One obtains

$$\begin{aligned}
\mathcal{M}_{2,\,+} = \quad & \mathrm{i}\frac{e}{\sqrt{2}\sin\theta_W} 2\sqrt{2k_{02}k_{0\,4}}\langle n_2(q)n_1(k_4)\rangle^*\langle n_1(q)n_1(k_2)\rangle \\
\mathcal{M}_{2,\,-} = \quad & \mathrm{i}\frac{e}{\sqrt{2}\sin\theta_W} 2\sqrt{2k_{02}k_{0\,4}}\langle n_1(q)n_1(k_4)\rangle^*\langle n_2(q)n_1(k_2)\rangle \\
\mathcal{M}_{2,\,0} = \quad & \mathrm{i}\frac{e}{\sqrt{2}\sin\theta_W}\frac{2}{M_{\mathrm{W}}}\sqrt{k_{02}k_{0\,4}}(\lambda_1(q)\langle n_1(q)n_1(k_4)\rangle^*\langle n_1(q)n_1(k_2)\rangle \\
& -\lambda_2(q)\langle n_2(q)n_1(k_4)\rangle^*\langle n_2(q)n_1(k_2)\rangle) \\
\mathcal{M}_{2,\,q} = \quad & i\frac{e}{\sqrt{2}\sin\theta_W} 2\sqrt{2k_{02}k_{0\,4}}(\lambda_1(q)\langle n_1(q)n_1(k_4)\rangle^*\langle n_1(q)n_1(k_2)\rangle \\
& +\lambda_2(q)\rangle n_2(q)n_1(k_4)\rangle^*\rangle n_2(q)n_1(k_2)\rangle).
\end{aligned} \tag{4.11}$$

Since neither $\mathcal{M}'_{1,i}$ nor $\mathcal{M}_{2,i}$ contain a gauge-boson propagator, in order to be able to calculate the amplitude of the full process $\mathcal{M}$, one needs to add the propagator by multiplying the sum (4.9) with $1/(q^2 - M_{\mathrm{W}}^2)$. To remain consistent, we have chosen to always add the propagator to the subamplitude in which the gauge boson is an outgoing particle, in this case $\mathcal{M}'_{1,i}$:

$$\mathcal{M}_{1,i} = \frac{\mathcal{M}'_{1,i}}{q^2 - M_{\mathrm{W}}^2} \tag{4.12}$$

## 4.5 Classification of building blocks

Since the process in the previous section involves a single gauge boson, we needed to apply the polarization sum to split the diagram into blocks only once. Figure 4.3 shows, however,

that the diagrams we need to consider in our calculation contain up to three gauge bosons that are being radiated from the quark legs. In those cases, the polarization sum has to be applied once for each gauge boson that couples to one of the quark lines. Great care needs to be taken, however, to keep track of the Lorentz indices as well as momenta of the internal bosonic propagators when combining them. Figure 4.5 illustrates how a diagram featuring three vector bosons can be split into four building blocks. Each splitting represents an insertion of one polarization sum. In our calculation, the formulas for combining the blocks have been implemented as Fortran subroutines on a case-by-case basis.

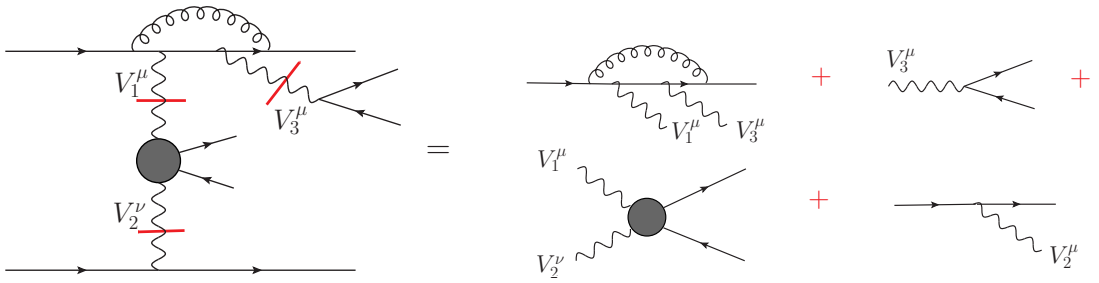


**Figure 4.5:** Example of a diagram split into four building blocks by applying the polarization sums (4.7) to cut three intermediate gauge bosons.

Cutting the Feynman diagrams in Figure 4.3 reveals that from the point of view of the kinematical and Lorentz structures, one can divide the building blocks into several types which can be classified according to their Lorentz and kinematic structure.

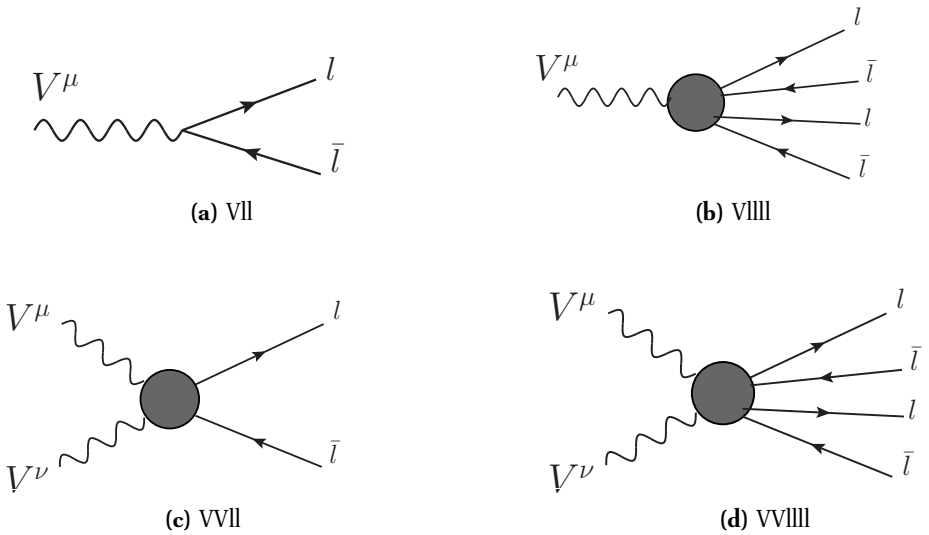


**(a)** Vll **(b)** Vllll

**(c)** VVll **(d)** VVllll

**Figure 4.6:** Building blocks involving leptons

Building blocks involving leptons are shown on Figure 4.6. Since they do not have any external or internal quarks or gluons, they do not play role in the next-to-leading-order corrections. Typically, they involve more than one Feynman diagram. The only exception is the simple block corresponding to the electroweak current in which the vector boson decays into two leptons (Figure 4.6a). Diagrams of type A (Figure 4.3a) contain building blocks with one vector boson in the initial state and four leptons in the final state (Figure 4.6b). Type B (Figure 4.3b) involve two vector bosons and two leptons. Building blocks with two external vector bosons are represented by a $4 \times 4$ array, each element corresponding to one term of the complete polarization sum constructed by cutting two gauge bosons. Cutting the vector-boson-fusion diagrams (Figure 4.3c) results in building blocks with two incoming vector bosons and 4 outgoing leptons (Figure 4.6d). These typically contain up to 80 Feynman diagrams, including Higgs production (Figure 4.7a) and vector-boson scattering diagrams. Figure 4.7b shows an example of a non-resonant diagram that is not included in calculations where only gauge boson production diagrams with subsequent leptonic decay are considered (e.g. [25, 26, 27]).

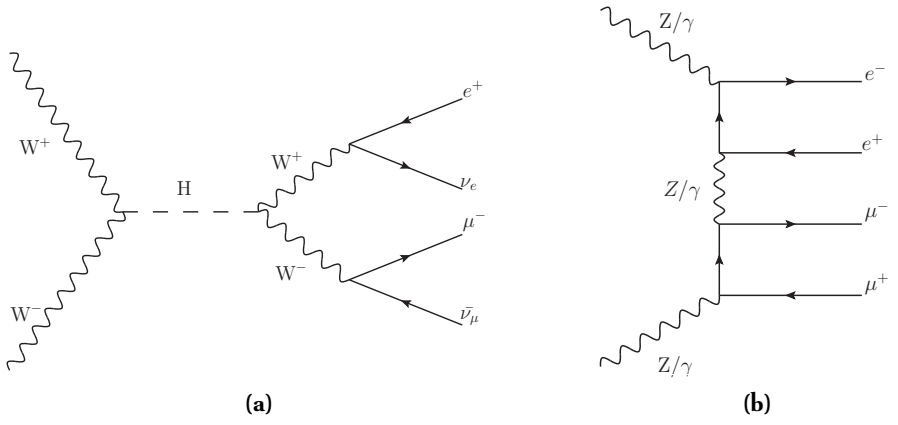


**Figure 4.7:** Example of a Higgs production (a) and non-resonant (b) electroweak building block belonging to VVllll.

Similarly to the leptonic building blocks, there are several generic types of blocks involving the quark legs. At leading order, each type is only formed by one diagram. These are shown in Figure 4.8. Vqq and qqV are building blocks that only contain one incoming or outgoing vector boson. As in the case of the leptonic building blocks, diagrams with two vector bosons, qqVV, V1qqV and V2qqV are represented by a $4 \times 4$ array. V1qqV and V2qqV correspond to diagrams with one incoming and one outgoing vector boson (Figure 4.8e and Figure 4.8d) and are used in diagrams of type D (Figure 4.3d). Even though they belong to the same physical process, we must distinguish between V1qqV and V2qqV because once combined in the polarization sum, each contributes to a different Feynman diagram. Additional diagrams that belong to type D are ones where both vector bosons decaying into lepton pairs are radiated from the same quark line. This results in a building block with three

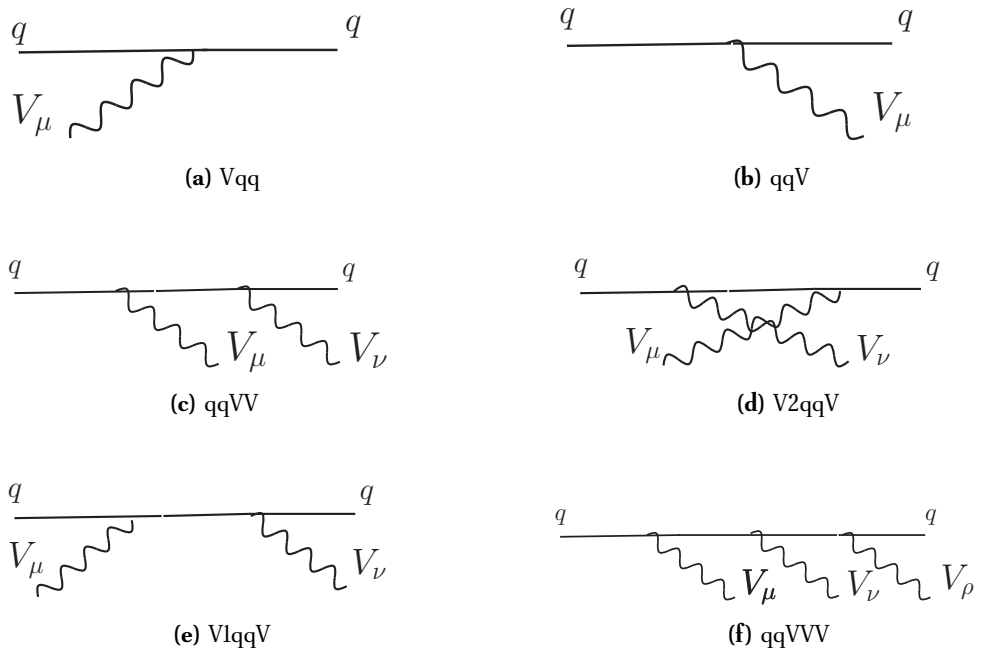


**Figure 4.8:** Leading-order building blocks involving quark legs. The diagrams (a) and (b), and (c), (d) and (e) can be derived from one another by crossing the relevant gauge boson field.

external vector bosons qqVVV (Figure 4.8f), represented by a $4 \times 4 \times 4$ array. In the building blocks that contain two or more W bosons with different electical charges, their order is automatically determined by charge conservation as there are no intermediate quarks with an electric charge $+5/3e$ or $-4/3e$.

In order to be able to construct diagrams for processes involving antiquarks, one needs to generate QCD blocks in which either quark leg can be crossed. As all blocks incorporate the WvdW formalism, crossing is performed by reversing the sign of the dotted spinors $\kappa_{i\dot{A}}$, as described in section 4.2.

Next-to-leading-order QCD corrections involve gluon couplings and as such are limited only to the quark legs. The virtual corrections are obtained by attaching a gluon loop to the quark in every possible way. Figure 4.8 illustrates how virtual corrections are applied to the building blocks from Figure 4.8. Since there is no need to distinguish between individual loop diagrams, the virtual corrections to the same leading order diagram in Figure 4.8 are summed up and contribute to a single building block, even though they may involve up to 8 Feynman diagrams, as is the case of qqVVV.

In addition to the one-loop virtual blocks, a corresponding set of counterterm blocks is included to compensate for the ultraviolet singularities (see Chapter 6). The counterterm building blocks are shown in Figure 4.8. The contributions to each quark line from the

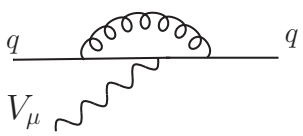


**(a)** Vqq

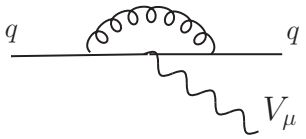


**(b)** qqV

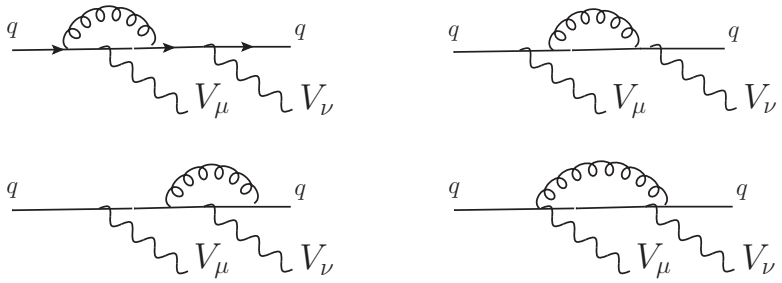


**(c)** qqVV

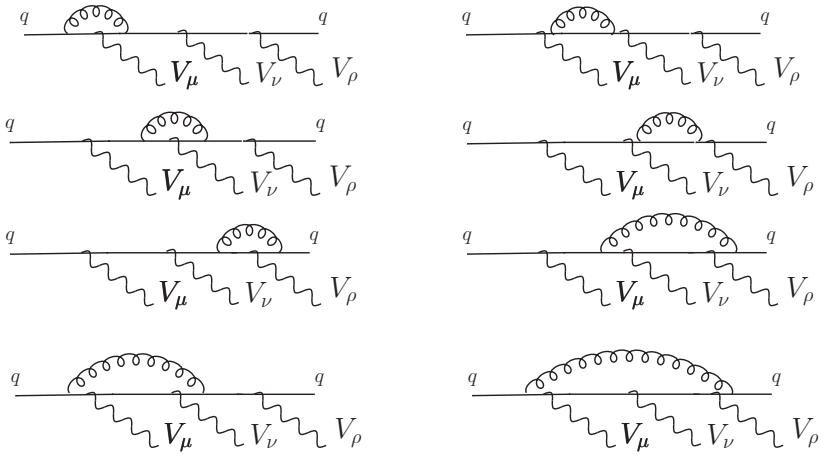


**(d)** qqVVV

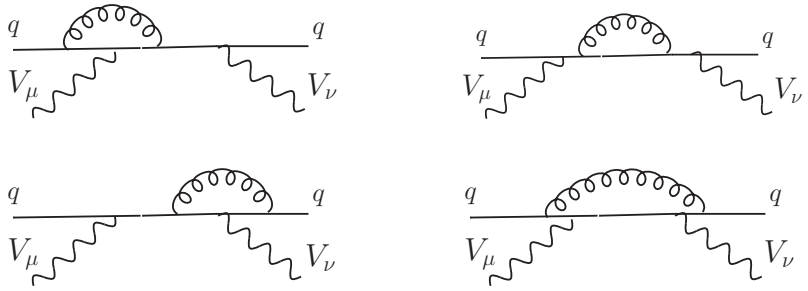


**(e)** VlqqV

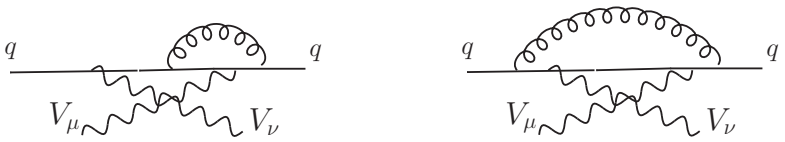


**(f)** V2qqV

**Figure 4.8:** Next-to-leading-order virtual blocks. As with the leading order (Figure 4.8), the blocks Vqq and qqV, and qqVV, V1qqV and V2qqV can be obtained by crossing the relevant gauge boson.

building blocks in Figures 4.8 and 4.8 are summed up in order to obtain UV-finite matrix elements.

Real QCD corrections are constructed by attaching an external gluon to the quark leg in every possible way as illustrated in Figure 4.8. Since the gluon, being a massless particle, has two possible polarizations, the resulting building blocks are represented by arrays $2 \times 4$ (one polarization sum), $2 \times 4 \times 4$ (two polarization sums) and $2 \times 4 \times 4 \times 4$ (three polarization

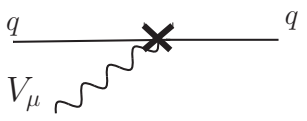


**(a)** Vqq

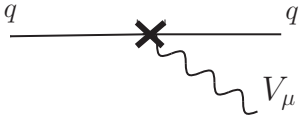


**(b)** qqV

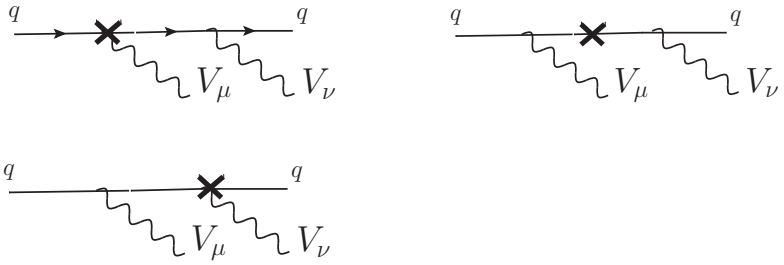


**(c)** qqVV

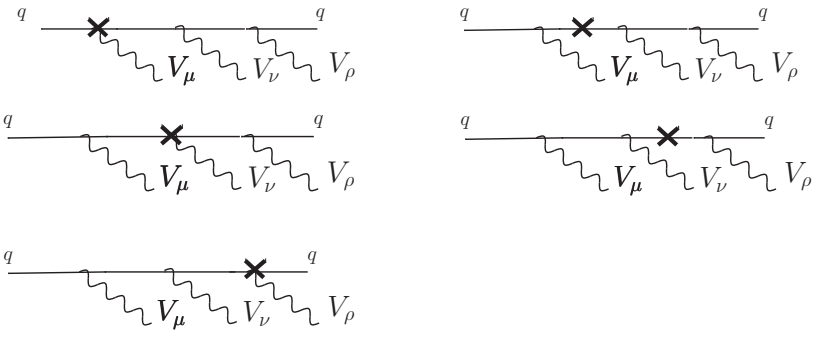


**(d)** qqVVV

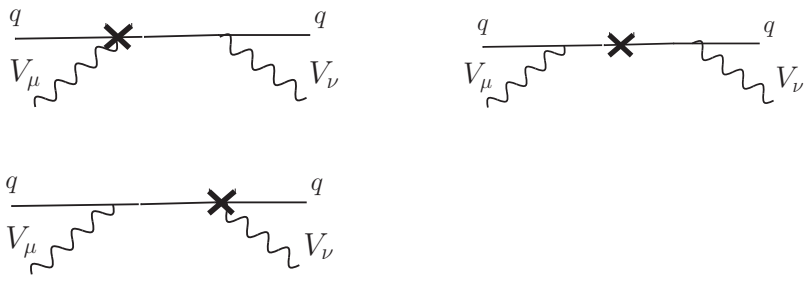


**(e)** VlqqV

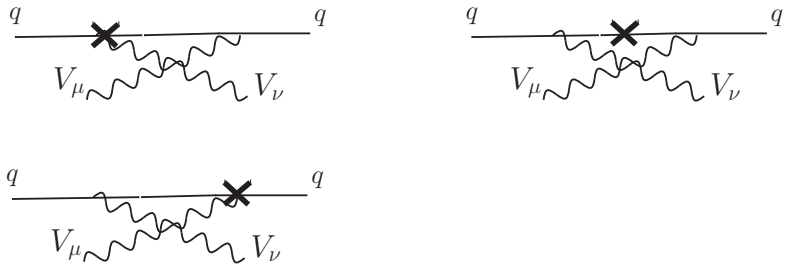


**(f)** VlqqV

**Figure 4.8:** Next-to-leading-order counterterm blocks corresponding to virtual building blocks in Figure 4.8.

sums). As in the previous case, the position of the gluon plays no role and all real radiation corrections to any quark leg from Figure 4.8 can be included in a single building block.

Next-to-leading-order corrections with initial-state gluon can be obtained from the diagrams in Figure 4.8 by applying the crossing symmetry to the outgoing gluon and/or the incoming quark.

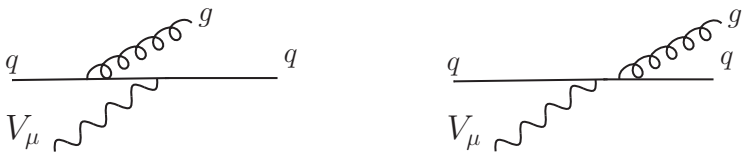


**(a)** Vqq

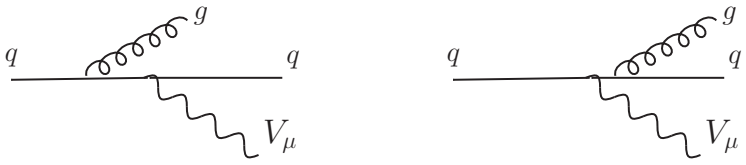


**(b)** qqV

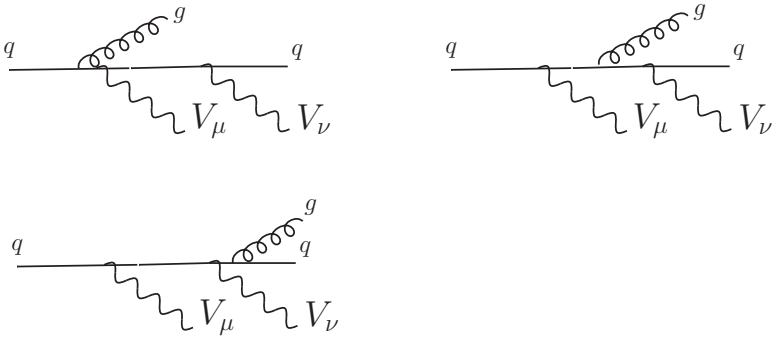


**(c)** qqVV

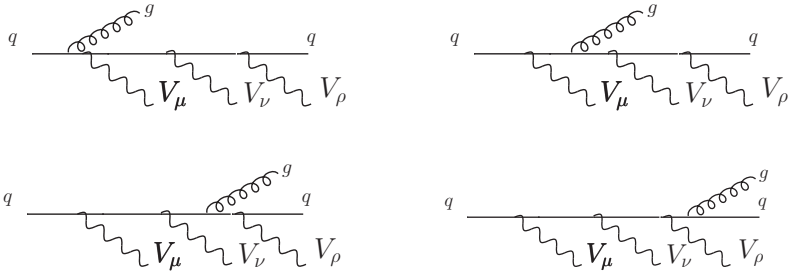


**(d)** qqVVV

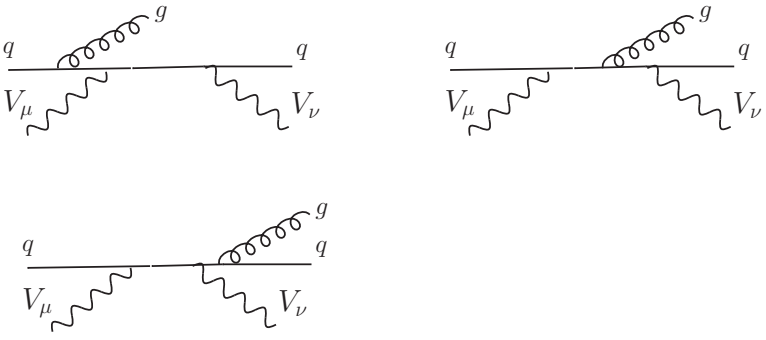


**(e)** VlqqV

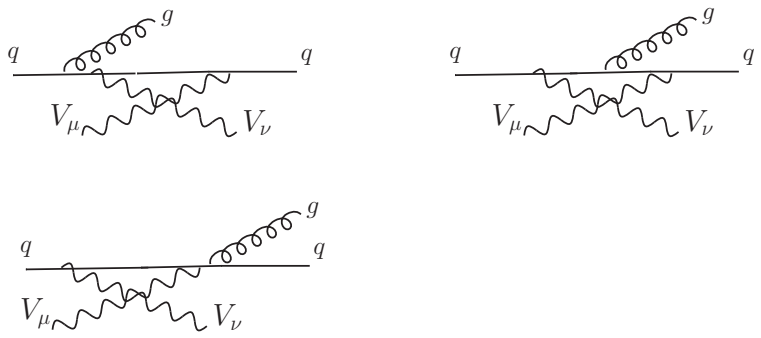


**(f)** V2qqV

**Figure 4.8:** Next-to-leading-order real radiation blocks

## 4.6 Kinematics of the building blocks

As mentioned earlier, one of the key advantages of the block approach is the fact that they allow us to use the same analytical expressions for evaluating different parts and types of Feynman diagrams. For instance, in type C diagrams (Figure 4.3c), the subdiagrams involving two quark legs often correspond to the same physical process and thus the helicity amplitude is the same. The only difference is that the quark momenta in one case are those of the upper quark leg and in the other case of the lower quark leg.

As this property is extensively used in our calculation, it is useful to assemble a list of all possible kinematic configurations of the individual building blocks so that they can later be used as a reference.

The momenta and helicities of the external particles of the leading-order and virtual-corrections subprocesses $q_1q_2 \to q_3q_4l_1l_2l_3l_4$ and for the real-radiation subprocesses $q_1q_2 \to q_3q_4l_1l_2l_3l_4g$ are denoted as shown in Table 4.1.

| | momenta | helicities | | momenta | helicities |
|---|---|---|---|---|---|
| $q_1$ | $k_1$ | $\lambda_1$ | $l_1$ | $k_5$ | $\lambda_5$ |
| $q_2$ | $k_2$ | $\lambda_2$ | $l_2$ | $k_6$ | $\lambda_6$ |
| $q_3$ | $k_3$ | $\lambda_3$ | $l_3$ | $k_7$ | $\lambda_7$ |
| $q_4$ | $k_4$ | $\lambda_4$ | $l_4$ | $k_8$ | $\lambda_8$ |
| g (NLO) | $k_9$ | $\lambda_9$ | | | |

**Table 4.1:** Notation for the momenta and helicities of the quarks, leptons and final-state gluon.

For the building blocks involving leptons, the list of all combinations required by the

calculation is shown in Table 4.2, where $k_i$ are external momenta of the complete subprocess as shown in Figure 4.1. The kinematic configurations of the building blocks involving quarks using the same notation for the external momenta can be found in Table 4.3.

| $Vll$ |
|---|
| $Vll_{56} = Vll(k_5 + k_6, k_5, k_6) \quad Vll_{78} = Vll(k_7 + k_8, k_7, k_8)$ |
| $Vllll$ |
| $Vllll = Vllll(k_5 + k_6 + k_7 + k_8, k_5, k_6, k_7, k_8)$ |
| $VVll$ |
| $VVll_{561} = Vll(k_1 - k_3 - k_7 - k_8, k_2 - k_4, k_5, k_6)$ |
| $VVll_{562} = Vll(k_1 - k_3, k_2 - k_4 - k_7 - k_8, k_5, k_6)$ |
| $VVll_{781} = Vll(k_1 - k_3 - k_5 - k_6, k_2 - k_4, k_7, k_8)$ |
| $VVll_{782} = Vll(k_1 - k_3, k_2 - k_4 - k_5 - k_6, k_7, k_8)$ |
| $VVllll$ |
| $VVllll = VVllll(k_1 - k_3, k_2 - k_4, k_5, k_6, k_7, k_8)$ |

**Table 4.2:** List of the kinematic configurations for the leptonic building blocks. The order of the momenta in the brackets corresponds to the order of particles in the name of the building block, e.g. in $Vll_{56}$, $k_5 + k_6$ is the momentum of the gauge boson, $k_5$ of the first lepton and $k_6$ of the second lepton.

## 4.7 Example: us→dce$^-$e$^+$

In this section we demonstrate how the QCD building blocks can be combined with the leptonic building blocks using multiple insertions of polarization sums. For the sake of brevity, we resort to calculating the vector-boson fusion diagrams (equivalent of type C in Figure 4.3) contributing to a less complicated process us→dce$^-$e$^+$ while implementing the same methodology as in case of diagrams with six particles in the final state. The considered diagrams are shown in Figure 4.9.

| $qqV$ | |
|---|---|
| $qqV_1 = qqV(k_1, k_3, k_3 - k_1)$ | $qqV_2 = qqV(k_2, k_4, k_4 - k_2)$ |
| $Vqq$ | |
| $Vqq_{13} = Vqq(k_3 - k_1, k_1, k_3)$ | $Vqq_{24} = Vqq(k_4 - k_2, k_2, k_4)$ |
| $qqVV$ | |
| $qqVV_{ij\,1,\ i=5,7;\ j=6,8} = qqVV(k_1, k_3, k_i + k_j, k_1 - k_3 - k_i - k_j)$ | |
| $qqVV_{ij\,2,\ i=5,7;\ j=6,8} = qqVV(k_1, k_3, k_1 - k_3 - k_i - k_j, k_i + k_j)$ | |
| $qqVV_{ij\,3,\ i=5,7;\ j=6,8} = qqVV(k_2, k_4, k_i + k_j, k_2 - k_4 - k_i - k_j)$ | |
| $qqVV_{ij\,4,\ i=5,7;\ j=6,8} = qqVV(k_2, k_4, k_2 - k_4 - k_i - k_j, k_i + k_j)$ | |
| $qqVV_1 = qqVV(k_1, k_3, k_5 + k_6 + k_7 + k_8, k_4 - k_2)$ | |
| $qqVV_2 = qqVV(k_1, k_3, k_4 - k_2, k_5 + k_6 + k_7 + k_8)$ | |
| $qqVV_3 = qqVV(k_2, k_4, k_5 + k_6 + k_7 + k_8, k_3 - k_1)$ | |
| $qqVV_4 = qqVV(k_2, k_4, k_3 - k_1, k_5 + k_6 + k_7 + k_8)$ | |
| $VXqqV, \quad X = 1, 2$ | |
| $VXqqV_{1378} = VXqqV(k_2 - k_4 - k_5 - k_6, k_1, k_3, k_7 + k_8)$ | |
| $VXqqV_{1356} = VXqqV(k_2 - k_4 - k_7 - k_8, k_1, k_3, k_5 + k_6)$ | |
| $VXqqV_{2478} = VXqqV(k_1 - k_3 - k_5 - k_6, k_2, k_4, k_7 + k_8)$ | |
| $VXqqV_{2456} = VXqqV(k_1 - k_3 - k_7 - k_8, k_2, k_4, k_5 + k_6)$ | |
| $qqVVV$ | |
| $qqVVV_{24ijkl\ \ i,k=5,7;\ j,l=6,8} = qqVVV(k_1, k_3, k_4 - k_2, k_i + k_j, k_k + k_l)$ | |
| $qqVVV_{13ijkl\ \ i,k=5,7;\ j,l=6,8} = qqVVV(k_2, k_4, k_3 - k_1, k_i + k_j, k_k + k_l)$ | |
| $qqVVV_{ij24kl\ \ i,k=5,7;\ j,l=6,8} = qqVVV(k_1, k_3, k_i + k_j, k_4 - k_2, k_k + k_l)$ | |
| $qqVVV_{ij13kl\ \ i,k=5,7;\ j,l=6,8} = qqVVV(k_2, k_4, k_i + k_j, k_3 - k_1, k_k + k_l)$ | |
| $qqVVV_{ijkl24\ \ i,k=5,7;\ j,l=6,8} = qqVVV(k_1, k_3, k_i + k_j, k_k + k_l, k_4 - k_2)$ | |
| $qqVVV_{ijkl13\ \ i,k=5,7;\ j,l=6,8} = qqVVV(k_2, k_4, k_i + k_j, k_k + k_l, k_3 - k_1)$ | |

**Table 4.3:** List of kinematic configurations of the QCD building blocks. As in Table 4.2, the order of the momenta in the brackets is the same as the order of particles in the name of the building block.

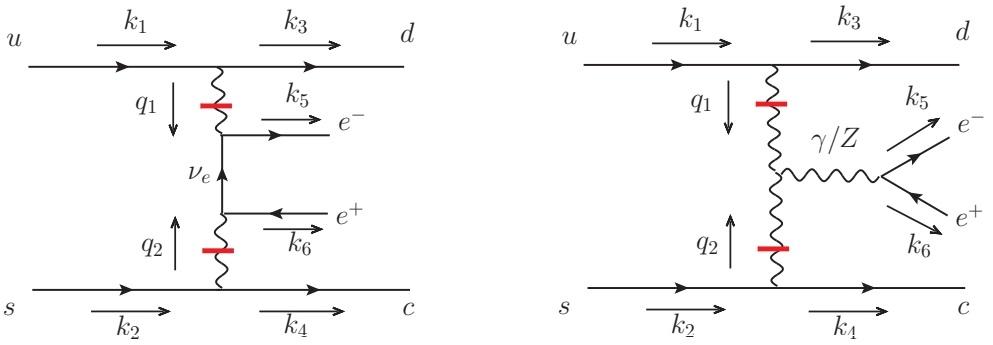


**Figure 4.9:** VBF diagrams contributing to the process us→dce$^-$e$^+$, with (red) lines indicating insertion of the polarization. In the diagram on the right, the vector boson decaying into electron-positron pair can be either photon or Z boson.

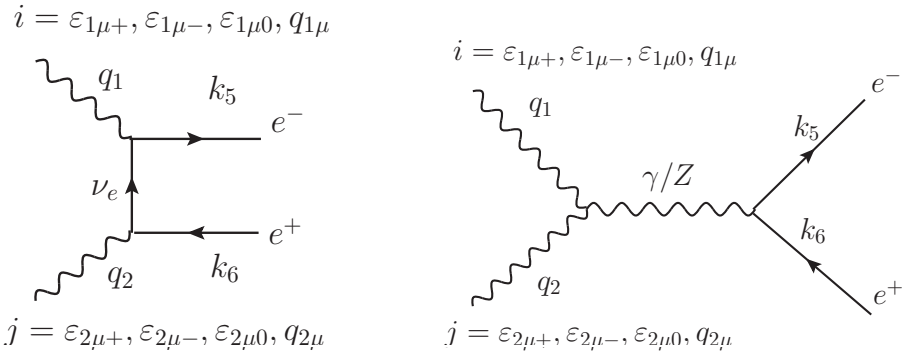


**(a)** $D_1$ **(b)** $D_2$ (γ), $D_3$ (Z)

**Figure 4.10:** Feynman diagrams $D_1$, $D_2$ and $D_3$ contributing to the leptonic building block $W^+W^- \to e^-e^+$.

Following the procedure from Section 4.3, both intermediate vector bosons can be cut using the polarization sums (4.7), creating two QCD and one leptonic building block per each of the diagrams. As can be seen in Figure 4.9, both QCD building blocks in all three diagrams are identical, and they need to be evaluated only once.

Their explicit form can be found in Section 4.4, after replacing $q \mapsto q_1$ for the upper leg and $q \mapsto q_2$ for the lower leg. Since $q_1 = k_3 - k_1$ and $q_2 = k_4 - k_2$, the two building blocks correspond to the variables denoted as $qqV_1$ and $Vqq_{24}$ in Table 4.3.

The three electroweak diagrams created by cutting two W bosons (Figure 4.10) contribute, according to Section 4.5, to a single leptonic building block denoted as $VVll$. Since it involves two vector bosons, $VVll$ is formed by an array of $4 \times 4$ combinations of $i$ and $j$ (Figure 4.10) as they label 16 terms arising from two polarization sums. Using notation from Section 4.3, the kinematic configuration of $VVll$ is $VVll(k_1 - k_3, k_2 - k_4, k_5, k_6)$. The resulting subamplitudes for the diagrams $D_1$ (Figure 4.10a), $D_2$ and $D_3$ (Figure 4.10b), evaluated

in WvdW formalism, read

$$
\begin{aligned}
D_1 =& \frac{2\alpha_S\pi}{\sin\theta_W}\frac{\mathrm{i}}{(q_1^2-2q_1\cdot k_5)}[2s_1(k_{5\dot{A}}e(k_2)^{\dot{A}B}k_{6B})(e(k_1)_{\dot{C}D}K(k_2)^{\dot{C}D})\\
&-2s_1(k_{5\dot{A}}e(k_2)^{\dot{A}B}k_{6B})(e(k_1)_{\dot{C}D}K(k_5)^{\dot{C}D})-2s_1(k_{5\dot{A}}K(k_2)^{\dot{A}B}k_{6B})(e(k_1)_{\dot{C}D}e(2)^{\dot{C}D})\\
&+s_1(k_{5\dot{A}}e(k_1)^{\dot{A}B}e(k_2)_{B\dot{C}}K(k_2)^{\dot{C}D}k_{6D})-s_1(k_{5\dot{A}}e(k_1)^{\dot{A}B}e(k_2)_{B\dot{C}}K(k_5)^{\dot{C}D}k_{6D})]\\
D_2 =& \frac{8\mathrm{i}\alpha_S\pi}{(q_1+q_2)^2}[s_1(k_{5\dot{A}}e(q_1)^{\dot{A}B}k_{6B})(e(q_2)_{\dot{C}D}K(q_1)^{\dot{C}D})-s_1(k_{5\dot{A}}e(q_2)^{\dot{A}B}k_{6B})(e(q_1)_{\dot{C}D}K(q_2)^{\dot{C}D})\\
&-s_2(k_5^Ae(q_2)_{A\dot{B}}k_6^{\dot{B}})(e(q_1)_{\dot{C}D}K(q_2)^{\dot{C}D})+s_2(k_5^Ae(q_1)_{A\dot{B}}k_6^{\dot{B}})(e(q_2)_{\dot{C}D}K(q_1)^{\dot{C}D})\\
&+\frac{1}{2}(s_1(k_{5\dot{A}}K(q_2)^{\dot{A}B}k_{6B})(e(q_1)_{\dot{C}D}e(q_2)^{\dot{C}D})-s_2(k_5^AK(q_1)_{A\dot{B}}k_6^{\dot{B}})(e(q_1)_{\dot{C}D}e(q_2)^{\dot{C}D})\\
&+s_2(k_5^AK(q_2)_{A\dot{B}}k_6^{\dot{B}})(e(q_1)_{\dot{C}D}e(q_2)^{\dot{C}D})+s_1(k_{5\dot{A}}e(q_1)^{\dot{A}B}k_{6B})(e(q_2)_{\dot{C}D}K(q_2)^{\dot{C}D})\\
&+s_2(k_5^Ae(q_1)_{A\dot{B}}k_6^{\dot{B}})(e(q_2)_{\dot{C}D}K(q_2)^{\dot{C}D})-s_1(k_{5\dot{A}}e(q_2)^{\dot{A}B}k_{6B})(e(q_1)_{\dot{C}D}K(q_1)^{\dot{C}D})\\
&-s_2(k_5^Ae(q_2)_{A\dot{B}}k_6^{\dot{B}})(e(q_1)_{\dot{C}D}K(q_1)^{\dot{C}D})-s_1(k_{5\dot{A}}K(q_1)^{\dot{A}B}k_{6B})(e(q_1)_{\dot{C}D}e(q_2)^{\dot{C}D}))]\\
D_3 =& -\frac{8\mathrm{i}\alpha_S\pi}{(q_1+q_2)^2-M_Z^2}[(1-\frac{1}{2\sin^2\theta_W})[s_1(k_{5\dot{A}}e(q_1)^{\dot{A}B}k_{6B})(e(q_2)_{\dot{C}D}K(q_1)^{\dot{C}D})\\
&-s_1(k_{5\dot{A}}e(q_2)^{\dot{A}B}k_{6B})(e(q_1)_{\dot{C}D}K(q_2)^{\dot{C}D})-s_2(k_5^Ae(q_2)_{A\dot{B}}k_6^{\dot{B}})(e(q_1)_{\dot{C}D}K(q_2)^{\dot{C}D})\\
&+s_2(k_5^Ae(q_1)_{A\dot{B}}k_6^{\dot{B}})(e(q_2)_{\dot{C}D}K(q_1)^{\dot{C}D})+\frac{1}{2}(s_1(k_{5\dot{A}}K(q_2)^{\dot{A}B}k_{6B})(e(q_1)_{\dot{C}D}e(q_2)^{\dot{C}D})\\
&-s_2(k_5^AK(q_1)_{A\dot{B}}k_6^{\dot{B}})(e(q_1)_{\dot{C}D}e(q_2)^{\dot{C}D})+s_2(k_5^AK(q_2)_{A\dot{B}}k_6^{\dot{B}})(e(q_1)_{\dot{C}D}e(q_2)^{\dot{C}D})\\
&+s_1(k_{5\dot{A}}e(q_1)^{\dot{A}B}k_{6B})(e(q_2)_{\dot{C}D}K(q_2)^{\dot{C}D})+s_2(k_5^Ae(q_1)_{A\dot{B}}k_6^{\dot{B}})(e(q_2)_{\dot{C}D}K(q_2)^{\dot{C}D})\\
&-s_1(k_{5\dot{A}}e(q_2)^{\dot{A}B}k_{6B})(e(q_1)_{\dot{C}D}K(q_1)^{\dot{C}D})-s_2(k_5^Ae(q_2)_{A\dot{B}}k_6^{\dot{B}})(e(q_1)_{\dot{C}D}K(q_1)^{\dot{C}D})\\
&-s_1(k_{5\dot{A}}K(q_1)^{\dot{A}B}k_{6B})(e(q_1)_{\dot{C}D}e(q_2)^{\dot{C}D}))],
\end{aligned}
\tag{4.13}
$$

where $s_1$ and $s_2$ are auxiliary variables that let us switch between the helicity configurations of the external electron-positron pair. Their values are $s_1 = 1$, $s_2 = 0$ if the helicities of the outgoing leptons are $\lambda_5 = -1$, $\lambda_6 = 1$, and $s_1 = 0$, $s_2 = 1$ if $\lambda_5 = 1$, $\lambda_6 = -1$. The tensor $e(q)_{\dot{A}B}$ stands for $\varepsilon_+(q)_{\dot{A}B}$, $\varepsilon_-(q)_{\dot{A}B}$, $\varepsilon_0(q)_{\dot{A}B}$ and $K(q)_{\dot{A}B}$, depending on the term in the polarization sum. Explicit forms of these tensors can be found in Appendix A. All of them can be written in terms of eigenvectors $n_{i\dot{A}}(q)$ which, once the dotted and undotted WvdW spinors are contracted, lead to scalar products similar to those presented in (4.10) and (4.11) for the QCD building blocks. In the end, the expressions form arrays $D_1(i,j)$, $D_2(i,j)$ and $D_3(i,j)$ which, once summed, form the full leptonic building block $WWee(i,j)$ that can be combined with the previously obtained building blocks (Section 4.8) $udW_{13}(i)$ and $Wdu_2(j)$ to produce the complete Born-level helicity amplitude $\mathcal{M}$ for the diagrams from Figure 4.9.

$$
\mathcal{M} = \sum_i \sum_j udW_{13}(i)WWee(i,j)Wdu_2(j) \tag{4.14}
$$

This formula is written in the form that is used througout this thesis for all processes required

for our calculation (see Appendix B). The summation symbol $\sum$ is merely symbolical and represents combining all terms of the polarization sum according to (4.7), including adding the necessary propagators for the intermediate vector bosons (in the computer code used in our calculation, these are included in the building blocks in which the vector boson is an outgoing particle) and dividing the last term of the sum in (4.7) with the square of the corresponding momentum.

This example demonstrates two primary advantages of using the polarization sums. First, each building block is a completely independent object, defined solely by the momenta flowing into its external lines. Any changes applied to one of the building blocks which have no effect on the overall kinematics of the diagram (couplings, virtual corrections) only require re-evaluation of that particular block while the remaining building blocks remain unchanged. In the example above, this means that applying gluon loops to the QCD building blocks $udW_{13}$ and $Wdu_2$, as is dictated by the virtual corrections, does not require recalculating the leptonic building block $WWee$.

Second advantage comes from the fact that once a database of all possible momentum configurations is built (all possibilities relevant to our calculation are listed in Section 4.3), many of them can be used to construct several subamplitudes while only evaluated once. The building blocks $udW_{13}$ and $Wdu_2$, for example, can be used in several instances in most generic types of diagrams from Figure 3.1.

Chapter 5

# Calculation of the leading-order helicity amplitudes

In this chapter, we present a method for constructing the absolute squares of the helicity amplitudes that has been used for calculating the leading order cross sections for all processes listed in Chapter 3.

The building blocks introduced in the previous chapter can be used to calculate all subamplitudes which, once summed up, result in the full amplitude for any of the subprocesses listed in Chapter 3, both at the leading order and at the next-to-leading order. Each subamplitude is constructed using one, two or three insertions of the polarization sum (4.7), cutting the intermediate vector bosons that couple to the quark lines.

In this chapter, we cover the calculation for the individual subprocesses at the leading order, specifying which building blocks are used to produce the subamplitudes and how they are combined. Since all channels, including their interferences, are considered, great care needs to be taken when constructing the squares of amplitudes for channels with several helicity configurations.

## 5.1 pp $\to$ jj $W^{\pm}W^{\pm}$

This is in many aspects the simplest process, as it involves only one subprocess and one combination of charges and helicities of the external particles. For pp $\to$ jj $W^+W^+$, the incoming quarks must carry positive, outgoing quarks negative and the lepton pairs positive charge. For pp $\to$ jj $W^-W^-$, the charge configuration is reversed. Only one combination of helicities is possible in both cases.

Any subprocess contributing to pp $\to$ jj $W^{\pm}W^{\pm}$ can thus be written as

$$q_{\pm}\begin{pmatrix}k_1\\ \mp\end{pmatrix}q_{\pm}\begin{pmatrix}k_2\\ \mp\end{pmatrix} \to q_{\mp}\begin{pmatrix}k_3\\ \mp\end{pmatrix}q_{\mp}\begin{pmatrix}k_4\\ \mp\end{pmatrix}l_{\pm}\begin{pmatrix}k_5\\ \pm\end{pmatrix}l_0\begin{pmatrix}k_6\\ \mp\end{pmatrix}l_{\pm}\begin{pmatrix}k_7\\ \pm\end{pmatrix}l_0\begin{pmatrix}k_8\\ \mp\end{pmatrix} \tag{5.1}$$

where the index $i$ next to $q_i$ and $l_i$ represents charge of the respective quark or lepton, the first row in the bracket denotes momentum and the second row the helicity of the fermion.

In the following, we show how to construct all relevant subamplitudes corresponding to the $t$-channel subprocess uc $\to$ ds$e^+\nu_e\mu^+\nu_\mu$ using the building blocks from the previous

chapter. Remaining channels and subprocesses can be obtained via crossing as discussed in Section 5.5.

In order to assemble the Feynman diagrams contributing to the subamplitudes from the building blocks listed in Section 4.5, it is useful to use the classification illustrated in Figure 4.3. For uc $\to$ dse$^+\nu_e\mu^+\nu_\mu$, electric charge of the external fermions limits the contributions only to types B, C and D. Type A is prohibited by the fact that one vector boson cannot give rise to two positively or negatively charged lepton pairs.

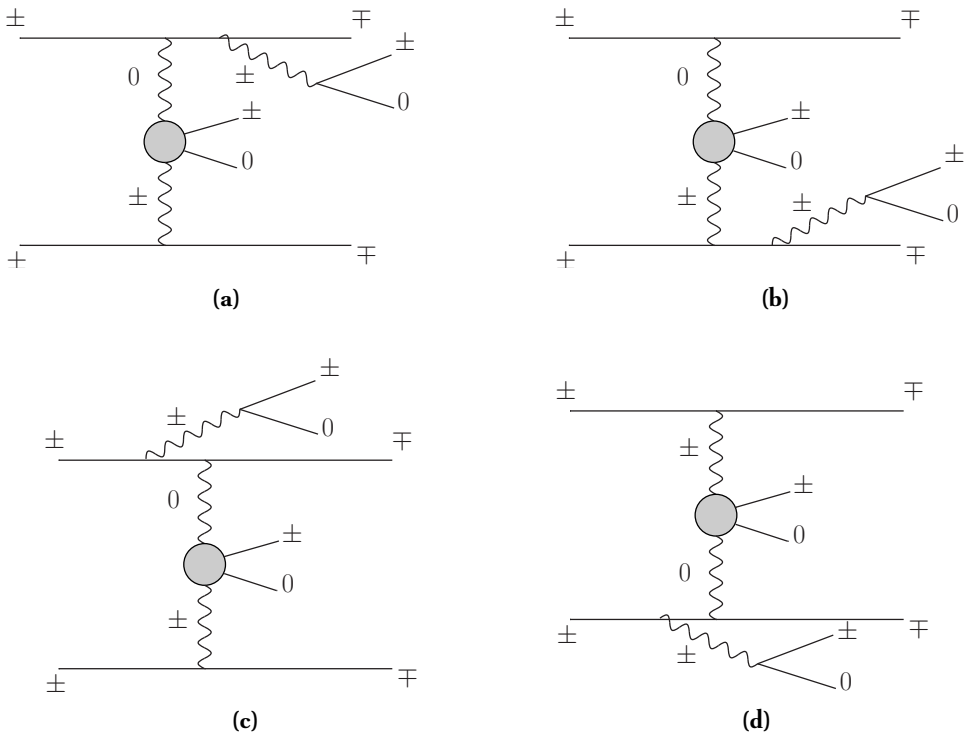


**Figure 5.1:** Type B diagrams in pp $\to$ jj $W^\pm W^\pm$ subprocesses. The first sign corresponds to uc $\to$ dse$^+\nu_e\mu^+\nu_\mu$ and the second to ds $\to$ uc$e^-\bar{\nu}_e\mu^-\bar{\nu}_\mu$.

Feynman diagrams that belong to types B, C and D are shown in Figures 5.1, 5.2, 5.3. To construct the polarization sums corresponding to each of these diagrams, we proceed by cutting all gauge bosons using relation (4.7) and splitting the amplitudes into leptonic or QCD building blocks. Individual fermions can be determined from the electric charge as denoted in Figures 5.1–5.3: "+" for the up-type quarks, $e^+$ and $\mu^+$; "−" for the down-type quarks, $e^-$ and $\mu^-$ and "0" for $\nu_i$ and $\bar{\nu}_i$. In case of gauge bosons, "0" stands for Z boson and $\gamma$, while "±" stands for $W^\pm$ (the correct sign is determined by charge conservation). As a result, we obtain a set of polarization sums, each corresponding to one of the configurations of fermions and gauge bosons. The complete list of the polarization sums for uc $\to$ dse$^+\nu_e\mu^+\nu_\mu$ can be found in Table B.1 and, once added up, they amount to the full colour-stripped amplitude. How to obtain the squared amplitude, including the colour and averaging factors is covered

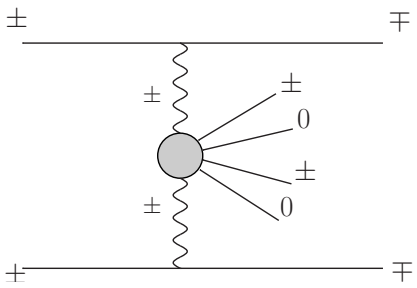


(a)

**Figure 5.2:** Type C diagram in pp $\to$ jj $W^{\pm}W^{\pm}$ subprocesses. The first sign corresponds to uc $\to$ dse$^{+}\nu_{e}\mu^{+}\nu_{\mu}$ and the second to ds $\to$ uc$e^{-}\bar{\nu}_{e}\mu^{-}\bar{\nu}_{\mu}$.

by Section 5.10.

Evaluation of the amplitude for ds $\to$ uce$^{-}\bar{\nu}_{e}\mu^{-}\bar{\nu}_{\mu}$, which is a $t$-channel subprocess corresponding to the $W^{-}W^{-}$ boson production is performed analogously, with building blocks that are charge-conjugated to the ones used in B.1.

## 5.2 pp $\to$ jj $W^{\pm}Z/\gamma$

All subprocesses contributing to pp $\to$ jj $W^{+}Z/\gamma$ can, in general, be expressed as

$$q_{+}\begin{pmatrix}k_1\\-\end{pmatrix}q_{\pm}\begin{pmatrix}k_2\\\mp\end{pmatrix}\to q_{-}\begin{pmatrix}k_3\\-\end{pmatrix}q_{\pm}\begin{pmatrix}k_4\\\pm\end{pmatrix}l_{+}\begin{pmatrix}k_5\\+\end{pmatrix}l_{0}\begin{pmatrix}k_6\\-\end{pmatrix}l_{+}\begin{pmatrix}k_7\\+\end{pmatrix}l_{-}\begin{pmatrix}k_8\\-\end{pmatrix}, \tag{5.2}$$

using the notation introduced in (5.1). Note that while (5.1) represented two different processes, here it only stands for the one involving intermediate production of the positively-charged W boson, while the $W^{-}Z/\gamma$ production process can be written as

$$q_{-}\begin{pmatrix}k_1\\+\end{pmatrix}q_{\pm}\begin{pmatrix}k_2\\\mp\end{pmatrix}\to q_{+}\begin{pmatrix}k_3\\+\end{pmatrix}q_{\pm}\begin{pmatrix}k_4\\\pm\end{pmatrix}l_{-}\begin{pmatrix}k_5\\-\end{pmatrix}l_{0}\begin{pmatrix}k_6\\+\end{pmatrix}l_{+}\begin{pmatrix}k_7\\+\end{pmatrix}l_{-}\begin{pmatrix}k_8\\-\end{pmatrix}. \tag{5.3}$$

The charge configurations corresponding to the $t$-channel Feynman diagram of types A, B, C, D from Figure 4.3 are shown in Figures 5.4, 5.5, 5.6 and 5.7, respectively.

To obtain the amplitude for the $W^{+}Z/\gamma$ production processes, we evaluate two $t$-channel subprocesses, uc $\to$ dce$^{+}\nu_{e}\mu^{+}\mu^{-}$ and us $\to$ dse$^{+}\nu_{e}\mu^{+}\mu^{-}$. As shown in Section 5.5, all remaining contributions necessary for evaluating the subprocesses listed in Chapter 3 can be obtained from these two via crossing symmetry.

Inserting specific fermion and gauge fields into the diagrams in Figures 5.4–5.7 and cutting the intermediate gauge bosons results in a series of polarization sums, total of which is the colour-stripped amplitude of the two subprocesses. The full list of polarization sums for uc $\to$ dce$^{+}\nu_{e}\mu^{+}\mu^{-}$ can be found in Table B.2 and for us $\to$ dse$^{+}\nu_{e}\mu^{+}\mu^{-}$ in Table B.3. Similarly to the previous case, the amplitude for the $W^{-}Z/\gamma$ production process can be obtained by charge conjugating of all building blocks that contribute to the polarization sums.

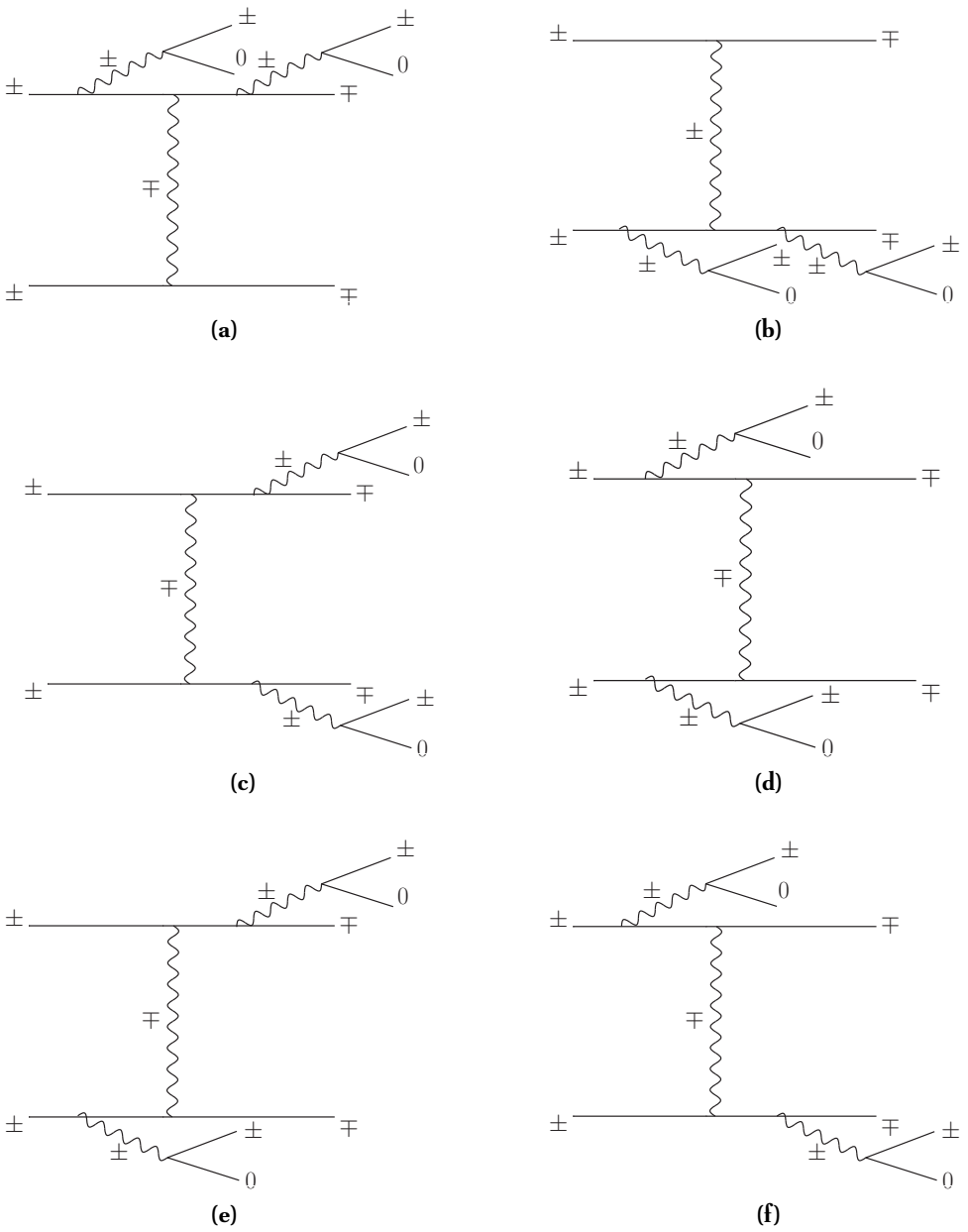


**Figure 5.3:** Type D diagrams in pp $\to$ jj $W^{\pm}W^{\pm}$ subprocesses. The first sign corresponds to uc $\to$ dse$^+\nu_e\mu^+\nu_\mu$ and the second to ds $\to$ uce$^-\bar{\nu}_e\mu^-\bar{\nu}_\mu$.

## 5.3 pp $\to$ jj $W^+W^-$

As can be seen in Table 3.1, the process involving $W^+W^-$ production consists of four generic subprocesses which cover all possibilities for the sum of electric charges of the incoming and outgoing quarks to be equal. First three of them, uc $\to$ uce$^+\nu_e\mu^-\bar{\nu}_\mu$, us $\to$ dce$^+\nu_e\mu^-\bar{\nu}_\mu$ and

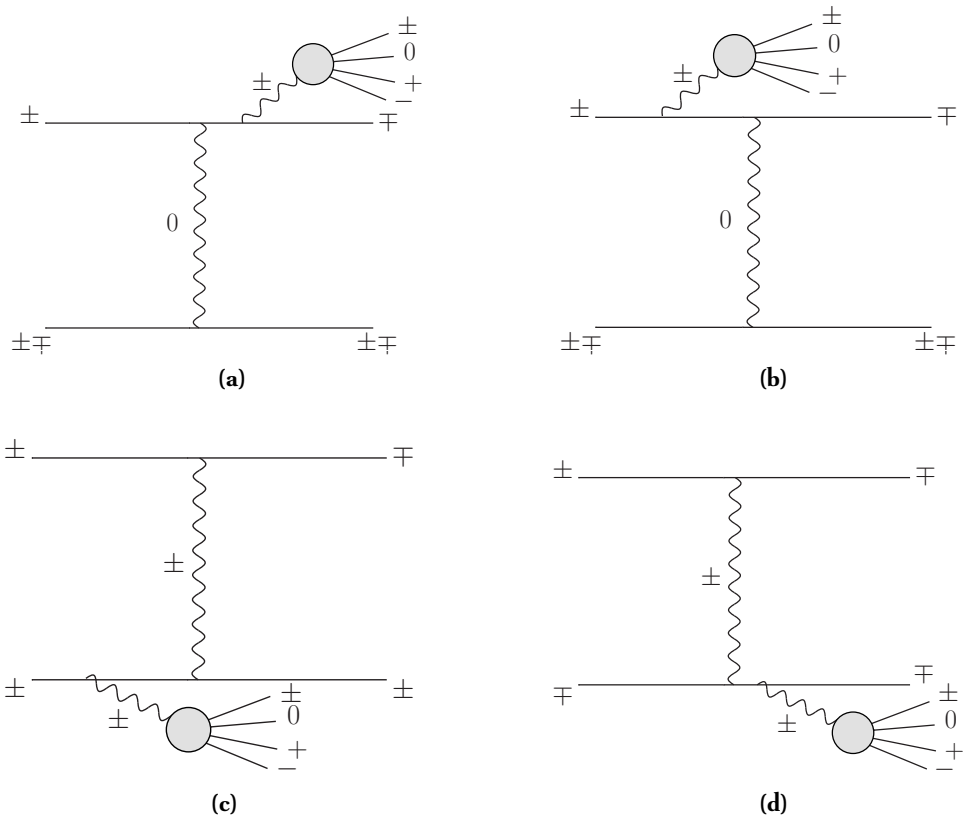


**Figure 5.4:** Type A diagrams in pp $\to$ jj $W^{\pm}Z/\gamma$ subprocesses. The upper sign corresponds to $W^+Z/\gamma$ production, the lower to $W^-Z/\gamma$ production.

us $\to$ use$^+\nu_e\mu^-\bar{\nu}_\mu$ can be expressed, using the same notation as in previous two sections, as

$$q_{\pm}\begin{pmatrix}k_1\\ \pm\end{pmatrix}q_{\pm\mp}\begin{pmatrix}k_2\\ \pm\end{pmatrix} \to q_{\pm}\begin{pmatrix}k_3\\ \pm\end{pmatrix}q_{\pm\mp}\begin{pmatrix}k_4\\ \pm\end{pmatrix}l_{+}\begin{pmatrix}k_5\\ +\end{pmatrix}l_{0}\begin{pmatrix}k_6\\ -\end{pmatrix}l_{-}\begin{pmatrix}k_7\\ -\end{pmatrix}l_{0}\begin{pmatrix}k_8\\ +\end{pmatrix}, \tag{5.4}$$

while the fourth, us $\to$ dce$^+\nu_e\mu^-\bar{\nu}_\mu$, corresponds to

$$q_{+}\begin{pmatrix}k_1\\ -\end{pmatrix}q_{-}\begin{pmatrix}k_2\\ +\end{pmatrix} \to q_{-}\begin{pmatrix}k_3\\ -\end{pmatrix}q_{+}\begin{pmatrix}k_4\\ +\end{pmatrix}l_{+}\begin{pmatrix}k_5\\ +\end{pmatrix}l_{0}\begin{pmatrix}k_6\\ -\end{pmatrix}l_{-}\begin{pmatrix}k_7\\ -\end{pmatrix}l_{0}\begin{pmatrix}k_8\\ +\end{pmatrix}. \tag{5.5}$$

The configurations of charges in the generic diagrams in Figure 4.3 are depicted in Figures 5.8–5.11 for all four cases. The lists of polarization sums obtained by cutting all intermediate vector bosons are presented in Table B.4 for uc $\to$ uce$^+\nu_e\mu^-\bar{\nu}_\mu$ and us $\to$ dce$^+\nu_e\mu^-\bar{\nu}_\mu$, Table B.5 for us $\to$ use$^+\nu_e\mu^-\bar{\nu}_\mu$ and in Table B.6 for us $\to$ dce$^+\nu_e\mu^-\bar{\nu}_\mu$. As in the previous cases, the remaining channels and interferences are generated via crossing (see Section 5.5).

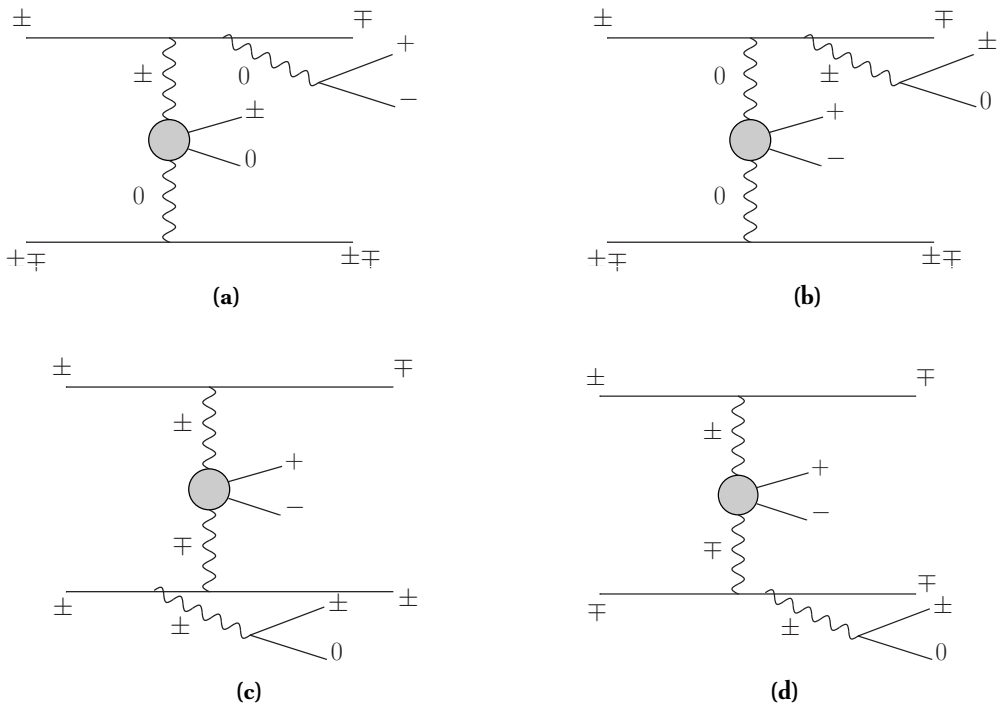


**Figure 5.5:** Type B diagrams in $pp \to jj\, W^{\pm}Z/\gamma$ subprocesses. The first sign corresponds to $W^{+}Z/\gamma$ production, the second to $W^{-}Z/\gamma$ production.

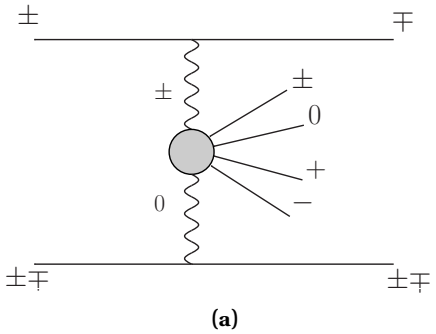


**Figure 5.6:** Type C diagram in $pp \to jj\, W^{\pm}Z/\gamma$ subprocesses. The first sign corresponds to $W^{+}Z/\gamma$ production, the second to $W^{-}Z/\gamma$ production.

## 5.4 $pp \to jj\, ZZ/Z\gamma/\gamma\gamma$

Contrary to the processes in the previous sections, two different leptonic final states must be considered in the production of neutral vector bosons, $e^{+}e^{-}\nu_{\mu}\bar{\nu}_{\mu}$ and $e^{+}e^{-}\mu^{+}\mu^{-}$ (final states with three or more neutrinos are not considered, as they cannot be discerned in experiments). Since the initial and final states of the quarks are identical to those in $W^{+}W^{-}$ production

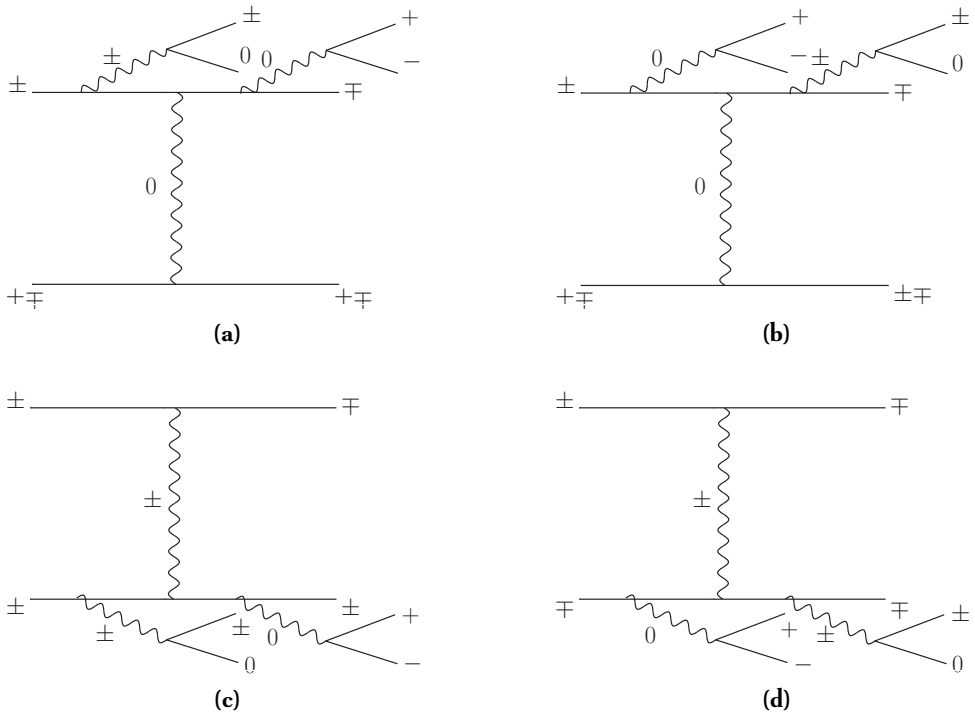


**Figure 5.7:** Type D diagrams in pp $\to$ jj $W^{\pm}Z/\gamma$ subprocesses. The first sign corresponds to $W^{+}Z/\gamma$ production, the second to $W^{-}Z/\gamma$ production. In all cases, the line with a neutral intermediate gauge boson can be radiated off all possible quark lines.

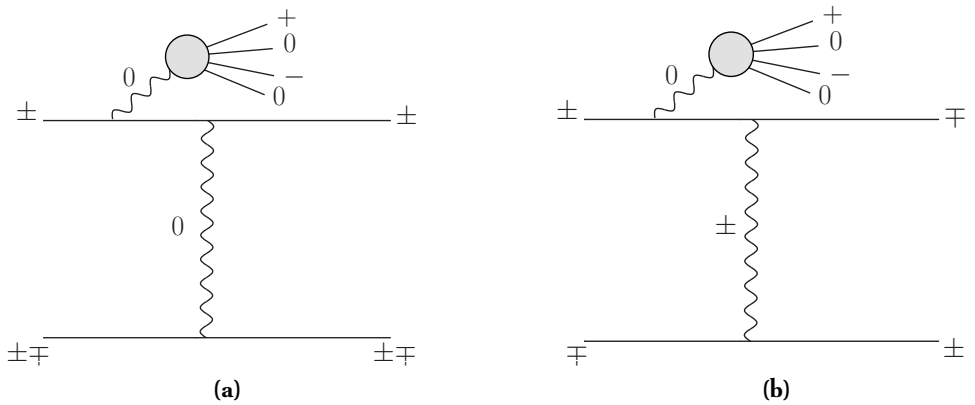


**Figure 5.8:** Type A diagrams in pp $\to$ jj $W^{+}W^{-}$ subprocesses. The neutral intermediate gauge boson connected to the leptonic tensor can be attached to any of the quark lines.

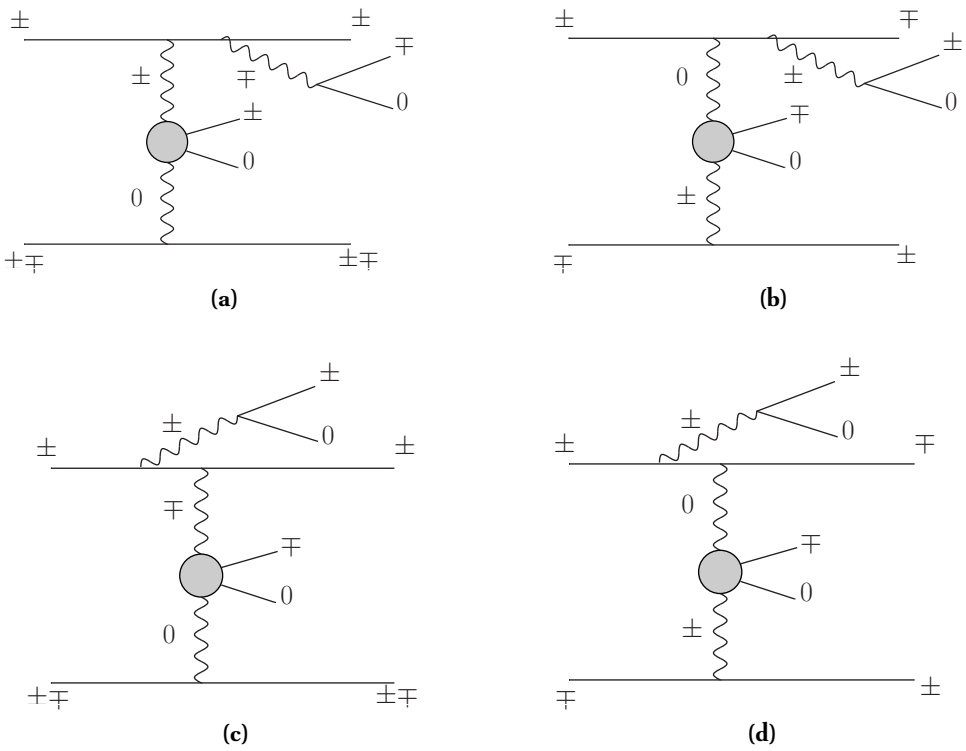


**Figure 5.9:** Type B diagrams in pp $\to$ jj $W^+W^-$ subprocesses.

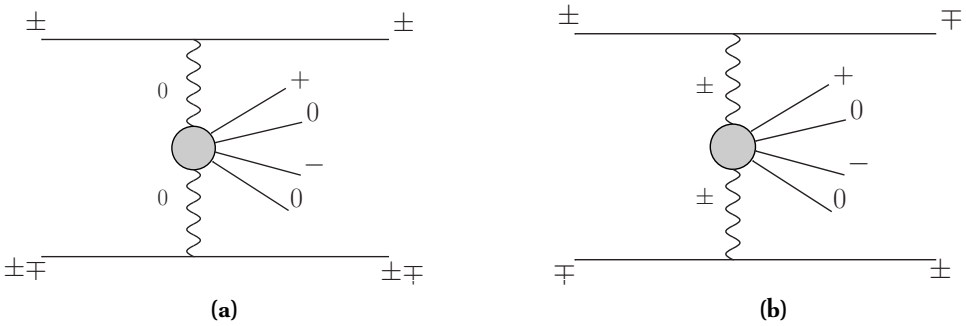


**Figure 5.10:** Type C diagrams in pp $\to$ jj $W^+W^-$ subprocesses.

(Section 5.3), we can write

$$q_{\pm}\begin{pmatrix}k_1\\ \pm\end{pmatrix}q_{\pm\mp}\begin{pmatrix}k_2\\ \pm\end{pmatrix} \to q_{\pm}\begin{pmatrix}k_3\\ \pm\end{pmatrix}q_{\pm\mp}\begin{pmatrix}k_4\\ \pm\end{pmatrix}l_{+}\begin{pmatrix}k_5\\ +\end{pmatrix}l_{-}\begin{pmatrix}k_6\\ -\end{pmatrix}l_{+0}\begin{pmatrix}k_7\\ \pm\end{pmatrix}l_{-0}\begin{pmatrix}k_8\\ \pm\end{pmatrix} \tag{5.6}$$

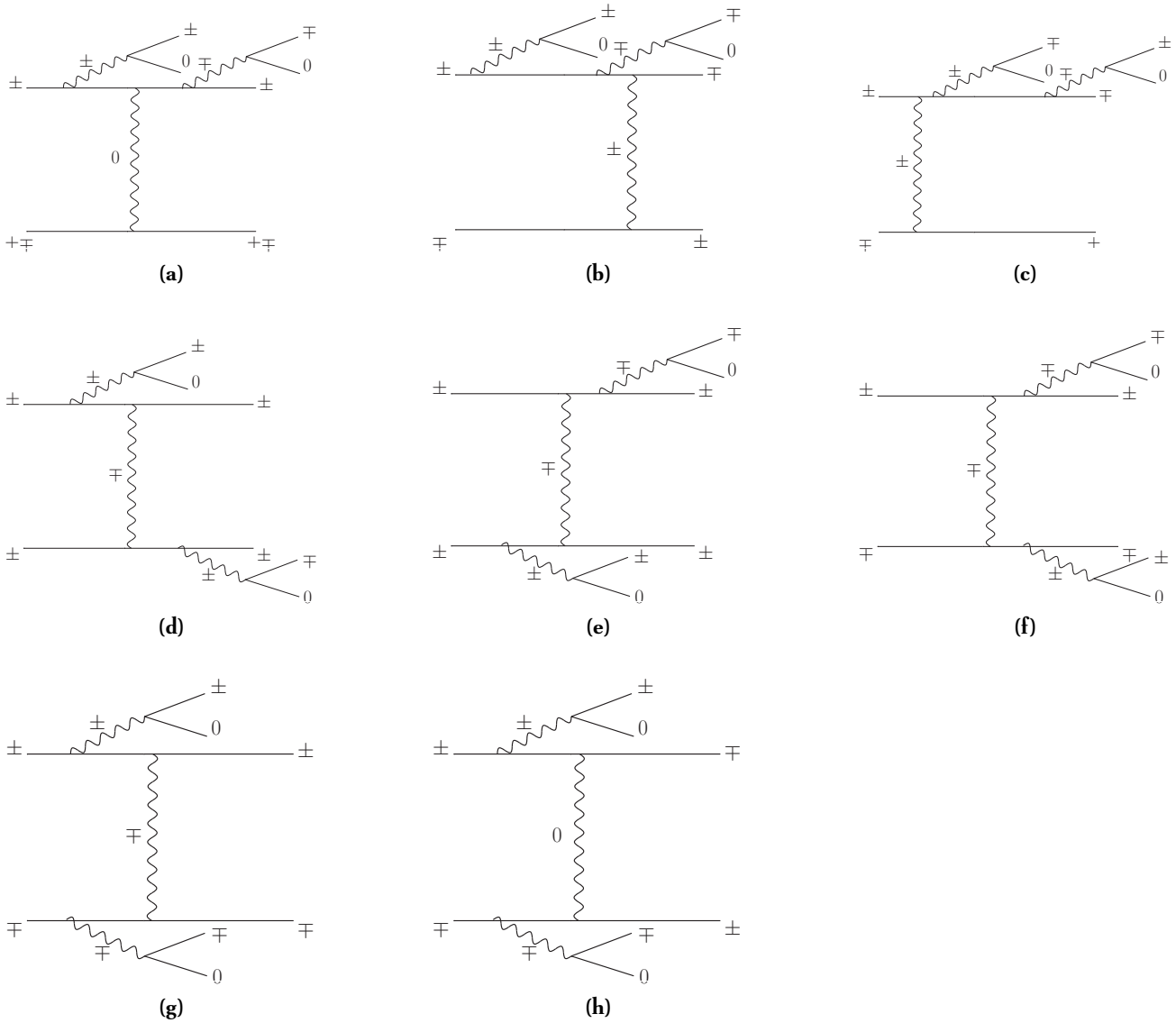


**Figure 5.11:** Type D diagrams in pp $\to$ jj $W^+W^-$ subprocesses.

for the subprocesses with the same initial- and final-quark states and

$$q_+\begin{pmatrix}k_1\\-\end{pmatrix}q_-\begin{pmatrix}k_2\\+\end{pmatrix}\to q_-\begin{pmatrix}k_3\\-\end{pmatrix}q_+\begin{pmatrix}k_4\\+\end{pmatrix}l_+\begin{pmatrix}k_5\\+\end{pmatrix}l_-\begin{pmatrix}k_6\\-\end{pmatrix}l_{+0}\begin{pmatrix}k_7\\\pm\end{pmatrix}l_{-0}\begin{pmatrix}k_8\\\pm\end{pmatrix} \tag{5.7}$$

for the subprocesses with charge transfer between the two quark legs. The subprocesses in (5.6) contain no charge transfer and, as a result, all combinations of polarizations for each initial- and final-state particle must be considered. The approach of splitting diagrams into building blocks offers an advantage in this case - instead of evaluating $2^4 = 16$ combinations,

we only need to calculate two per each building block (or four in case of the leptonic building blocks with four leptons in the final state), which is $2 \cdot 4 = 8$ combinations in total.

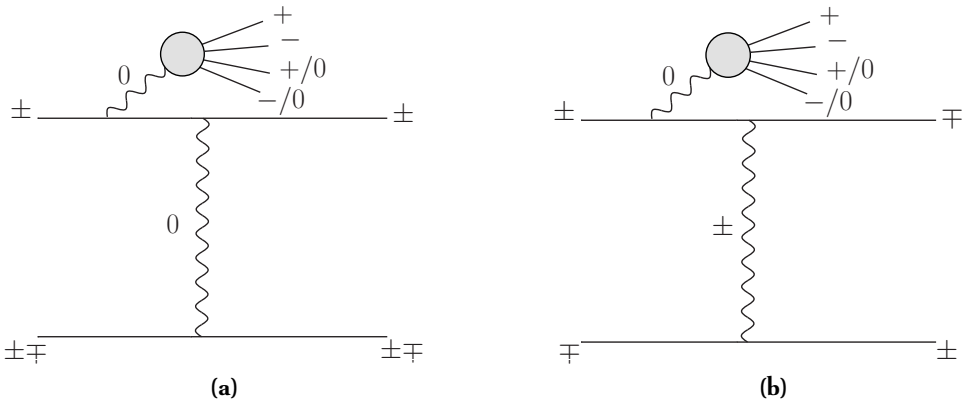


**Figure 5.12:** Type A diagrams in pp $\to$ jj ZZ/Z$\gamma$/$\gamma\gamma$ subprocesses.

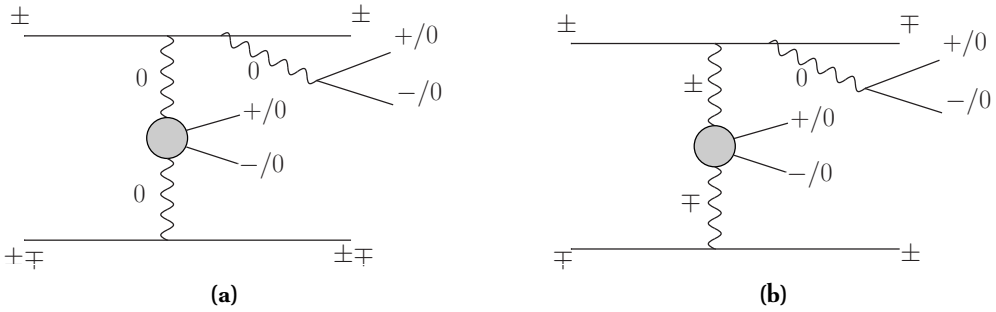


**Figure 5.13:** Type B diagrams in pp $\to$ jj ZZ/Z$\gamma$/$\gamma\gamma$ subprocesses.

Figures 5.12–5.15 show examples of diagrams corresponding to the generic types in Figure 4.3. In all four cases, the diagram on the left corresponds to the subprocesses from (5.6) and the diagram on the right to (5.7). The diagrams shown in Figures 5.12, 5.13 and 5.15 are only symbolical; the vector bosons decaying into electrically neutral leptonic pairs can be radiated from any position on the quark lines.

The polarization sums corresponding to diagrams in Figures 5.12–5.15 are listed in Tables B.7 (type (5.6)) and B.8 (type (5.7)). Note that the tables only contain sums for the subprocesses with $e^+e^-\mu^+\mu^-$ in the final state. The other set, $e^+e^-\nu_\mu\bar{\nu}_\mu$, can be obtained simply by replacing 'e'$\to$'$\nu$' in all building blocks. One must, however, keep in mind that photons do not couple to neutrinos and remove all sums containing the building block $Gee$ that might arise this way.

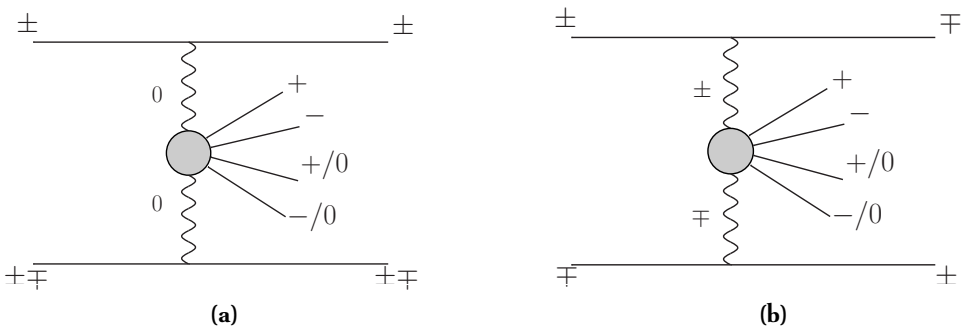


**Figure 5.14:** Type C diagrams in pp → jj ZZ/Zγ/γγ subprocesses.

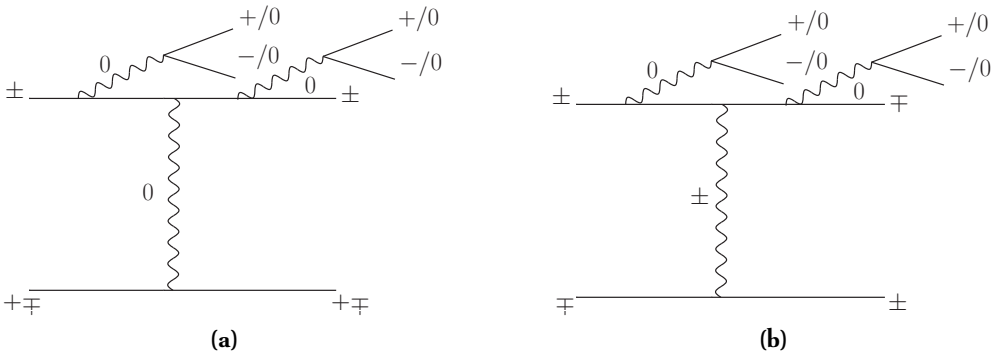


**Figure 5.15:** Type D diagrams in pp → jj ZZ/Zγ/γγ subprocesses.

## 5.5 Crossing symmetry

The previous sections of this chapter covered the construction of the subamplitudes contributing to each of the subprocesses listed in Chapter 3. Using the kinematic setup of the building blocks written down in Section 4.6 results in a generic *t*-channel subprocess with quarks in the initial and final state (e.g. uc → dse$^+\nu_e\mu^+\nu_\mu$). In order to obtain subprocesses involving external antiquarks and the two remaining combinations, we need to evaluate these building blocks after applying the crossing symmetry and/or swapping momenta of one or both quark lines.

All possible configurations of quark and antiquark states in the *t*-channel diagrams are listed in Figure 5.16. Figure 5.16a corresponds to the setup in Table 4.1 which we will consider as default. Diagrams with antiquark external states in the upper line (Figure 5.16b) can be obtained by crossing the momenta $k_1$ and $k_3$ of the quarks in the building blocks representing upper leg of the *t*-channel diagrams. In a similar manner, diagrams in Figure 5.16c can be obtained by crossing the lower quark legs $k_2$ and $k_4$ and diagrams in Figure 5.16d by crossing both quark lines.

Note that while applying the crossing symmetry implies swapping the momenta, one

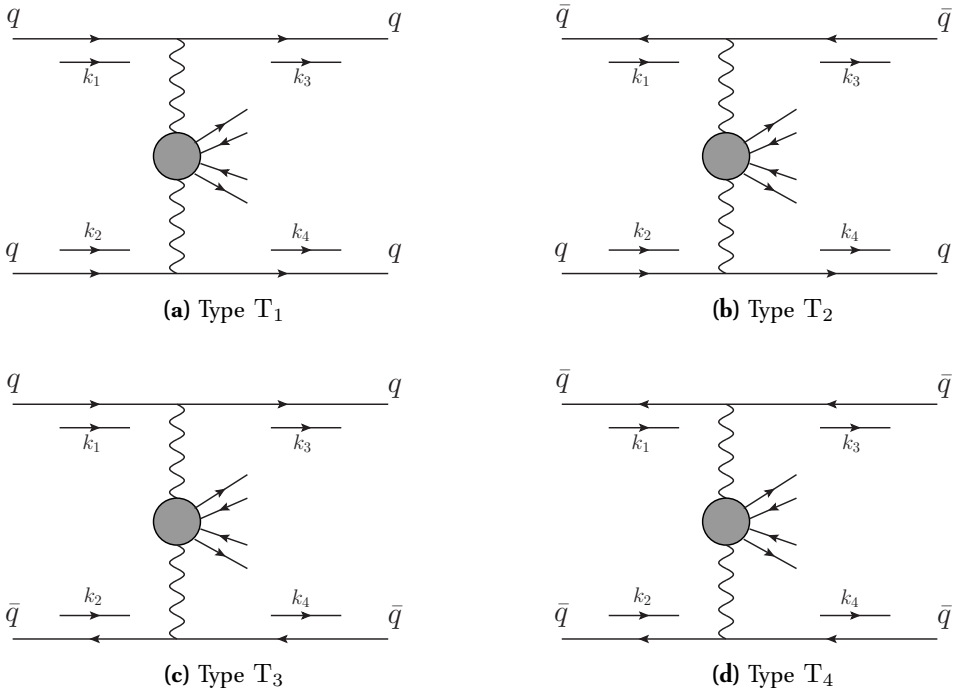


**Figure 5.16:** *t*-channel diagrams with external quarks and antiquarks. Diagrams $\mathrm{T}_2$, $\mathrm{T}_3$ and $\mathrm{T}_4$ can be obtained from $\mathrm{T}_1$ via crossing symmetry.

should do so only in case of the WvdW spinors corresponding to the quarks in question and not when evaluating the momenta of the intermediate vector bosons, since the kinematics of the process remains the same. For instance, the building block $udW(k_1, k_3, k_1 - k_3)$ (see notation in Section 4.3) becomes $ud\mathrm{W}(-k_3, -k_1, k_1 - k_3)$, where the momentum $k_1 - k_3$ of the W boson, once squared, corresponds to the Mandelstam variable $t$ and does not change with crossing. For this reason we need to differentiate between crossing the quarks to create antiquarks and globally swapping momenta to construct different kinematic channels.

*u*-channel diagrams in Figure 5.17 can be obtained by first swapping the momenta $k_3$ and $k_4$ in all building blocks (including the momenta of the intermediate vector bosons) and then crossing relevant quark lines to produce the antiquarks in diagrams 5.17b, 5.17c and 5.17d. For example, the crossed building block $ud\mathrm{W}_1$ in diagram $\mathrm{U}_2$ turns into $ud\mathrm{W}(-k_4, -k_1, k_1 - k_4)$, where the square momentum of W boson corresponds to the Mandelstam variable $u$.

Obtaining the *s*-channel diagrams in Figure 5.18, starting with diagram $\mathrm{T}_1$ requires first swapping the final-state momenta and subsequently crossing one initial-state and one final-state quark from two different quark lines. Diagram $\mathrm{S}_1$ (Figure 5.18a), for instance, can be obtained from diagram $\mathrm{T}_1$ (Figure 5.16a) by first swapping the momenta $k_4$ and $k_1$, and then applying the crossing symmetry on the same quark lines, while diagram $\mathrm{S}_3$ (Figure 5.18b) can be produced by applying the same procedure on diagram $\mathrm{U}_1$ (Figure 5.17a).

The algorithm outlined in this section allows us to construct all subprocesses required

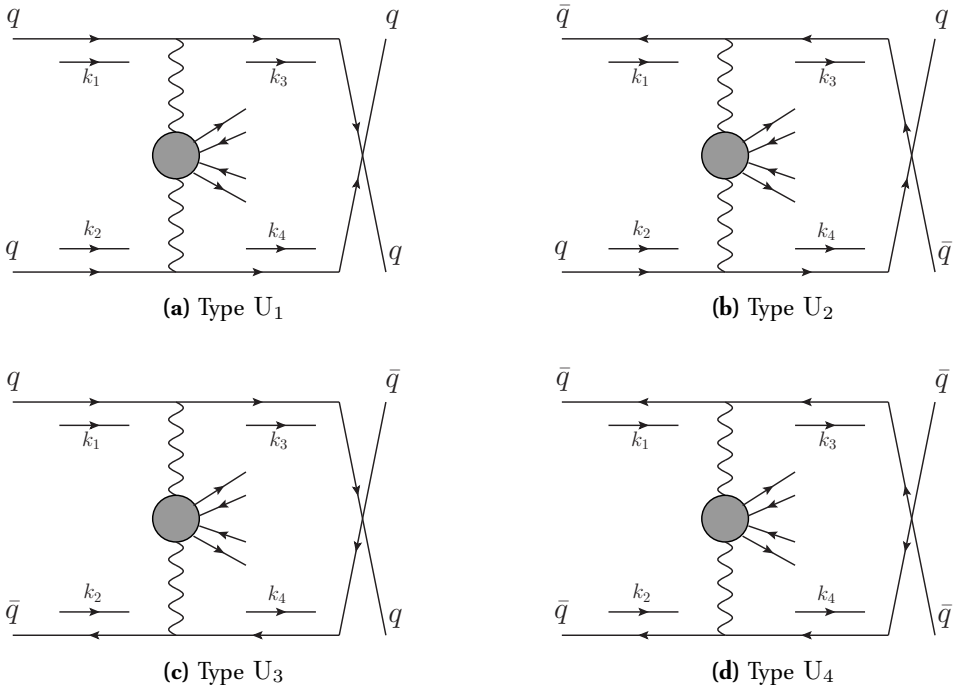


**Figure 5.17:** $u$-channel diagrams with external quarks and antiquarks. Diagrams $\mathrm{U}_2$, $\mathrm{U}_3$ and $\mathrm{U}_4$ can be obtained from $\mathrm{T}_1$ by swapping momenta 3 and 4 and crossing the relevant quark lines.

for our calculation from one generic $t$-channel subprocess by applying crossing symmetry and exchanging external momenta flowing into the quark lines. In the cases where the charges of the quark lines do not coincide (e.g. uc $\to$ dce$^+\nu_\mathrm{e}\mu^+\mu^-$), some of the subprocesses are constructed from $t$-channel diagrams obtained by swapping momentum $k_1$ with $k_2$ and momentum $k_3$ with $k_4$ (for instance dc $\to$ dse$^+\nu_\mathrm{e}\mu^+\mu^-$ from us $\to$ dse$^+\nu_\mathrm{e}\mu^+\mu^-$).

## 5.6 Numerical evaluation

The code for producing numerical values of the leading-order amplitudes has been generated using a combination of freely available tools, modified to support the polarization sums algorithm outlined in Chapter 4. First, the Feynman diagrams for each building block are created in Mathematica [46] using FeynArts package [47]. The analytical expressions for the matrix elements are converted into the helicity formalism by means of FormCalc 6 package [48], which also introduces abbreviations for the fermion chains that helps to speed up the code significantly.

At this point, a number of modifications is introduced, mostly centered around creating arrays of amplitudes, elements of which represent terms in the polarization sums. To do that, each polarization vector is replaced with either $\varepsilon_{+,\,\dot{A}B}$, $\varepsilon_{-,\,\dot{A}B}$, $\varepsilon_{0,\,\dot{A}B}$ or $K_{\dot{A}B}$ according to

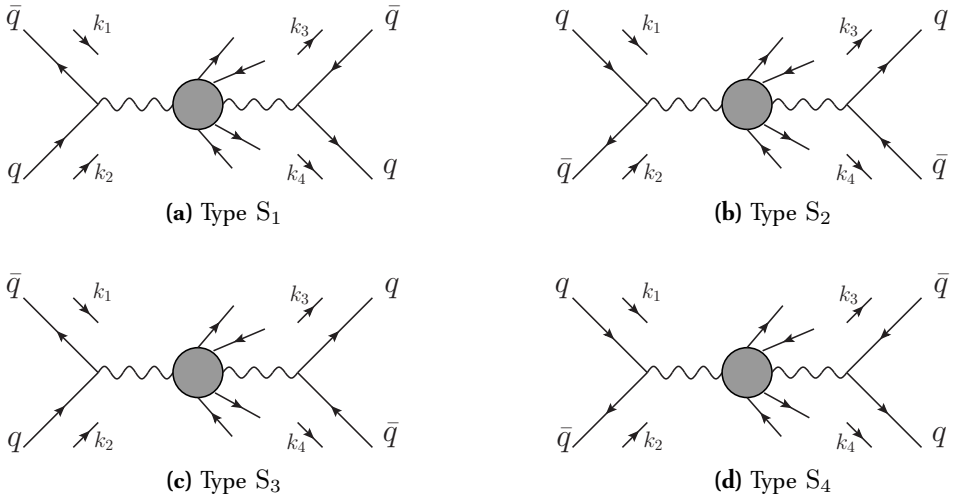


**(a)** Type $\mathrm{S}_1$ **(b)** Type $\mathrm{S}_2$

**(c)** Type $\mathrm{S}_3$ **(d)** Type $\mathrm{S}_4$

**Figure 5.18:** $s$-channel diagrams with external quarks and antiquarks. Diagram $\mathrm{S}_1$ can be obtained from $\mathrm{T}_1$ by swapping and crossing momenta $k_4$ and $k_1$, diagram $\mathrm{S}_2$ by crossing and swapping momenta $k_3$ and $k_2$, while diagrams $\mathrm{S}_3$ and $\mathrm{S}_4$ by doing the same with diagram $\mathrm{U}_1$.

the array index (see Section 4.8) and all kinematical objects are broken into WvdW spinors (A.9). Subsequently, spinors with contracted helicity indices are resolved as scalar products which are abbreviated again since they typically occur multiple times. The scalar products which originate in contracting two dotted indices and contain spinors corresponding to one of the external quark lines are multiplied by a variable that takes value +1 if the particle in question is a quark and -1 if it is an antiquark. This, combined with exchanging the relevant momenta amounts to applying the crossing symmetry according to Section 4.2.

Arrays containing analytical expressions that contribute to the polarization sum, as well as all abbreviations are then exported from Mathematica into Fortran 95 using a set of functions provided by Mathematica and FormCalc. Each building block is stored in a separate module and can be initiated with subroutines that supply the momenta and helicities for the particles in the building block. The results are stored in complex arrays that serve as arguments of the polarization sums implemented in a way similar to that in Tables B.1–B.8.

The Fortran code for each process is contained in a single function that can be called from within a Monte Carlo program and returns an array of full squared amplitudes for each subprocess, channel (treating interferences separately to preserve an option to turn them on and off), quark-antiquark configuration and includes all relevant colour and averaging factors evaluated in Sections 5.9 and 5.10. The only arguments of the function are momenta of the particle phase space and the choice of the width scheme (see Chapter 2).

## 5.7 Numerical checks

In order to ensure correctness of the leading-order calculation, the matrix elements have been checked in a number of ways, using several publicly available tools. First, as a consistency check, a comparison has been performed against numerical results generated purely in FormCalc 6 [48], using its Fortran interface. Due to complexity of the considered processes, we were only able to produce and compare the numerical results at the diagram level. Since the helicity amplitudes for both codes are resolved using the same algorithm (the differences arise after the helicity fermion chains are generated and Fierz transformations are applied), they are expected to yield identical results for the same set of parameters. Indeed, the two numerical results for individual diagrams or group of diagrams agree up to 15 digits for a set of random phase-space points, which corresponds to double precision numerical accuracy. This check assures that the polarization sums and building blocks have been constructed correctly and in addition provides a convenient debugging tool.

Another, more independent check was carried out using MadGraph 4 [49] which is presented as a tree-level matrix element creator based on the Helas library [50]. Because the version we used for comparison employs the unitary gauge while our calculation implements the t' Hooft–Feynman gauge, a diagram-level comparison is not possible. Further, in order to insure that the two numerical results are compatible, all widths have to be set to zero. For a small set of random phase-space points, we performed a comparison of all leading-order amplitudes that contribute to the subprocesses listed in Chapter 3, including interference terms. In each case, we have found an agreement of more than 8 digits.

## 5.8 Subprocesses with equal matrix elements

Due to the large number of subprocesses contributing to the cross section of the vector-boson-fusion production modes, it is desirable to limit the number of subprocesses which need to be calculated and decrease the computer time. This can be achieved by taking into account some of the approximations mentioned in Chapter 2.

One reduction in the number of required matrix elements comes from an observation that for massless quarks and for the CKM matrix approximated by a unit matrix, the subprocesses have the same matrix elements if the first-generation quarks (antiquarks) are interchanged with their second-generation counterparts and vice versa. For instance, the subprocesses uu $\to$ dde$^+\nu_e\mu^+\nu_\mu$ and cc $\to$ sse$^+\nu_e\mu^+\nu_\mu$ required for the $W^+W^+$ production (Table 3.2) only differ in the parton distribution functions, and the matrix elements only have to be computed once. The same can be applied to subprocesses involving two different generations of quarks - for example, gc $\to$ $\bar{\text{u}}$dce$^+\nu_e\mu^+\mu^-$ and gu $\to$ $\bar{\text{c}}$sue$^+\nu_e\mu^+\mu^-$ (Table 3.6) are formed by identical matrix elements. Care needs to be taken with those subprocesses that contain two incoming quarks (or antiquarks) of different generations (e.g. uc $\to$ dse$^+\nu_e\mu^+\nu_\mu$) - reversing the generations of the quark lines would simply result in the same subprocess (cu $\to$ sde$^+\nu_e\mu^+\nu_\mu$) and including it in the calculation would lead to double counting. At the same time, processes with reversed momenta assigned to the incoming partons (e.g. cu $\to$ dse$^+\nu_e\mu^+\nu_\mu$) correspond to a different kinematical channel and need to be included.

## 5.9 Colour structure of the LO amplitudes

Previous sections of this chapter describe the means of obtaining the polarized matrix elements for the subprocesses discussed in Chapter 3. These, however, do not include contributions arising from the colour structure of external quarks and gluons which involves generators $T^a_{ij}$ of the fundamental and adjoint representations of the $SU(3)_C$ group.

When calculating squares of amplitudes, $SU(3)_C$ generators are traced over and we are left with multiplying factors that depend on the colour and kinematical structure of the diagrams.

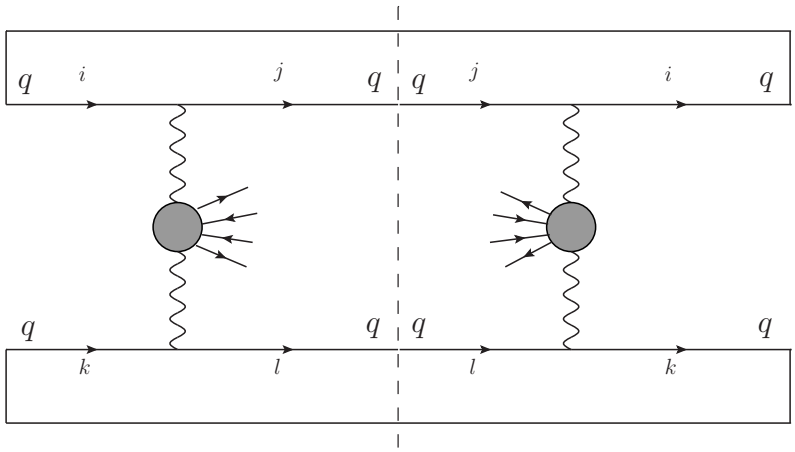


**(a)** $|\mathcal{M}^{\alpha}|^2$

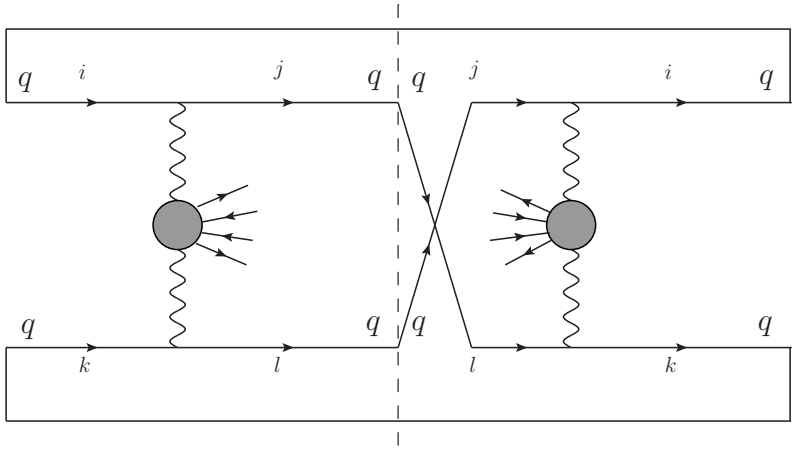


**(b)** $\mathcal{M}^{\alpha}\mathcal{M}^{\beta *}$

**Figure 5.19:** Illustration of how quark legs close in case of no interference (a) and in case of an interference between *t*- and *u*-channel diagrams (b).

At leading order, two types of colour structures can be encountered, depending on whether the two quark lines are of the same flavour or not. Since we do not consider gluon

exchange between the quark legs and no external gluon is present at LO, the color factors in this case are trivial. The full amplitude $\mathcal{M}_c$ can be written as a contraction of a color-stripped amplitude $\mathcal{M}$ and two Kronecker deltas, indices of which run from 1 to 3:

$$\mathcal{M}_c = \delta_{ji}\delta_{lk} \times \mathcal{M}^{\alpha}. \tag{5.8}$$

If the flavours of the quark chains are different (Figure 5.19a), as in $\mathrm{uc} \to \mathrm{dse}^{+}\nu_{\mathrm{e}}\mu^{+}\nu_{\mu}$, the squared matrix element contains two traces

$$\sum_{\text{colours}} |\mathcal{M}_c|^2 = \delta_{ji}\delta_{ij}\delta_{lk}\delta_{kl}|\mathcal{M}|^2 = 9|\mathcal{M}^{\alpha}|^2. \tag{5.9}$$

If both quark lines carry the same flavour, as in $\mathrm{uu} \to \mathrm{dde}^{+}\nu_{\mathrm{e}}\mu^{+}\nu_{\mu}$, the amplitude contains contributions from two different channels $\mathcal{M} = \mathcal{M}^{\alpha} + \mathcal{M}^{\beta}$. Squaring this amplitude results in additional interference terms containing only one rather than two quark lines (Figure 5.19b)

$$\begin{aligned}\sum_{\text{colours}} |\mathcal{M}_c|^2 &= \delta_{ji}\delta_{ij}\delta_{lk}\delta_{kl}(|\mathcal{M}^{\alpha}|^2 + \mathcal{M}^{\beta}|^2) - \delta_{ij}\delta_{jl}\delta_{lk}\delta_{ki}(\mathcal{M}^{\alpha}\mathcal{M}^{\beta *} + \mathcal{M}^{\beta}\mathcal{M}^{\alpha *}) \\ &= 9(|\mathcal{M}^{\alpha}|^2 + \mathcal{M}^{\beta}|^2) - 3(\mathcal{M}^{\alpha}\mathcal{M}^{\beta *} + \mathcal{M}^{\beta}\mathcal{M}^{\alpha *}).\end{aligned} \tag{5.10}$$

## 5.10 Evaluating squares of LO amplitudes

Most of the subprocesses in our calculation involve more then one combination of helicities for the external quarks and leptons. To obtain the final unpolarized matrix elements, one needs to evaluate the sum of the squared amplitude for each individual combination, as well as to collect the averaging factors for colours and helicities of the external particles. Helicities of the final-state particles can be summed since they are not observed for the considered processes.

At leading order, this includes the colour factor 9 or 3 as shown in the previous subsection, a colour averaging factor $1/3$ and a helicity averaging factor $1/2$ for each incoming quark or antiquark. In addition to these factors, a symmetry factor $1/2$ for identical final state particles arises in the phase-space integration and is included at a later point when constructing specific subprocesses.

Absolute squares of the leading order helicity amplitudes can be thus written as

$$\begin{aligned}&|\mathcal{M}_c(q_1, q_2 \to q_3, q_4, l_1, l_2, l_3, l_4)|^2 = C\frac{1}{9}\frac{1}{4}\sum_{\{\lambda\}}\sum_{\{c\}} \\ &|\mathcal{M}(q_1(\lambda_1, c_1), q_2(\lambda_2, c_2) \to q_3(\lambda_3, c_3), q_4(\lambda_4, c_4), l_1(\lambda_5), l_2(\lambda_6), l_3(\lambda_7), l_4(\lambda_8))|^2,\end{aligned} \tag{5.11}$$

where $\lambda_i$ represents helicity of the given fermion and $\{\lambda\}$ are all possible combinations thereof, while $c_i$ stands for colours of quarks, $\{c\}$ for their combinations and $C = 3$ represents the colour factor for interference terms and $C = 9$ for non-interference contributions. Since

all our diagrams involve two quark legs without any color transfer, different color combinations result in identical matrix elements and the latter sum amounts to a factor 9. This leaves us with

$$\frac{1}{4}\sum_{\{\lambda\}}|\mathcal{M}^{\alpha}|^2 \tag{5.12}$$

in case there is no interference between channels and with

$$\frac{1}{12}\sum_{\{\lambda\}}(\mathcal{M}^{\alpha}\mathcal{M}^{\beta *}+\mathcal{M}^{\beta}\mathcal{M}^{\alpha *}) \tag{5.13}$$

for the interference terms.

Chapter 6

# Evaluating the NLO QCD cross section using dipole subtraction method

The next-to-leading-order QCD contributions considered in this calculation are of the order $\alpha_S \alpha_{EW}^6$. (see Chapter 2). The next-to-leading-order calculation consists of two parts - the virtual corrections obtained by attaching a gluon in all possible ways, and the real corrections in which an outgoing gluon is attached to one of the quark legs or an initial-state gluon replaces an initial-state quark while this quark becomes outgoing.

Each of these parts leads to different types of singularities that need to be handled in order to evaluate NLO cross sections. Virtual corrections give rise to ultraviolet singularities that appear if the momentum in certain loop integrals becomes large and to infrared singularities which also show up in the radiative corrections in configurations with vanishing-momentum (soft) partons and with small angles (collinearity) between two partons.

While the ultraviolet singularities can be removed via the process of renormalization, as shown in Section 6.2.2, the cancellation of the infrared divergencies can be achieved by applying the Kinoshita-Lee-Nauenberg theorem ([51], [52]). One of its consequences is that the infrared singularities originating in the virtual corrections, once regularized, must be cancelled against the corresponding infrared divergencies in the real contributions.

This means, however, that since the virtual and real corrections have a different number of final-state partons, the divergencies are cancelled in phase-space volumes of different dimensionality and therefore have to be integrated separately over two different regions of phase space.

In general, there are at least two methods how this can be performed. One method, known as phase-space-slicing ([53, 54, 55]), relies on dividing the phase space into an infrared-safe and infrared-divergent regions. In this case, the central issue lies in adjusting the criteria of the slicing in such a way that the unphysical division of the phase space does not leave a trace and the dependence on the slicing parameters is minimized.

The other method is, in general, based on subtracting and subsequently adding a so-called subtraction term which has the same singular properties in the soft and collinear limit as the radiative corrections and at the same time is easily integrated over the phase space of both real and virtual matrix elements. Since the subtraction term contains the same infrared

poles, it cancels both real and virtual singularities at the integrand level.

The subtraction technique used in this calculation is the dipole formalism developed by Catani and Seymour [56] and represents an algorithm for finding universal subtraction terms in a process-independent manner and can thus straightforwardly be incorporated into general purpose Monte Carlo codes. A brief overview of this method is presented in Section 6.1.

The presence of initial-state hadrons gives rise to an additional type of collinear singularity which is not cancelled by the real and virtual contributions. These divergencies have their origin in non-applicability of the perturbative QCD to the non-perturbatively described structure of hadrons and are related to the fact that the momenta of partons have to be kept fixed. They can, however, be factorized and compensated for by redefining the parton distributions in a completely process-independent manner ([56]). This procedure, while removing the collinear divergencies by renormalizing the PDFs, introduces an artificial dependence on the factorization scale $\mu_F$ which decreases when higher orders of the perturbation theory are taken into account.

## 6.1 Overview of the dipole subtraction method

At next-to-leading order, the cross sections for processes with two hadronic initial states with momenta $p_a$ and $p_b$ are given by

$$\begin{aligned}\sigma(p_a,p_b,\mu_F) &= \underbrace{\int_m \mathrm{d}\sigma^{\mathrm{B}}(p_a,p_b)}_{\sigma^{\mathrm{LO}}} \\ &+ \underbrace{\int_{m+1}\mathrm{d}\sigma^{\mathrm{R}}(p_a,p_b)+\int_m \mathrm{d}\sigma^{\mathrm{V}}(p_a,p_b)+\int_m \mathrm{d}\sigma^{\mathrm{C}}(p_a,p_b,\mu_F)}_{\sigma^{\mathrm{NLO}}},\end{aligned} \tag{6.1}$$

where the symbol B stands for the Born level contribution, R denotes real radiation QCD corrections which contain one additional particle in the final state, and V labels virtual QCD corrections. Collinear divergencies that come from initial-state partons are compensated by process-independent counterterms which are denoted with label C.

The integration symbol implies integration over the sum of all configurations of $m$ (in case of B, V and C), or $m+1$ (in case of R) particle phase space. The integrands $\mathrm{d}\sigma^i$ are exclusive partonic cross sections that can be symbolically written in the following way

$$\mathrm{d}\sigma^{\mathrm{B}}(p_a,p_b) = \mathrm{d}\Phi^{(m)}(p_a,p_b)F_{\mathrm{jet}}^{(m)}(p_a,p_b,...)|\mathcal{M}_m^{\mathrm{B}}(p_a,p_b,...)|^2 \tag{6.2}$$

$$\mathrm{d}\sigma^{\mathrm{R}}(p_a,p_b) = \mathrm{d}\Phi^{(m+1)}(p_a,p_b)F_{\mathrm{jet}}^{(m+1)}(p_a,p_b,...)|\mathcal{M}_{m+1}^{\mathrm{R}}(p_a,p_b,...)|^2 \tag{6.3}$$

$$\mathrm{d}\sigma^{\mathrm{V}}(p_a,p_b) = \mathrm{d}\Phi^{(m)}(p_a,p_b)F_{\mathrm{jet}}^{(m)}(p_a,p_b,...)|\mathcal{M}_m^{\mathrm{V}}(p_a,p_b,...)|^2 \tag{6.4}$$

$$\mathrm{d}\sigma^{\mathrm{C}}(p_a,p_b) = \int_0^1 \mathrm{d}x\Gamma_1(x)\mathrm{d}\sigma^{\mathrm{B}}(xp_a,p_b)+\int_0^1 \mathrm{d}x\Gamma_2(x)\mathrm{d}\sigma^{\mathrm{B}}(p_a,xp_b). \tag{6.5}$$

$\mathrm{d}\Phi$ denotes the $m$, or $m+1$ particle phase space and $\mathcal{M}$ is the matrix element of the respective subprocess, $\Gamma(x)$ is a process independent factor that is divergent if $D \to 4$ and $F_{\text{jet}}$ is a process-independent jet observable, a quantity defined in such a way that its value is not dependent on the soft and collinear partons produced in the final state ([56]).

In order for the collinear and soft divergencies appearing in $\sigma^{\text{NLO}}$ to cancel using the dipole subtraction method, the jet-defining function $F_{\text{jet}}^{(m)}(q_1, ..., q_m)$ in (6.3) and (6.4) has to be defined in such a way that its value is independent of the soft and collinear final state particles, i.e. $F_{\text{jet}}^{(m+1)}(q_1, ..., q_m, q_{m+1} = \lambda q) \to F_{\text{jet}}^{(m)}(q_1, ..., q_m)$ if $\lambda \to 0$, and $F_{\text{jet}}^{(m+1)}(q_1, ..., q_i, q_j) \to F_{\text{jet}}^{(m)}(q_1, ..., q_{ij})$ if $q_i \to x q_{ij}$, $q_j \to (1-x) q_{ij}$ and, in the case of initial-state singularities, the collinear singularities should be factorizable according to $F_{\text{jet}}^{(m+1)}(p_a, p_b, q_1, ..., q_m, q_{m+1}) \to F_{\text{jet}}^{(m)}(x p_a, p_b, q_1, ..., q_m)$ for $q_{m+1} \to (1-x) p_a$.

At Born level, the phase-space integration in (6.1) is finite and $\sigma^{\text{LO}}$ can safely be evaluated in four dimensions. $\mathrm{d}\sigma^{\text{R}}$ and $\mathrm{d}\sigma^{\text{V}}$ both contain collinear and soft singularities which cancel each other upon performing the integration over the relevant phase space. Since they are both separately divergent, they need to be regularized before they are evaluated numerically. In our calculation, the scheme used to control the divergencies is dimensional regularization, which means that the contributions to $\mathrm{d}\sigma^{V}$ in (6.1) are understood to be defined in $D = 4 - 2\varepsilon$ dimensional phase space. The divergencies are thus manifested via single (infrared and ultraviolet) poles $1/\varepsilon$ and double (infrared) poles $1/\varepsilon^2$.

The solution for performing the cancellation of the infrared divergencies appearing in the real and virtual contributions offered by the Catani-Seymour subtraction method is based on constructing an auxiliary cross section $\mathrm{d}\sigma^{\text{A}}$ for the real cross section with the same singular structure, but simple enough to be integrated analytically in a manner which is process independent. The subtracted real cross section is rendered finite and can be safely integrated numerically in 4 dimensions:

$$\sigma^{\text{NLO}} = \int_{m+1} \left[ \mathrm{d}^{(4)}\sigma^{\text{R}} - \mathrm{d}^{(4)}\sigma^{\text{A}} \right] + \int_{m+1} \mathrm{d}^{(D)}\sigma^{\text{A}} + \int_{m} \mathrm{d}^{(D)}\sigma^{\text{V}} + \int_{m} \mathrm{d}^{(D)}\sigma^{\text{C}}. \tag{6.6}$$

The last three terms of (6.6) now contain all remaining singularities. The singular structure of the subtraction term $\int_1 \mathrm{d}\sigma^{\text{A}}$ integrated over the one-parton phase space which gives rise to the infrared singularities compensates for divergencies in both the virtual contribution $\mathrm{d}\sigma^{\text{V}}$ as well as of the collinear counterterm $\mathrm{d}\sigma^{\text{C}}$. $\mathrm{d}\sigma^{\text{A}}$ can thus be broken into two parts, $\mathrm{d}\sigma^{\text{A}}_{\text{V}}$ and $\mathrm{d}\sigma^{\text{A}}_{\text{C}}$, so that $\int_1 \mathrm{d}\sigma^{\text{A}} = \int_1 \mathrm{d}\sigma^{\text{A}}_{\text{V}} + \int_1 \mathrm{d}\sigma^{\text{A}}_{\text{C}}$, each responsible for subtracting singularities in the relevant part of the remaining NLO cross section.

If one is able to analytically integrate $\sigma^{\text{A}}_{\text{V}}$ over the one-parton phase space, the poles in $\mathrm{d}\sigma^{\text{V}}$ and $\int_1 \mathrm{d}\sigma^{\text{A}}_{\text{V}}$ cancel each other and the integration over the remaining $m$-particle phase space can then be evaluated numerically in 4 dimensions. In a similar way, the integral $\int_1 \mathrm{d}\sigma^{\text{A}}_{\text{C}}$ subtracts the collinear poles in $\sigma^{\text{C}}$, leaving us with

$$\sigma^{NLO} = \int_{m+1} \left[ \mathrm{d}\sigma^{\text{R}} - \mathrm{d}\sigma^{\text{A}} \right]^{(D\to 4)} + \int_{m} \left[ \mathrm{d}\sigma^{\text{V}} + \int_1 \mathrm{d}\sigma^{\text{A}}_{\text{V}} \right]^{(D\to 4)} + \int_{m} \left[ \mathrm{d}\sigma^{\text{C}} + \int_1 \mathrm{d}\sigma^{\text{A}}_{\text{C}} \right]^{(D\to 4)}, \tag{6.7}$$

where all three integrands are now finite.

The key ingredient required for the subtraction method to work is the actual form of the subtraction term $\mathrm{d}\sigma^{\mathrm{A}}$ which needs to copy the infrared singularities of real corrections and at the same time be analytically integrable over one-particle phase space in which they originate. The dipole subtraction method provides a systematic recipe for constructing such a $\mathrm{d}\sigma^{\mathrm{A}}$ in a process-independent way in a form that is convenient for numerical Monte Carlo techniques. The dipole subtraction term can be symbolically written as

$$\mathrm{d}^{(D)}\sigma^{\mathrm{A}} = \sum_{\text{dipoles}} \mathrm{d}^{(4)}\hat{\sigma}^{\mathrm{B}} \otimes \mathrm{d}^{(D)}V_{\text{dipole}}. \tag{6.8}$$

This is known as the dipole factorization formula. $\hat{\sigma}^{\mathrm{B}}$ denotes the spin and colour projection of the Born cross section and is convoluted with dipole factors $V_{\text{dipole}}$ that are completely universal and can be incorporated into a generic Monte Carlo code. At the same time, this structure allows us to factorize the $m+1$ parton phase space into $m$-parton phase space and the one parton phase space in which the infrared singularities originate. Thanks to this setup, the only analytical integration that needs to be performed is that of the dipole terms:

$$\begin{aligned}\int_{m+1} \mathrm{d}\sigma^{\mathrm{A}} &= \sum_{\text{dipoles}} \int_m \mathrm{d}\hat{\sigma}^{\mathrm{B}} \otimes \int_1 \left[\mathrm{d}V^{\mathrm{V}}_{\text{dipole}} + \mathrm{d}V^{\mathrm{C}}_{\text{dipole}}\right] \\ &= \int_m \left[\mathrm{d}\hat{\sigma}^{\mathrm{B}} \otimes \mathbf{I}\right] + \int_0^1 \mathrm{d}x \int_m \left[\mathrm{d}\hat{\sigma}^{\mathrm{B}} \otimes (\mathbf{P}+\mathbf{K})\right]. \end{aligned} \tag{6.9}$$

The operator **I** contains all singularities necessary to subtract those in the virtual corrections, while the factors **P** and **K** are operators dependent on the longitudinal momentum fraction $x$ convoluted with a colour projected Born cross section $\hat{\sigma}^{\mathrm{B}}(xp)$.

Note: Cross sections that have identified hadrons in the final state in addition to jets require further introduction of fragmentation functions. These are typically included in another operator customarily denoted as **H**. As it is not relevant to our calculation it can be safely omitted.

The complete cross section at next-to-leading order after implementing the counterterm can be thus written as

$$\begin{aligned}\sigma(p) = &\int_m \mathrm{d}^{(4)}\sigma^{\mathrm{B}}(p) + \int_{m+1} \left[\mathrm{d}^{(4)}\sigma^{\mathrm{R}}(p) - \sum_{\text{dipoles}} \mathrm{d}^{(4)}\hat{\sigma}^{\mathrm{B}}(p) \otimes \mathrm{d}^{(D)}V_{\text{dipole}}\right] \\ &+ \int_m \left[\mathrm{d}^{(D)}\sigma^{\mathrm{V}}(p) + \mathrm{d}^{(4)}\hat{\sigma}^{\mathrm{B}}(p) \otimes \mathbf{I}\right]_{(D\to 4)} \\ &+ \int_0^1 \mathrm{d}x \int_m \left[\mathrm{d}^{(4)}\hat{\sigma}^{\mathrm{B}}(xp) \otimes (\mathbf{P}+\mathbf{K})(x)\right]. \end{aligned} \tag{6.10}$$

The process-dependent ingredients which are necessary for the full next-to-leading order calculation using the procedure described above are:

1. Born-level level matrix elements $\mathcal{M}^{\mathrm{B}}$ needed for $\mathrm{d}\sigma^{\mathrm{B}}$ according to (6.2), evaluated in four dimensions. The method for obtaining this contribution for the considered subprocesses has been discussed in Chapter 5.

2. Real radiation matrix elements $\mathcal{M}^{\mathrm{R}}$ needed for $\mathrm{d}\sigma^{\mathrm{R}}$ according to (6.3), evaluated in four dimensions. Construction of the real emmision matrix elements is covered by Section 6.3

3. One-loop virtual matrix elements $\mathcal{M}^{\mathrm{V}}$ needed for $\mathrm{d}\sigma^{\mathrm{V}}$ according to (6.4) with renormalized ultraviolet divergencies and infrared divergencies regularized using dimensional regularization, evaluated in $D$ dimensions. Obtaining this contribution is subject of Section 6.2.

4. A set of colour projected Born-level matrix elements required to construct $\mathrm{d}\hat{\sigma}^{\mathrm{B}}$, evaluated in four dimensions. This term is discussed in more detail in Section 6.6. Note that in a general partonic process involving external gluons, $\mathrm{d}\hat{\sigma}^{B}$ contains an additional term involving Born-level matrix elements projected over polarizations of the gluons. As we only consider quark initial and final states in our calculations, these terms are not necessary.

Operators **I**, **P**, **K**, as well as $\mathrm{d}V_{\mathrm{dipole}}$ are universal and can therefore be implemented in a process-independent fashion in a Monte Carlo program. In the following, all expressions for the operators implicitly assume massless partons.

In the case of two incoming partons with the momenta $p_a$ and $p_b$, and the outgoing particles with momenta $p_1, ..., p_m$ the explicit form of the **I** operator can be written as

$$\begin{aligned}\mathbf{I}(p_1,...,p_m,p_a,p_b,\varepsilon) = -\frac{\alpha_S}{2\pi}\frac{1}{\Gamma(1-\varepsilon)}\Bigg[&\sum_i \frac{1}{\mathbf{T}_i^2}\nu_i(\varepsilon)\Bigg[\sum_{k\neq i}\mathbf{T}_i\cdot\mathbf{T}_k\left(\frac{4\pi\mu^2}{2p_i\cdot p_k}\right)^{\varepsilon}\\ &+\mathbf{T}_i\cdot\mathbf{T}_a\left(\frac{4\pi\mu^2}{2p_i\cdot p_a}\right)^{\varepsilon}+\mathbf{T}_i\cdot\mathbf{T}_b\left(\frac{4\pi\mu^2}{2p_i\cdot p_b}\right)^{\varepsilon}\Bigg]\\ &+\frac{1}{\mathbf{T}_a^2}\nu_a(\varepsilon)\left[\sum_i\mathbf{T}_i\cdot\mathbf{T}_a\left(\frac{4\pi\mu^2}{2p_i\cdot p_a}\right)^{\varepsilon}+\mathbf{T}_b\cdot\mathbf{T}_a\left(\frac{4\pi\mu^2}{2p_b\cdot p_a}\right)^{\varepsilon}\right]\\ &+\frac{1}{\mathbf{T}_b^2}\nu_b(\varepsilon)\left[\sum_i\mathbf{T}_i\cdot\mathbf{T}_b\left(\frac{4\pi\mu^2}{2p_i\cdot p_b}\right)^{\varepsilon}+\mathbf{T}_b\cdot\mathbf{T}_a\left(\frac{4\pi\mu^2}{2p_b\cdot p_a}\right)^{\varepsilon}\right]\Bigg]. \end{aligned} \tag{6.11}$$

Since all partons in the considered hard process are quarks (or antiquarks), this expression can be simplified considerably. $\mathbf{T}_i^2$ is the Casimir operator of the corresponding colour-charge algebra ($C_{\mathrm{F}}$, in case $i$ is a quark), and $\mathbf{T}_i\cdot\mathbf{T}_j$ give rise to the colour-correlated matrix elements (see Section 6.6). The $\varepsilon$-dependent singular factors $\nu_i$ for $i = q, \bar{q}$ are defined as follows:

$$\nu_{qg}(\varepsilon) = C_{\mathrm{F}}\left[\frac{1}{\varepsilon^2}+\frac{3}{2\varepsilon}-\frac{\pi^2}{2}+5\right]+\mathcal{O}(\varepsilon). \tag{6.12}$$

Inserting this into (6.11), we obtain he following expression for our class of processes

$$\begin{aligned}\mathbf{I}(p_1,p_2,p_3,p_4,\varepsilon) = -\frac{\alpha_S}{2\pi}\frac{1}{\Gamma(1-\varepsilon)}\nu_{qg}(\varepsilon)\frac{2}{C_{\mathrm{F}}}\left[\mathbf{T}_3\cdot\mathbf{T}_4\left(\frac{4\pi\mu^2}{2p_3\cdot p_4}\right)^{\varepsilon}\right.\\ +\mathbf{T}_3\cdot\mathbf{T}_1\left(\frac{4\pi\mu^2}{2p_3\cdot p_1}\right)^{\varepsilon}+\mathbf{T}_4\cdot\mathbf{T}_1\left(\frac{4\pi\mu^2}{2p_4\cdot p_1}\right)^{\varepsilon}+\mathbf{T}_3\cdot\mathbf{T}_2\left(\frac{4\pi\mu^2}{2p_3\cdot p_2}\right)^{\varepsilon}\\ \left.+\mathbf{T}_4\cdot\mathbf{T}_2\left(\frac{4\pi\mu^2}{2p_4\cdot p_2}\right)^{\varepsilon}+\mathbf{T}_1\cdot\mathbf{T}_2\left(\frac{4\pi\mu^2}{2p_1\cdot p_2}\right)^{\varepsilon}\right].\end{aligned}$$

For each Mandelstam channel, only two of the colour-correlated matrix elements have non-zero value. This expression shows explicitly the pole structure of the integrated dipoles (and therefore of the virtual matrix elements) and can be used for verification and debugging of the virtual amplitudes (see Section 6.2.5).

Operators **P** and **K**, unlike **I**, have no $\varepsilon$ poles. They represent a remainder of absorbing the initial- and final-state singularities in the parton distribution and fragmentation functions, and therefore contain dependence on the factorization scale $\mu_F$. They are evaluated at the phase space that is a result of the momentum mapping from $m+1$ to $m$ parton phase spaces (characterized by the longitudinal momentum fraction $x$ involved in the collinear splitting of the incoming parton) in such a way that it exactly factorizes [56].

In the following, index $a$ and $b$ refers to the incoming parton before emitting a quark or gluon, and $a'$ to the parton entering the hard process after the splitting. This time, $a$ can be either quark or gluon, while $a'$ is always a quark (or antiquark). The explicit form of the operator **P** is

$$\begin{aligned}\mathbf{P}^{a,a'}(p_1,...,p_m,p_b;xp_a,x;\mu_F^2) =&\frac{\alpha_S}{2\pi}P^{aa'}(x)\frac{1}{\mathbf{T}_{a'}^2}\left[\sum_{i=3,4}\mathbf{T}_i\cdot\mathbf{T}_{a'}\ln\frac{\mu_F^2}{2xp_a\cdot p_i}\right.\\ &\left.+\mathbf{T}_b\cdot\mathbf{T}_{a'}\ln\frac{\mu_F^2}{2xp_a\cdot p_b}\right],\end{aligned}\tag{6.13}$$

where $P^{aa'}$ are the regularized Altarelli-Parisi probabilities, evaluated at four dimensions [57]:

$$P^{qq}(x) = P^{\bar{q}\bar{q}}(x) = C_{\mathrm{F}}\left(\frac{1+x^2}{1-x}\right)_+ \tag{6.14}$$

$$P^{gq}(x) = P^{g\bar{q}}(x) = T_R[x^2+(1-x)^2]. \tag{6.15}$$

Here, $T_R = 1/2$ is a colour factor associated with gluon splitting into a quark-antiquark pair. The expression above involves a so-called plus-distribution $[F(x)]_+$ which is defined by its action on a generic test function $g(x)$

$$\int_0^1 \mathrm{d}x g(x)[F(x)]_+ \equiv \int_0^1 \mathrm{d}x[g(x)-g(1)]F(x). \tag{6.16}$$

The operator $\mathbf{K}^{a,a'}$ depends only on the momentum fraction $x$ and consists of a a kernel $\bar{K}^{aa'}(x)$ associated with the parton splitting functions, $K_{\text{F.S.}}^{aa'}(x)$ related to the definition of the

factorization scheme, $\tilde{K}^{aa'}(x)$ arising from the parton-parton correlations in the initial state, and additional terms related to the initial-state collinear divergencies in the real corrections.

$$\mathbf{K}^{a,a'}(x) = \frac{\alpha_S}{2\pi}\left\{\bar{K}^{aa'}(x) - K^{aa'}_{\text{F.S.}}(x) + \delta^{aa'}\sum_i \mathbf{T}_i\cdot\mathbf{T}_a\frac{\gamma_i}{\mathbf{T}_i^2}\left[\left(\frac{1}{1-x}\right)_+ + \delta(1-x)\right]\right\} - \frac{\alpha_S}{2\pi}\mathbf{T}_b\cdot\mathbf{T}_{a'}\frac{1}{\mathbf{T}_{a'}^2}\tilde{K}^{aa'}(x). \tag{6.17}$$

The factorization scheme of collinear singularities applied in this calculation is the $\overline{\text{MS}}$ scheme, which is defined by setting the kernel $K^{aa'}_{\text{F.S.}}(x) = 0$. The explicit forms of the remaining terms are as follows:

$$\bar{K}^{qq}(x) = \bar{K}^{\bar{q}\bar{q}}(x) = C_{\text{F}}\left[\left(\frac{2}{1-x}\ln\frac{1-x}{x}\right)_+ - (1+x)\ln\frac{1-x}{x} + (1-x)\right] - \delta(1-x)(5-\pi^2)C_{\text{F}}, \tag{6.18}$$

$$\bar{K}^{gq}(x) = \bar{K}^{g\bar{q}}(x) = P^{gq}(x)\ln\frac{1-x}{x} + T_R\,2x(1-x), \tag{6.19}$$

$$\tilde{K}^{ab}(x) = P^{ab}_{\text{reg}}(x)\ln(1-x) + \delta^{ab}\mathbf{T}_a^2\left[\left(\frac{2}{1-x}\ln(2-x)\right)_+ - \frac{\pi^2}{3}\delta(1-x)\right], \tag{6.20}$$

$$P^{ab}_{\text{reg}}(x) = P^{ab}(x) \qquad \text{if } a\neq b, \qquad P^{qq}_{\text{reg}}(x) = -C_{\text{F}}(1+x), \tag{6.21}$$

$$\gamma_i = \frac{3}{2}C_{\text{F}}. \tag{6.22}$$

The resulting $\mathbf{K}^{a,a'}(x)$ corresponding to the quark-splitting real radiation diagrams (for which $\delta^{aa'} = 1$) can be written as

$$\mathbf{K}^{a,a'}(x)\Big|_{a=\text{q}} = \frac{\alpha_S}{2\pi}\left\{\bar{K}^{qq}(x) + \sum_{i=3,4}\mathbf{T}_i\cdot\mathbf{T}_a\frac{3}{2}\left[\left(\frac{1}{1-x}\right)_+ + \delta(1-x)\right] - \mathbf{T}_b\cdot\mathbf{T}_{a'}\left[-(1+x)\ln(1-x) + \left(\frac{2}{1-x}\ln(2-x)\right)_+ - \frac{\pi^2}{3}\delta(1-x)\right]\right\}\Bigg|_{a=\text{q}}, \tag{6.23}$$

while in the case of gluon-initiated real radiation diagrams $\delta^{aa'} = 0$ and the insertion operator takes the following form:

$$\mathbf{K}^{a,a'}(x)\Big|_{a=\text{g}} = \frac{\alpha_S}{2\pi}\left[P^{gq}(x)\left(\ln\frac{1-x}{x} - \mathbf{T}_b\cdot\mathbf{T}_{a'}\frac{3}{4}\ln(1-x)\right) + x(1-x)\right]\Bigg|_{a=\text{g}}. \tag{6.24}$$

The symbolic sum over the non-integrated dipoles subtracting the soft and collinear singularities in the real corrections is based on the fact that any real matrix element in $m+1$

parton phase space can be factorized into an $m$ parton phase space and a singular term. In the case of two incoming partons, the sum in (6.10) takes the following form

$$\sum_{\text{dipoles}} \mathrm{d}^{(4)}\hat{\sigma}^{\mathrm{B}}(p) \otimes \mathrm{d}^{(D)}V_{\text{dipole}}$$
$$= \left[\sum_{k\neq i\neq j} \mathcal{D}_{ij,k} + \left\{\sum_{i\neq j} \mathcal{D}_{ij}{}^{a} + \sum_{k\neq i} \mathcal{D}_{k}{}^{ai} + \sum_{i} \mathcal{D}^{ai,b} + (a \leftrightarrow b)\right\}\right] \mathrm{d}\Phi^{m+1}. \quad (6.25)$$

where the expressions such as $\mathcal{D}_{ij,k}$ represent the dipole functions generating the limit where the partons $i$ and $j$ become soft or collinear. The third index, $k$, belongs to a third parton which is called spectator, while the parton before the splitting occurs is called emitter and is referred to as $(ij)$. The lower indices in (6.25) are understood to correspond to the partons in the final state and are labelled $i, j, k$, while the upper indices are in the initial state and are labelled $a, b$. $\mathcal{D}_{ij,k}$ therefore represents final state emitter and spectator, $\mathcal{D}_{ij}{}^{a}$ a final state emitter and initial-state spectator,$\mathcal{D}_{k}{}^{ai}$ an initial-state emitter and final-state spectator and $\mathcal{D}^{ai,b}$ both emitter and spectator in the initial state.

Symbolically, each dipole function is of the following form:

$$\begin{aligned}
\mathcal{D}_{ij,k} &=_m \langle 1,...,\tilde{ij},...,k,...,m|1,...,\tilde{ij},...,k,...,m\rangle_m \otimes \mathbf{V}_{ij,k},\\
\mathcal{D}^{a}_{ij} &=_m \langle 1,...,a,...,\tilde{ij},...,m|1,...,a,...,\tilde{ij},...,m\rangle_m \otimes \mathbf{V}^{a}_{ij},\\
\mathcal{D}^{ai}_{k} &=_m \langle 1,...,\tilde{ai},...,k,...,m|1,...,\tilde{ai},...,k,...,m\rangle_m \otimes \mathbf{V}^{ai}_{k},\\
\mathcal{D}^{ai,b} &=_m \langle 1,...,\tilde{ai},...,b,...,m|1,...,\tilde{ai},...,b,...,m\rangle_m \otimes \mathbf{V}^{ai,b},
\end{aligned} \quad (6.26)$$

where e.g. $\mathbf{V}_{ij,k}$ is the splitting kernel; an operator which describes splitting of the parton $ij$ into partons $i$ and $j$, while ${}_m\langle ...|...\rangle_m$ represents the colour-correlated matrix element living in the mapped $m$-parton phase space, obtained by the factorizable, process-independent mapping $p_i, p_j, p_k \mapsto \tilde{p}_{ij}, \tilde{p}_k$ in such a way that the masses of all partons remain on-shell.

The necessity to distinguish between initial- and final-state particles results in four different types of splitting kernels. Their explicit forms, as well as a detailed derivation of all expressions listed above can be found in [56, 58].

## 6.2 Virtual QCD corrections

Despite the fact that the processes presented in Chapter 3 are fairly complex, the block structure brought about by the polarization sums renders the calculation of purely QCD NLO corrections relatively straightforward, provided the interference terms between $t$-, $u$- and $s$-channel are neglected (a verification for this assumption is offered in Chapter 7). All considered Feynman diagrams share a similar structure - a pair of quark legs emits gauge bosons which eventually decay into leptonic pairs (see Figure 4.3). The QCD corrections therefore only affect the quark legs.

The method of using the polarization sums to cut the full diagrams into building blocks, presented in Section 4.3, facilitates this task by allowing for the real and virtual corrections to

only be applied to the selected building blocks. For virtual corrections, this means attaching a gluon loop to the QCD building blocks in every possible way, leading to diagrams listed in Figure 4.8. One can see that each building block may contain up to eight ($qqVVV$) loop diagrams.

Adding a loop has no influence on the overall kinematics of the full diagram, and therefore the one-loop matrix elements corresponding to the QCD virtual corrections can be obtained using the leading-order polarization sums listed in Appendix B simply by replacing one of the tree-level QCD building blocks with its virtual counterpart while the rest of the polarization sum remains unchanged. This has to be repeated once for each quark line, and each polarization sum will henceforth contribute twice, once for each replaced QCD block.

### 6.2.1 Evaluation with FormCalc and Coli

Similarly to the leading-order building blocks, the analytical expressions for the virtual amplitudes have been generated in Mathematica [46] using FeynArts [47] and FormCalc ([59, 48]), modified to accommodate the polarization sums and further abbreviations, and then exported into a Fortran code, where each building block is represented by a subroutine that evaluates a set of arrays corresponding to the components of the polarization sums.

All divergencies of the loop diagrams appear in tensor integrals, which, as can be seen in Figure 4.8, are given by two, three, four and five-point functions. These tensor functions can be decomposed and expressed by means of scalar integrals through a procedure known as tensor reduction (see [60, 61]).

In our calculation, the tensor reduction is performed in Fortran by means of the Coli library [61, 62, 63, 64, 65] which is based on the tensor reduction scheme developed by Denner and Dittmaier [62] and supports both mass and dimensional regularization scheme.

### 6.2.2 Renormalization of the UV divergencies

Scalar integrals which are contained in the virtual matrix elements after tensor reduction, contain both infrared and ultraviolet divergencies. While the infrared divergencies have to be taken care of by dipole subtraction, the ultraviolet singularities can be renormalized at the amplitude level by adding additional counterterm contributions that stem from the renormalization procedure. In the framework of our calculation, the renormalization of the ultraviolet terms is achieved by adding the counterterm blocks (as listed in Figure 4.8) to the corresponding virtual blocks.

The renormalization conditions have been chosen according to the on-shell renormalization scheme [66]. As a consequence, we can omit all contributions coming from the external self-energy diagrams (building blocks with gluon loops on the external quark lines) and their respective counterterms as they are fully cancelled by one another.

Since we are only interested in the QCD corrections to the leading order matrix elements and the virtual contributions are formed by gluon loops attached to the quark lines, the only renormalization constants taken into account are wave-function renormalization con-

stants $\delta Z_q$ which renormalize the quark fields $\psi_q$ according to the following transformation

$$\psi_q^0 = \psi_q(1 + \delta Z_q/2). \tag{6.27}$$

In the dimensional regularization scheme, while distinguishing between infrared and ultraviolet divergencies, $\delta Z_q$ takes the following form (Eq. (2.28) in [67])

$$\delta Z_q = -\frac{\alpha_s}{3\pi}\left(\Delta_1^{UV}(\mu_R) - \Delta_1^{IR}(\mu_R)\right), \tag{6.28}$$

where $\Delta_1^{UV}(\mu_R)$ and $\Delta_1^{IR}(\mu_R)$ represent the $1/\varepsilon$ ultraviolet or infrared poles.

While evaluating the virtual corrections with FormCalc using dimensional regularization scheme, one encounters a complication related to the fact that FormCalc 5 by default assumes mass regularization for infrared divergencies. Due to this, rational terms of infrared origin are not included in the amplitude. This results in the wave-function renormalization constant $\delta Z_q$ being evaluated as

$$\begin{aligned}
\delta Z_{q\,\mathrm{FC}} &= \frac{\alpha_s}{3\pi} - \frac{2\alpha_s}{3\pi}(B_0(0,0,0) + B_1(0,0,0)) \\
&= \frac{\alpha_s}{3\pi} - \frac{2\alpha_s}{3\pi}(B_0(0,0,0) + \frac{1}{2p^2}(A_0(0) - A_0(0) - (p^2 B_0(0,0,0)))) \\
&= \frac{\alpha_s}{3\pi} - \frac{\alpha_s}{3\pi}B_0(0,0,0) = \frac{\alpha_s}{3\pi} - \frac{\alpha_s}{3\pi}(\Delta_1^{UV} - \Delta_1^{IR}),
\end{aligned} \tag{6.29}$$

which is not consistent with (6.28). This can, however, be easily remedied by manually shifting the value

$$\delta Z_{q\,\mathrm{FC}} \;\; \mapsto \;\; \delta Z_{q\,\mathrm{FC}} - \frac{\alpha_s}{3\pi}. \tag{6.30}$$

### 6.2.3 Conventions for infrared poles

Due to the fact that the Catani-Seymour method and the Coli library used to evaluate tensor integrals use different conventions for $\varepsilon$-dependent pre-factors, the positions of the infrared poles and constant terms are shifted with respect to one another.

Coli writes expressions containing IR poles while factorizing out $\Gamma(1+\varepsilon)$ and $(4\pi)^\varepsilon$ so that the virtual amplitude can be written as

$$\mathcal{M}_{\mathrm{Coli}} = \Gamma(1+\varepsilon)(4\pi)^\varepsilon \left(\frac{A}{\varepsilon^2} + \frac{B}{\varepsilon} + C\right), \tag{6.31}$$

where $A$, $B$ and $C$ represent the double and single $\varepsilon$ poles and the constant term, respectively.

On the other hand, the convention for the integrated subtraction terms prescribed by the Catani-Seymour method is to factorize out $1/\Gamma(1-\varepsilon)$ and $(4\pi\mu^2/Q^2)^\varepsilon$ (see e.g. 6.11) and the terms of the **I**-operator applied to the Born matrix elements take the following form

$$D_{\mathrm{CS}} = \frac{1}{\Gamma(1-\varepsilon)}\left(\frac{4\pi\mu^2}{Q^2}\right)^\varepsilon \left(\frac{A'}{\varepsilon^2} + \frac{B'}{\varepsilon} + C'\right), \tag{6.32}$$

where $Q^2$ stands for products of the corresponding momentum pairs.

In order to unify these two conventions, we expand the pre-factors in (6.32), using the following expansions:

$$\frac{1}{\Gamma(1-x)\Gamma(1+x)} = 1 - \frac{\pi^2}{6}x^2 + \mathcal{O}(x^3) \tag{6.33}$$

$$(a)^x = 1 + \ln(a)x + \frac{1}{2}\ln^2(a)x^2 + \mathcal{O}(x^3). \tag{6.34}$$

This induces a shift in the poles $A'$, $B'$ and $C'$ so that

$$D_{\text{Coli}} = \Gamma(1+\varepsilon)(4\pi)^\varepsilon \left(\frac{A''}{\varepsilon^2} + \frac{B''}{\varepsilon} + C''\right), \tag{6.35}$$

where $D_{\text{Coli}}$ are the same integrated dipole terms written in Coli convention, and

$$\begin{aligned} A'' &= A' \\ B'' &= B' + A' \ln\left(\frac{\mu^2}{Q^2}\right) \\ C'' &= C' + B' \ln\left(\frac{\mu^2}{Q^2}\right) + A' \left[\frac{1}{2}\ln^2\left(\frac{\mu^2}{Q^2}\right) - \frac{\pi^2}{6}\right]. \end{aligned} \tag{6.36}$$

### 6.2.4 Example: virtual corrections to us $\to$ dc

In this section, we present an example of how the virtual corrections are calculated and combined in the polarization sums. For sake of simplicity, we continue with the example process introduced in Section 4.8, which has the advantage of conveying the main concepts without the complexity added by large number of external particles that are present in the vector-boson-fusion subprocesses.

As explained in the previous sections, the virtual corrections are obtained by combining the results from the one-loop and counterterm contributions:

$$\mathcal{M}^{\text{V}} = \mathcal{M}^{\text{L}} + \mathcal{M}^{\text{C}}. \tag{6.37}$$

Taking into account QCD corrections only, this requires evaluation of the following Feynman diagrams:

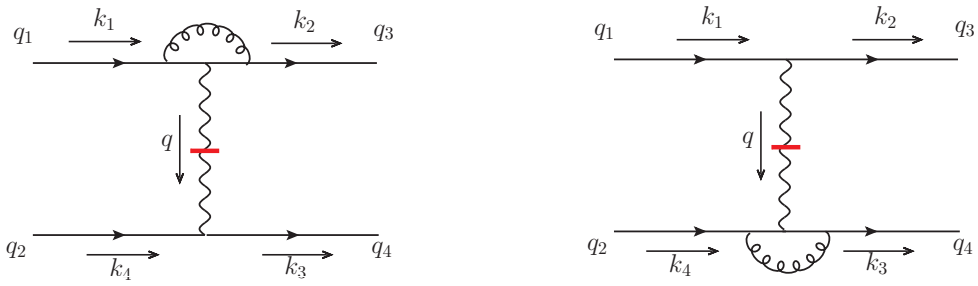


**Figure 6.1:** One-loop diagrams for us $\to$ dc corresponding to the amplitude $\mathcal{M}^{\text{L}}$

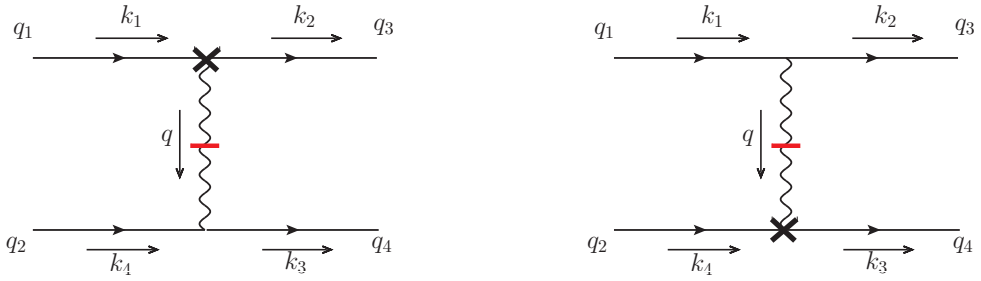


**Figure 6.2:** Counterterm diagrams for us $\to$ dc corresponding to the amplitude $\mathcal{M}^{\mathrm{C}}$

Once the procedure of cutting the intermediate W boson connecting the two quark lines is applied (4.9), we are left with two building blocks per diagram. In each case, one of the building blocks is a Born-level subdiagram for which we can directly apply the Born-level result obtained in (4.10) and (4.11). Since both quark lines have only one gauge boson coupling at the leading order, the remaining one-loop subdiagrams turn out to be simple triangle vertex diagrams:

$\mathcal{M}_{L1,\,i} =$

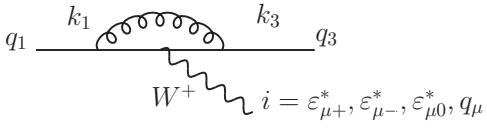


$\mathcal{M}_{L2,\,i} =$

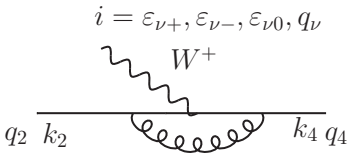


The matrix elements corresponding to both diagrams can be written as

$$\begin{aligned}\mathcal{M}_{L,\,i} =& \frac{\mathrm{i}\alpha_S e}{3\sqrt{2}\pi \sin\theta_W}\left[-S_1 + 2S_1 B_0(q^2,0,0) + 2S_2 C_0(0,q^2,0,0,0,0)\right.\\ &-4S_1 C_{00}(0,q^2,0,0,0,0) + 2S_2 C_1(0,q^2,0,0,0,0) - 4S_3 C_{12}(0,q^2,0,0,0,0)\\ &\left.+4S_4 C_2(0,q^2,0,0,0,0) - 4S_5 C_{22}(0,q^2,0,0,0,0)\right], \end{aligned} \tag{6.38}$$

where $S_j$ represent abbreviations for the purely kinematic expressions appearing in the matrix elements. Their form depends on the diagram as well as on the polarization of the intermediate W boson determining which term of the polarization sum the matrix element corresponds to (similarly as in Section 4.8). In the following, the explicit expressions of $S_j$ in WvdW formalism are given for $\mathcal{M}_{L1,\,+}$, $\mathcal{M}_{L1,\,-}$, $\mathcal{M}_{L1,\,0}$ and $\mathcal{M}_{L1,\,k}$, respectively.

$$
\begin{aligned}
\varepsilon^*_{+\nu}:\ S_1 =& 2\sqrt{2k_{01}k_{03}}\langle n_1(k_3)n_1(q)\rangle^*\langle n_1(k_1)n_2(q)\rangle \\
S_2 =& 8\sqrt{2k_{01}^3k_{03}^3}\langle n_1(k_1)n_1(k_3)\rangle^*\langle n_1(k_3)n_1(q)\rangle\langle n_1(k_3)n_2(q)\rangle^*\langle n_1(k_1)n_2(q)\rangle \\
S_3 =& 2\sqrt{k_{01}k_{03}}(\langle n_1(k_3)n_1(q)\rangle^*\langle n_1(k_1)n_1(q)\rangle\lambda_1(q) + \langle n_1(k_3)n_2(q)\rangle^*\langle n_1(k_1)n_2(q)\rangle\lambda_2(q)) \\
& \sqrt{2}k_{03}\langle n_1(k_3), n_1(q)\rangle^*\langle n_1(k_3)n_2(q)\rangle \\
S_4 =& \frac{1}{2}[-2(2\sqrt{k_{01}k_{03}}(\langle n_1(k_3)n_1(q)\rangle^*\langle n_1(k_1)n_1(q)\rangle\lambda_1(q) \\
& + \langle n_1(k_3)n_2(q)\rangle^*\langle n_1(k_1)n_2(q)\rangle\lambda_2(q)))\sqrt{2}k_{01}\langle n_1(k_1), n_1(q)\rangle^*\langle n_1(k_1)n_2(q)\rangle \\
& + 2(2\sqrt{2k_{01}k_{03}}\langle n_1(k_3)n_1(q)\rangle^*\langle n_1(k_1)n_2(q)\rangle)(2k_{01}k_{03}\langle n_1(k_1), n_1(k_3)\rangle^*\langle n_1(k_1)n_1(k_3)\rangle) \\
& + 8\sqrt{2k_{01}^3k_{03}^3}\langle n_1(k_1)n_1(k_3)\rangle^*\langle n_1(k_3)n_1(q)\rangle\langle n_1(k_3)n_2(q)\rangle^*\langle n_1(k_1)n_2(q)\rangle \\
& + 4\sqrt{2k_{01}^3k_{03}}(\langle n_1(k_1)n_1(q)\rangle^*\langle n_1(k_1)n_1(q)\rangle\lambda_1(q)\langle n_1(k_3)n_2(q)\rangle^*\langle n_1(k_1)n_2(q)\rangle\lambda_2(q) \\
& - 4\sqrt{2k_{01}k_{03}^3}\langle n_1(k_3), n_1(q)\rangle^*\ \langle n_1(k_3), n_2(q)\rangle(\langle n_1(k_3)n_1(q)\rangle^*\langle n_1(k_1)n_1(q)\rangle\lambda_1(q)] \\
S_5 =& 2\sqrt{k_{01}k_{03}}(\langle n_1(k_3)n_1(q)\rangle^*\langle n_1(k_1)n_1(q)\rangle\lambda_1(q) + \langle n_1(k_3)n_2(q)\rangle^*\langle n_1(k_1)n_2(q)\rangle\lambda_2(q)) \\
& \sqrt{2}k_{01}\langle n_1(k_1), n_1(q)\rangle^*\langle n_1(k_1)n_2(q)\rangle
\end{aligned}
$$

$$
\begin{aligned}
\varepsilon^*_{-\nu}:\ S_1 =& 2\sqrt{2k_{01}k_{03}}\langle n_1(k_3)n_2(q)\rangle^*\langle n_1(k_1)n_1(q)\rangle \\
S_2 =& 8\sqrt{2k_{01}^3k_{03}^3}\langle n_1(k_1)n_1(k_3)\rangle^*\langle n_1(k_3)n_2(q)\rangle^*\langle n_1(k_1), n_1(k_3)\rangle\langle n_1(k_1)n_1(q)\rangle \\
S_3 =& 2\sqrt{k_{01}k_{03}}(\langle n_1(k_3), n_1(q)\rangle^*\langle n_1(k_1), n_1(q)\rangle\lambda_1(q) \\
& + \langle n_1(k_3), n_2(q)\rangle^*\langle n_1(k_1), n_2(q)\rangle\lambda_2(q))\sqrt{2}\langle n_1(k_3)n_2(q)\rangle^*k_{03}\langle n_1(k_3)n_1(q) \\
S_4 =& \frac{1}{2}[2(2\sqrt{k_{01}k_{03}}(\langle n_1(k_3), n_1(q)\rangle^*\langle n_1(k_1), n_1(q)\rangle\lambda_1(q) \\
& + \langle n_1(k_3), n_2(q)\rangle^*\langle n_1(k_1), n_2(q)\rangle\lambda_2(q))\sqrt{2}\langle n_1(k_1)n_2(q)\rangle^*k_{01}\langle n_1(k_1)n_1(q))\rangle \\
& + 2(2\sqrt{2k_{01}k_{03}}\langle n_1(k_3)n_1(q)\rangle^*\langle n_1(k_1)n_2(q)\rangle \\
& 2\langle n_1(k_1)n_1(k_3)\rangle^*k_{01}k_{03}\langle n_1(k_1)n_1(k_3)\rangle) \\
& + 8\sqrt{2k_{01}^3k_{03}^3}\langle n_1(k_1)n_1(k_3)\rangle^*\langle n_1(k_3)n_2(q)\rangle^*\langle n_1(k_1), n_1(k_3)\rangle\langle n_1(k_1)n_1(q)\rangle \\
& + 4\sqrt{2k_{01}^3k_{03}}\langle n_1(k_3)n_2(q)\rangle^*\langle n_1(k_1)n_1(q)\rangle(\langle n_1(k_1)n_1(q)\rangle^*\langle n_1(k_1)n_1(q)\rangle\lambda_1(q) \\
& - 4\sqrt{2k_{01}k_{03}^3}\langle n_1(k_3), n_2(q)\rangle^*\langle n_1(k_3), n_1(q)\rangle(\langle n_1(k_3)n_1(q)\rangle^*\langle n_1(k_1)n_1(q)\rangle\lambda_1(q) \\
& + \langle n_1(k_3)n_2(q)\rangle^*\langle n_1(k_1)n_2(q)]\lambda_2(q))] \\
S_5 =& 2\sqrt{k_{01}k_{03}}(\langle n_1(k_3), n_1(q)\rangle^*\langle n_1(k_1), n_1(q)\rangle\lambda_1(q) + \langle n_1(k_3), n_2(q)\rangle^*\langle n_1(k_1), n_2(q)\rangle\lambda_2(q)) \\
& \sqrt{2}\langle n_1(k_1)n_2(q)\rangle^*k_{01}\langle n_1(k_1)n_1(q)
\end{aligned}
$$

$$
\begin{aligned}
\varepsilon^*_{0\nu}:\ S_1 =& \frac{2\sqrt{k_{01}k_{03}}}{\sqrt{q^2}}[\langle n_1(k_3)n_1(q)\rangle^*\langle n_1(k_1)n_1(q)\rangle\lambda_1(q) - \langle n_1(k_3)n_2(q)\rangle^*\langle n_1(k_1)n_2(q)\rangle\lambda_2(q)]\\
S_2 =& \frac{8\sqrt{k_{01}^3k_{03}^3}}{\sqrt{q^2}}[\langle n_1(k_1)n_1(k_3)\rangle^*\langle n_1(k_1)n_1(k_3)\rangle(\langle n_1(k_3),n_1(q)\rangle^*\langle n_1(k_1)n_1(q)\rangle\lambda_1(q)\\
& - \langle n_1(k_3),n_2(q)\rangle^*\langle n_1(k_1)n_2(q)\rangle\lambda_2(q))]\\
S_3 =& 2\sqrt{k_{01}k_{03}}(\langle n_1(k_3)n_1(q)\rangle^*\langle n_1(k_1)n_1(q)]\lambda_1(q) + \langle n_1(k_3)n_2(q)\rangle^*\langle n_1(k_1)n_2(q)]\lambda_2(q))\\
& \frac{1}{\sqrt{q^2}}[k_{03}(\langle n_1(k_3)n_1(q)\rangle^*\langle n_1(k_3)n_1(q)\rangle\lambda_1(q) - \langle n_1(k_3)n_2(q)\rangle^*\langle n_1(k_3)n_2(q)\rangle\lambda_2(q))]\\
S_4 =& \frac{1}{2}[(\frac{4\sqrt{k_{01}k_{03}}}{\sqrt{q^2}}(\langle n_1(k_3)n_1(q)\rangle^*\langle n_1(k_1)n_1(q)]\lambda_1(q) + \langle n_1(k_3)n_2(q)\rangle^*\langle n_1(k_1)n_2(q)]\lambda_2(q))\\
& [k_{01}(\langle n_1(k_1)n_1(q)\rangle^*\langle n_1(k_1)n_1(q)\rangle\lambda_1(q) - \langle n_1(k_1)n_2(q)\rangle^*\langle n_1(k_1)n_2(q)\rangle\lambda_2(q))])\\
& + 2(\frac{1}{\sqrt{q^2}}[2\sqrt{k_{01}k_{03}}(\langle n_1(k_3)n_1(q)\rangle^*\langle n_1(k_1)n_1(q)\rangle\lambda_1(q)\\
& - \langle n_1(k_3)n_2(q)\rangle^*\langle n_1(k_1)n_2(q)\rangle\lambda_2(q))]2\langle n_1(k_1)n_1(k_3)\rangle^*k_{01}k_{03}\langle n_1(k_1)n_1(k_3)\rangle)\\
& + \frac{1}{\sqrt{q^2}}[8\sqrt{k_{01}^3k_{03}^3}\langle n_1(k_1)n_1(k_3)\rangle^*\langle n_1(k_1)n_1(k_3)\rangle(\langle n_1(k_3),n_1(q)\rangle^*\langle n_1(k_1)n_1(q)\rangle\lambda_1(q)\\
& - \langle n_1(k_3),n_2(q)\rangle^*\langle n_1(k_1)n_2(q)\rangle\lambda_2(q))]\\
& + \frac{1}{\sqrt{q^2}}[4\sqrt{k_{01}^3k_{03}}(\langle n_1(k_1)n_1(q)\rangle^*\langle n_1(k_1)n_1(q)\rangle\lambda_1(q)\\
& + \langle n_1(k_1)n_2(q)\rangle^*\langle n_1(k_1)n_2(q)\rangle\lambda_2(q))(\langle n_1(k_3)n_1(q)\rangle^*\langle n_1(k_1)n_1(q)\rangle\lambda_1(q)\\
& - \langle n_1(k_3)n_2(q)\rangle^*\langle n_1(k_1)n_2(q)\rangle\lambda_2(q))] - 2\langle n_1(k_1)n_1(k_3)\rangle^*k_{01}k_{03}\langle n_1(k_1)n_1(k_3)\rangle]\\
S_5 =& 2\sqrt{k_{01}k_{03}}(\langle n_1(k_3)n_1(q)\rangle^*\langle n_1(k_1)n_1(q)]\lambda_1(q) + \langle n_1(k_3)n_2(q)\rangle^*\langle n_1(k_1)n_2(q)]\lambda_2(q))\\
& \frac{1}{\sqrt{q^2}}[k_{01}(\langle n_1(k_1)n_1(q)\rangle^*\langle n_1(k_1)n_1(q)\rangle\lambda_1(q) - \langle n_1(k_1)n_2(q)\rangle^*\langle n_1(k_1)n_2(q)\rangle\lambda_2(q))]\\
q_\nu:\ S_1 =& 2\sqrt{k_{01}k_{03}}(\langle n_1(k_3)n_1(q)\rangle^*\langle n_1(k_1)n_1(q)\rangle\lambda_1(q) + \langle n_1(k_3)n_2(q)\rangle^*\langle n_1(k_1)n_2(q)\rangle\lambda_2(q))\\
S_2 =& 8\langle n_1(k_1)n_1(k_3)\rangle^*\sqrt{k_{01}^3k_{03}^3}\langle n_1(k_1)n_1(k_3)\rangle(\langle n_1(k_3)n_1(q)\rangle^*\langle n_1(k_1)n_1(q)\rangle\lambda_1(q)\\
S_3 =& 2\sqrt{k_{01}k_{03}}(\langle n_1(k_3)n_1(q)\rangle^*\langle n_1(k_1)n_1(q)\rangle\lambda_1(q) + \langle n_1(k_3)n_2(q)\rangle^*\langle n_1(k_1)n_2(q)\rangle\lambda_2(q))\\
& k_{03}(\langle n_1(k_3)n_1(q)\rangle^*\langle n_1(k_3)n_1(q)\rangle\lambda_1(q) + \langle n_1(k_3)n_2(q)\rangle^*\langle n_1(k_3)n_2(q)\rangle\lambda_2(q))
\end{aligned}
$$

$$
\begin{aligned}
S_4 =& \frac{1}{2}[2(2\sqrt{k_{01}k_{03}}(\langle n_1(k_3)n_1(q)\rangle^*\langle n_1(k_1)n_1(q)\rangle\lambda_1(q) + \langle n_1(k_3)n_2(q)\rangle^*\langle n_1(k_1)n_2(q)\rangle\lambda_2(q))\\
& k_{01}(\langle n_1(k_1)n_1(q)\rangle^*\langle n_1(k_1)n_1(q)\lambda_1(q) + \langle n_1(k_1)n_2(q)v\langle n_1(k_1)n_2(q)\rangle\lambda_2(q)))\\
& + 2(2\sqrt{k_{01}k_{03}}(\langle n_1(k_3)n_1(q)\rangle^*\langle n_1(k_1)n_1(q)\rangle\lambda_1(q) + \langle n_1(k_3)n_2(q)\rangle^*\langle n_1(k_1)n_2(q)\rangle\lambda_2(q))\\
& 2k_{01}k_{03}\langle n_1(k_1)n_1(k_3)\rangle^*\langle n_1(k_1)n_1(k_3))\rangle\\
& + 8\langle n_1(k_1)n_1(k_3)\rangle^*\sqrt{k_{01}^3k_{03}^3}\langle n_1(k_1)n_1(k_3)\rangle(\langle n_1(k_3)n_1(q)\rangle^*\langle n_1(k_1)n_1(q)\rangle\lambda_1(q)\\
& + 4\sqrt{k_{01}^3k_{03}}(\langle n_1(k_1)n_1(q)\rangle^*\langle n_1(k_1)n_1(q)\rangle\lambda_1(q) + \langle n_1(k_1)n_2(q)\rangle^*\langle n_1(k_1)n_2(q)\rangle\lambda_2(q))\\
& (\langle n_1(k_3)n_1(q)\rangle^*\langle n_1(k_1)n_1(q)\rangle\lambda_1(q) + \langle n_1(k_3)n_2(q)\rangle^*\langle n_1(k_1)n_2(q)\rangle\lambda_2(q))\\
& - 4\sqrt{k_{01}k_{03}^3}(\langle n_1(k_3)n_1(q)\rangle^*\langle n_1(k_1)n_1(q)\rangle\lambda_1(q) + \langle n_1(k_3)n_2(q)\rangle^*\langle n_1(k_1)n_2(q)\rangle\lambda_2(q))\\
& (\langle n_1(k_3)n_1(q)\rangle^*\langle n_1(k_3)n_1(q)\rangle\lambda_1(q) + \langle n_1(k_3)n_2(q)\rangle^*\langle n_1(k_3)n_2(q)\rangle\lambda_2(q))]\\
S_5 =& 2\sqrt{k_{01}k_{03}}(\langle n_1(k_3)n_1(q)\rangle^*\langle n_1(k_1)n_1(q)\rangle\lambda_1(q) + \langle n_1(k_3)n_2(q)\rangle^*\langle n_1(k_1)n_2(q)\rangle\lambda_2(q))\\
& k_{01}(\langle n_1(k_1)n_1(q)\rangle^*\langle n_1(k_1)n_1(q)\lambda_1(q) + \langle n_1(k_1)n_2(q)v\langle n_1(k_1)n_2(q)\rangle\lambda_2(q)).
\end{aligned}
\tag{6.39}
$$

The subdiagram for the lower quark leg from the diagram in Figure 6.1 has a kinematic structure that is very similar to the building block for the upper leg, aside from the fact that the W boson is considered an incoming particle in the former, and an outgoing particle in the latter. This allows us to express the matrix element for both legs using the same expression (6.38) with only the following changes being applied to the kinematic abbreviations from (6.39): the momenta of the incoming and outgoing quarks should be replaced by their lower-leg equivalents ($k_1 \mapsto k_2$, $k_3 \mapsto k_4$) and, due to the structure of the polarization vectors in the WvdW formalism ((A.22) and (A.23)), to obtain the expressions for the $i =$"$\varepsilon_{+\nu}$" component of the polarization sum, the expressions $S_i$ corresponding to $i =$"$\varepsilon^*_{+\nu}$" should be swapped with those corresponding to $i = \varepsilon^*_{-\nu}$ and vice versa. The expressions for the $i =$"$\varepsilon_{0\nu}$" and $i =$"$q_\nu$" remain unchanged.

The two counterterm building blocks obtained by cutting the diagram in Figure 6.2 are:

$\mathcal{M}_{C1,i} =$

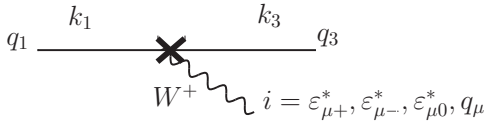


$\mathcal{M}_{C2,i} =$

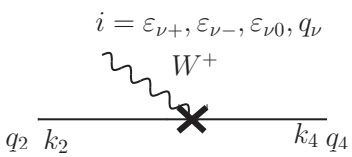


Due to the nature of the calculation, in which we only take into account the wave-function renormalization constants for the quark legs, the amplitude structure of both coun-

terterm blocks is relatively simple in comparison:

$$\mathcal{M}_{C,i} = -\frac{e\alpha_s}{3\sqrt{2}\pi \sin\theta_W} S_1(B_0(0,0,0) + B_1(0,0,0)). \tag{6.40}$$

The tensor functions here originate in the wave function renormalization constant $\delta Z_q$ (6.28), while $S_1$ again represents the fermion chain which takes a different form for each of the four components of the polarization sum. For the upper quark leg, the components $S_1$ are identical to those in (6.39).

As in the case of one-loop matrix elements, we can obtain the fermion chain $S_1$ for the lower quark leg simply by replacing $k_1 \mapsto k_2$ and $k_3 \mapsto k_4$ and swapping the first two components.

We have thus obtained all six building blocks necessary to evaluate the virtual corrections to us $\to$ dc: the tree-level building blocks $\mathcal{M}_{1,i}$ and $\mathcal{M}_{2,i}$ ((4.10) and (4.11)), the one-loop triangle diagrams $\mathcal{M}_{L1,i}$ and $\mathcal{M}_{L2,i}$ (6.38) and the corresponding counterterm diagrams $\mathcal{M}_{C1,i}$ and $\mathcal{M}_{C2,i}$ (6.40). The resulting helicity amplitude corresponding to diagrams in Figures 6.1 and 6.2 can be constructed in the following way

$$\begin{aligned}\mathcal{M}^{\mathrm{V}} = &- \sum_{i=\{\varepsilon_+,\varepsilon_-,\varepsilon_0\}} \frac{\mathcal{M}_{1,i}\mathcal{M}_{L2,i} + \mathcal{M}_{2,i}\mathcal{M}_{L1,i} + \mathcal{M}_{1,i}\mathcal{M}_{C2,i} + \mathcal{M}_{2,i}\mathcal{M}_{C1,i}}{q^2 - M_{\mathrm{W}}^2} \\ &+ \frac{1}{q^2}\frac{\mathcal{M}_{1,q}\mathcal{M}_{L2,q} + \mathcal{M}_{2,q}\mathcal{M}_{L1,q} + \mathcal{M}_{1,q}\mathcal{M}_{C2,q} + \mathcal{M}_{2,q}\mathcal{M}_{C1,q}}{q^2 - M_{\mathrm{W}}^2}.\end{aligned} \tag{6.41}$$

In the Fortran code used for the calculation of the VBF diagrams, the virtual corrections of the individual building blocks are stored in the same array as their tree-level counterparts. For instance, the Born results for the block u $\to$ d from (4.10) is stored in $udW_1(1,i)$ while the sum of (6.38) and (6.40) stored in $udW_1(2,i)$. This approach allows us to use the subroutines for the virtual polarization sums as they are implemented for the Born amplitudes (see Appendix B) with a small modification, so that the formula (6.41) turns into

$$\sum_{a=1}^{2}\sum_{\substack{b=1\\b\neq a}}^{2}\sum_{i} udW_1(a,i)Wdu_2(b,i), \tag{6.42}$$

using the notation for building blocks introduced in Section 4.3.

### 6.2.5 Verification of the virtual matrix elements

Several checks have been performed to verify various aspects of the Fortran code for virtual matrix elements.

1. LoopTools comparison
   The Fortran code has been implemented with the option to use either Coli or LoopTools 2.4 [59] to perform the reduction of tensor functions into scalar integrals. LoopTools is

a library compatible with the FormCalc output which uses the Denner-Dittmaier reduction scheme [61] for five-point functions and the Passarino-Veltmann reduction scheme [60] for lower-point functions. It uses dimensional regularization for UV singularities and mass regularization for IR singularities. For selected phase-space points, the matrix elements have been generated with tensor reduction performed in both Coli and LoopTools, using mass renormalization for IR divergencies. The two results agreed at $10^{-8}$ level.

For another consistency check, selected virtual building blocks have also been generated using purely FormCalc + LoopTools combination in Mathematica, leading to a similar level of agreement.

2. Subtraction of UV divergencies
If the renormalization procedure mentioned in the previous section has been implemented correctly, the resulting amplitude should contain no dependency on the ultraviolet regulator $\varepsilon_{UV} = 2/(4-D)$. This has been checked by varying the value of $\varepsilon_{UV}$ from $10^{-5}$ to $10^{5}$, the resulting amplitude stays unchanged up to the level of $10^{-11}$.

3. Check of the infrared poles
It can be shown [28] that the UV renormalized virtual QCD building blocks listed in Figure 4.8 can, due to their relatively simple structure, be expressed as the corresponding Born amplitudes multiplied by a fixed divergent term which copies the infrared pole structure and an additional constant term:

$$\mathcal{M}^{V}_{block} = \mathcal{M}^{B}_{block}\frac{\alpha_S(\mu_R)}{4\pi}C_{\mathrm{F}}\left(\frac{1}{Q^2}\right)^{\varepsilon_{\mathrm{IR}}}\left[-\frac{2}{\varepsilon^2_{\mathrm{IR}}}-\frac{3}{\varepsilon_{\mathrm{IR}}}\right]+\mathcal{O}(\varepsilon_{\mathrm{IR}})+\text{finite term}, \quad (6.43)$$

where $\mathcal{M}^{V}_{block}$ and $\mathcal{M}^{B}_{block}$ is an array of matrix elements corresponding to the virtual and Born-level QCD building blocks (Figure 4.8 and 4.8, respectively), $\varepsilon_{\mathrm{IR}}$ stands for the infrared pole $\varepsilon_{\mathrm{IR}} = 2/(4-D)$ and $Q^2 = -(p_1-p_2)^2 = 2p_1\cdot p_2$ is two times the scalar product of the two quark momenta involved in the given building block. Staying true to the notation introduced in Table 4.1, in the $t$-channel diagrams its value is $Q^2_{t1} = 2k_1\cdot k_3$ or $Q^2_{t2} = 2k_2\cdot k_4$, depending on the quark leg, in the $u$-channel diagrams it is $Q^2_{u1} = 2k_1\cdot k_4$ or $Q^2_{u2} = 2k_2\cdot k_3$ and in the $s$-channel diagrams $Q^2_{s1} = -2k_1\cdot k_2$ or $Q^2_{s2} = -2k_3\cdot k_4$.

To extend the relation (6.43) to the full matrix element, we need to account for both quark lines that appear in the complete subprocess. The next-to-leading order contribution $\mathcal{M}^{V*}\mathcal{M}^{\mathrm{B}}+\mathcal{M}^{B*}\mathcal{M}^{\mathrm{V}}$ can thus be expressed using the squared Born amplitude $|\mathcal{M}^{\mathrm{B}}|^2$ as

$$\begin{aligned}&\mathcal{M}^{*\mathrm{V}}\mathcal{M}^{\mathrm{B}}+\mathcal{M}^{*\mathrm{B}}\mathcal{M}^{\mathrm{V}} = \\ &2|\mathcal{M}^{\mathrm{B}}|^2\frac{\alpha_S(\mu_R)}{4\pi}C_{\mathrm{F}}\left[-\frac{2}{\varepsilon^2_{\mathrm{IR}}}-\frac{3}{\varepsilon_{\mathrm{IR}}}\right]\left[\left(\frac{1}{Q^2_{i1}}\right)^{\varepsilon_{\mathrm{IR}}}+\left(\frac{1}{Q^2_{i2}}\right)^{\varepsilon_{\mathrm{IR}}}\right]_{i=t,u,s} \\ &+\mathcal{O}(\varepsilon_{\mathrm{IR}})+\text{finite term}\end{aligned} \quad (6.44)$$

which upon expanding $(1/Q_{i1})^{\varepsilon}$ and $(1/Q_{i2})^{\varepsilon}$ turns into

$$\begin{aligned}
&\mathcal{M}^{*\mathrm{V}}\mathcal{M}^{\mathrm{B}} + \mathcal{M}^{*\mathrm{B}}\mathcal{M}^{\mathrm{V}} = \\
&2|\mathcal{M}^{\mathrm{B}}|^2 \frac{\alpha_S(\mu_R)}{4\pi} C_{\mathrm{F}} \left[ -\frac{4}{\varepsilon_{\mathrm{IR}}^2} - \frac{2}{\varepsilon_{\mathrm{IR}}} \left( 3 + \log\left( \frac{1}{Q_{i1}^2 Q_{i2}^2} \right) \right) \right. \\
&\left. + \left[ -\log\frac{1}{Q_{i1}^2} \left( 3 + \log\frac{1}{Q_{i1}^2} \right) \right] + \left[ -\log\frac{1}{Q_{i2}^2} \left( 3 + \log\frac{1}{Q_{i2}^2} \right) \right] \right]_{i=t,u,s} \\
&+ \mathcal{O}(\varepsilon_{\mathrm{IR}}) + \text{finite term.}
\end{aligned} \tag{6.45}$$

The relation above serves as a very effective check and debugging tool since it allows us to verify the infrared structure both for the entire virtual amplitude as well as for each individual building block. Aside from infrared divergencies, the relation (6.45) is also sensitive to leftover UV poles that were not removed by renormalization, and provides an additional verification that all ultraviolet counterterms are accounted for.

Moreover, in the building blocks involving only one vector boson (such as $qqV$ in Figure 4.8), the finite term from Eq. (6.43) is equal to $\pi^2/3 - 8$ [28] (using dimensional regularization). This allows us, once expanding the exponential term as in (6.45), to verify the entire virtual building blocks $qqV$ and $Vqq$, including both constant and IR divergent contribution. This check demonstrates, among other things, that the shift from the dimensional reduction scheme utilized by FormCalc to the dimensional regularization scheme (6.30) has been implemented correctly.

## 6.3 Real radiation QCD corrections

The matrix elements for the real emission processes $\mathcal{M}^{\mathrm{R}}$ contain soft and collinear divergencies originating in phase-space regions where one of the external partons has either low momentum, or is collinear with another incoming or outgoing parton. As discussed in Section 6.1, these divergencies cancel against those arising from the virtual contributions and, within the framework of the dipole subtraction method, are compensated by the process-independent dipole subtraction term. The divergencies do not need to be regularized and $\mathcal{M}^{\mathrm{R}}$ may be evaluated in four dimensions.

### 6.3.1 Building blocks and evaluation of the real matrix elements

Since our calculation only involves QCD corrections to the relevant Born amplitudes, the real-radiation diagrams that contribute to the next-to-leading-order are constructed by attaching an external gluon to the leading-order diagrams in every possible way. As gluons only couple to quarks and gluons, the leptonic sections of the full diagrams are unaffected by this procedure, similarly as in the case of the virtual corrections. The only additional building blocks necessary to construct real emission diagrams are the ones involving quark lines with an initial- or final-state gluon attached to them. The building blocks with a gluon in the final state are listed in Figure 4.8. We do not need to generate the building blocks with a gluon

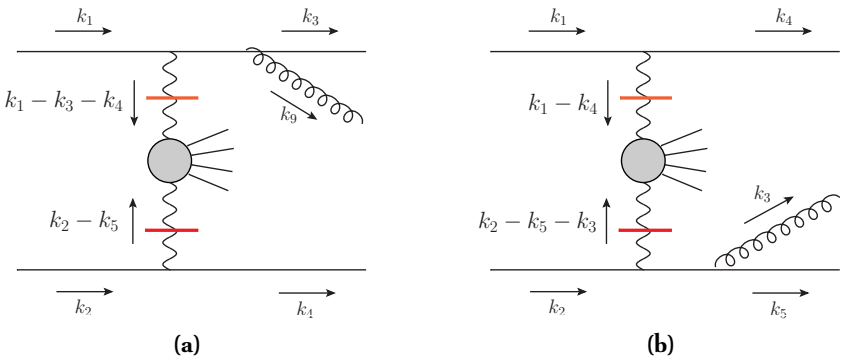


**Figure 6.3:** Demonstrating shifts of the momenta in a diagram of type C when a gluon line is attached to the upper (a) and the lower (b) quark leg. Notation of the momenta are in correspondence with Table 4.1.

in the initial state, however, as they can be obtained from the first set using the crossing symmetry.

Analytic expressions for the real radiation building blocks are generated using the WvdW formalism in the same way as Born-level QCD building blocks. Unlike the remaining vector bosons, which are cut by inserting polarization sums and are thus treated as off-shell particles with virtual masses [according to (A.22) and (A.23)] , gluons are external massless gauge bosons with only two polarization states (A.24) and one additional degree of freedom manifesting itself as a gauge spinor $g_{\pm,A}$, the value of which may be chosen arbitrarily.

The full real radiation matrix elements $\mathcal{M}^{\mathrm{R}}$ are evaluated using the same set of polarization sums as in the case of the Born matrix elements, with several alterations. At the first perturbative order in $\alpha_S$, only one gluon emitted from one of the two quark lines is needed because each gluon coupling contributes $\sqrt{\alpha_S}$ to the non-squared matrix element. Each polarization sum therefore contributes twice - once for each quark line replaced by a corresponding real emission building block, similarly as in the virtual case.

Constructing polarization sums for the real emission diagrams introduces one additional subtlety compared to the virtual corrections. If an additional gluon is attached to one of the quark lines, kinematics of the remaining blocks has to be changed accordingly due to momentum conservation. For instance, in the case of type C diagram in Figure 4.3, attaching a gluon leg to the upper quark line results in shifting the momentum of $V_1$ as illustrated in Figure 6.3a while a gluon leg on the lower quark line shifts the momentum of $V_2$ (Figure 6.3b). For this reason, the momenta in most of the building blocks need to be adjusted with respect to which quark line radiates the external quark. New kinematic configurations for the building blocks that undergo shifts can be found in Tables 6.1 and 6.2.

The resulting real radiation matrix elements are obtained by generating the relevant building blocks, inserting them into the polarization sums from Chapter 5 and summing over the two quark lines to which the gluon can be attached.

| $VVll$ | |
|---|---|
| $Vll_{561}$ | $Vll(k_1 - k_3 - k_7 - k_8 - xk_9, k_2 - k_4 - yk_9, k_5, k_6)$ |
| $Vll_{562}$ | $Vll(k_1 - k_3 - xk_9, k_2 - k_4 - k_7 - k_8 - yk_9, k_5, k_6)$ |
| $Vll_{781}$ | $Vll(k_1 - k_3 - k_5 - k_6 - xk_9, k_2 - k_4 - yk_9, k_7, k_8)$ |
| $Vll_{562}$ | $Vll(k_1 - k_3 - xk_9, k_2 - k_4 - k_5 - k_6 - yk_9, k_7, k_8)$ |
| $VVllll$ | |
| $VVllll$ | $VVllll(k_1 - k_3 - xk_9, k_2 - k_4 - yk_9, k_5, k_6, k_7, k_8)$ |

**Table 6.1:** List of kinematic configurations for the real-emission leptonic building blocks, following the same notation as Table 4.2. If the gluon is radiated from the first quark line, $x = 1$ and $y = 0$; if it is emitted from the second quark line then $x = 0$ and $y = 1$.

### 6.3.2 Matrix elements with an initial-state gluon

While the matrix elements with final-state gluons mimic the setup of channels and crossing rules from section 5.5, diagrams with initial-state gluons are of a different structure since they feature one incoming gluon and one incoming quark (or antiquark) and three outgoing quark states (two quarks and one antiquark, or vice versa). A complete list of all considered subprocesses with a gluon in the initial state can be found in Tables 3.3, 3.6 and 3.9.

The initial-state-gluon diagrams can be derived from the ones with a gluon in the final state by crossing the one of the incoming quarks with the outgoing gluon. All subprocesses with a gluon in the initial state required for our calculation can be obtained by applying crossing symmetry to either a $t$-channel or $u$-channel final-state-gluon diagram. Depending on which of the incoming quarks is crossed, one encounters two general structures illustrated in Figure 6.4. If an initial-state quark is crossed with the final-state gluon emitted from the same quark line, the vector boson(s) connecting the two quark lines is space-like (Figures 6.4a and 6.4b) and the resulting diagram is either $t$-channel or a $u$-channel. If, however, it is crossed with a quark from the other quark line, the resulting diagram is an $s$-channel and the vector boson running between the quark lines is time-like (Figures 6.4c and 6.4d). Even though these two types of diagrams contribute to the same subprocess, one has to distinguish between them in order to combine them with a matching subtraction term. Should one, for instance, neglect $s$-channel diagrams in the NLO calculation, which may be well justified by an appropriate selection of cuts, the $s$-channel diagrams of the type shown in Figures 6.4c and 6.4d should be excluded from the given subprocess.

Figure 6.4 illustrates how diagrams of type $GQ \to \bar{Q}QQ$ can be obtained via crossing symmetry. In order to produce diagrams of type $G\bar{Q} \to Q\bar{Q}\bar{Q}$, one should start with $\bar{Q}\bar{Q} \to G\bar{Q}\bar{Q}$. Diagrams with initial-state gluon as a second incoming parton are derived in analogical manner. Any remaining subprocesses listed in Tables 3.3, 3.6 and 3.9 can be

| $qqV$ |
|---|
| $qqV_1 = qqV(k_1, k_3, k_3 - k_1 - xk_9) \qquad qqV_2 = qqV(k_2, k_4, k_4 - k_2 - yk_9)$ |
| $Vqq$ |
| $Vqq_{13} = Vqq(k_3 - k_1 + xk_9, k_1, k_3) \qquad Vqq_{24} = Vqq(k_4 - k_2 + yk_9, k_2, k_4)$ |
| $qqVV$ |
| $qqVV_{ij\,1,\ i=5,7;\ j=6,8} = qqVV(k_1, k_3, k_i + k_j, k_1 - k_3 - k_i - k_j - xk_9)$ |
| $qqVV_{ij\,2,\ i=5,7;\ j=6,8} = qqVV(k_1, k_3, k_1 - k_3 - k_i - k_j, k_i + k_j - xk_9)$ |
| $qqVV_{ij\,3,\ i=5,7;\ j=6,8} = qqVV(k_2, k_4, k_i + k_j, k_2 - k_4 - k_i - k_j - yk_9)$ |
| $qqVV_{ij\,4,\ i=5,7;\ j=6,8} = qqVV(k_2, k_4, k_2 - k_4 - k_i - k_j, k_i + k_j - yk_9)$ |
| $qqVV_1 = qqVV(k_1, k_3, k_5 + k_6 + k_7 + k_8, k_4 - k_2 + yk_9)$ |
| $qqVV_2 = qqVV(k_1, k_3, k_4 - k_2 + yk_9, k_5 + k_6 + k_7 + k_8)$ |
| $qqVV_3 = qqVV(k_2, k_4, k_5 + k_6 + k_7 + k_8, k_3 - k_1 + xk_9)$ |
| $qqVV_4 = qqVV(k_2, k_4, k_3 - k_1 + xk_9, k_5 + k_6 + k_7 + k_8)$ |
| $VXqqV, \quad X = 1, 2$ |
| $VXqqV_{1378} = VXqqV(k_2 - k_4 - k_5 - k_6 - yk_9, k_1, k_3, k_7 + k_8)$ |
| $VXqqV_{1356} = VXqqV(k_2 - k_4 - k_7 - k_8 - yk_9, k_1, k_3, k_5 + k_6)$ |
| $VXqqV_{2478} = VXqqV(k_1 - k_3 - k_5 - k_6 - xk_9, k_2, k_4, k_7 + k_8)$ |
| $VXqqV_{2456} = VXqqV(k_1 - k_3 - k_7 - k_8 - xk_9, k_2, k_4, k_5 + k_6)$ |
| $qqVVV$ |
| $qqVVV_{24ijkl\ \ i,k=5,7;\ j,l=6,8} = qqVVV(k_1, k_3, k_4 - k_2 + yk_9, k_i + k_j, k_k + k_l)$ |
| $qqVVV_{13ijkl\ \ i,k=5,7;\ j,l=6,8} = qqVVV(k_2, k_4, k_3 - k_1 + xk_9, k_i + k_j, k_k + k_l)$ |
| $qqVVV_{ij24kl\ \ i,k=5,7;\ j,l=6,8} = qqVVV(k_1, k_3, k_i + k_j, k_4 - k_2 + yk_9, k_k + k_l)$ |
| $qqVVV_{ij13kl\ \ i,k=5,7;\ j,l=6,8} = qqVVV(k_2, k_4, k_i + k_j, k_3 - k_1 + xk_9, k_k + k_l)$ |
| $qqVVV_{ijkl24\ \ i,k=5,7;\ j,l=6,8} = qqVVV(k_1, k_3, k_i + k_j, k_k + k_l, k_4 - k_2 + yk_9)$ |
| $qqVVV_{ijkl13\ \ i,k=5,7;\ j,l=6,8} = qqVVV(k_2, k_4, k_i + k_j, k_k + k_l, k_3 - k_1 + xk_9)$ |

**Table 6.2:** List of kinematic configurations for the real-emission QCD building blocks, following the same notation as Table 4.3. If the gluon is radiated from the first quark line, $x = 1$ and $y = 0$; if it is emitted from the second quark line then $x = 0$ and $y = 1$.

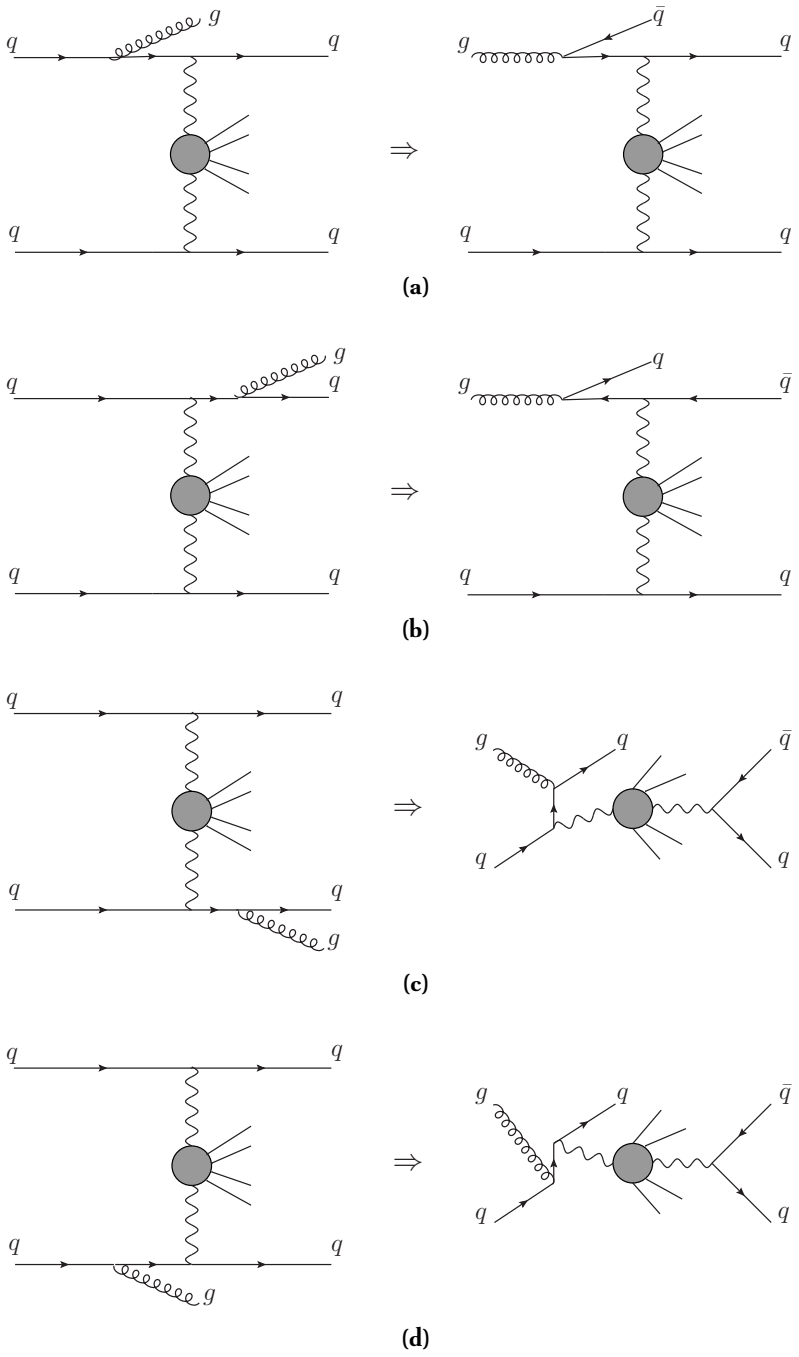


**Figure 6.4:** Examples of channels with a gluon in the initial state derived from a type C diagram (Figure 4.3c). The diagrams in the column on the right are obtained by crossing the final-state gluon with the upper incoming quark in the diagrams on the left.

obtained by applying the same crossing procedure to $u$-channel diagrams instead of $t$-channel. Similarly as in case of virtual contributions, interferences between individual channels are neglected in our calculation.

Care needs to be taken so that the crossing and the kinematic changes are performed consistently across all building blocks forming the given diagram.

### 6.3.3 Generation and verification of real matrix elements

All real emission matrix elements used in our calculation have been generated in the same way as the Born and virtual contributions. FeynArts and FormCalc were used to generate analytical expressions for the building blocks, which were modified in Mathematica to accommodate the framework of the polarization sums and subsequently exported into a Fortran module file.

Since real radiation diagrams are evaluated at tree level, the numerical results can be verified per phase-space point using one of the universally available tools. Similarly as in the leading order calculation, we compared our matrix elements with automatically generated results provided by MadGraph 4.3.0 generated with single precision accuracy. For a number of random phase-space points, including ones close to collinear regions of the phase space, we found a full agreement at $10^{-8}$ level with a setup that had, due to differences in the gauge, decay widths of all intermediate fields set to zero.

Another check that has been performed pointwise is matching of the matrix elements and the corresponding subtraction terms in the soft and collinear regions of the phase space. The dipole subtraction terms are constructed in such a way that their structure in those regions exactly mimics that of the real emission amplitudes and should cancel the divergencies for this class of phase-space points. Since there is a direct correspondence between real radiation amplitudes and the Born amplitudes that contribute to the subtraction terms, the subtraction also works on the subamplitude or diagram level and can be thus used as a debugging tool as well as a consistency check. Accuracy of the subtraction in this case depends on how close the phase-space point is to the collinear or soft region, which can be measured by the relative size of a relevant invariant $s_{ij} = (p_i + p_j)^2 = 2E_iE_j(1 - \cos\theta)$ (assuming $m_i = m_j = 0$). If one of the particles is soft ($E_i \to 0$) or if they get collinear ($\theta \to 0$), the invariant $s_{ij}$ becomes small and, since it is present in the massless propagator, it gives rise to a singularity.

## 6.4 Colour structure of the NLO amplitudes

The next-to-leading order subprocesses contain one colour structure in addition to those that appear at the leading order. It arises in the real-emission amplitudes, while the virtual amplitudes share the same colour structure as the Born amplitude explained in Section 5.9.

In case of the real corrections, the full matrix elements $\mathcal{M}_c$ can be written as a contraction of the colour-stripped amplitudes evaluated as described in Section 6.3 with a $SU(3)_C$ generator $T^c_{ij}$ and a delta function which arises trivially from the quark leg with no

gluon emission

$$\mathcal{M}^{\mathrm{C}} = \delta_{kl} T^c_{ij} \mathcal{M}^{\alpha}. \tag{6.46}$$

In case of the splitting involving quarks, $T^c_{ij}$ are colour charge matrices of the fundamental representation of $SU(3)_C$ $t^c_{ij}$.

The absolute square of the full amplitude results in the contraction of the Kronecker delta, and a trace over the colour generators $t^c_{ij}$:

$$|\mathcal{M}^c|^2 = \delta_{kl}\delta_{lk} \mathrm{Tr}\left[t^c t^c\right] |\mathcal{M}^{\alpha}|^2 = 3 \cdot 4 |\mathcal{M}^{\alpha}|^2 = 12 |\mathcal{M}^{\alpha}|^2 \tag{6.47}$$

This colour factor is shared by both initial- and final-state gluon processes. The colour factors for interference terms between channels do not need to be evaluated since we do not include these in our NLO calculation.

## 6.5 Evaluating squares of the NLO amplitudes

The procedure for obtaining unpolarized matrix elements at next-to-leading order requires, similarly to the case of the leading order (Section 5.10), collecting all colour factors and colour- and helicity averaging factors given by the incoming partons. Since the virtual diagrams involving a gluon loop have the same external structure as the leading-order diagrams, the above mentioned factors are the same as in the Born amplitude and the squared virtual matrix elements can be obtained according to (5.11).

The absolute squares real contributions involving a final-state gluon can be written as

$$|\mathcal{M}_c(q_1, q_2 \to q_3, q_4, l_1, l_2, l_3, l_4, g)|^2 = C \frac{1}{9} \frac{1}{4} \sum_{\{\sigma\}} \sum_{\{c\}}$$
$$|\mathcal{M}(q_1(\sigma_1, c_1), q_2(\sigma_2, c_2) \to q_3(\sigma_3, c_3), q_4(\sigma_4, c_4), l_1(\sigma_5), l_2(\sigma_6), l_3(\sigma_7), l_4(\sigma_8), g(\sigma_9, c_5))|^2, \tag{6.48}$$

where $C = 12$ is the colour factor obtained in the previous section.

In a similar fashion, the squared amplitude corresponding to the initial-state gluon is

$$|\mathcal{M}_c(g, q_1 \to q_2, q_3, q_4, l_1, l_2, l_3, l_4, g)|^2 = C \frac{1}{24} \frac{1}{4} \sum_{\{\sigma\}} \sum_{\{c\}}$$
$$|\mathcal{M}(g(\sigma_1, c_1), q_1(\sigma_2, c_2) \to q_2(\sigma_3, c_3), q_3(\sigma_4, c_4), q_4(\sigma_9, c_5), l_1(\sigma_6), l_2(\sigma_7), l_3(\sigma_8), l_4(\sigma_9))|^2, \tag{6.49}$$

where, in contrast to (6.48), we account for the number of colours and polarizations of the incoming gluon.

## 6.6 Colour-projected Born matrix elements

The key ingredient in the mechanism of the dipole subtraction method is the structure of the individual subtraction terms consisting of the matrix element at the Born level combined with the universal insertion operators **I**, **P** and **K** [56], role of which is to mirror the infrared behaviour of the next-to-leading-order matrix elements. They act on colour and spin space and their insertion in the Born matrix elements leads to so-called colour-projected (correlated) matrix elements which are of following form:

$$|\mathcal{M}_m^{i,j}|^2 =_m \langle 1,...,m|\mathbf{T}_i \cdot \mathbf{T}_j|1,...,m\rangle_m. \tag{6.50}$$

$|1,...,m\rangle_m$ in this case represents a vector in colour and helicity space such that $|\mathcal{M}_m|^2 =_m \langle 1,...,m|1,...,m\rangle_m$ and $\mathbf{T}_i$ is a colour-charge operator associated with gluon emission acting in the colour space according to the following:

$$\langle c_1,...,c_i,...c_m,c|\mathbf{T}_i|\ b_1,...,b_i,...b_m\rangle = \delta_{c_1b_1}...(T_i)^c_{c_ib_i}...\delta_{c_mb_m} \tag{6.51}$$

where $(T_i)^a_{a_ib_i}$ are $SU(3)$ colour matrices in the adjoint representation ($f_{cab}$ ) if the emitting particle $i$ is a gluon, and in the fundamental representation if the emitting particle $i$ is a quark, as is the case in our calculation. More specifically,

$$\text{Outgoing parton} \qquad (T_i)^c_{c_ib_i} = \begin{cases} t^c_{c_ib_i} & \text{if } i = \text{quark} \\ -t^c_{b_ic_i} & \text{if } i = \text{antiquark} \end{cases} \qquad \text{Incoming parton} \qquad (T_a)^c_{c_ab_a} = \begin{cases} -t^c_{b_ac_a} & \text{if } a = \text{quark} \\ t^c_{c_ab_a} & \text{if } a = \text{antiquark} \end{cases}$$

For the product $\mathbf{T}_i \cdot \mathbf{T}_j$ appearing in (6.50) and for the matrices of the fundamental representation $t^c_{ij}$, the colour-charge algebra leads to following relations [35]:

$$\mathbf{T}_i \cdot \mathbf{T}_j = \mathbf{T}_j \cdot \mathbf{T}_i \qquad \mathbf{T}_i^2 = C_i \tag{6.52}$$

$$(t^c)_{ij}(t^c)_{kl} = \frac{1}{2}\left(\delta_{il}\delta_{kj} - \frac{1}{N_C}\delta_{ij}\delta_{kl}\right) \qquad \mathrm{Tr}[t^c t^c]_{(N_C=3)} = 4 \tag{6.53}$$

where $C_i$ is the quadratic Casimir operator for the given representation of particle $i$. In our case, $i$ is either a quark or an antiquark and thus $C_i = C_\mathrm{F} = (N_C^2 - 1)/(2N_C) = 4/3$.

The definition of the colour-projected amplitude from (6.50), denoting the colour indices of the external partons of the Born process $a_i$ and $b_i$, can be written as

$$|\mathcal{M}^{i,j}(\{p\})|^2 = \frac{1}{n_c(a)n_c(b)} \left(\mathcal{M}^{a_1...a_m}(\{p\})\right)^* T^c_{b_ia_i} T^c_{b_ja_j} \mathcal{M}^{a_1...a_m}(\{p\}) \tag{6.54}$$

Factors $n_c(a)$ and $n_c(b)$ represent number of colours of the incoming partons and indices $i$ and $j$ label all possible combinations of the spectator and emitter pairs.

Relation (6.54) suggests that the colour-projected matrix elements can be obtained by computing the squared Born matrix elements and adding a colour structure generated by

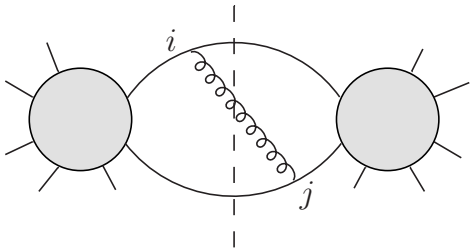


**Figure 6.5:** The colour matrices for the colour-projected matrix elements are constructed by connecting the emitter ($i$) and the spectator ($j$) with a gluon line.

attaching a gluon that connects the emitter and the spectator as shown in Figure 6.5. This allows the subtraction terms to emulate the colour structure of the NLO matrix elements.

All subprocesses considered in our calculation at the leading order are formed by two initial-state and two final-state quarks. This means that there are four different combinations for colour correlation per kinematic channel. Due to the fact that all considered Feynman diagrams contain two quark lines that contribute the same colour factor, and the operators $\mathbf{T}_i$ commute (6.52), the number of colour-correlated matrix elements that need to be calculated can be reduced to three: $\mathbf{T}_1 \cdot \mathbf{T}_3$, $\mathbf{T}_1 \cdot \mathbf{T}_4$ and $\mathbf{T}_1 \cdot \mathbf{T}_2$.

For each kinematic channel, only one of these combinations gives non-zero contribution while the remaining two are rendered zero if the gluon couples to quark lines that are not connected when the relevant diagram is squared. For $t$-channel, this is illustrated in Figure 6.6. As can be seen, the only contributing combination comes from $\mathbf{T}_1 \cdot \mathbf{T}_3$ (Figure 6.6a) where the matrices of the fundamental representation $t^c_{ij}$ are traced over (according to relation (6.53)), whereas the combinations $\mathbf{T}_3 \cdot \mathbf{T}_4$ (Figure 6.6b) and $\mathbf{T}_1 \cdot \mathbf{T}_4$ (Figure 6.6c) remain zero due to the fact that $t^c_{ij}$ are antisymmetric. A similar situation arises in case of the $u$-channel and $s$-channel, where only $\mathbf{T}_1 \cdot \mathbf{T}_4$ and $\mathbf{T}_3 \cdot \mathbf{T}_4$ gives non-zero contribution (Figure 6.7a and 6.7b, respectively). For interferences between individual channels, all combinantions of $\mathbf{T}_i$ are non-zero since the quark lines form only one closed loop (illustrated in Figure 5.19b). Since we have chosen to neglect the interference channels at the next-to-leading order, we do not need to evaluate subtraction terms for them.

The resulting colour-correlated matrix elements contributing to the subtraction terms for non-interfering channels are

$$\begin{aligned}
\mathbf{T}_1 \cdot \mathbf{T}_3 = \mathbf{T}_3 \cdot \mathbf{T}_1 = \mathbf{T}_2 \cdot \mathbf{T}_4 = \mathbf{T}_4 \cdot \mathbf{T}_2 &= -\frac{4}{3}|\mathcal{M}^{\mathrm{B}}_t|^2 \\
\mathbf{T}_1 \cdot \mathbf{T}_4 = \mathbf{T}_4 \cdot \mathbf{T}_1 = \mathbf{T}_2 \cdot \mathbf{T}_3 = \mathbf{T}_3 \cdot \mathbf{T}_2 &= -\frac{4}{3}|\mathcal{M}^{\mathrm{B}}_u|^2 \\
\mathbf{T}_1 \cdot \mathbf{T}_2 = \mathbf{T}_2 \cdot \mathbf{T}_1 = \mathbf{T}_3 \cdot \mathbf{T}_4 = \mathbf{T}_4 \cdot \mathbf{T}_3 &= -\frac{4}{3}|\mathcal{M}^{\mathrm{B}}_s|^2,
\end{aligned} \tag{6.55}$$

where $\mathcal{M}^{\mathrm{B}}_t$, $\mathcal{M}^{\mathrm{B}}_u$ and $\mathcal{M}^{\mathrm{B}}_s$ are the Born matrix elements formed by the $t$-channel, $u$-channel and $s$-channel diagrams, respectively. The factor -4/3 comes from $T^c_{b_i a_i} T^c_{b_j a_j}$ and $\delta_{b_i a_i} \delta b_j a_j$ (evaluated in Figures 6.6a, 6.7a and 6.7b), divided by $n_c(a) n_c(b) = 9$.

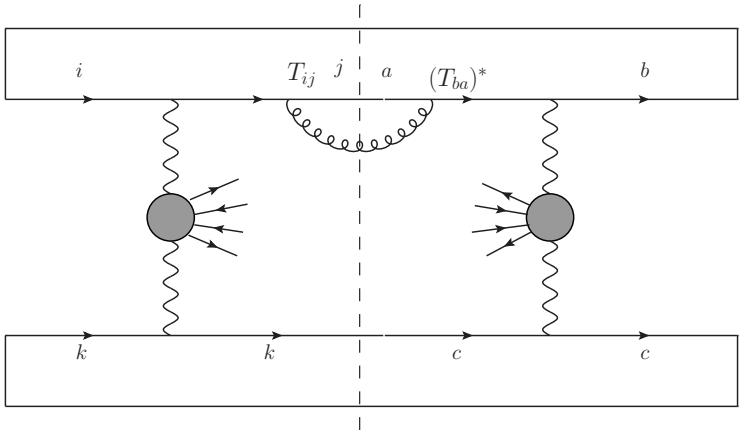


**(a)** $\mathrm{C}\delta_{kc}\delta_{ck}\delta_{bi}T_{ij}\delta_{ja}(T_{ba})^* = -3t_{ij}t_{ji} = -12$

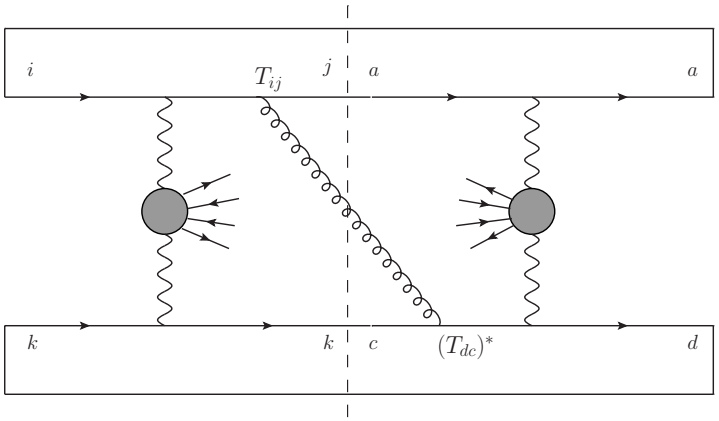


**(b)** $\mathrm{C}T_{ij}\delta_{ja}\delta_{ai}\delta_{ck}(T_{dc})^*\delta_{dk} = -t_{ii}t_{cc} = 0$

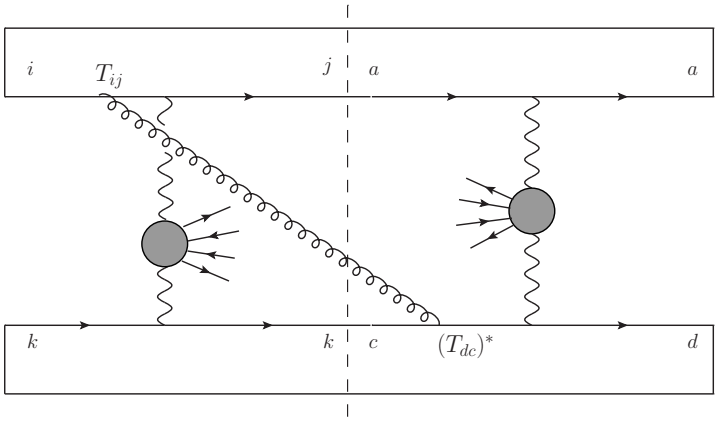


**(c)** $\mathrm{C}T_{ij}\delta_{ja}\delta_{ai}\delta_{ck}(T_{dc})^*\delta_{dk} = -t_{ii}t_{cc} = 0$

**Figure 6.6**

In a general case, the dipole subtraction terms contain an additional operator acting on spin space [56]. Since the real matrix elements in our calculation do not contain gluons splitting into external quarks, which corresponds to external gluons at the Born level, all spin matrixes are diagonal in the helicity space and we do not need to consider spin correlation.

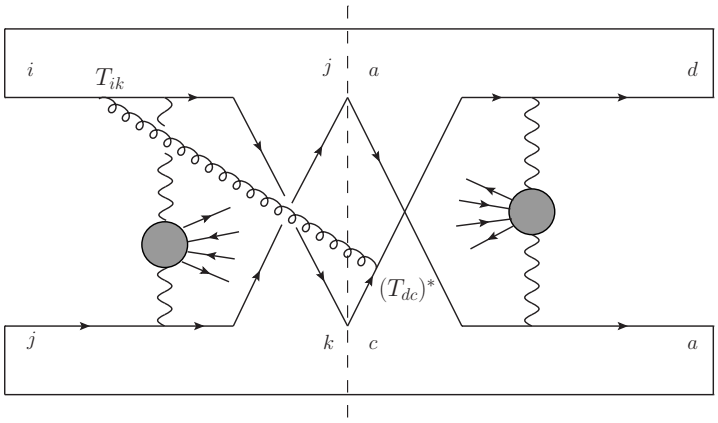


**(a)** C=$T_{ik}\delta_{kc}(T_{dc})^*\delta_{ja}\delta_{aj}\delta_{di} = -3t_{ik}t_{ki} = -12$

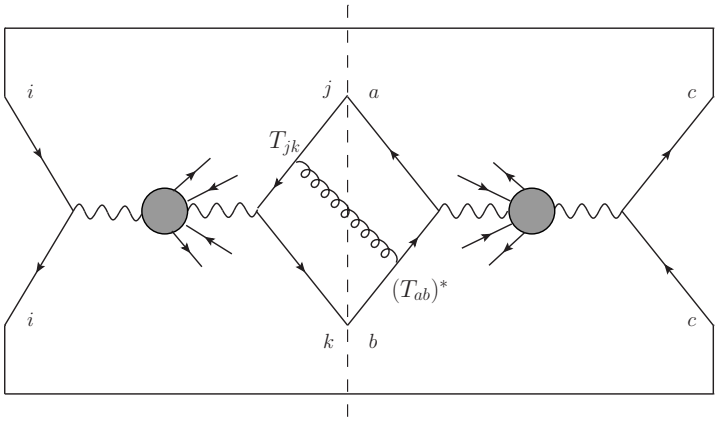


**(b)** C=$\delta_{ci}\delta_{ic}T_{jk}\delta_{kb}(T_{ab})^*\delta_{ja} = -3t_{jk}t_{kj} = -12$

**Figure 6.7**

Chapter 7

# Numerical results

## 7.1 Numerical integration

### 7.1.1 Total cross section

The cross section for a partonic process involving two initial-state hadrons is given as a convolution of the parton distribution functions and the partonic cross section $\hat{\sigma}_{ab}$ as defined in (2.3). Combining this with the dipole subtraction method as outlined in Section 6.1, one obtains the following expression for the total cross section with NLO corrections:

$$\begin{aligned}
\sigma_{pp}^{\text{NLO}}(p_a,p_b) &= \int_m \int_0^1 \mathrm{d}x_1 \int_0^1 \mathrm{d}x_2 f_a^{NLO}(x_1,\mu_F) f_b^{NLO}(x_2,\mu_F) \\
&\quad \Bigg\{ \mathrm{d}\hat{\sigma}_{ab}^{B}(p_a,p_b) + \mathrm{d}\hat{\sigma}_{ab}^{V}(p_a,p_b) + \mathrm{d}\hat{\sigma}_{ab}^{B}(p_a,p_b) \otimes \mathbf{I}_{ab} \\
&+ \int_0^1 \mathrm{d}z_1 \; \mathrm{d}\hat{\sigma}_{ab}^{B}(z_1 p_a,p_b) \left(\mathbf{K}_{ab}(z_1) + \mathbf{P}_{ab}(z_1)\right) \\
&+ \int_0^1 \mathrm{d}z_2 \; \mathrm{d}\hat{\sigma}_{ab}^{B}(p_a,z_2 p_b) \left(\mathbf{K}_{ab}(z_2) + \mathbf{P}_{ab}(z_2)\right) \Bigg\} \\
&+ \int_{m+1} \int_0^1 \mathrm{d}x_1 \int_0^1 \mathrm{d}x_2 f_a^{NLO}(x_1,\mu_F) f_b^{NLO}(x_2,\mu_F) \\
&\quad \left( \mathrm{d}\hat{\sigma}_{ab}^{R}(p_a,p_b) - \sum_{\text{dipoles}} \mathrm{d}\hat{\sigma}^{B}(\tilde{p}_a,\tilde{p}_b) \otimes \mathrm{d}V_{\text{dipole}} \right) .
\end{aligned} \tag{7.1}$$

The partonic cross sections appearing in (7.1) can be symbolically written as ([56])

$$\mathrm{d}\hat{\sigma}(p_a,p_b) = \mathrm{d}\Phi^{(m)}(p_a,p_b,q_1,...,q_m) |\mathcal{M}_m(p_a,p_b,q_1,...,q_m)|^2 F_{\text{jet}}^{(m)}(q_1,...,q_m), \tag{7.2}$$

where $|\mathcal{M}_m(p_a,p_b,q_1,...,q_m)|^2$ is the squared QCD matrix element (or $2\mathrm{Re}(\mathcal{M}^{\mathrm{V}}\mathcal{M}^{\mathrm{B}*})$ in case of the virtual corrections) for the incoming momenta $p_a, p_b$ and outgoing momenta $q_1,...,q_m$ including all polarization and colour factors, and $\mathrm{d}\Phi^{(m)}$ is the element of the phase

space volume defined as

$$\mathrm{d}\Phi^{(m)}(p_a, p_b, q_1, ..., q_m) = \frac{(2\pi)^{(4-3m)}}{2\sqrt{(p_a + p_b)^2}} \mathrm{d}\phi^{(m)}(p_a, p_b; q_1, ..., q_m), \tag{7.3}$$

where

$$\mathrm{d}\phi^{(m)}(p_a, p_b, q_1, ..., q_m) = \left[\prod_{i=1}^{m} \mathrm{d}^4 q_i \delta(q_i^2 - m_i^2)\theta(k_i^0)\right] \delta^{(4)}\left(p_a + p_b - \sum_{i=1}^{m} q_i\right). \tag{7.4}$$

The jet observables should be defined in such a way that they minimize non-perturbative effects of hadronizations, are insensitive to soft and collinear divergencies, and the recombination procedure should be analogical on both partonic and hadronic level so that comparisons between theoretical predictions and experimental measurements are possible (see Section 6.1). In our calculations, we apply the $k_T$ algorithm (see [68, 69, 70]) which defines a collinearity measure between two protojets denoted as $i$ and $j$ as

$$y_{ij} = \frac{\Delta R_{ij}^2}{D^2} \min(p_{T,i}^2, p_{T,j}^2), \tag{7.5}$$

where $p_{T,i}$ and $p_{T,j}$ are the transverse energies of the respective jets, $D$ is a resolution parameter of the algorithm, and $\Delta R_{ij}$ is a measure of distance between two particles

$$\Delta R_{ij} = \sqrt{(y_i - y_j)^2 + (\phi_i - \phi_j)^2}, \tag{7.6}$$

where $y_i$, $y_j$ and $\phi_i$, $\phi_j$ are the rapidities and azimuthal angles of the two protojets, respectively. The algorithm looks for the smallest value among $p_{T,i}^2$, $p_{T,j}^2$ and $y_{ij}$, and if the smallest is $y_{ij}$ the two protojets are recombined into one jet by summing their four-momenta. If $p_{T,k}^2$ is the smallest, the respective particle $k$ is defined as a jet. Starting with all final-state partons as protojets, this procedure is repeated until all objects are included into jets.

### 7.1.2 Monte Carlo

The phase-space integration shown in (7.1) over many final-state particles cannot be performed analytically by present means. Instead, the customarily used method is numerical Monte Carlo integration combined with the phase-space generator and phase-space cuts to simulate collider events.

Monte Carlo technique is based on random numbers and provides an estimate of the integral of a function $f(p)$ over a $d$-dimensional region $R$ of volume $V$, $I = \int_R \mathrm{d}^d x f(x)$ as

$$I_{\mathrm{MC}} = \frac{V}{N} \sum_{i=1}^{N} f(x_i), \tag{7.7}$$

where $x_i$ are random points chosen from the region $R$. In the limit $N \to \infty$, $I_{\text{MC}} \to I$. The measure of error in approximating $I$ with a finite set of $N$ random numbers can be estimated using standard deviation $\delta I_{\text{MC}}$ given by

$$\delta I_{\text{MC}} = V \sqrt{\frac{\sum_{i=1}^{N} (f(x_i))^2 - (\sum_{i=1}^{N} f(x_i))^2}{N(N-1)}}. \tag{7.8}$$

In general, the integrands in perturbative cross sections contain peak structures caused by the presence of propagators in the matrix elements. The performance of the numerical integration can be significantly improved if one is able to predict this structure in order to flatten the integrand. This can be achieved by using a method called importance sampling which introduces a distribution $g(x)$ that is similar to the integrand function so that

$$\sigma = \int_R \frac{f(x)}{g(x)} g(x) \mathrm{d}x \equiv \int_R w(x) g(x). \tag{7.9}$$

By sampling the points from the probability distribution $g(x)$ rather than uniformly, more points are chosen around the peak where the dominant contribution comes from, and since $f(x)/g(x)$ is flatter than $f(x)$, the error is reduced.

In general, the cross section (7.1) can be written in the following form [71]:

$$\sigma = \int_V \mathrm{d}\Phi \rho(p(\Phi)) f(p(\Phi)), \tag{7.10}$$

where $\Phi$ is a set of mappings between phase-space variables and the respective momenta, $f$ consists of matrix elements and dipole contributions, and $\rho$ is the phase space density. For a random generation of phase-space points, a further mapping is introduced to transform variables $\Phi$ to uniformly distributed variables $\mathbf{r}_i \in (0, 1)$ to obtain

$$\sigma = \int_0^1 \mathrm{d}\mathbf{r} \frac{f(p(\Phi(\mathbf{r})))}{g(\Phi(\mathbf{r}))}, \tag{7.11}$$

where $g$ represents the probability density of the phase space events

$$\frac{1}{g(\Phi(\mathbf{r}))} = \rho(p(\Phi(\mathbf{r}))) \left| \frac{\partial \Phi(\mathbf{r})}{\partial \mathbf{r}} \right|. \tag{7.12}$$

The mapping between random numbers $\mathbf{r}$ is chosen so that it mimics the structure of massless and Breit-Wigner propagators inside the squared amplitude. For most QCD processes, however, this selection would describe at best several diagrams contained in the matrix elements. The solution to this problem is presented by the multi-channel Monte Carlo method which combines several mappings (channels) into a single probability density $g_{\text{tot}}$ by introducing so-called "a-priori weights" $\alpha_k$, $k = 1, ..., N$, $\sum^N \alpha_k = 1$, where $N$ is the number of channels (i.e. diagrams with different peak structure). Different mappings $\Phi_k$ for each individual channel $k(r)$ are introduced, and the total probability density is obtained as

$g_{\text{tot}} = \sum_i^N \alpha_i g_i(p\ (\Phi_{k(r)}(\mathbf{r}))_)$, where $r$ is an additional variable for selecting the channel used to generate the respective phase-space point. For more details, see [72][73].

In the numerical integration, the numbers $\mathbf{r}$ and $r$ are generated randomly from the interval $(0, 1)$, while importance sampling is realized through the weights

$$\omega_j = \frac{f(k_i(\Phi_{k(r_j)}(\mathbf{r}_j)))}{g_{\text{tot}}(\Phi_{k(r_j)}(\mathbf{r}_j))}, \tag{7.13}$$

and the cross section is then given by

$$\sigma_{\text{MC}} = \frac{1}{N}\sum_{j=1}^{N}\omega_j, \tag{7.14}$$

with the standard deviation

$$\delta\sigma_{\text{MC}} = \sqrt{\frac{\sum_{j=1}^N(\omega_j)^2 - (\sum_{j=1}^N \omega_j)^2}{N(N-1)}}. \tag{7.15}$$

Further optimization can be achieved by modifying the a-priori weights $\alpha_k$ in order to minimize the Monte Carlo error, as suggested in [74].

## 7.2 Input parameters and cuts

### 7.2.1 Input parameters

All electroweak Standard Model parameters used in the calculation are determined from the values of Z boson mass $M_{\text{Z}}$, W boson mass $M_{\text{W}}$, Higgs boson mass $M_{\text{H}}$, and Fermi coupling constant $G_F$ [75].

The Weinberg angle $\Theta_W$ which defines mixing between mass eigenstates of electroweak gauge bosons is defined as

$$\cos\Theta_W = \frac{M_{\text{W}}}{M_{\text{Z}}}. \tag{7.16}$$

The fine structure constant $\alpha_{\text{EW}}$ is evaluated from $G_F$, $M_{\text{W}}$ and $\Theta_W$ according to the formula

$$\alpha_{\text{EW}} = \frac{\sqrt{2}M_{\text{W}}^2 G_F \sin^2\Theta_W}{\pi}, \tag{7.17}$$

which takes into account dominant effects from the electroweak coupling renormalization [76]. The elementary electric charge $e$ is defined as

$$e = \sqrt{4\pi\alpha_{\text{EW}}}. \tag{7.18}$$

For both leading- and next-to-leading order, we use the NLO value of the strong coupling constant $\alpha_S$ according to the formula (2.2) for $N_C = 3$ and $Q^2 = \mu_R^2$. Its value is extracted from the PDF set (CTEQ or MSTW) that is applied in the calculation.

The decay widths of the unstable intermediate vector bosons are calculated at NLO QCD level according to the following formulas [71]

$$\begin{aligned}
\Gamma_{\mathrm{W}} &= \frac{\alpha_{\mathrm{EW}}}{6} M_{\mathrm{W}} \left[ 3 \left( \frac{1}{\sqrt{2}\sin\Theta_W} \right)^2 + 2 \left( \frac{1}{\sqrt{2}\sin\Theta_W} \right)^2 \left( 1 + \frac{\alpha_S(M_{\mathrm{Z}})}{\pi} \right) \right], \\
\Gamma_{\mathrm{Z}} &= \frac{\alpha_{\mathrm{EW}}}{6} M_{\mathrm{Z}} \left[ \sum_l \left( \left( -Q_l \frac{\cos\Theta_W}{\sin\Theta_W} \right)^2 + \left( -Q_l \frac{\cos\Theta_W}{\sin\Theta_W} + \frac{I_l^3}{\cos\Theta_W \sin\Theta_W} \right)^2 \right) + \right. \\
&\quad \left. \sum_q \left( \left( -Q_q \frac{\cos\Theta_W}{\sin\Theta_W} \right)^2 + \left( -Q_q \frac{\cos\Theta_W}{\sin\Theta_W} + \frac{I_q^3}{\cos\Theta_W \sin\Theta_W} \right)^2 \right) \left( 1 + \frac{\alpha_S(M_{\mathrm{Z}})}{\pi} \right) \right],
\end{aligned} \tag{7.19}$$

where indices $l$ run over all lepton generations, $q$ runs over five light quarks, and $Q_l$, $Q_q$ and $I_l^3$ $I_q^3$ are the charges and third isospin components of the respective leptons and quarks.

In the fixed width scheme, the above widths are only applied to the masses in the propagators (see (2.4)), while in the complex mass scheme, the redefined complex masses are used also in the definition of the Weinberg angle (2.6), rendering it complex.

The decay width of the Higgs boson $\Gamma_{\mathrm{H}}$ depends on the chosen mass and its values are taken from [77].

### 7.2.2 Phase-space cuts

A number of kinematic cuts has been imposed at the Monte Carlo level in order to enhance regions of the phase-space where VBF-type processes can be observed experimentally and reduce QCD background. Generally, these cuts require presence of two hard "tagging" jets with large rapidity separation typical for vector boson fusion. Further, a set of lepton cuts is applied to ensure the charged leptons are well-observable and separated from jets.

Unless stated otherwise, we use the following cuts, proposed in [31].

At parton level, before the recombination procedure is applied, the outgoing partons must fulfill

$$|\eta_{\mathrm{j}}| = \left| \frac{1}{2} \ln \frac{p_0 + p_z}{p_0 - p_z} \right| \leq 5 \tag{7.20}$$

in order to be considered protojets. To construct jets from partons, the $k_T$ recombination algorithm has been used (see Section 7.1.1), with the resolution parameter $D$ set to $0.7$.

In order to clearly distinguish the hard jets from the QCD background, at least two jets must satisfy the transverse momentum and rapidity cut

$$p_{T,\mathrm{j}} = \sqrt{p_x^2 + p_y^2} \geq 20 \text{ GeV}, \tag{7.21}$$

$$|y_{\mathrm{j}}| = \left| \frac{1}{2} \ln \frac{p_0 + p_z}{p_0 - p_z} \right| \leq 4.5. \tag{7.22}$$

The two jets with the highest transverse momentum are denoted as tagging jets. The following cuts involving jets are only imposed on the tagging jets.

We require the invariant mass of the two hard jets to be at least 600 GeV

$$M_{\mathrm{jj}} = \sqrt{(p_{0,1} + p_{0,2})^2 - (\vec{\mathbf{p}}_1 + \vec{\mathbf{p}}_2)^2} > 600\mathrm{GeV}. \tag{7.23}$$

Further, the hard jets must be located in the opposite hemispheres of the detector

$$y_{j,1} \times y_{j,2} < 0, \tag{7.24}$$

with a large rapidity separation in order to further suppress the gluon-induced production mode

$$\Delta y_{\mathrm{jj}} = |y_{\mathrm{j},1} - y_{\mathrm{j},2}| > 4. \tag{7.25}$$

In order to allow for the leptons to be easily detected, the charged leptons are also required to pass transverse energy and rapidity cuts

$$p_{\mathrm{T,l}} \geq 20 \text{ GeV}, \tag{7.26}$$
$$|y_l| \leq 2.5. \tag{7.27}$$

In addition, they should be well separated from one another and from the two tagging jets by imposing

$$\Delta R_{\mathrm{jl}} \geq 0.4, \tag{7.28}$$
$$\Delta R_{\mathrm{ll}} \geq 0.1, \tag{7.29}$$

where the quantity $\Delta R_{ij}$ is a measure of distance in rapidity and azimuthal angle, as defined in 7.6.

Finally, the rapidities of the jets are required to fall between the tagging jet rapidities

$$y_{\mathrm{j,min}} < y_{\mathrm{l}} < y_{\mathrm{j,max}}. \tag{7.30}$$

## 7.3 Comparison with existing results for pp $\rightarrow$ jje$^+\nu_{\mathrm{e}}\mu^+\nu_\mu$

In order to insure correctness of the calculation, comparisons with available results and tools have been performed at each step. The matrix elements for each subprocess have been verified for a set of phase-space points as described in the respective sections of Chapters 5 and 6. This section provides an overview of the comparisons of the full integrated cross section and distributions of the process pp $\rightarrow$ jje$^+\nu_{\mathrm{e}}\mu^+\nu_\mu$ with several previously published results. All results of our calculation have been produced using Monte Carlo code originally developed for [78], using tree-level amplitudes generated with Open Loops technique [79] and virtual amplitudes created using methods described in the previous chapters of this thesis.

1. Sherpa 1.3.1 [80], an automated Monte Carlo event generator has been used to test the parts of the calculation that involve tree-level matrix elements, i.e. the LO and real radiation cross section, taking into account $s$-channel diagrams as well as interferences

| Channel ($XX \to XX e^+\nu_e\mu^+\nu_\mu$,) | $\sigma$[fb] | $\sigma_{\text{Sherpa}}$[fb] |
|---|---|---|
| uu → dd, cc → ss | 2.714(2) | 2.711(3) |
| uc → ds, cu → ds | 0.3079(4) | 0.3079(3) |
| $\bar{d}\bar{d} \to \bar{u}\bar{u}$, $\bar{s}\bar{s} \to \bar{c}\bar{c}$ | 0.06556(4) | 0.06547(5) |
| $\bar{d}\bar{s} \to \bar{u}\bar{c}$, $\bar{s}\bar{d} \to \bar{u}\bar{c}$ | 0.05553(2) | 0.05549(5) |
| $u\bar{d} \to d\bar{u}$, $\bar{d}u \to d\bar{u}$, $c\bar{s} \to s\bar{c}$, $\bar{s}c \to s\bar{c}$ | 0.7657(2) | 0.7656(7) |
| $u\bar{d} \to s\bar{c}$, $\bar{d}u \to s\bar{c}$, $c\bar{s} \to d\bar{u}$, $\bar{s}c \to d\bar{u}$ | 0.004338(1) | 0.004328(4) |
| $\bar{s}u \to \bar{c}d$, $u\bar{s} \to \bar{c}d$, $\bar{d}c \to \bar{u}s$, $c\bar{d} \to \bar{u}s$ | 0.4452(1) | 0.4451(4) |
| total | 4.3559(9) | 4.355(3) |

**Table 7.1:** Comparison of the integrated cross section $\sigma$ with Sherpa-produced cross section $\sigma_{\text{Sherpa}}$ for the $W^+W^+$ production processes at the leading order, using SM parameters (7.31) and kinematic cuts (7.32). The error estimates are shown in the brackets, and affect the last digit of the result.

between kinematic channels. The events have been generated at the centre of mass energy of $\sqrt{s} = 14$ TeV.

The SM input parameters have been chosen as

$$\begin{aligned} M_W &= 80.423 \text{ GeV} & \Gamma_W &= 2.04759951 \text{ GeV}, \\ M_Z &= 91.188 \text{ GeV} & \Gamma_Z &= 2.44140351 \text{ GeV}, \\ M_H &= 120 \text{ GeV} & \Gamma_H &= 3.48 \times 10^{-3} \text{ GeV} \\ G_F &= 1.166 \times 10^{-5} \text{ GeV}^{-2} & \alpha_S(M_Z) &= 0.1202633610889 \end{aligned} \tag{7.31}$$

and the complex-mass scheme has been used to treat the unstable intermediate particles. The factorization and renormalization scale have been chosen as $\mu_F = \mu_R = M_W$. For LO, we have used CTEQ6 PDF set, while for the real radiation process we use CTEQ6M [81, 82].

Since the dipoles have not been included in the Sherpa run, integrating the real cross section over the phase space selected by the cuts from Section 7.2.2 would result in collinear and soft singularities. In order to prevent that, only the following two kinematic cuts have been used:

$$\begin{aligned} p_{T\text{j}} &\geq 50 \text{ GeV}, \\ M_{\text{jj}} &\geq 200 \text{ GeV}. \end{aligned} \tag{7.32}$$

In the real case, these cuts have been applied to all three jets (or pairs of jets, in case of $M_{\text{jj}}$), insuring that none of the final-state partons becomes soft or collinear and thus rendering the cross section finite. Additionally, the $k_T$ recombination algorithm with

| Channel ($XX \to \mathrm{g}XX\mathrm{e}^+\nu_\mathrm{e}\mu^+\nu_\mu$) | $\sigma$[fb] | $\sigma_{\mathrm{Sherpa}}$[fb] |
|---|---|---|
| $\mathrm{uu} \to \mathrm{dd}$, $\mathrm{cc} \to \mathrm{ss}$ | 0.2813(4) | 0.2810(5) |
| $\mathrm{uc} \to \mathrm{ds}$, $\mathrm{cu} \to \mathrm{ds}$ | 0.020335(2) | 0.02037(4) |
| $\bar{\mathrm{d}}\bar{\mathrm{d}} \to \bar{\mathrm{u}}\bar{\mathrm{u}}$, $\bar{\mathrm{s}}\bar{\mathrm{s}} \to \bar{\mathrm{c}}\bar{\mathrm{c}}$ | 0.002824(5) | 0.002821(4) |
| $\bar{\mathrm{d}}\bar{\mathrm{s}} \to \bar{\mathrm{u}}\bar{\mathrm{c}}$, $\bar{\mathrm{s}}\bar{\mathrm{d}} \to \bar{\mathrm{u}}\bar{\mathrm{c}}$ | 0.002456(1) | 0.002446(6) |
| $\mathrm{u}\bar{\mathrm{d}} \to \mathrm{d}\bar{\mathrm{u}}$, $\bar{\mathrm{d}}\mathrm{u} \to \mathrm{d}\bar{\mathrm{u}}$, $\mathrm{c}\bar{\mathrm{s}} \to \mathrm{s}\bar{\mathrm{c}}$, $\bar{\mathrm{s}}\mathrm{c} \to \mathrm{s}\bar{\mathrm{c}}$ | 0.04403(9) | 0.04424(9) |
| $\mathrm{u}\bar{\mathrm{d}} \to \mathrm{s}\bar{\mathrm{c}}$, $\bar{\mathrm{d}}\mathrm{u} \to \mathrm{s}\bar{\mathrm{c}}$, $\mathrm{c}\bar{\mathrm{s}} \to \mathrm{d}\bar{\mathrm{u}}$, $\bar{\mathrm{s}}\mathrm{c} \to \mathrm{d}\bar{\mathrm{u}}$ | 0.001068(1) | 0.001068(2) |
| $\bar{\mathrm{s}}\mathrm{u} \to \bar{\mathrm{c}}\mathrm{d}$, $\mathrm{u}\bar{\mathrm{s}} \to \bar{\mathrm{c}}\mathrm{d}$, $\bar{\mathrm{d}}\mathrm{c} \to \bar{\mathrm{u}}\mathrm{s}$, $\mathrm{c}\bar{\mathrm{d}} \to \bar{\mathrm{u}}\mathrm{s}$ | 0.02427(3) | 0.02424(4) |
| Channel ($\mathrm{g}X \to XXX\mathrm{e}^+\nu_\mathrm{e}\mu^+\nu_\mu$) | $\sigma$/fb | $\sigma_{\mathrm{Sherpa}}$/fb |
| $\mathrm{gu} \to \mathrm{dd}\bar{\mathrm{u}}$, $\mathrm{ug} \to \mathrm{dd}\bar{\mathrm{u}}$, $\mathrm{gc} \to \mathrm{ss}\bar{\mathrm{c}}$, $\mathrm{cg} \to \mathrm{ss}\bar{\mathrm{c}}$ | 0.03314(6) | 0.03312(6) |
| $\mathrm{gu} \to \mathrm{ds}\bar{\mathrm{c}}$, $\mathrm{ug} \to \mathrm{ds}\bar{\mathrm{c}}$, $\mathrm{gc} \to \mathrm{sd}\bar{\mathrm{u}}$, $\mathrm{cg} \to \mathrm{sd}\bar{\mathrm{u}}$ | 0.03311(4) | 0.03316(6) |
| $\mathrm{g}\bar{\mathrm{d}} \to \mathrm{d}\bar{\mathrm{u}}\bar{\mathrm{u}}$, $\bar{\mathrm{d}}\mathrm{g} \to \mathrm{d}\bar{\mathrm{u}}\bar{\mathrm{u}}$, $\mathrm{g}\bar{\mathrm{s}} \to \mathrm{s}\bar{\mathrm{c}}\bar{\mathrm{c}}$, $\bar{\mathrm{s}}\mathrm{g} \to \mathrm{s}\bar{\mathrm{c}}\bar{\mathrm{c}}$ | 0.003530(7) | 0.003536(7) |
| $\mathrm{g}\bar{\mathrm{d}} \to \mathrm{s}\bar{\mathrm{u}}\bar{\mathrm{c}}$, $\bar{\mathrm{d}}\mathrm{g} \to \mathrm{s}\bar{\mathrm{u}}\bar{\mathrm{c}}$, $\mathrm{g}\bar{\mathrm{s}} \to \mathrm{d}\bar{\mathrm{u}}\bar{\mathrm{c}}$, $\bar{\mathrm{s}}\mathrm{g} \to \mathrm{d}\bar{\mathrm{u}}\bar{\mathrm{c}}$ | 0.003532(5) | 0.003531(5) |
| total | 0.4492(5) | 0.4492(6) |

**Table 7.2:** Comparison of the integrated cross section $\sigma$ with Sherpa-produced cross section $\sigma_{\mathrm{Sherpa}}$ for the $\mathrm{W}^+\mathrm{W}^+$ production processes at the next-to-leading order, using SM parameters 7.31 and kinematic cuts 7.32. The error estimates are shown in the brackets, and affect the last digit of the result.

$D = 0.7$ has been applied in both runs, which means that any recombination taking place results in the event being cut away.

The resulting integrated cross sections for both calculations are shown in Table 7.1 for the leading order processes $\mathrm{pp} \to \mathrm{jj}\ \mathrm{e}^+\nu_\mathrm{e}\mu^+\nu_\mu$, and in Table 7.2 for the processes $\mathrm{pp} \to \mathrm{jjj}\ \mathrm{e}^+\nu_\mathrm{e}\mu^+\nu_\mu$. Both total and channel-wise results are in very good agreement within accuracy estimated by the standard deviation.

2. The first results for NLO QCD corrections to pp $\to$ jj $e^+\nu_e\mu^+\nu_\mu$ have been published in [31]. We reproduced the calculation with the same setup, input parameters and cuts. The events have been generated at the centre of mass energy of $\sqrt{s} = 14$ TeV. In the matrix elements for all subprocesses, we neglected $s$-channel diagrams and interferences between $t-$ and $u-$channels.

   The following SM parameters have been used:

$$
\begin{aligned}
&M_{\mathrm{W}} = 80.423 \text{ GeV} && \Gamma_{\mathrm{W}} = 2.100 \text{ GeV},\\
&M_{\mathrm{Z}} = 91.188 \text{ GeV} && \Gamma_{\mathrm{Z}} = 2.510 \text{ GeV},\\
&M_{\mathrm{H}} = 120 \text{ GeV} && \Gamma_{\mathrm{H}} = 4.41 \times 10^{-3} \text{ GeV}\\
&G_F = 1.16639 \times 10^{-5} \text{ GeV}^{-2}\\
&\alpha_{S,\,\mathrm{CTEQ6M}}(M_{\mathrm{Z}}) = 0.1179815096735043\\
&\alpha_{S,\,\mathrm{MSTW08}}(M_{\mathrm{W}}) = 0.1225462477617477
\end{aligned}
\tag{7.33}
$$

   Fixed width scheme (see Chapter 1) has been used to treat the massive propagators, with the exception of the Higgs couplings where the $M_{\mathrm{Z}}$ and $M_{\mathrm{W}}$ have been kept complex due to technical reasons. The factorization and renormalization scale have been set to $\mu_F = \mu_R = M_{\mathrm{W}}$. The second, dynamic scale $\mu_F = \mu_R = Q$ used in [31] has not been implemented because of the fact that it may take different values for different diagrams involved in a subprocess which poses technical difficulties with our setup. The PDF's have been evaluated by two different PDF sets, CTEQ6 [81, 82] (CTEQ6L1 for LO, CTEQ6M for NLO) and MSTW2008 [83].

   The values of the VBF cuts are set as listed in Section 7.2.2, with the exception of the requirement that the charged leptons fall between the tagging jets in rapidity (7.30) which has been omitted entirely [1].

   The LO and NLO results for both PDF sets are shown in Table 7.3. For both LO and NLO cross sections, the relative deviation between the results of the two calculations is only of the order of $\sim 0.2\%$ or even smaller. These small discrepancies can be attributed to the slight differences in applying the width scheme (see above). However, they could as well be explained by statistical fluctuations, possibly combined with an underestimated error of the results in [31] which do not state their statistical error explicitly. The differences between the two PDF sets are at the level of 5% at LO, and of 2% at NLO.

3. In [32], the results for pp $\to$ jj $e^+\nu_e\mu^+\nu_\mu$ have been presented at the centre of mass energy of $\sqrt{s} = 7$ TeV. While the main focus of [32] lies in inclusion of the parton shower effects, the NLO QCD result for the cross section is also presented.

   The setup is very similar to the one in [31] as it uses the same framework. The following

[1] Private communication during comparisons revealed that in the results presented in [31], this cut has been omitted. A corrected version of the article can be found at arXiv:hep-ph/0907.0580.

| PDF set | $\sigma$[fb] | $\sigma_{\text{JOZ}}$[fb] | $\delta$[%] |
|---|---|---|---|
| Leading order | | | |
| CTEQ6L1 | 1.4746(7) | 1.478 | -0.23(7) |
| MSTW08 | 1.4061(7) | 1.409 | -0.21(7) |
| Next-to-leading order | | | |
| CTEQ6M | 1.405(1) | 1.404 | +0.1(1) |
| MSTW08 | 1.372(1) | 1.372 | -0.0(1) |

**Table 7.3:** Comparison of the integrated cross section $\sigma$ with cross sections presented in [31] $\sigma_{\text{JOZ}}$ for the $W^+W^+$ production processes at the next-to-leading order, using SM parameters (7.33). The error estimates are shown in the brackets, and affect the last digit of the result. In the error estimate for the deviation between the two results, we assumed the $\sigma_{\text{JOZ}}$ error to be of the same size as our stated error.

input parameters have been used

$$\begin{aligned} &M_{\text{W}} = 80.419 \text{ GeV} && \Gamma_{\text{W}} = 2.099 \text{ GeV}, \\ &M_{\text{Z}} = 91.188 \text{ GeV} && \Gamma_{\text{Z}} = 2.510 \text{ GeV}, \\ &M_{\text{H}} = 120 \text{ GeV} && \Gamma_{\text{H}} = 4.41 \times 10^{-3} \text{ GeV} \\ &G_F = 1.16639 \times 10^{-5} \text{ GeV}^{-2} \\ &\alpha_{S,\,\text{MSTW08}}(M_{\text{W}}) = 0.1225472040133158 \end{aligned} \tag{7.34}$$

and the factorization and renormalization scale have been set to a dynamic value defined as

$$\begin{aligned} \mu_R = \mu_F = \tfrac{p_{T,\text{j1}} + p_{T,\text{j2}} + E_{T,W_1} + E_{T,W_2}}{2}, \\ \text{where} \qquad E_{T,W} = \sqrt{M_{\text{W}}^2 + p_{T,W}^2}. \end{aligned} \tag{7.35}$$

Here, $p_{T,W}^2$ represents the transverse momentum of the same-type lepton-neutrino pair, and $p_{T,\text{j1}}$ are the transverse momenta of the two final-state jets of the underlying process. This choice of scale is slightly different from the one in [32] where the jets of the underlying Born process were used. Another difference between the two calculations lies in the width scheme; while our calculation used complex mass scheme, the results in [32] have been obtained using the fixed width scheme. The NLO set of PDF's from MSTW08 [83] has been used.

The full set of VBF cuts from Section 7.2.2 has been applied, and the jet recombination has been performed using $k_T$ algorithm with a resolution parameter $D = 0.4$.

The results of the calculation are shown in Table 7.4. The agreement for the total NLO cross section is of the order of 2.3%. Considering small differences in the choice of

scale and width scheme and in particular the statistical error of the result, this deviation can be considered acceptable.

| PDF set | $\sigma$[fb] | $\sigma_{\text{JO}}$[fb] | $\delta$[%] |
|---|---|---|---|
| Leading order | | | |
| MSTW08 | 0.16836(8) | / | / |
| Next-to-leading order | | | |
| MSTW08 | 0.1961(2) | 0.201(3) | -2.3(1.5) |

**Table 7.4:** Comparison of the integrated cross section $\sigma$ with cross sections presented in [32] $\sigma_{\text{JO}}$ for the $W^+W^+$ production processes at the next-to-leading order, using SM parameters 7.34. The error estimates are shown in the brackets, and affect the last digit of the result.

## 7.4 Results for pp $\to$ jj $e^+\nu_e\mu^+\nu_\mu$

### 7.4.1 Setup

For numerical discussion, we evaluate the total cross section and distribution for the NLO QCD corrections to pp $\to$ jj $e^+\nu_e\mu^+\nu_\mu$ at the centre of mass energy $\sqrt{s} = 14$ TeV, using the following SM parameters

$$\begin{aligned} M_{\text{W}} &= 80.399 \text{ GeV} & \Gamma_{\text{W}} &= 2.099736097449861 \text{ GeV}, \\ M_{\text{Z}} &= 91.1876 \text{ GeV} & \Gamma_{\text{Z}} &= 2.509659634331562 \text{ GeV}, \\ M_{\text{H}} &= 125 \text{ GeV} & \Gamma_{\text{H}} &= 4.07 \times 10^{-3} \text{ GeV} \\ G_F &= 1.16637 \times 10^{-5} \text{ GeV}^{-2} & \alpha_S(M_{\text{W}}) &= 0.1225519862138941, \end{aligned} \tag{7.36}$$

where $\Gamma_{\text{W}}$ and $\Gamma_{\text{Z}}$ are evaluated according to formulas (7.19).

For the treatment of the resonances in the massive propagators, we have used the complex-mass scheme [see (2.5), (2.6)]. The kinematic cuts have been applied exactly as specified in Section 7.2.2, while the jet reconstruction has been performed using the $k_T$ algorithm with the resolution parameter $D = 0.7$.

The LO cross section has been evaluated for two different setups. In the first, we only take into account the $t$-channel and $u$-channel diagrams, and completely disregard the interferences between them. This approximation corresponds to the setup in [31]. In the second, we calculate the complete cross section including $t$-, $u$- and $s$-channel diagrams and all interferences in order to compare and verify legitimacy of the above approximation.

For the NLO cross section, the $s$-channel diagrams and interferences are neglected both in virtual and real corrections.

For the parton distributions functions, we have used the MSTW2008 [83].

All cross sections and distributions have been produced using Monte Carlo code developed for [78], using tree-level amplitudes generated with Open Loops technique [79] while the virtual corrections were calculated according to the method described in the previous chapters.

### 7.4.2 Scale dependence and cross section

As mentioned in Chapter 2, the renormalization- and factorization-scale dependence is an artifact of using the perturbative expansion up to a finite order. Their values can, however, be freely chosen to reduce the impact of the higher-order corrections.

In our calculation, two types of scales have been chosen to demonstrate their effects on the behaviour of the NLO distributions for selected observable quantities. In the fixed scale choice (FS), both factorization and renormalization scales have been set to the multiple of the mass of W boson which is involved in the scattering process

$$\mu_F = \mu_R = \xi M_{\mathrm{W}}, \tag{7.37}$$

where $\xi$ is a variable scale parameter. The second choice is a dynamic scale (DS) involving transverse momenta of the two outgoing hard jets

$$\mu_F = \mu_R = \xi \sqrt{p_{T,\mathrm{jet}_1} \cdot p_{T,\mathrm{jet}_2}}. \tag{7.38}$$

This scale has been chosen to flatten the variation of the $K$ factor in the $p_{T,\mathrm{j}}$, as well as other distributions involving jets with high $p_T$, as is demonstrated later.

The dependence of the total cross section on the parameter $\xi$ for both scale choices is demonstrated in Figure 7.1, for a variation in $\xi$ in the range $\frac{1}{8} < \xi < 8$. In a more range $\frac{1}{2} < \xi < 2$, the scale variation of the LO cross section which only depends on $\xi$ via $\mu_F$ (as $\mu_R$ only enters in $\alpha_S(\mu_R)$) is of the order of 20%, while at NLO it is reduced down to about 2% of the total cross section for both scale choices. For lower values of $\xi$, the scale dependence for DS is less pronounced ($\sim 8\%$ of the total cross section at $\xi = 1$) than in the case of FS ($\sim 20\%$ of the total cross section at $\xi = 1$).

In the remaining distributions shown in the following sections, the scale parameter is assumed to be fixed at the value $\xi = 1$, where the $K$ factor defined as $\sigma^{\mathrm{NLO}}/\sigma^{\mathrm{LO}}$ gives the following values for FS and DS, respectively:

$$K_{\mathrm{FS}} = 0.976 \qquad K_{\mathrm{DS}} = 1.056. \tag{7.39}$$

The dedicated VBF cuts listed in Section 7.2.2 give preference to $t$- and $u$-channel kinematics, whereas $s$-channel configurations are strongly suppressed by the requirement of the final-state jets with large rapidity separation and invariant mass. Moreover, interference between $t$- and $u$-channel with identical final-state quarks is prohibited by the condition that jets have to be located in the forward and backward regions of the detector. It can therefore be argued [31] that the $s$-channel and interference contributions can safely be neglected if the VBF cuts are applied. In order to verify this claim, the LO cross section has been evaluated

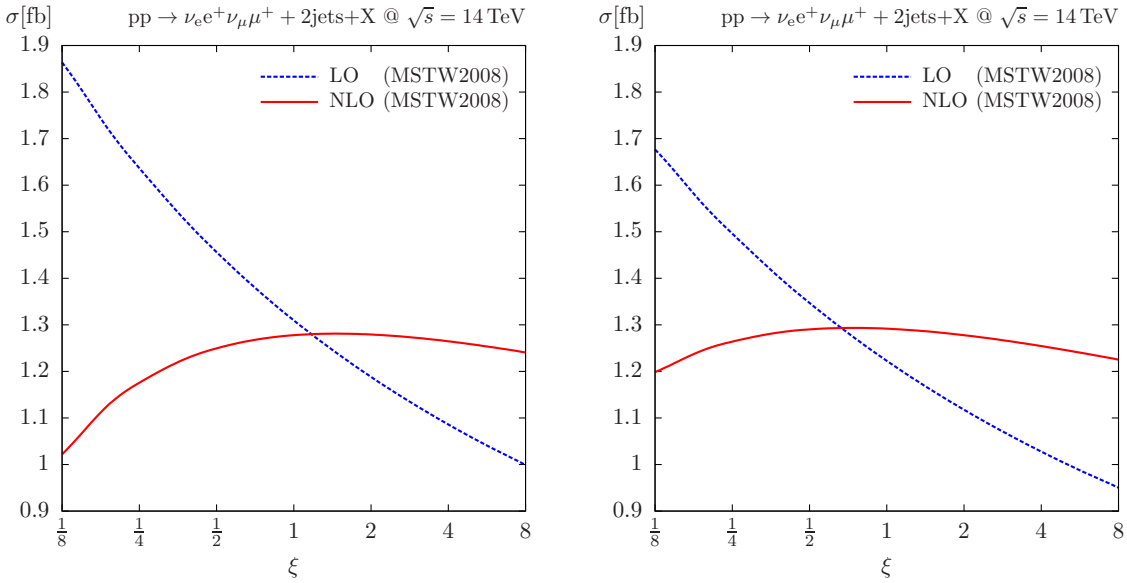


**(a)** $\mu_F = \mu_R = \xi M_W$ **(b)** $\mu_F = \mu_R = \xi\sqrt{p_{T,\text{jet}_1} \cdot p_{T,\text{jet}_2}}$

**Figure 7.1:** Scale dependence of the LO (dotted blue line) and NLO (solid red line) cross section for the fixed (Figure 7.1a) and dynamic scale (Figure 7.1b) as a function of the scale parameter $\xi$.

independently using both setups. The results (obtained using the dynamic scale with selected values of parameter $\xi$) can be found in the left column in Table 7.5. Here, $\sigma^{\text{LO}}_{\text{full}}$ stands for cross section that includes all channels and interferences, while $\sigma^{\text{LO}}_{\text{VBF}}$ only contains $t$- and $u$-channel contributions. The results for both configurations are in perfect agreement within the stated numerical accuracy for all values of $\xi$. However, this result may be accidental to some extend: very small positive $s$-channel contributions in the $u\bar{d} \to d\bar{u}$ channel compensate negative interference contributions in the $uu \to dd$ channel (all others are either not affected ($uc \to ds$, $\bar{d}\bar{s} \to \bar{u}\bar{c}$, $u\bar{s} \to d\bar{c}$) or numerically irrelevant ($\bar{d}\bar{d} \to \bar{u}\bar{u}$, $u\bar{d} \to s\bar{c}$). In addition, the same random numbers are used in order to avoid fake effects from fluctuations in the difference which is assumed to be tiny. Nevertheless, these effects are very small and $\sigma^{\text{LO}}_{\text{VBF}}$ can be considered a very good approximation of the full LO cross section. For this reason, NLO cross section has been evaluated using only $t$- and $u$-channel contributions in order to improve the speed of the calculation. The values of $\sigma^{\text{NLO}}_{\text{VBF}}$ for different values of $\xi$ can be found in the second column in Figure 7.5.

| $\xi$ | $\sigma^{\text{LO}}_{\text{full}}$[fb] | $\sigma^{\text{LO}}_{\text{VBF}}$[fb] | $\sigma^{\text{NLO}}_{\text{VBF}}[fb]$ |
|---|---|---|---|
| 1/8 | 1.6766(5) | 1.6765(5) | 1.198(2) |
| 1/4 | 1.4959(5) | 1.4959(4) | 1.264(1) |
| 1/2 | 1.3470(4) | 1.3470(4) | 1.2903(9) |
| 1 | 1.2227(3) | 1.2227(4) | 1.2917(8) |
| 2 | 1.1176(3) | 1.1176(3) | 1.2778(7) |
| 4 | 1.0277(3) | 1.0277(3) | 1.2544(6) |
| 8 | 0.9501(3) | 0.9501(3) | 1.2253(6) |

**Table 7.5:** Integrated cross section for the leading order including all channels and interferences $\sigma^{\text{LO}}_{\text{full}}$, for the leading order while neglecting $s$-channel diagrams and interferences $\sigma^{\text{LO}}_{\text{VBF}}$ and for the next-to-leading order while neglecting $s$-channel diagrams and interferences $\sigma^{\text{NLO}}_{\text{VBF}}$, using SM parameters (7.36) and the dynamic scale (7.38). The error estimates are shown in the brackets, and affect the last digit of the result.

### 7.4.3 Jet distributions

Accurate predictions for the leading jet distributions and their theoretical uncertainties play an important role in the LHC analyses of the products of collisions. One of the most distinguishing features of the weak boson fusion processes are two hard tagging jets falling in the far-forward and backward regions of the detector, typically scattered at small angles to the beam direction. This allows for a very efficient identification of the event and suppression of the QCD background by applying a suitable set of jet cuts, albeit at the cost of reducing the size of the cross section.

All distributions shown in this and the following section are evaluated using kinematic cuts from Section 7.2.2 and the MSTW2008 PDF set [83]. Two plots are presented for each observable: the one on the left depicts the LO and NLO prediction, uncertainty of which is indicated by error bands resulting from variation of the given scale within $1/2 < \xi < 2$, while the plot on the right shows the LO and NLO prediction normalized to the LO result at the central scale, i.e. $K_{\text{LO}}(\xi) = \text{d}\sigma_{\text{LO}}(\xi)/\text{d}\sigma_{\text{LO}}(\xi = 1)$ (dotted blue line), and $K_{\text{NLO}}(\xi) = \text{d}\sigma_{\text{NLO}}(\xi)/\text{d}\sigma_{\text{LO}}(\xi = 1)$ (solid red line). The blue band in this case corresponds to the relative scale uncertainty of the cross section at the leading order, and the central curve of the red band represents $K_{\text{NLO}}(\xi = 1)$.

Figure 7.2 on the left shows the LO and NLO cross section as a function of the transverse momentum of the harder (in terms of $p_T$) of the two tagging jets in the range $20 \text{ GeV} < p_{T_{\text{jet, max}}} < 400 \text{ GeV}$, taking into account the cut imposed on the minimum value of $p_T$. Figure 7.2a shows the dependence for the fixed scale (7.37) and Figure 7.2b for the dynamic scale (7.38). In both cases, the distribution has a peak at $\sim 110$ GeV, confirming the preference of the high $p_T$ regions by the VBF tagging jets, while the probability to find a jet

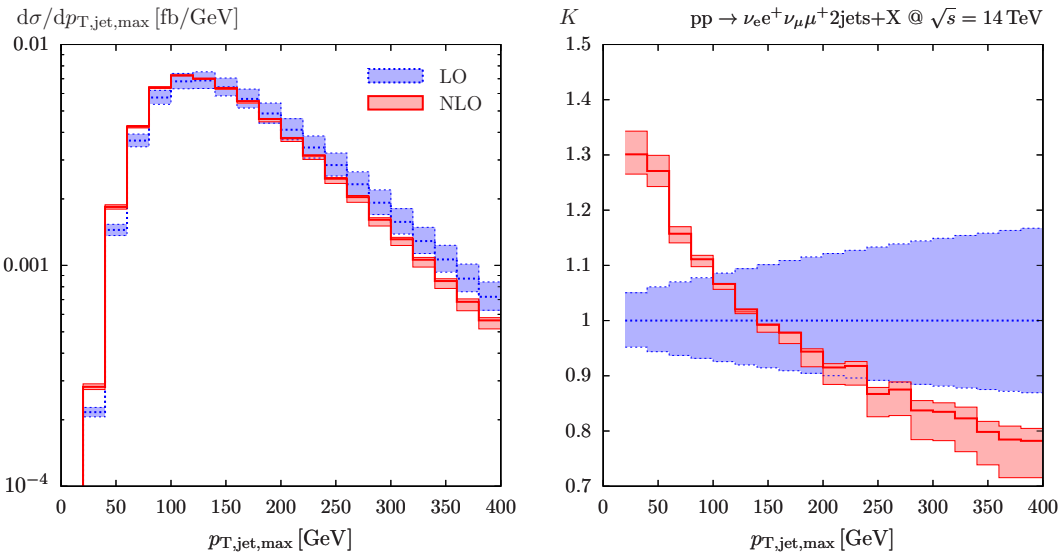


**(a)** $\mu_F = \mu_R = M_W$

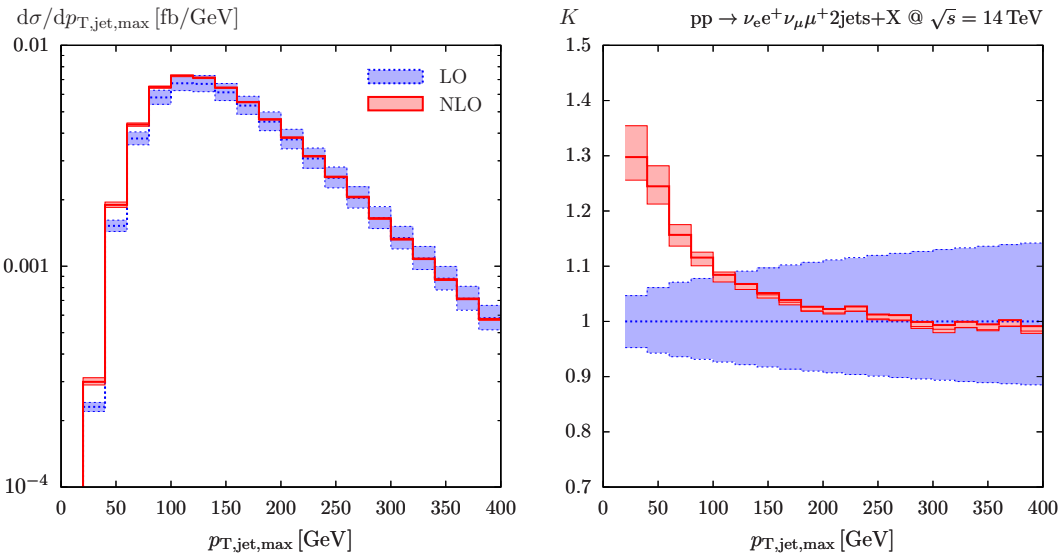


**(b)** $\mu_F = \mu_R = \sqrt{p_{T,\text{jet}_1} \cdot p_{T,\text{jet}_2}}$

**Figure 7.2:** Transverse momentum distribution of the tagging jet with the higher $p_T$ for the fixed (Figure 7.2a) and dynamic scale (Figure 7.2b) on the left and the corresponding $K$ factor represented by solid (red) line on the right.

at lower values of $p_T$ is slightly larger at NLO than at LO.

The plots on the left in Figure 7.2 show the $p_{T,\text{jet,max}}$-dependent $K(p_{T,\text{jet,max}})$ factor for the distribution, which is defined as

$$K(X) = \frac{\mathrm{d}\sigma(X)/\mathrm{d}X}{\mathrm{d}\sigma^{\text{LO}}(X)/\mathrm{d}X}, \tag{7.40}$$

where $X$ in general represents the considered kinematical observable. One can observe that $K(p_{T,\text{jet,max}})$ grows noticeably in low $p_T$ regions for both FS and DS towards the value 1.3, while in the larger $p_T$ regions it drops to 0.8 in case of FS (Figure 7.2a), and remains very close to 1 when one goes to the dynamic scale (Figure 7.2b), which is a behaviour that motivated the choice of DS in the first place.

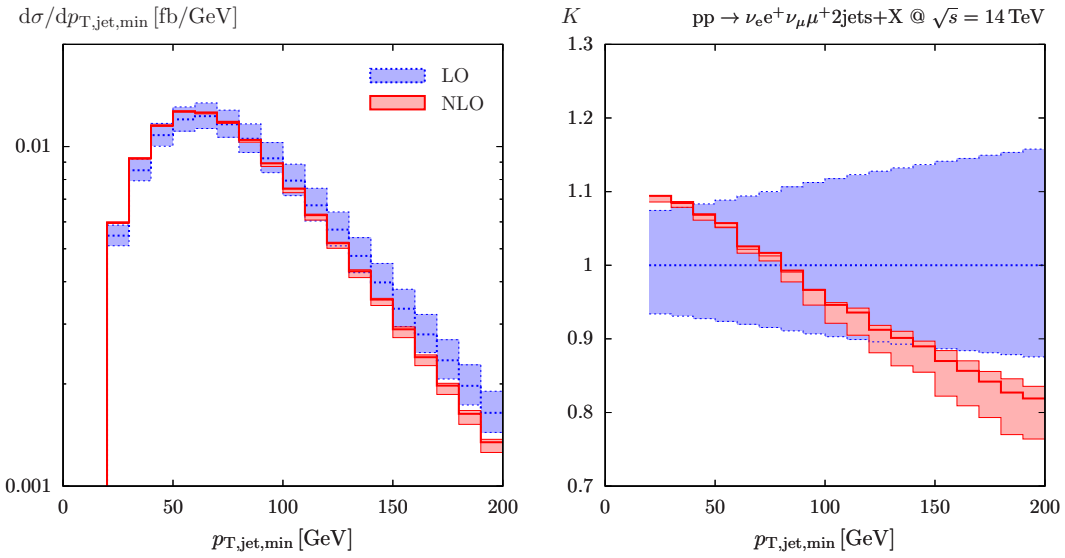


**(a)** $\mu_F = \mu_R = M_\text{W}$

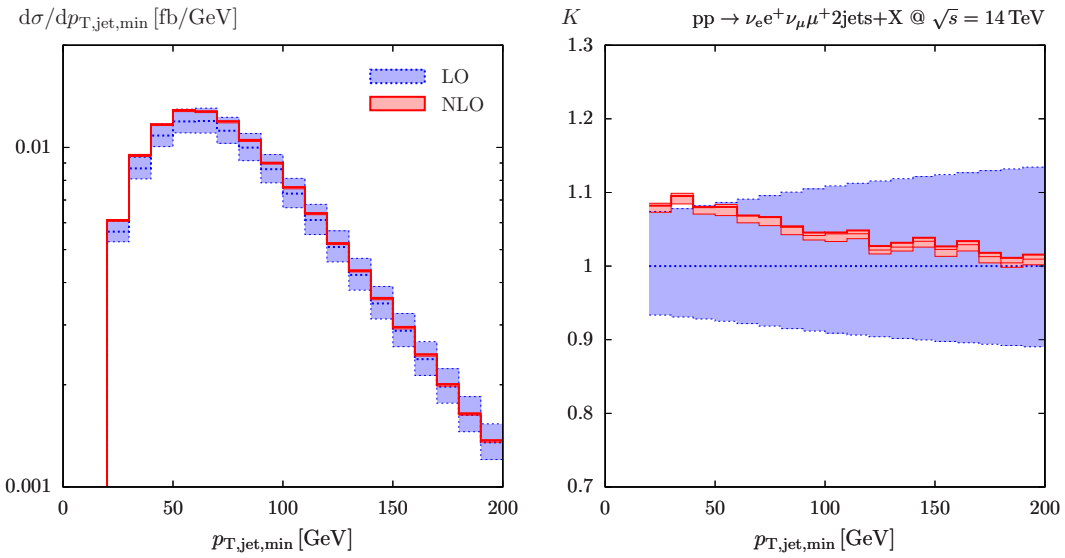


**(b)** $\mu_F = \mu_R = \sqrt{p_{T,\text{jet}_1} \cdot p_{T,\text{jet}_2}}$

**Figure 7.3:** Transverse momentum distribution of the tagging jet with the lower $p_T$ for the fixed (Figure 7.3a) and dynamic scale (Figure 7.3b) on the left and the corresponding $K$ factor represented by solid (red) line on the right.

A similar behaviour can be observed with the transverse momentum of the softer tagging jet $p_{T,\text{jet,min}}$, as shown in Figure 7.3. Here, the peak of the distribution is at $\sim 60$ GeV, indicating that the cut of 20 GeV on the tagging jets does not impose any significant reduction to the overall cross section. The variance of $K(p_{T,\text{jet,min}})$ is less pronounced as in the case of $p_{T,\text{jet,max}}$, while the choice of DS again shows an improvement at reducing contributions from higher order corrections.

Rapidity of the tagging jets is another distinguishing feature of the VBF processes, as it exhibits very little jet activity in its central region. Absolute rapidity distributions for the harder (in terms of $p_T$) and softer of the two tagging jets are shown in Figures 7.4 and 7.5, respectively. One can see that the probability to find the harder jet peaks at absolute rapidity of $\sim 2.7$ while the softer jet is most likely to be found with absolute rapidity of $\sim 3.1$. This is in sharp contrast to the rapidity behaviour for the QCD production mode for $W^+W^+$ which is characterized by a gluon exchanged between the quark legs, while the W bosons are radiated from the quarks. For the gluon-mediated process, the jet rapidity peaks at value 0, dominating the central rapidity region [32]. This process thus constitutes background which can be suppressed dramatically by imposing a cut on the separation of individual jet rapidities $\Delta y_{\text{jj}}$ (7.25).

One can see from Figures 7.4 and 7.5 that for both scale choices, the rapidity-dependent $K$ factor for the hard jet $K(|y_{\text{jet, hard}}|)$ has a tendency to grow for large values of rapidity. This might be attributed to the fact that while only two final-state partons are present at LO, in NLO the tagging jets are selected from up to three partons which might lead to greater dispersion in the rapidity distribution (see discussion in [31]). As in the case of the transverse momentum distributions, the DS shows a slight improvement over FS in variation of the $K$ factor (Figures 7.4b and 7.5b).

At hadron colliders, QCD processes typically occur at smaller invariant mass than EW processes. Due to the back-to-back geometry and large momentum of the tagging jets in VBF, the invariant mass $M_{\text{jj}}$ defined in (7.23) can easily exceed 1 TeV, which is not the case for any QCD background process, particularly if they involve gluons which prefer smaller momentum fractions than valence quarks. For this reason, invariant mass cuts are applied to distinguish these types of processes. Figure 7.6 provides a distribution for the invariant mass of the tagging jets for both FS and DS. The peak for both LO and NLO is located at approximately 1100 GeV. The behaviour of the distributions as well as the $K$ factor $K(M_{\text{jj}})$ is in good correspondence to those shown in [31], in particular for the fixed scale which is set to $M_{\text{W}}$ in both cases. While the dynamic scale in [31] is set to the momentum transfer between the incoming and outgoing parton rather than to $\sqrt{p_{T,\text{jet}_1} \cdot p_{T,\text{jet}_2}}$, it has a similar effect on the behaviour of the NLO distribution, reducing the $K$ factor and its variance.

### 7.4.4 Lepton distributions

The decay products of the intermediate gauge bosons in VBF processes can be found almost exclusively in between the tagging jets, in the central detector. To this end, jet–lepton separation cuts like $\Delta R_{lj}$ (7.28) are imposed.

The high leptonic activity in the central region can be well observed in the rapidity

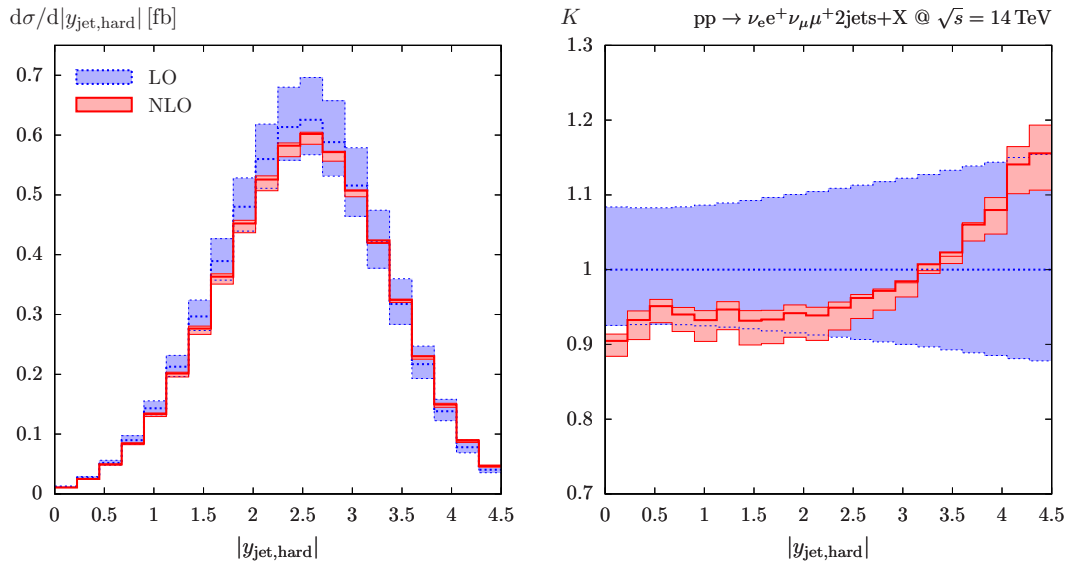


**(a)** $\mu_F = \mu_R = M_W$

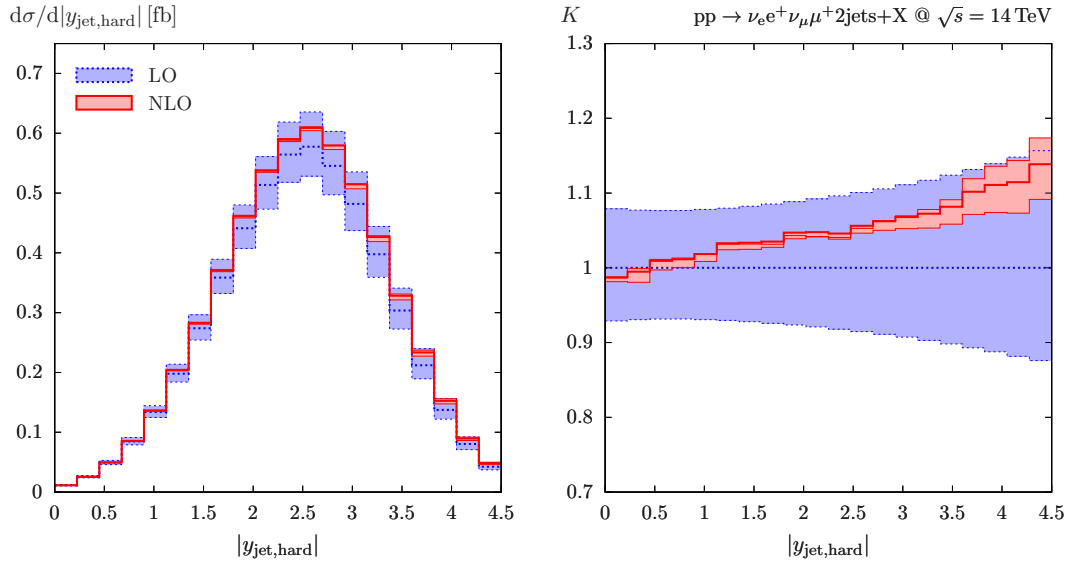


**(b)** $\mu_F = \mu_R = \sqrt{p_{T,\text{jet}_1} \cdot p_{T,\text{jet}_2}}$

**Figure 7.4:** Absolute rapidity distribution for the harder of the two tagging jets for the fixed (Figure 7.4a) and dynamic scale (Figure 7.4b) on the left and the corresponding $K$ factor represented by solid (red) line on the right.

distribution of the hardest (in $p_T$) charged lepton shown in Figure 7.7. This and all the remaining plots in this section are evaluated using the dynamic scale (7.1b). The distribution shows a very clear preference for the rapidities close to zero, while decreasing quickly as the values approach those of the tagging jets. One can also notice a small and uniform increase for the NLO cross section, with $K(y_{\text{l,hard}}) \sim 1.05$ across the entire range.

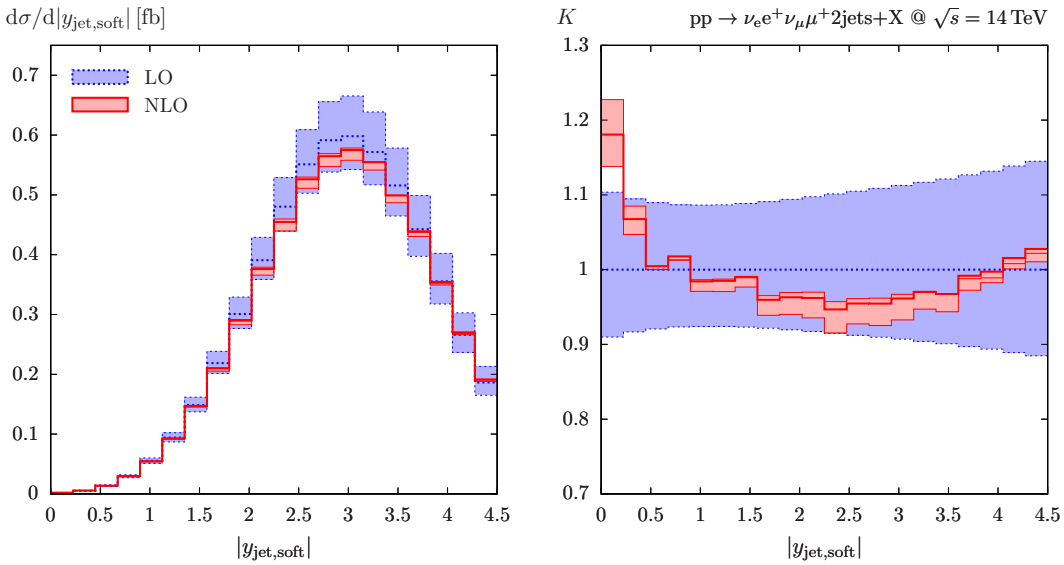


**(a)** $\mu_F = \mu_R = M_W$

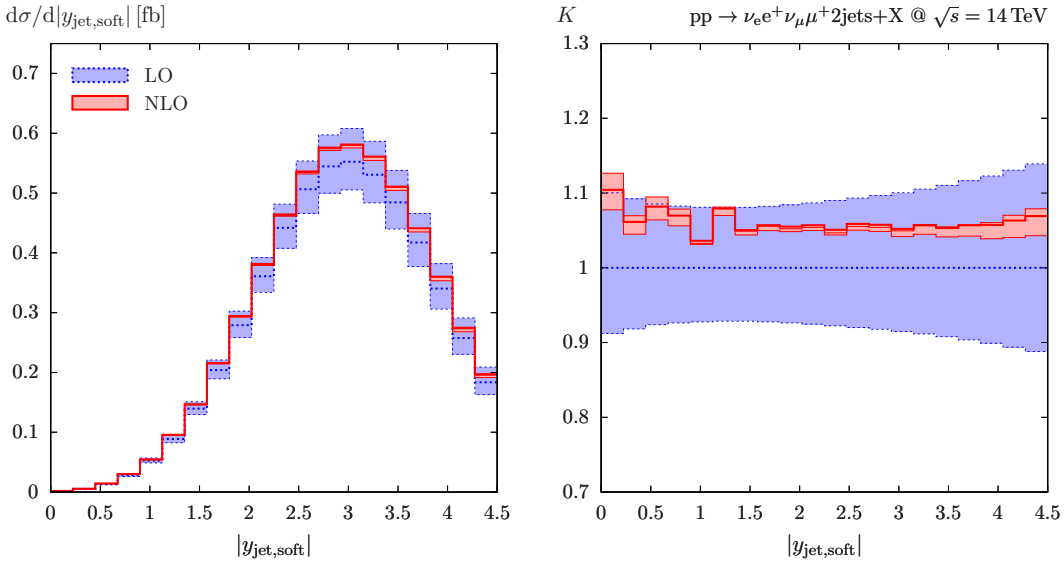


**(b)** $\mu_F = \mu_R = \sqrt{p_{T,\text{jet}_1} \cdot p_{T,\text{jet}_2}}$

**Figure 7.5:** Absolute rapidity distribution for the softer of the two tagging jets $|y_{\text{j,soft}}|$ for the fixed (Figure 7.4a) and dynamic scale (Figure 7.5b) on the left and the corresponding $K$ factor represented by solid (red) line on the right.

Figure 7.8 shows the distribution of the transverse momentum for the hardest charged lepton (Figure 7.8a) and of the missing $p_T$ corresponding to the vectorial sum of the transverse momenta of the electron neutrino and muon neutrino from the W decays (Figure 7.8b). The drop in the low-$p_T$ region in Figure 7.8a reflects the cut imposed on the transverse momentum of the charged leptons (7.26). Both distributions suggest a small enhancement of the NLO

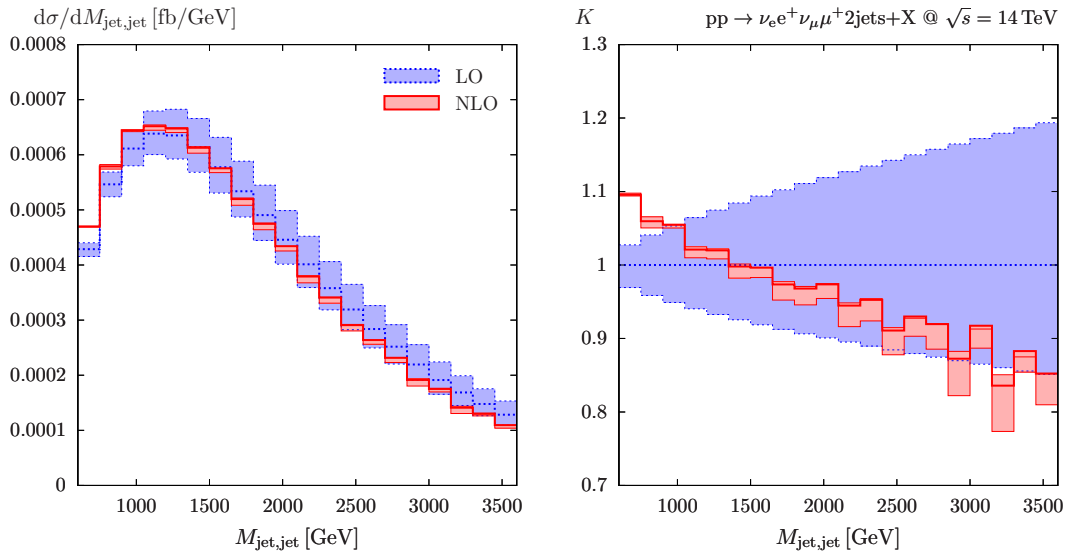


**(a)** $\mu_F = \mu_R = M_{\mathrm{W}}$

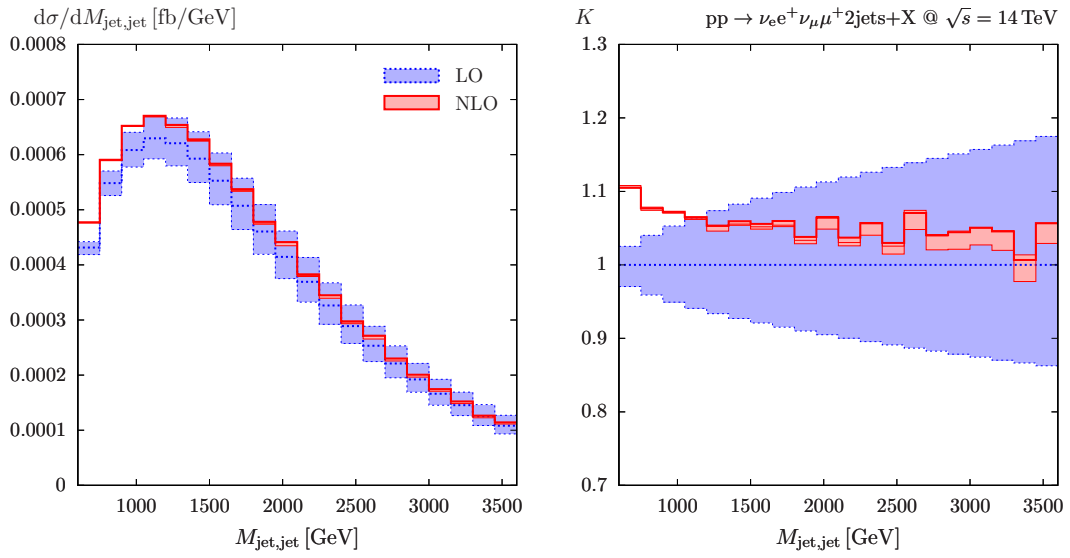


**(b)** $\mu_F = \mu_R = \sqrt{p_{T,\mathrm{jet}_1} \cdot p_{T,\mathrm{jet}_2}}$

**Figure 7.6:** Invariant mass distribution for the two tagging jets $M_{jj}$ for the fixed (Figure 7.6a) and dynamic scale (Figure 7.6b) on the left and the corresponding $K$ factor represented by solid (red) line on the right.

cross section in the low-$p_T$ region, similar to that observed in the tagging jets (Figures 7.2b and 7.3b).

The invariant mass distribution for the lepton pairs traces the relativistic Breit–Wigner distribution around the value $M_{\mathrm{W}}$, width of which is determined by $\Gamma_{\mathrm{W}}$. This is shown in Figure 7.9 which sees the cross section as a function of the invariant mass of the two lepton

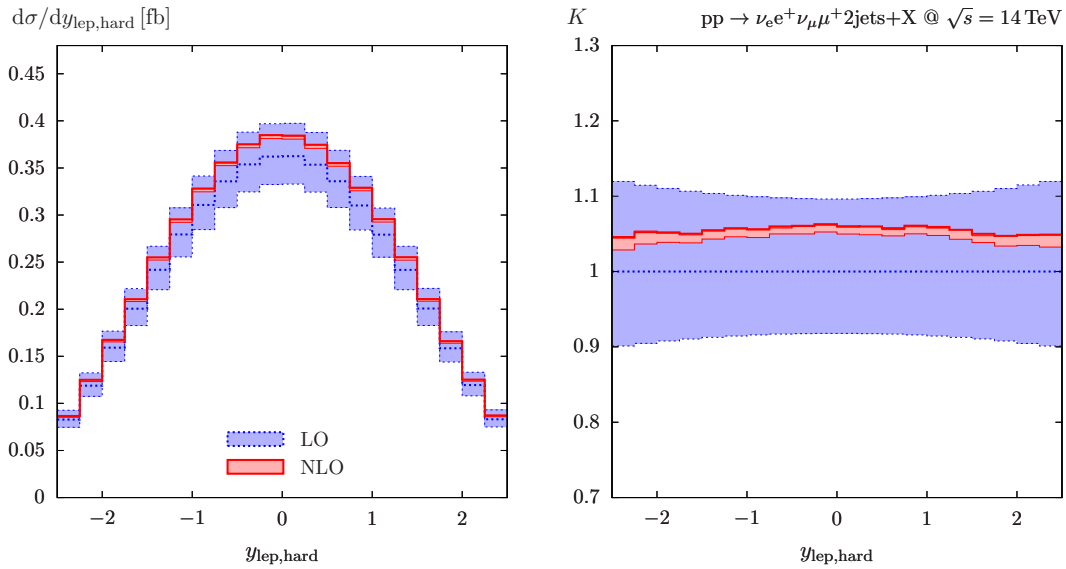


**Figure 7.7:** Rapidity distribution for the hardest charged lepton on the left and the corresponding $K$ factor represented by solid (red) line on the right.

pairs, defined according to (7.23). Figure 7.9a presents the distribution of $M_{e\nu_e}$ corresponding to $e^+\nu_e$ and Figure 7.9b shows the invariant mass $M_{\mu\nu_\mu}$ of $\mu^+\nu_\mu$. As expected, the two distributions appear to be identical, with both peaks for both lepton pairs lying at the value of $M_W$, taking into account the resolution of the bins. The central value is the same for LO and NLO distribution as the QCD corrections do not affect electroweak sector.

Angular distributions of the decay products of the VBF processes are of particular interest to the Higgs searches at colliders as the leptons have a tendency to fly in the same direction in case of a Higgs signal [84, 85]. This is not the case in the $W^+W^+$ production processes where a Higgs decay into both intermediate vector bosons in question is prohibited by the charges and the W bosons and therefore the final-state leptons are located preferentially in the opposite directions. This is demonstrated in Figure 7.10 which shows the distribution of the azimuthal angle $\phi_{ll}$ separating the charged leptons $e^+$ and $\mu^+$ in the plane transverse to the beam direction, which is a quantity invariant to boosts along the beam axis. Similarly as with other leptonic observables, the NLO corrections have only a modest effect in this distribution, as exhibited by a constant $K$ factor $\sim 1.05$.

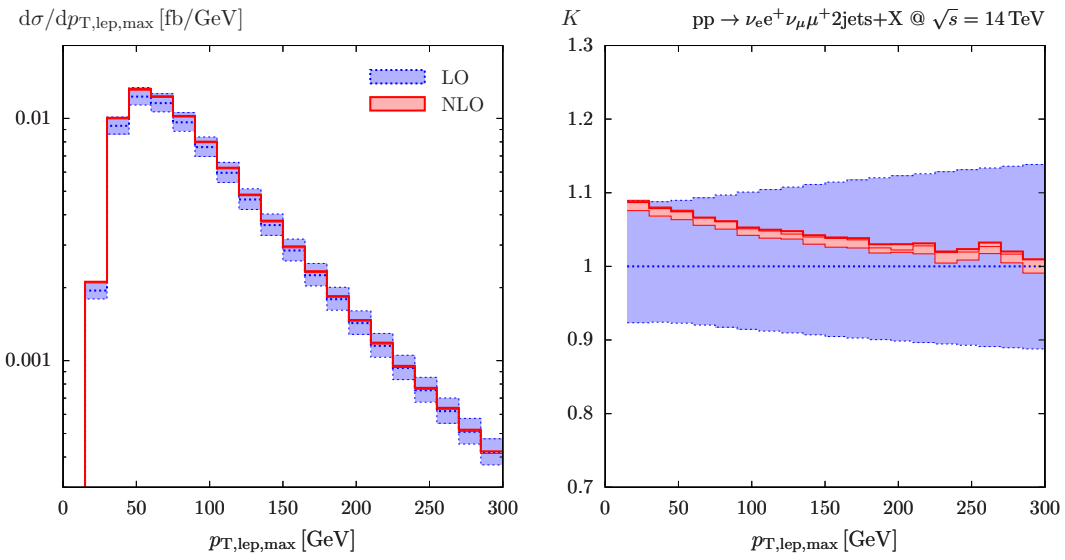


**(a)**

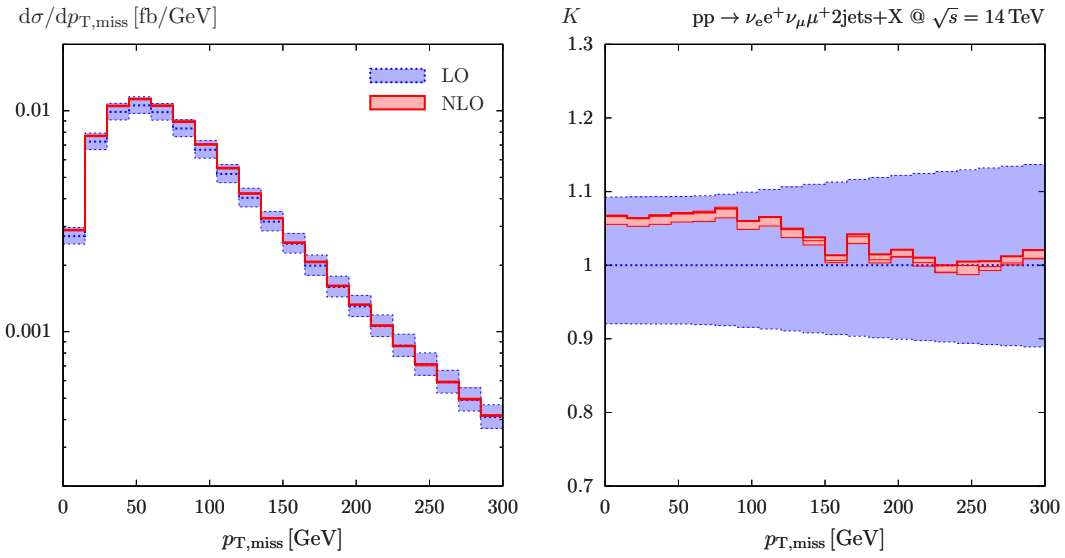


**(b)**

**Figure 7.8:** Distribution of the transverse momentum of the hardest charged lepton (Figure 7.8a) and the missing transverse momentum produced by two outgoing neutrinos (Figure 7.8b) on the left and the corresponding $K$ factor represented by solid (red) line on the right.

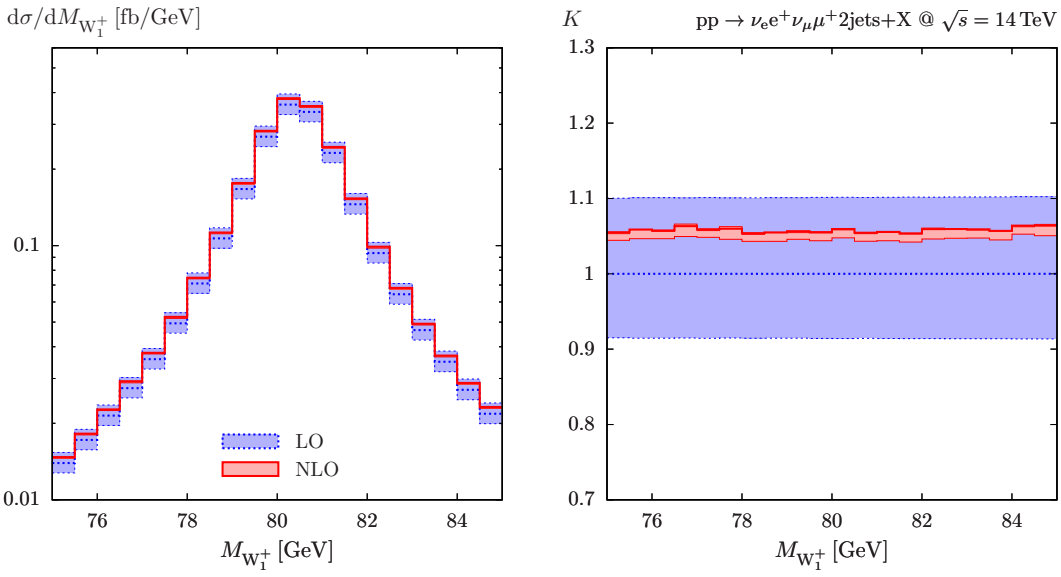


**(a)**

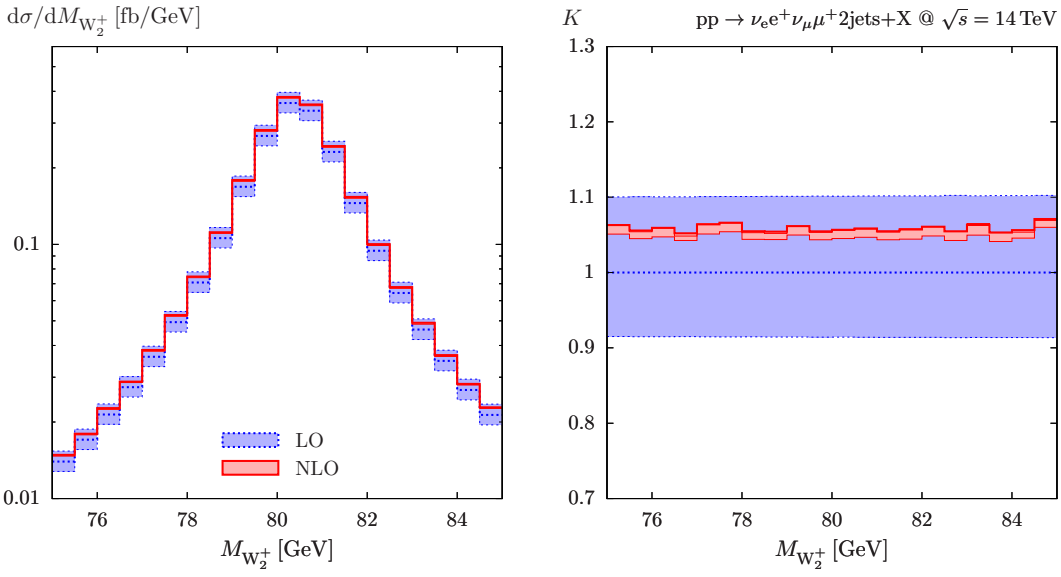


**(b)**

**Figure 7.9:** Invariant mass distribution for the first ($e^+\nu_e$ - Figure 7.9a) and second ($\mu^+\nu_\mu$ - Figure 7.9b) lepton pair on the left and the corresponding $K$ factor represented by solid (red) line on the right.

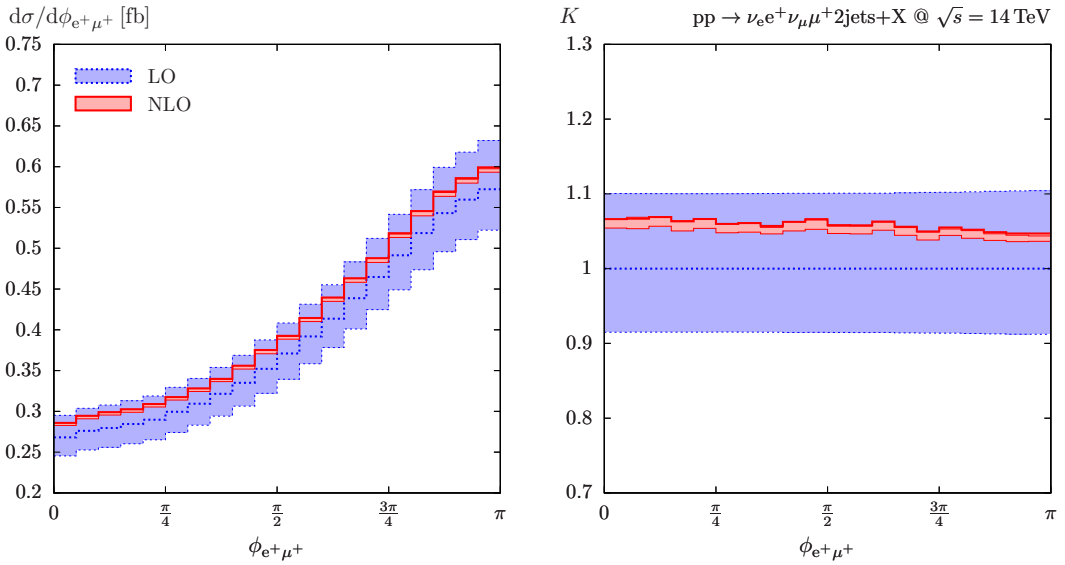


**Figure 7.10:** Distribution of the azimuthal angle between the charged leptons $e^+$ and $\mu^+$ on the left and the corresponding $K$ factor represented by solid (red) line on the right.

Chapter 8

# Summary and outlook

This thesis presents a method for evaluating the NLO QCD corrections to the electroweak production mode of the process class pp $\to$ jj4l at order $\alpha_{\text{EW}}^6 \alpha_S$, including both resonant contributions where the final-state leptons are produced via gauge boson decay as well as non-resonant ones. The Feynman diagrams are divided into independent building blocks using polarization sums and evaluated with the FeynArts + FormCalc package in Mathematica using the Weyl van der Waerden helicity formalism and subsequently exported into Fortran modules. The block structure separates the electroweak and QCD sectors of the diagrams, allowing one to apply the QCD corrections only to building blocks involving quark lines while electroweak building blocks are evaluated merely at tree level. This improves both effectiveness and speed of the Fortran code. Tensor reduction and evaluation of the scalar integrals in the virtual corrections is performed by the Coli package in Fortran. The IR divergencies appearing in both virtual and real corrections are controlled by using the Catani Seymour dipole subtraction formalism which introduces subtraction terms that cancel the corresponding singular expressions.

The phase-space integration is carried out by a multichannel Monte Carlo generator implemented in C++ that supports weight optimization and automatic evaluation of the process-independent subtraction terms originating in the dipole subtraction formalism. Moreover, additional channels adapted to the peak structure of the dipole terms are included in order to improve performance of the integration. The generator allows for an implementation of experimental cuts which are chosen to enhance contributions of the vector-boson-fusion kinematics and suppress QCD background.

Results are presented for the process pp $\to$ jje$^+\nu_{\text{e}}\mu^+\nu_\mu$ associated with VBF production of an intermediate $\text{W}^+\text{W}^+$ pair. The impact of the $s$-channel diagrams and interferences between $t-$ and $u-$ channels, which were neglected in the NLO calculation, is analyzed at the leading order and found to be entirely negligible when using the choice of cuts selected to enhance the gauge boson fusion kinematics. The NLO corrections were found to be around 5% of the leading order cross section. The remaining uncertainties of the higher perturbative orders can be estimated by varying the renormalization and factorization scale of the NLO cross section. The scale dependence of the cross section at NLO is suppressed, amounting to about 2% for the fixed scale $\mu = \xi M_{\text{W}}$ as well as for the dynamical scale $\mu = \xi \sqrt{p_{T,\text{jet}_1} \cdot p_{T,\text{jet}_2}}$, when varying $\xi$ from 1/2 to 2, while the LO results change significantly,

by up to 20%. Furthermore, a set of kinematical distributions for jets and final-state leptons has been presented, demonstrating the effects of the NLO corrections and impact of the two scale choices.

Although a complete calculation of all four possible VBF processes is not performed in this thesis, all building blocks and polarization sums as well as the methodology necessary to construct corresponding amplitudes are provided. Further phenomenological studies of the remaining gauge-boson-production modes are in progress.

Appendix A

# Overview of the Weyl van der Waerden formalism

This section provides a short introduction into Weyl van der Waerden (WvdW) formalism which has been used to evaluate all matrix elements in this work.

First, let us consider the two fundamental irreducible representations of the Lorentz group $(1/2, 0)$ and $(0, 1/2)$. They are non-equivalent, which means that we have to distinguish between two types of WvdW spinors - covariant and contravariant. For this reason, covariant spinors are usually written with an undotted lower index ($\psi_A$) and contravariant spinors with a dotted upper index ($\psi^{\dot{A}}$). One can convert one type of spinor into the other using complex conjugation

$$\psi_{\dot{A}} = (\psi_A)^* \qquad \psi^A = (\psi^{\dot{A}})^* \tag{A.1}$$

and contraction with an antisymmetric $2 \times 2$ matrix $\varepsilon = i\sigma^2$, where $\sigma^2$ is the second of the three Pauli matrices (see e.g. [35]).

$$\varepsilon^{AB} = \varepsilon^{\dot{A}\dot{B}} = \varepsilon_{AB} = \varepsilon_{\dot{A}\dot{B}} = \begin{pmatrix} 0 & +1 \\ -1 & 0 \end{pmatrix} \tag{A.2}$$

Both dotted and undotted indices can then be raised and lowered in the following way

$$\psi^A = \varepsilon^{AB}\psi_B \qquad \psi^{\dot{A}} = \varepsilon^{\dot{A}\dot{B}}\psi_{\dot{B}} \qquad \psi_A = \psi^{\mathrm{B}}\varepsilon_{BA} \qquad \psi_{\dot{A}} = \psi^{\dot{B}}\varepsilon_{\dot{B}\dot{A}} \tag{A.3}$$

The quadratic forms

$$\langle\phi\psi\rangle = \phi_A\psi^A = \phi_1\psi_2 - \phi_2\psi_1 \qquad [\phi\psi] = \phi_{\dot{A}}\psi^{\dot{A}} = (\phi_1\psi_2 - \phi_2\psi_1)^* \tag{A.4}$$

are invariant under transformations of $SL(2, C)$. They also define a convention to sum from lower left to the upper right, while the other direction would result in a relative minus sign.

Minkowski 4-vectors belong to the $(1/2, 1/2)$ representation of the Lorentz group. Transition from the usual form of a 4-vector $k^\mu = (k^0, k^1, k^2, k^3)$ to the formalism that uses dotted and undotted indices can be achieved by contracting the 4-vector with the Pauli matrix:

$$K_{\dot{A}B} = k^\mu \sigma_{\mu,\dot{A}B} = \begin{pmatrix} k^0 + k^3 & k^1 + \mathrm{i}k^2 \\ k^1 - \mathrm{i}k^2 & k^0 - k^3 \end{pmatrix}. \tag{A.5}$$

Indices of the Pauli matrices can be raised and lowered in an analogous way, by contracting with two antisymmetric tensors

$$\sigma^{\mu}_{\dot{A}B} = \sigma^{\mu,\dot{C}D}\varepsilon_{\dot{C}\dot{A}}\varepsilon_{DB} \qquad \Rightarrow \qquad K^{\mu}_{\dot{A}B} = K^{\mu,\dot{C}D}\varepsilon_{\dot{C}\dot{A}}\varepsilon_{DB}. \tag{A.6}$$

Simple identities satisfied by $\sigma$ matrices lead us to relations between the Minkowski inner product of two 4-vectors and their equivalents in the spinor representation

$$2k \cdot p = 2k_{\mu}g^{\mu\nu}p_{\nu} = k_{\mu}\sigma^{\mu}_{\dot{A}B}\sigma^{\nu,\dot{A}B}p_{\nu} = K_{\dot{A}B}P^{\dot{A}B} \tag{A.7}$$

Since our objective is to reduce the kinematic expressions appearing in the amplitudes into scalar products involving WvdW spinors, we need to find a way to express $K_{\dot{A}B}$ in terms of spinors as well. Since the Pauli matrices are Hermitian, $K_{\dot{A}B}$ are Hermitian as long as the components of the 4-vector $k^{\mu}$ are real. As such, we can decompose it into its eigenvectors $n_{i,A}$ $(i = 1, 2)$ and eigenvalues $\lambda_i$.

$$\lambda_{1,2} = k^0 \pm |\mathbf{k}| \tag{A.8}$$

$$n_{1,A} = \begin{pmatrix} e^{-i\phi}\cos\frac{\theta}{2} \\ \sin\frac{\theta}{2} \end{pmatrix} \qquad n_{2,A} = \begin{pmatrix} \sin\frac{\theta}{2} \\ -e^{+i\phi}\cos\frac{\theta}{2} \end{pmatrix}, \tag{A.9}$$

where $\phi$ and $\theta$ represent the polar and azimuthal angles of the 4-momentum

$$k^{\mu} = (k^0, |\mathbf{k}|\sin\theta\cos\phi, |\mathbf{k}|\sin\theta\sin\phi, |\mathbf{k}|\cos\theta). \tag{A.10}$$

For future reference, it is useful to write the eigenvectors (A.9) in terms of 4-momentum components $k^{\mu} = \{k^0, k^x, k^y, k^z\}$. From the definition of the polar angle $\phi$ it is easy to see that

$$e^{-i\phi} = \frac{k^x - ik^y}{\sqrt{(k^x)^2 + (k^y)^2}} \qquad e^{+i\phi} = \frac{k^x + ik^y}{\sqrt{(k^x)^2 + (k^y)^2}}. \tag{A.11}$$

Similarly, from the definition of the azimuthal angle $\theta$ we get

$$\cos\frac{\theta}{2} = \sqrt{\frac{1}{2}(1 + \frac{k^z}{k})} \qquad \sin\frac{\theta}{2} = \sqrt{\frac{1}{2}(1 - \frac{k^z}{k})}, \tag{A.12}$$

where $k = \sqrt{(k^x)^2 + (k^y)^2 + (k^z)^2}$. In this convention, special care needs to be taken if $k^x = 0,\ k^y = 0$ (particle is moving along the $z-$axis) in which case $\phi$ is set to an arbitrary value.

The decomposition of $K_{\dot{A}B}$ into eigenvectors (A.9) takes the form

$$K_{\dot{A}B} = \sum_{i=1,2} \lambda_i n_{i,\dot{A}} n_{i,B} \tag{A.13}$$

or, for $k^2 > 0$

$$K_{\dot{A}B} = \sum_{i=1,2} \kappa_{i,\dot{A}}\kappa_{i,B}, \quad \kappa_{i,A} = \sqrt{\lambda_i}n_{i,A}. \tag{A.14}$$

One can verify that the choice of $n_{i,A}$ in (A.9) insures that the scalar products are conveniently orthonormal and antisymmetric

$$\langle n_i n_i \rangle = 0, \qquad \langle n_2 n_1 \rangle = -\langle n_1 n_2 \rangle = 1. \tag{A.15}$$

The particles we are dealing with in our calculation are massless fermions with spin $1/2$ (e.g. quarks and leptons), massive spin-1 particles (W and Z bosons and off-shell photons) and massless spin-1 particles (gluons). Let us have a look at how each of these three cases are described in the WvdW formalism. Representation of Dirac spinors $\Psi$ in terms of WvdW spinors is very straightforward:

$$\Psi = \begin{pmatrix} \phi_A \\ \psi^{\dot{A}} \end{pmatrix}. \tag{A.16}$$

Massless fermions only satisfy the massless modification of the Dirac equation

$$i\gamma_\mu \partial^\mu \Psi = 0 \tag{A.17}$$

Moreover, if $k^2 = 0$, the second eigenvalue $\lambda_2$ from (A.8) vanishes, and the matrix $K_{\dot{A}B}$ becomes effectively a simple product of two spinors

$$K_{\dot{A}B} = k_{\dot{A}} k_B, \qquad k_A = \sqrt{2k^0} n_{1,A}. \tag{A.18}$$

After inserting $(A.16)$ and (A.18), the solution decouples into

$$K_{A\dot{B}} \psi_k^{(\pm),\dot{B}} = 0, \qquad K^{\dot{A}B} \phi_{k,B}^{(\pm)} = 0. \tag{A.19}$$

The list of wave functions $\Psi_\sigma^{(\pm)}(k)$ satisfying these relations can be found in Table A.1.

Relations (A.4) and (A.9) in the massless case lead to the following expression for the scalar product of spinors $k_A$ and $p_A$ associated with the light-like momenta according to (A.10)

$$\langle kp \rangle = \varepsilon^{AB} k_A p_B = 2\sqrt{k_0 p_{\,0}} \left[ \mathrm{e}^{-\mathrm{i}\phi_k} \cos\frac{\theta_k}{2} \sin\frac{\theta_p}{2} - \mathrm{e}^{-\mathrm{i}\phi_p} \cos\frac{\theta_p}{2} \sin\frac{\theta_k}{2} \right]. \tag{A.20}$$

Fields with spin 1 are represented by polarization vectors $\varepsilon^\mu$ which transform into WvdW formalism in the same way as ordinary 4-vectors under Lorentz transformation. To obtain their equivalent in the WvdW formalism, we contract them with the Pauli matrices according to (A.5).

For a massive spin-1 particle with the helicity basis $\varepsilon_i^\mu(k)$ chosen as

$$\begin{aligned} \varepsilon_\pm^\mu(k) &= \frac{e^{\mp i\psi}}{\sqrt{2}} (0, -\cos\theta\cos\psi \pm i\sin\phi, -\cos\theta\sin\phi \mp i\cos\phi, \sin\theta), \\ \varepsilon_0^\mu(k) &= \frac{k^0}{m} \left( \frac{|\mathbf{k}|}{k^0}, \cos\phi\sin\theta, \sin\phi\sin\theta, \cos\theta \right) \end{aligned} \tag{A.21}$$

| Incoming fermions | Outgoing fermions |
|---|---|
| $\Psi_R^+(k) = \begin{pmatrix} k_A \\ 0 \end{pmatrix}$ | $\bar{\Psi}_R^+(k) = \begin{pmatrix} 0, & k_{\dot{A}} \end{pmatrix}$ |
| $\Psi_L^+(k) = \begin{pmatrix} 0 \\ k^{\dot{A}} \end{pmatrix}$ | $\bar{\Psi}_L^+(k) = \begin{pmatrix} k^A, & 0 \end{pmatrix}$ |
| **Incoming antifermions** | **Outgoing antifermions** |
| $\Psi_L^-(k') = \begin{pmatrix} k'^A, & 0 \end{pmatrix}$ | $\bar{\Psi}_L^-(k') = \begin{pmatrix} 0 \\ k'^{\dot{A}} \end{pmatrix}$ |
| $\Psi_R^-(k') = \begin{pmatrix} 0, & k'_{\dot{A}} \end{pmatrix}$ | $\bar{\Psi}_R^-(k') = \begin{pmatrix} k'_A \\ 0 \end{pmatrix}$ |

**Table A.1:** Weyl van der Waerden spinors representing massless right-handed $\sigma = R$ and left-handed $\sigma = L$ fermions and antifermions

we obtain

$$\begin{aligned} \varepsilon_{+,\,\dot{A}B}(k) &= \sqrt{2} n_{2,\dot{A}} n_{1,B}, \\ \varepsilon_{-,\,\dot{A}B}(k) &= \sqrt{2} n_{1,\dot{A}} n_{2,B}, \\ \varepsilon_{0,\,\dot{A}B}(k) &= \frac{1}{m}(\kappa_{1,\dot{A}}\kappa_{1,B} - \kappa_{2,\dot{A}}\kappa_{2,B}), \end{aligned} \tag{A.22}$$

where $n_{i,A}$ and $\kappa_{i,A}$ are defined in (A.9) and (A.14), respectively.

In order to obtain matrices $\varepsilon^*_{i,\dot{A}B}$ corresponding to the outgoing spin-1 particles, it is not enough to take complex conjugate of $\varepsilon_{i,\dot{A}B}$, but one has to perform contraction of $\varepsilon_i^{*\mu}$ from (A.21) with $\sigma$ matrices, which does not necessarily lead to the same result as both objects are complex. Once we have done this, we get the following matrices:

$$\begin{aligned} \varepsilon^*_{+,\,\dot{A}B}(k) &= \sqrt{2} n_{1,\dot{A}} n_{2,B}, \\ \varepsilon^*_{-,\,\dot{A}B}(k) &= \sqrt{2} n_{2,\dot{A}} n_{1,B}, \\ \varepsilon^*_{0,\,\dot{A}B}(k) &= \frac{1}{m}(\kappa_{1,\dot{A}}\kappa_{1,B} - \kappa_{2,\dot{A}}\kappa_{2,B}). \end{aligned} \tag{A.23}$$

In case of a massless spin-1 field, the longitudinal polarization $\varepsilon_0^\mu$ from (A.21) does not correspond to a physical state. This fact is reflected by arbitrariness of gauge of the two other polarization vectors, $\varepsilon_+^\mu$ and $\varepsilon_-^\mu$. In WvdW formalism, this freedom manifests itself in form of

so-called gauge spinors $g_{\pm}^{A}$, leading to the following expressions for matrices $\varepsilon_{\pm,A}$:

$$\varepsilon_{+,\,\dot{A}B}(k) = \frac{\sqrt{2}g_{+,\dot{A}}k_B}{\langle g_+ k\rangle^*}, \qquad \varepsilon^*_{+,\dot{A}B}(k) = \frac{\sqrt{2}k_{\dot{A}}g_{+,B}}{\langle g_+ k\rangle},$$
$$\varepsilon_{-,\,\dot{A}B}(k) = \frac{\sqrt{2}k_{\dot{A}}g_{-,B}}{\langle g_- k\rangle}, \qquad \varepsilon^*_{-,\dot{A}B}(k) = \frac{\sqrt{2}g_{-,\dot{A}}k_B}{\langle g_- k\rangle^*}. \tag{A.24}$$

Spinors $g_{\pm,A}$ are arbitrary with $\langle g_\pm k\rangle \neq 0$. In analytical calculation, the freedom of choice when selecting $g_{\pm,A}$ can help simplify algebraic expressions.

Appendix B

# List of polarization sums

In this section, we present a list of all polarization sums that are necessary to construct the processes discussed in Chapter 3. They rely on the notation for the building blocks introduced in Section 4.3, which leads to evaluation of $t$-channel Born diagrams. The procedure for obtaining other channels as well as diagrams involving antiquarks is outlined in Section 5.5. With only few small modifications, these sums lend themselves to be used to calculate both virtual and real QCD corrections to the Born level, as illustrated in Chapter 6.

Note that for the sake of clarity, the notation used in the following lists is purely symbolic, as the symbol $\sum$ represents the entire polarization sum

$$\sum_i \mathcal{M}_1(i)\mathcal{M}_2(i) := -\sum_{i=\{+,-,0\}} [\mathcal{M}_1(i)\mathcal{M}_2(i)] + \frac{\mathcal{M}_1(i=\text{"}q\text{"})\mathcal{M}_2(i=\text{"}q\text{"})}{q^2}, \qquad \text{(B.1)}$$

where $q$ is momentum of the intermediate vector boson propagator which has been cut.

Since the diagrams containing the electrically neutral vector bosons Z and $\gamma$ have an identical structure from the perspective of polarization sums, the following lists contain only one representative where all neutral vector bosons have been replaced by $X$, $Y$ or $V$. For instance, in Table B.5, the polarization sum

$$\sum_i \sum_j (uuX_1(i), XYe\nu e\nu(i,j), ddY2(j)$$

stands for

$$\sum_i \sum_j (uuG_1(i), GGe\nu e\nu(i,j), ddG2(j)$$
$$\sum_i \sum_j (uuG_1(i), GZe\nu e\nu(i,j), ddZ2(j)$$
$$\sum_i \sum_j (uuZ_1(i), ZZe\nu e\nu(i,j), ddZ2(j).$$

| Diagram | Polarization sum |
|---|---|
| | $\sum_i \sum_j \sum_k We^+\nu_{78}(i)udXW_{782}(j,i)XWe^+\nu_{561}(k,j)udW_2(k)$ |
| 5.1a | $\sum_i \sum_j \sum_k We^+\nu_{56}(i)udXW_{562}(j,i)XWe^+\nu_{781}(k,j)udW_2(k)$ |
| | $\sum_i \sum_j \sum_k udW_1(i)WXe^+\nu_{562}(i,j)udXW_{784}(j,k)We^+\nu_{78}(k)$ |
| 5.1b | $\sum_i \sum_j \sum_k udW_1(i)WXe^+\nu_{782}(i,j)udXW_{564}(j,k)We^+\nu_{56}(k)$ |
| | $\sum_i \sum_j \sum_k We^+\nu_{78}(i)udWX_{781}(i,j)XWe^+\nu_{561}(k,j)udW_2(k)$ |
| 5.1c | $\sum_i \sum_j \sum_k We^+\nu_{56}(i)udWX_{561}(i,j)XWe^+\nu_{781}(k,j)udW_2(k)$ |
| | $\sum_i \sum_j \sum_k udW_1(i)WXe^+\nu_{562}(i,j)udWX_{783}(k,j)We^+\nu_{78}(k)$ |
| 5.1d | $\sum_i \sum_j \sum_k udW_1(i)WXe^+\nu_{782}(i,j)udWX_{563}(k,j)We^+\nu_{56}(k)$ |
| 5.2 | $\sum_i \sum_j udW_1(i)WWe^+\nu\mu^+\nu(i,j)udW_2(j)$ |
| | $\sum_i \sum_j \sum_k udWWW_{562478}(i,j,k)We^+\nu_{56}(i)Wud_{24}(j)We^+\nu_{78}(k)$ |
| 5.3a | $\sum_i \sum_j \sum_k udWWW_{782456}(i,j,k)We^+\nu_{78}(i)Wud_{24}(j)We^+\nu_{56}(k)$ |
| | $\sum_i \sum_j \sum_k udWWW_{561378}(i,j,k)We^+\nu_{56}(i)Wud_{13}(j)We^+\nu_{78}(k)$ |
| 5.3b | $\sum_i \sum_j \sum_k udWWW_{781356}(i,j,k)We^+\nu_{78}(i)Wud_{13}(j)We^+\nu_{56}(k)$ |
| | $\sum_i \sum_j \sum_k We^+\nu_{56}(i)udXW_{562}(j,i)X1udW_{2478}(j,k)We^+\nu_{78(k)}$ |
| 5.3c | $\sum_i \sum_j \sum_k We^+\nu_{78}(i)udXW_{782}(j,i)X1udW_{2456}(j,k)We^+\nu_{56(k)}$ |
| | $\sum_i \sum_j \sum_k We^+\nu_{56}(i)udWX_{561}(i,j)X2udW_{2478}(j,k)We^+\nu_{78(k)}$ |
| 5.3d | $\sum_i \sum_j \sum_k We^+\nu_{78}(i)udWX_{781}(i,j)X2udW_{2456}(j,k)We^+\nu_{56(k)}$ |
| | $\sum_i \sum_j \sum_k We^+\nu_{56}(i)udXW_{562}(j,i)X2udW_{2478}(j,k)We^+\nu_{78(k)}$ |
| 5.3e | $\sum_i \sum_j \sum_k We^+\nu_{78}(i)udXW_{782}(j,i)X2udW_{2456}(j,k)We^+\nu_{56(k)}$ |
| | $\sum_i \sum_j \sum_k We^+\nu_{56}(i)udWX_{561}(i,j)X1udW_{2478}(j,k)We^+\nu_{78(k)}$ |
| 5.3f | $\sum_i \sum_j \sum_k We^+\nu_{78}(i)udWX_{781}(i,j)X1udW_{2456}(j,k)We^+\nu_{56(k)}$ |

**Table B.1:** List of polarization sums corresponding to diagrams in Figures 5.1–5.3 for the subprocess uc $\to$ dse$^+\nu_e\mu^+\nu_\mu$.

| Diagram | Polarization sum |
|---|---|
| 5.4a | $\sum_i \sum_j (Xuu_{24}(i), udXW_2(i,j), We^+\nu ee(j)$ |
| 5.4b | $\sum_i \sum_j (We^+\nu ee(i), udWX(i,j), Xuu_{24}(j)$ |
| 5.4c | $\sum_i \sum_j (We^+\nu ee(i), uuWW_3(i,j), Wud_{13}(j)$ |
| 5.5a | $\sum_i \sum_j \sum_k (udW_1(i), WXe^+\nu_{562}(i,j), uuXY_{783}(k,j), Yee_{78}(k)$ |
| | $\sum_i \sum_j \sum_k (udW_1(i), WXe^+\nu_{562}(i,j), uuXY_{784}(j,k), Yee_{78}(k)$ |
| | $\sum_i \sum_j \sum_k (Xee_{78}(i), udXW_{781}(i,j), WYe^+\nu_{561}(j,k), uuY_2(k)$ |
| | $\sum_i \sum_j \sum_k (Xee_{78}(i), udWX_{782}(j,i), WYe^+\nu_{561}(j,k), uuY_2(k)$ |
| 5.5b | $\sum_i \sum_j \sum_k (We^+\nu_{56}(i), udWX_{561}(i,j), XYee_{781}(j,k), uuY_2(k)$ |
| | $\sum_i \sum_j \sum_k (We^+\nu_{56}(i), udXW_{562}(j,i), XYee_{781}(j,k), uuY_2(k)$ |
| 5.5c | $\sum_i \sum_j \sum_k (udW_1(i), WWee_{782}(i,j), uuWW_{563}(k,j), We^+\nu_{56}(k)$ |
| 5.6 | $\sum_i \sum_j (udW_1(i), WXe^+\nu ee(i,j), uuX2(j)$ |
| 5.7a | $\sum_i \sum_j \sum_k (We^+\nu_{56}(i), udWX_{561}(i,j), X2uuY_{2478}(j,k), Yee_{78}(k)$ |
| | $\sum_i \sum_j \sum_k (We^+\nu_{56}(i), udWX_{561}(i,j), X1uuY_{2478}(j,k), Yee_{78}(k)$ |
| | $\sum_i \sum_j \sum_k (udWXY_{562478}(i,j,k), We^+\nu_{56}(k), Xuu_{24}(j), Yee_{78}(i)$ |
| | $\sum_i \sum_j \sum_k (udXWY_{785624}(i,j,k), Xee_{78}(k), We^+\nu_{56}(j), Yuu_{24}(i)$ |
| | $\sum_i \sum_j \sum_k (udWXY_{567824}(i,j,k), We^+\nu_{56}(k), Xee_{78}(j), Yuu_{24}(i)$ |
| 5.7c | $\sum_i \sum_j \sum_k (Xee_{78}(i), udXW_{781}(i,j), W2uuW_{2456}(j,k), We^+\nu_{56}(k)$ |
| | $\sum_i \sum_j \sum_k (Xee_{78}(i), udWX_{782}(j,i), W2uuW_{2456}(j,k), We^+\nu_{56}(k)$ |
| | $\sum_i \sum_j \sum_k (uuWWX_{561378}(i,j,k), We^+\nu_{56}(k), Wud_{13}(j), Xee_{78}(i)$ |
| | $\sum_i \sum_j \sum_k (uuXWW_{785613}(i,j,k), Xee_{78}(k), We^+\nu_{56}(j), Wud_{13}(i)$ |
| | $\sum_i \sum_j \sum_k (uuWXW_{567813}(i,j,k), We^+\nu_{56}(k), Xee_{78}(j), Wud_{13}(i)$ |
| 5.7b | $\sum_i \sum_j \sum_k (We^+\nu_{56}(i), udXW_{562}(j,i), X1uuY_{2478}(j,k), Yee_{78}(k)$ |
| | $\sum_i \sum_j \sum_k (We^+\nu_{56}(i), udXW_{562}(j,i), X2uuY_{2478}(j,k), Yee_{78}(k)$ |
| | $\sum_i \sum_j \sum_k (udXYW_{247856}(i,j,k), Xuu_{24}(i), Yee_{78}(j), We^+\nu_{56}(k)$ |
| | $\sum_i \sum_j \sum_k (udXWY_{245678}(i,j,k), Xuu_{24}(i), We^+\nu_{56}(j), Yee_{78}(k)$ |
| | $\sum_i \sum_j \sum_k (udXYW_{782456}(i,j,k), Xee_{78}(i), Yuu_{24}(j), We^+\nu_{56}(k)$ |

**Table B.2:** List of polarization sums corresponding to diagrams in Figures 5.4–5.7 for the subprocess uc $\to$ dce$^+\nu_e\mu^+\mu^-$.

| Diagram | Polarization sum |
|---|---|
| 5.4a | $\sum_i \sum_j (Xdd_{24}(i), udXW_2(i,j), We^+\nu ee(j)$ |
| 5.4b | $\sum_i \sum_j (We^+\nu ee(i), udWX_1(i,j), Xdd_{24}(j)$ |
| 5.4d | $\sum_i \sum_j (Wud_{13}(i), ddWW_4(i,j), We^+\nu ee(j)$ |
| 5.5a | $\sum_i \sum_j \sum_k (udW_1(i), WXe^+\nu_{562}(i,j), ddYX_{783}(k,j), Yee_{78}(k)$ |
| | $\sum_i \sum_j \sum_k (udW_1(i), WXe^+\nu_{562}(i,j), ddXY_{784}(j,k), Yee_{78}(k)$ |
| | $\sum_i \sum_j \sum_k (Xee_{78}(i), udXW_{781}(i,j), WYe^+\nu_{561}(j,k), ddY_2(k)$ |
| | $\sum_i \sum_j \sum_k (Xee_{78}(i), udWX_{782}(j,i), WYe^+\nu_{561}(j,k), ddY_2(k)$ |
| 5.5b | $\sum_i \sum_j \sum_k (We^+\nu_{56}(i), udWX_{561}(i,j), XYee_{781}(j,k), ddY_2(k)$ |
| | $\sum_i \sum_j \sum_k (We^+\nu_{56}(i), udXW_{562}(j,i), XYee_{781}(j,k), ddY_2(k)$ |
| 5.5d | $\sum_i \sum_j \sum_k (udW_1(i), WWee_{782}(i,j), ddWW_{564}(j,k), We^+\nu_{56}(k)$ |
| 5.6 | $\sum_i \sum_j (udW_1(i), WXe^+\nu ee(i,j), ddX2$ |
| 5.7a | $\sum_i \sum_j \sum_k (We^+\nu_{56}(i), udWX_{561}(i,j), X2ddY_{2478}(j,k), Yee_{78}(k)$ |
| | $\sum_i \sum_j \sum_k (We^+\nu_{56}(i), udWX_{561}(i,j), X1ddY_{2478}(j,k), Yee_{78}(k)$ |
| | $\sum_i \sum_j \sum_k (udWXY_{562478}(i,j,k), We^+\nu_{56}(i), Xdd_{24}(j), Yee_{78}(k)$ |
| | $\sum_i \sum_j \sum_k (udXWY_{785624}(i,j,k), Xee_{78}(i), We^+\nu_{56}(j), Ydd_{24}(k)$ |
| | $\sum_i \sum_j \sum_k (udWXY_{567824}(i,j,k), We^+\nu_{56}(i), Xee_{78}(j), Ydd_{24}(k)$ |
| 5.7d | $\sum_i \sum_j \sum_k (Xee_{78}(i), udXW_{781}(i,j), W1ddW_{2456}(j,k), We^+\nu_{56}(k)$ |
| | $\sum_i \sum_j \sum_k (Xee_{78}(i), udWX_{782}(j,i), W1ddW_{2456}(j,k), We^+\nu_{56}(k)$ |
| | $\sum_i \sum_j \sum_k (ddWXW_{137856}(i,j,k), Wud_{13}(i), Xee_{78}(j), We^+\nu_{56}(k)$ |
| | $\sum_i \sum_j \sum_k (ddWWX_{135678}(i,j,k), Wud_{13}(i), We^+\nu_{56}(j), Xee_{78}(k)$ |
| | $\sum_i \sum_j \sum_k (ddXWW_{78_{13}56}(i,j,k), Xee_{78}(i), Wud_{13}(j), We^+\nu_{56}(k)$ |
| 5.7b | $\sum_i \sum_j \sum_k (We^+\nu_{56}(i), udXW_{562}(j,i), X1ddY_{2478}(j,k), Yee_{78}(k)$ |
| | $\sum_i \sum_j \sum_k (We^+\nu_{56}(i), udXW_{562}(j,i), X2ddY_{2478}(j,k), Yee_{78}(k)$ |
| | $\sum_i \sum_j \sum_k (udXYW_{247856}(i,j,k), Xdd_{24}(i), Yee_{78}(j), We^+\nu_{56}(k)$ |
| | $\sum_i \sum_j \sum_k (udXWY_{245678}(i,j,k), Xdd_{24}(i), We^+\nu_{56}(j), Yee_{78}(k)$ |
| | $\sum_i \sum_j \sum_k (udXYW_{782456}(i,j,k), Xee_{78}(i), Ydd_{24}(j), We^+\nu_{56}(k)$ |

**Table B.3:** List of polarization sums corresponding to diagrams in Figures 5.4–5.7 for the subprocess us $\to$ dse$^+\nu_e\mu^+\mu^-$.

| Diagram | Polarization sum |
|---|---|
| 5.8a | $\sum_i \sum_j (Xe\nu e\nu(i), uuXY_1(i,j), Yuu_{24}(j)$ |
| | $\sum_i \sum_j (Xuu_{24}(i), uuXY_2(i,j), Ye\nu e\nu(j)$ |
| | $\sum_i \sum_j (Xe\nu e\nu(i), uuXY_3(i,j), Yuu_{13}(j)$ |
| | $\sum_i \sum_j (Xuu_{13}(i), uuXY_4(i,j), Ye\nu e\nu(j)$ |
| 5.9a | $\sum_i \sum_j \sum_k (We^-\nu_{78}(i), uuWW_{782}(j,i), WXe^+\nu_{561}(j,k), uuX_2(k)$ |
| | $\sum_i \sum_j \sum_k (uuX_1(i), XWe^+\nu_{562}(j,i), uuWW_{784}(j,k), We^-\nu_{78}(k)$ |
| 5.9c | $\sum_i \sum_j \sum_k (uuX_1(i), XWe^-\nu_{782}(j,i), uuWW_{563}(k,j), We^+\nu_{56}(k)$ |
| | $\sum_i \sum_j \sum_k (We^+\nu_{56}(i), uuWW_{561}(i,j), WXe^-\nu_{781}(j,k), uuX_2(k)$ |
| 5.10a | $\sum_i \sum_j (uuX_1(i), XYe\nu e\nu(i,j), uuY2(j)$ |
| 5.11a | $\sum_i \sum_j \sum_k (uuXWW_{245678}(i,j,k), Xuu_{24}(i), We^+\nu_{56}(j), We^-\nu_{78}(k)$ |
| | $\sum_i \sum_j \sum_k (uuXWW_{135678}(i,j,k), Xuu_{13}(i), We^+\nu_{56}(j), We^-\nu_{78}(k)$ |
| | $\sum_i \sum_j \sum_k (uuWXW_{562478}(i,j,k), We^+\nu_{56}(i), Xuu_{24}(j), We^-\nu_{78}(k)$ |
| | $\sum_i \sum_j \sum_k (uuWWX_{567824}(i,j,k), We^+\nu_{56}(i), We^-\nu_{78}(j), Xuu_{24}(k)$ |
| | $\sum_i \sum_j \sum_k (uuWXW_{561378}(i,j,k), We^+\nu_{56}(i), Xuu_{13}(j), We^-\nu_{78}(k)$ |
| | $\sum_i \sum_j \sum_k (uuWWX_{567813}(i,j,k), We^+\nu_{56}(i), We^-\nu_{78}(j), Xuu_{13}(k)$ |
| 5.11d | $\sum_i \sum_j \sum_k (We^+\nu_{56}(i), uuWW_{561}(i,j), W1uuW_{2478}(j,k), We^-\nu_{78}(k)$ |
| 5.11e | $\sum_i \sum_j \sum_k (We^-\nu_{78}(i), uuWW_{782}(j,i), W2uuW_{2456}(j,k), We^+\nu_{56}(k)$ |

**Table B.4:** List of polarization sums corresponding to diagrams in Figures 5.8–5.11 for the subprocess uc $\to$ uce$^+\nu_e\mu^-\nu_\mu$. Polarization sums for the process ds $\to$ dse$^+\nu_e\mu^-\nu_\mu$ can be obtained by replacing all up-type quarks by down-type quarks and reversing charges of leptons. The left column remains unchanged.

| Diagram | Polarization sum |
|---|---|
| 5.8a | $\sum_i \sum_j (Xe\nu e\nu(i), uuXY_1(i,j), Ydd_{24}(j)$ |
| | $\sum_i \sum_j (Xdd_{24}(i), uuXY_2(i,j), Ye\nu e\nu(j)$ |
| | $\sum_i \sum_j (Xe\nu e\nu(i), ddXX_3(i,j), Yuu_{13}(j)$ |
| | $\sum_i \sum_j (Xuu_{13}(i), ddXY_4(i,j), Ye\nu e\nu(j)$ |
| 5.9a | $\sum_i \sum_j \sum_k (uuX_1(i), XWe^-\nu_{782}(j,i), ddWW_{564}(j,k), We^+\nu_{56}(k)$ |
| | $\sum_i \sum_j \sum_k (We^-\nu_{78}(i), uuWW_{782}(j,i), WXe^+\nu_{561}(j,k), ddX_2(k)$ |
| 5.9c | $\sum_i \sum_j \sum_k (We^+\nu_{56}(i), uuWW_{561}(i,j), WXe^-\nu_{781}(j,k), ddX_2(k)$ |
| | $\sum_i \sum_j \sum_k (uuX_1(i), XWe^+\nu_{562}(j,i), ddWW_{783}(k,j), We^-\nu_{78}(k)$ |
| 5.10a | $\sum_i \sum_j (uuX_1(i), XYe\nu e\nu(i,j), ddY2(j)$ |
| 5.11a | $\sum_i \sum_j \sum_k (uuXWW_{245678}(i,j,k), Xdd_{24}(i), We^+\nu_{56}(j), We^-\nu_{78}(k)$ |
| | $\sum_i \sum_j \sum_k (uuWXW_{562478}(i,j,k), We^+\nu_{56}(i), Xdd_{24}(j), We^-\nu_{78}(k)$ |
| | $\sum_i \sum_j \sum_k (uuWWX_{567824}(i,j,k), We^+\nu_{56}(i), We^-\nu_{78}(j), Xdd_{24}(k)$ |
| | $\sum_i \sum_j \sum_k (ddXWW_{137856}(i,j,k), Xuu_{13}(i), We^-\nu_{78}(j), We^+\nu_{56}(k)$ |
| | $\sum_i \sum_j \sum_k (ddWXW_{781356}(i,j,k), We^-\nu_{78}(i), Xuu_{13}(j), We^+\nu_{56}(k)$ |
| | $\sum_i \sum_j \sum_k (ddWWX_{785613}(i,j,k), We^-\nu_{78}(i), We^+\nu_{56}(j), Xuu_{13}(ki)$ |
| 5.11g | $\sum_i \sum_j \sum_k (We^+\nu_{56}(i), uuWW_{561}(i,j), W2ddW_{2478}(j,k), We^-\nu_{78}(k)$ |
| 5.11f | $\sum_i \sum_j \sum_k (We^-\nu_{78}(i), uuWW_{782}(j,i), W1ddW_{2456}(j,k), We^+\nu_{56}(k)$ |

**Table B.5:** List of polarization sums corresponding to diagrams in Figures 5.8–5.11 for the subprocess us $\to$ use$^+\nu_e\mu^-\nu_\mu$.

| Diagram | Polarization sum |
|---|---|
| 5.8b | $\sum_i \sum_j (Xe\nu e\nu(i), udXW_1(i,j), Wdu_{24}(j)$ |
| | $\sum_i \sum_j (Wdu_{24}(i), udWX_2(i,j), Xe\nu e\nu(j)$ |
| | $\sum_i \sum_j (Xe\nu e\nu(i), duXW_3(i,j), Wud_{13}(j)$ |
| | $\sum_i \sum_j (Wud_{13}(i), duWX_4(i,j), Xe\nu e\nu(j)$ |
| 5.9b | $\sum_i \sum_j \sum_k (udW_1(i), WXe^+\nu_{562}(i,j), duXW_{784}(j,k), We^-\nu_{78}(k)$ |
| | $\sum_i \sum_j \sum_k (We^+\nu_{56}(i), udXW_{562}(j,i), XWe^-\nu_{781}(k,j), duW_2(k)$ |
| 5.9d | $\sum_i \sum_j \sum_k (udW_1(i), WXe^+\nu_{562}(i,j), duWX_{783}(k,j), We^-\nu_{78}(k)$ |
| | $\sum_i \sum_j \sum_k (We^+\nu_{56}(i), udWX_{561}(i,j), XWe^-\nu_{781}(k,j), duW_2(k)$ |
| 5.10b | $\sum_i \sum_j (udW_1(i), WWevev(i,j), duW2(j)$ |
| 5.11b | $\sum_i \sum_j \sum_k (udWWW_{567824}(i,j,k), We^+\nu_{56}(i), We^-\nu_{78}(j), Wdu_{24}(k)$ |
| | $\sum_i \sum_j \sum_k (duWWW_{785613}(i,j,k), We^-\nu_{78}(i), We^+\nu_{56}(j), Wud_{13}(k)$ |
| 5.11c | $\sum_i \sum_j \sum_k (udWWW_{247856}(i,j,k), Wdu_{24}(i), We^-\nu_{78}(j), We^+\nu_{56}(k)$ |
| | $\sum_i \sum_j \sum_k (duWWW_{135678}(i,j,k), Wud_{13}(i), We^+\nu_{56}(j), We^-\nu_{78}(k)$ |
| 5.11h | $\sum_i \sum_j \sum_k (We^+\nu_{56}(i), udWX_{561}(i,j), X2duW_{2478}(j,k), We^-\nu_{78}(k)$ |
| | $\sum_i \sum_j \sum_k (We^+\nu_{56}(i), udXW_{562}(j,i), X1duW_{2478}(j,k), We^-\nu_{78}(k)$ |
| | $\sum_i \sum_j \sum_k (We^+\nu_{56}(i), udWX_{561}(i,j), X1duW_{2478}(j,k), We^-\nu_{78}(k)$ |
| | $\sum_i \sum_j \sum_k (We^+\nu_{56}(i), udXW_{562}(j,i), X2duW_{2478}(j,k), We^-\nu_{78}(k)$ |

**Table B.6:** List of polarization sums corresponding to diagrams in Figures 5.8–5.11 for the subprocess us $\to$ dce$^+\nu_e\mu^-\nu_\mu$.

| Diagram | Polarization sum |
|---|---|
| 5.12a | $\sum_i \sum_j (Xeevv(i), uuXY_1(i,j), Yuu_{24}(j)$ |
| | $\sum_i \sum_j (Xuu_{24}(i), uuXY_2(i,j), Yeevv(j)$ |
| | $\sum_i \sum_j (Xeevv(i), uuXY_3(i,j), Yuu_{13}(j)$ |
| | $\sum_i \sum_j (Xuu_{13}(i), uuXY_4(i,j), Yeevv(j)$ |

| Diagram | Polarization sum |
|---|---|
| 5.13a | $\sum_i \sum_j \sum_k (uuX_1(i), XYee_{562}(i,j), uuVY_{783}(k,j), Vvv_{78}(k)$ |
| | $\sum_i \sum_j \sum_k (uuX_1(i), XYee_{562}(i,j), uuYV_{784}(j,k), Vvv_{78}(k)$ |
| | $\sum_i \sum_j \sum_k (uuX_1(i), XYvv_{782}(i,j), uuVY_{563}(k,j), Vee_{56}(k)$ |
| | $\sum_i \sum_j \sum_k (uuX_1(i), XYvv_{782}(i,j), uuYV_{564}(j,k), Vee_{56}(k)$ |
| | $\sum_i \sum_j \sum_k (Xvv_{78}(i), uuXY_{781}(i,j), YVee_{561}(j,k), uuV_2(k)$ |
| | $\sum_i \sum_j \sum_k (Xvv_{78}(i), uuYX_{782}(j,i), YVee_{561}(j,k), uuV_2(k)$ |
| | $\sum_i \sum_j \sum_k (Xee_{56}(i), uuXY_{561}(i,j), YVvv_{781}(j,k), uuV_2(k)$ |
| | $\sum_i \sum_j \sum_k (Xee_{56}(i), uuYX_{562}(j,i), YVvv_{781}(j,k), uuV_2(k)$ |
| 5.14a | $\sum_i \sum_j (uuX_1(i), XYeevv(i,j), uuY2(j)$ |
| 5.15a | $\sum_i \sum_j \sum_k (Xee_{56}(i), uuXY_{561}(i,j), Y2uuV_{2478}(j,k), Vvv_{78}(k)$ |
| | $\sum_i \sum_j \sum_k (Xvv_{78}(i), uuXY_{781}(i,j), Y2uuV_{2456}(j,k), Vee_{56}(k)$ |
| | $\sum_i \sum_j \sum_k (Xee_{56}(i), uuXY_{561}(i,j), Y1uuV_{2478}(j,k), Vvv_{78}(k)$ |
| | $\sum_i \sum_j \sum_k (Xvv_{78}(i), uuXY_{781}(i,j), Y1uuV_{2456}(j,k), Vee_{56}(k)$ |
| | $\sum_i \sum_j \sum_k (Xee_{56}(i), uuYX_{562}(j,i), Y1uuV_{2478}(j,k), Vvv_{78}(k)$ |
| | $\sum_i \sum_j \sum_k (Xvv_{78}(i), uuYX_{782}(j,i), Y1uuV_{2456}(j,k), Vee_{56}(k)$ |
| | $\sum_i \sum_j \sum_k (Xee_{56}(i), uuYX_{562}(j,i), Y2uuV_{2478}(j,k), Vvv_{78}(k)$ |
| | $\sum_i \sum_j \sum_k (Xvv_{78}(i), uuYX_{782}(j,i), Y2uuV_{2456}(j,k), Vee_{56}(k)$ |
| | $\sum_i \sum_j \sum_k (uuXYV_{245678}(i,j,k), Xuu_{24}(i), Yee_{56}(j), Vvv_{78}(k)$ |
| | $\sum_i \sum_j \sum_k (uuXYV_{247856}(i,j,k), Xuu_{24}(i), Yvv_{78}(j), Vee_{56}(k)$ |
| | $\sum_i \sum_j \sum_k (uuXYV_{782456}(i,j,k), Xvv_{78}(i), Yuu_{24}(j), Vee_{56}(k)$ |
| | $\sum_i \sum_j \sum_k (uuXYV_{562478}(i,j,k), Xee_{56}(i), Yuu_{24}(j), Vvv_{78}(k)$ |
| | $\sum_i \sum_j \sum_k (uuXYV_{567824}(i,j,k), Xee_{56}(i), Yvv_{78}(j), Vuu_{24}(k)$ |
| | $\sum_i \sum_j \sum_k (uuXYV_{785624}(i,j,k), Xvv_{78}(i), Yee_{56}(j), Vuu_{24}(k)$ |
| | $\sum_i \sum_j \sum_k (uuXYV_{135678}(i,j,k), Xuu_{13}(i), Yee_{56}(j), Vvv_{78}(k)$ |
| | $\sum_i \sum_j \sum_k (uuXYV_{137856}(i,j,k), Xuu_{13}(i), Yvv_{78}(j), Vee_{56}(k)$ |
| | $\sum_i \sum_j \sum_k (uuXYV_{781356}(i,j,k), Xvv_{78}(i), Yuu_{13}(j), Vee_{56}(k)$ |
| | $\sum_i \sum_j \sum_k (uuXYV_{561378}(i,j,k), Xee_{56}(i), Yuu_{13}(j), Vvv_{78}(k)$ |
| | $\sum_i \sum_j \sum_k (uuXYV_{567813}(i,j,k), Xee_{56}(i), Yvv_{78}(j), Vuu_{13}(k)$ |
| | $\sum_i \sum_j \sum_k (uuXYV_{785613}(i,j,k), Xvv_{78}(i), Yee_{56}(j), Vuu_{13}(k)$ |

**Table B.7:** List of polarization sums corresponding to diagrams in Figures 5.12–5.15 for the subprocess uc $\to$ uce$^+$e$^-\mu^+\mu^-$ and uc $\to$ uce$^+$e$^-\bar{\nu}_\mu\nu_\mu$. Polarization sums for the process ds $\to$ dse$^+$e$^-\mu^+\mu^-$ and ds $\to$ dse$^+$e$^-\bar{\nu}_\mu\nu_\mu$ can be obtained using complex conjugation, i.e. by replacing all up-type quarks by down-type quarks and reversing charges of leptons. The left column remains unchanged.

| Diagram | Polarization sum |
|---|---|
| 5.12b | $\sum_i \sum_j (Xeevv(i), udXW_1(i,j), Wdu_{24}(j)$ |
| | $\sum_i \sum_j (Wdu_{24}(i), udWX_2(i,j), Xeevv(j)$ |
| | $\sum_i \sum_j (Xeevv(i), duXW_3(i,j), Wud_{13}(j)$ |
| | $\sum_i \sum_j (Wud_{13}(i), duWX_4(i,j), Xeevv(j)$ |
| 5.13b | $\sum_i \sum_j \sum_k (udW_1(i), WWee_{562}(i,j), duXW_{783}(k,j), Xvv_{78}(k)$ |
| | $\sum_i \sum_j \sum_k (udW_1(i), WWee_{562}(i,j), duWX_{784}(j,k), Xvv_{78}(k)$ |
| | $\sum_i \sum_j \sum_k (udW_1(i), WWvv_{782}(i,j), duXW_{563}(k,j), Xee_{56}(k)$ |
| | $\sum_i \sum_j \sum_k (udW_1(i), WWvv_{782}(i,j), duWX_{564}(j,k), Xee_{56}(k)$ |
| | $\sum_i \sum_j \sum_k (Xvv_{78}(i), udXW_{781}(i,j), WWee_{561}(j,k), duW_2(k)$ |
| | $\sum_i \sum_j \sum_k (Xvv_{78}(i), udWX_{782}(j,i), WWee_{561}(j,k), duW_2(k)$ |
| | $\sum_i \sum_j \sum_k (Xee_{56}(i), udXW_{561}(i,j), WWvv_{781}(j,k), duW_2(k)$ |
| | $\sum_i \sum_j \sum_k (Xee_{56}(i), udWX_{562}(j,i), WWvv_{781}(j,k), duW_2(k)$ |
| 5.14b | $\sum_i \sum_j (udW_1(i), WWeevv(i,j), duW2(j)$ |
| 5.15b | $\sum_i \sum_j \sum_k (Xee_{56}(i), udXW_{561}(i,j), W2duY_{2478}(j,k), Yvv_{78}(k)$ |
| | $\sum_i \sum_j \sum_k (Xvv_{78}(i), udXW_{781}(i,j), W2duY_{2456}(j,k), Yee_{56}(k)$ |
| | $\sum_i \sum_j \sum_k (Xee_{56}(i), udXW_{561}(i,j), W1duY_{2478}(j,k), Yvv_{78}(k)$ |
| | $\sum_i \sum_j \sum_k (Xvv_{78}(i), udXW_{781}(i,j), W1duY_{2456}(j,k), Yee_{56}(k)$ |
| | $\sum_i \sum_j \sum_k (Xee_{56}(i), udWX_{562}(j,i), W1duY_{2478}(j,k), Yvv_{78}(k)$ |
| | $\sum_i \sum_j \sum_k (Xvv_{78}(i), udWX_{782}(j,i), W1duY_{2456}(j,k), Yee_{56}(k)$ |
| | $\sum_i \sum_j \sum_k (Xee_{56}(i), udWX_{562}(j,i), W2duY_{2478}(j,k), Yvv_{78}(k)$ |
| | $\sum_i \sum_j \sum_k (Xvv_{78}(i), udWX_{782}(j,i), W2duY_{2456}(j,k), Yee_{56}(k)$ |
| | $\sum_i \sum_j \sum_k (udWXY_{245678}(i,j,k), Wdu_{24}(i), Xee_{56}(j), Yvv_{78}(k)$ |
| | $\sum_i \sum_j \sum_k (udWXY_{247856}(i,j,k), Wdu_{24}(i), Xvv_{78}(j), Yee_{56}(k)$ |
| | $\sum_i \sum_j \sum_k (udXWY_{782456}(i,j,k), Xvv_{78}(i), Wdu_{24}(j), Yee_{56}(k)$ |
| | $\sum_i \sum_j \sum_k (udXWY_{562478}(i,j,k), Xee_{56}(i), Wdu_{24}(j), Yvv_{78}(k)$ |
| | $\sum_i \sum_j \sum_k (udXYW_{567824}(i,j,k), Xee_{56}(i), Yvv_{78}(j), Wdu_{24}(k)$ |
| | $\sum_i \sum_j \sum_k (udXYW_{785624}(i,j,k), Xvv_{78}(i), Yee_{56}(j), Wdu_{24}(k)$ |
| | $\sum_i \sum_j \sum_k (duWXY_{135678}(i,j,k), Wud_{13}(i), Xee_{56}(j), Yvv_{78}(k)$ |
| | $\sum_i \sum_j \sum_k (duWXY_{137856}(i,j,k), Wud_{13}(i), Xvv_{78}(j), Yee_{56}(k)$ |
| | $\sum_i \sum_j \sum_k (duXWY_{781356}(i,j,k), Xvv_{78}(i), Wud_{13}(j), Yee_{56}(k)$ |
| | $\sum_i \sum_j \sum_k (duXWY_{561378}(i,j,k), Xee_{56}(i), Wud_{13}(j), Yvv_{78}(k)$ |
| | $\sum_i \sum_j \sum_k (duXYW_{567813}(i,j,k), Xee_{56}(i), Yvv_{78}(j), Wud_{13}(k)$ |
| | $\sum_i \sum_j \sum_k (duXYW_{785613}(i,j,k), Xvv_{78}(i), Yee_{56}(j), Wud_{13}(k)$ |

**Table B.8:** List of polarization sums corresponding to diagrams in Figures 5.12–5.15 for the subprocess uc $\to$ uce$^+$e$^-\mu^+\mu^-$ and uc $\to$ uce$^+$e$^-\bar{\nu}_\mu\nu_\mu$.

# Bibliography


[1] J. Schwinger *Ann. Phys. 2, 407* (1957).

[2] T. D. Lee and C. N. Yang *Phys. Rev. 108, 1611* (1957).

[3] S. L. Glashow *Nucl. Phys. 22, 579* (1961).

[4] S. Weinberg *Phys. Rev. Lett. 19, 1264* (1967).

[5] A. Salam, *Weak and electromagnetic interactions*, in *Elementary particle theory* (N. Svartholm, ed.), pp. 367–377, Almquist & Wiksell.

[6] S. L. G. J. D. Bjorken *Phys. Rev. Lett. 11, 255* (1964).

[7] M. G.-M. H. Fritzsch and H. Leutwyler *Phys. Lett. B47, 4, 365* (1973).

[8] S. Weinberg *Phys.Rev.Lett. 31, 494* (1973).

[9] D. J. Gross and F. Wilczek *Phys. Rev. D9, 980* (1974).

[10] A. Salam and J. C. Ward *Nuovo Cim. 19, 165* (1961).

[11] J. Goldstone *Nuovo Cim. 19, 154* (1961).

[12] Y. Nambu *Phys. Rev. Lett. 4, 380* (1962).

[13] P. W. Higgs *Phys. Lett. 12, 132* (1964).

[14] F. Englert and R. Brout *Phys. Rev. Lett. 13, 321* (1964).

[15] C. R. H. G. S. Guralnik and T. W. B. Kibble *Phys. Rev. Lett. 13, 585* (1964).

[16] G. A. et al. (UA1 Collab.) *Phys. Lett. B 126, 398* (1983).

[17] P. B. et al. (UA2 Collab.) *Phys. Lett. B 129, 130* (1983).

[18] F. A. et al. (CDF Collab.) *Phys. Rev. Lett. 74, 2626* (1995).

[19] S. A. et al. (DØ Collab.) *Phys. Rev. Lett. 74, 2632* (1995).

[20] V. Hankele, G. Klämke, and D. Zeppenfeld, *Higgs + 2 jets as a probe for CP properties*, hep-ph/0605117.

[21] A. Belyaev and L. Reina, *pp → t anti-t H, H → tau+ tau-: Toward a model independent determination of the Higgs boson couplings at the LHC*, *JHEP* **0208** (2002) 041, [hep-ph/0205270].

[22] D. Zeppenfeld, *Higgs couplings at the LHC*, *eConf* **C010630** (2001) P123, [hep-ph/0203123].

[23] J. Bagger, V. D. Barger, K.-m. Cheung, J. F. Gunion, T. Han, *et. al.*, *CERN LHC analysis of the strongly interacting W W system: Gold plated modes*, *Phys.Rev.* **D52** (1995) 3878–3889, [hep-ph/9504426].

[24] A. Ballestrero, D. B. Franzosi, and E. Maina, *Vector-Vector scattering at the LHC with two charged leptons and two neutrinos in the final state*, *JHEP* **1106** (2011) 013, [hep-ph/1011.1514].

[25] T. Melia, K. Melnikov, R. Rontsch, and G. Zanderighi, *Next-to-leading order QCD predictions for $W^+W^+jj$ production at the LHC*, *JHEP* **1012** (2010) 053, [hep-ph/1007.5313].

[26] T. Melia, K. Melnikov, R. Rontsch, and G. Zanderighi, *NLO QCD corrections for $W^+W^-$ pair production in association with two jets at hadron colliders*, *Phys.Rev.* **D83** (2011) 114043, [hep-ph/1104.2327].

[27] N. Greiner, G. Heinrich, P. Mastrolia, G. Ossola, T. Reiter, *et. al.*, *NLO QCD corrections to the production of W+ W- plus two jets at the LHC*, *Phys.Lett.* **B713** (2012) 277–283, [hep-ph/1202.6004].

[28] B. Jäger, C. Oleari, and D. Zeppenfeld, *Next-to-leading order QCD corrections to W+ W- production via vector-boson fusion*, *JHEP* **07** (2006) 015, [hep-ph/0603177].

[29] B. Jäger, C. Oleari, and D. Zeppenfeld, *Next-to-leading order QCD corrections to Z boson pair production via vector-boson fusion*, *Phys. Rev.* **D73** (2006) 113006, [hep-ph/0604200].

[30] G. Bozzi, B. Jäger, C. Oleari, and D. Zeppenfeld, *Next-to-leading order QCD corrections to W+Z and W-Z production via vector-boson fusion*, *Phys. Rev.* **D75** (2007) 073004, [hep-ph/0701105].

[31] B. Jäger, C. Oleari, and D. Zeppenfeld, *Next-to-leading order QCD corrections to W+W+jj and W-W-jj production via weak-boson fusion*, *Phys. Rev.* **D80** (2009) 034022, [hep-ph/0907.0580].

[32] B. Jäger and G. Zanderighi, *NLO corrections to electroweak and QCD production of W+W+ plus two jets in the POWHEGBOX*, *JHEP* **1111** (2011) 055, [hep-ph/1108.0864].

[33] P. Nason, *A New method for combining NLO QCD with shower Monte Carlo algorithms*, *JHEP* **0411** (2004) 040, [hep-ph/0409146].

[34] S. Frixione, P. Nason, and C. Oleari, *Matching NLO QCD computations with Parton Shower simulations: the POWHEG method*, *JHEP* **0711** (2007) 070, [hep-ph/0709.2092].

[35] M. E. Peskin and D. V. Schroeder, *An Introduction to Quantum Field Theory (Frontiers in Physics)*. Perseus Books, 2008.

[36] F. Halzen and A. D. Martin, *Quarks and Leptons*. 1985.

[37] C. G. Callan, *Broken scale invariance in scalar field theory*, *Phys. Rev. D* **2** (Oct, 1970) 1541–1547.

[38] K. Symanzik, *Small distance behaviour in field theory and power counting*, *Communications in Mathematical Physics* **18** (1970) 227–246. 10.1007/BF01649434.

[39] W. J. S. R. K. Ellis and B. R. Webber. Cambridge University Press, 1996.

[40] A. Denner, S. Dittmaier, M. Roth, and D. Wackeroth, *Predictions for all processes e+ e- → 4 fermions + gamma*, *Nucl.Phys.* **B560** (1999) 33–65, [hep-ph/9904472].

[41] A. Denner, S. Dittmaier, M. Roth, and L. Wieders, *Electroweak corrections to charged-current e+ e- → 4 fermion processes: Technical details and further results*, *Nucl.Phys.* **B724** (2005) 247–294, [hep-ph/0505042].

[42] A. Denner and S. Dittmaier, *The Complex-mass scheme for perturbative calculations with unstable particles*, *Nucl.Phys.Proc.Suppl.* **160** (2006) 22–26, [hep-ph/0605312].

[43] S. Dittmaier, *Weyl-van-der-Waerden formalism for helicity amplitudes of massive particles*, *Phys. Rev.* **D59** (1998) 016007, [hep-ph/9805445].

[44] H. Weyl, *The theory of groups and quantum mechanics*. Dover books on advanced mathematics. Dover Publications, 1950.

[45] B. Waerden, *Group theory and quantum mechanics (Die gruppentheoretische Methode in der Quantenmechanik, engl.) With 10 fig.* 1974.

[46] W. R. Inc., *Mathematica 7.0*, 2008.

[47] T. Hahn, *Generating Feynman diagrams and amplitudes with FeynArts 3*, *Comput. Phys. Commun.* **140** (2001) 418–431, [hep-ph/0012260].

[48] T. Hahn, *FormCalc 6*, *PoS* **ACAT08** (2008) 121, [hep-ph/0901.1528].

[49] J. Alwall, P. Demin, S. de Visscher, R. Frederix, M. Herquet, *et. al.*, *MadGraph/MadEvent v4: The New Web Generation*, *JHEP* **0709** (2007) 028, [0706.2334].

[50] H. Murayama, I. Watanabe, and K. Hagiwara, *HELAS: HELicity amplitude subroutines for Feynman diagram evaluations*, . KEK-91-11.

[51] T. Kinoshita, *Mass singularities of Feynman amplitudes*, *J. Math. Phys.* **3** (1962) 650–677.

[52] T. D. Lee and M. Nauenberg, *Degenerate Systems and Mass Singularities*, *Phys. Rev.* **133** (1964) B1549–B1562.

[53] B. W. Harris and J. F. Owens, *The two cutoff phase space slicing method*, *PHYS.REV.D* **65** (2002) 094032.

[54] K. Fabricius, I. Schmitt, G. Kramer, and G. Schierholz *Z. Phys.* **C11** (1981) 315.

[55] W. T. Giele, E. W. N. Glover, and D. A. Kosower, *Higher order corrections to jet cross-sections in hadron colliders*, *Nucl. Phys.* **B403** (1993) 633–670, [hep-ph/9302225].

[56] S. Catani and M. H. Seymour, *A general algorithm for calculating jet cross sections in NLO QCD*, *Nucl. Phys.* **B485** (1997) 291–419, [hep-ph/9605323].

[57] G. Altarelli and G. Parisi, *Asymptotic Freedom in Parton Language*, *Nucl.Phys.* **B126** (1977) 298.

[58] S. Catani, S. Dittmaier, M. H. Seymour, and Z. Trocsanyi, *The Dipole formalism for next-to-leading order QCD calculations with massive partons*, *Nucl.Phys.* **B627** (2002) 189–265, [hep-ph/0201036].

[59] T. Hahn and M. Perez-Victoria, *Automatized one-loop calculations in four and D dimensions*, *Comput. Phys. Commun.* **118** (1999) 153–165, [hep-ph/9807565].

[60] G. Passarino and M. Veltman, *One-loop corrections for e+e- annihilation into [mu]+[mu]- in the weinberg model*, *Nuclear Physics B* **160** (1979), no. 1 151 – 207.

[61] A. Denner and S. Dittmaier, *Reduction schemes for one-loop tensor integrals*, *Nucl. Phys.* **B734** (2006) 62–115, [hep-ph/0509141].

[62] A. Denner and S. Dittmaier, *Reduction of one-loop tensor 5-point integrals*, *Nucl. Phys.* **B658** (2003) 175–202, [hep-ph/0212259].

[63] A. Denner, U. Nierste, and R. Scharf, *A Compact expression for the scalar one loop four point function*, *Nucl. Phys.* **B367** (1991) 637–656.

[64] W. Beenakker and A. Denner, *Infrared Divergent Scalar Box Integrals with Applications in the Electroweak Standard Model*, *Nucl. Phys.* **B338** (1990) 349–370.

[65] A. Denner and S. Dittmaier, *Scalar one-loop 4-point integrals*, *Nucl.Phys.* **B844** (2011) 199–242, [hep-ph/1005.2076].

[66] M. B. H. Spiesberger and W. Hollik *Fortschr. Phys. 34* (1986) 687.

[67] W. Beenakker *et. al., NLO QCD corrections to t anti-t H production in hadron collisions. ((U)), Nucl. Phys.* **B653** (2003) 151–203, [hep-ph/0211352].

[68] S. Catani, Y. L. Dokshitzer, and B. R. Webber, *The k⊥-clustering algorithm for jets in deep inelastic scattering and hadron collisions, Physics Letters, Section B: Nuclear, Elementary Particle and High-Energy Physics* **285** (1992), no. 3 291–299.

[69] S. Catani, Y. L. Dokshitzer, M. H. Seymour, and B. R. Webber, *Longitudinally-invariant k⊥-clustering algorithms for hadron-hadron collisions, Nuclear Physics B* **406** (1993), no. 1-2 187–224.

[70] S. D. Ellis and D. E. Soper, *Successive combination jet algorithm for hadron collisions, Phys.Rev.* **D48** (1993) 3160–3166, [hep-ph/9305266].

[71] S. Kallweit, *Precision Calculations for Gauge-Boson Pair Production with a Hadronic Jet at Hadron Colliders.* PhD thesis, LMU Munich, 2008.

[72] F. A. Berends, R. Pittau, and R. Kleiss, *All electroweak four fermion processes in electron - positron collisions, Nucl.Phys.* **B424** (1994) 308–342, [hep-ph/9404313].

[73] F. Berends, P. Daverveldt, and R. Kleiss, *Complete lowest-order calculations for four-lepton final states in electron-positron collisions, Nuclear Physics B* **253** (1985), no. 0 441 – 463.

[74] R. Kleiss and R. Pittau, *Weight optimization in multichannel Monte Carlo, Comput.Phys.Commun.* **83** (1994) 141–146, [hep-ph/9405257].

[75] J. Beringer and others (Particle Data Group) *Phys. Rev.* **D86, 010001** (2012).

[76] S. Dittmaier and M. Kramer, *Electroweak radiative corrections to W boson production at hadron colliders, Phys.Rev.* **D65** (2002) 073007, [hep-ph/0109062].

[77] S. Dittmaier, C. Mariotti, G. Passarino, R. Tanaka, *et. al., Handbook of LHC Higgs Cross Sections: 2. Differential Distributions,* hep-ph/1201.3084.

[78] A. Denner, S. Dittmaier, S. Kallweit, and S. Pozzorini, *NLO QCD corrections to off-shell top-antitop production with leptonic decays at hadron colliders,* hep-ph/1207.5018.

[79] F. Cascioli, P. Maierhofer, and S. Pozzorini, *Scattering Amplitudes with Open Loops, Phys.Rev.Lett.* **108** (2012) [hep-ph/1111.5206].

[80] T. Gleisberg, S. Höche, F. Krauss, M. Schonherr, S. Schumann, *et. al., Event generation with SHERPA 1.1, JHEP* **0902** (2009) 007, [hep-ph/0811.4622].

[81] J. Pumplin, D. Stump, J. Huston, H. Lai, P. M. Nadolsky, *et. al., New generation of parton distributions with uncertainties from global QCD analysis, JHEP* **0207** (2002) 012, [hep-ph/0201195].

[82] D. Stump, J. Huston, J. Pumplin, W.-K. Tung, H. Lai, *et. al., Inclusive jet production, parton distributions, and the search for new physics, JHEP* **0310** (2003) 046, [hep-ph/0303013].

[83] A. Martin, W. Stirling, R. Thorne, and G. Watt, *Parton distributions for the LHC, Eur.Phys.J.* **C63** (2009) 189–285, [hep-ph/0901.0002].

[84] M. Dittmar and H. K. Dreiner, *h0 → W+ W- → lepton+ lepton- lepton-neutrino anti-lepton-neutrino as the dominant SM Higgs search mode at the LHC for M(h0) = 155-GeV - 180-GeV*, hep-ph/9703401.

[85] D. L. Rainwater and D. Zeppenfeld, *Observing H → W(*) W(*) → e+- muon-+ missing-p(T) in weak boson fusion with dual forward jet tagging at the CERN LHC, Phys.Rev.* **D60** (1999) 113004, [hep-ph/9906218].

# Acknowledgments

First of all, I would like say thanks to two people whom I will never be able to thank enough: to Ansgar Denner, whose advise, experience and attention to detail made everything possible, and to Dr. Stefan Kallweit who came and offered to help when I needed it most.

My special thanks go to Thomas Gehrmann for the help and support he showed me during my stay at the Institute for Theoretical Physics in Zurich, especially over the last year, and to Germán Rodrigo for giving me an opportunity to finish my thesis in Valencia and for his continuous and continuing support.

The contents of this thesis would have been far less accurate and understandable were it not for Ansgar Denner and his invaluable comments, suggestions and corrections and for Stefan Kallweit, Michal Jedinák and Panos Stamoulis who had the patience to read parts of the manuscript and found many mistakes I would have otherwise missed.

I would also like to express my gratitude to Alexander Mück who helped to get me started, to Philipp Maierhöfer who provided us with Open Loops tree-level matrix elements, to Barbara Jäger for her help with comparisons with previously published results and to Marek Schönherr for discussing the finer points of Sherpa with me.

When working on this thesis, I was lucky enough to stay at three institutes filled with wonderful people. First was the Paul Scherrer Institute which I will forever associate with joyful lunchtime discussions, cowbells and pink mammoths. I would like to thank all former and present members of the particle theory group, namely to Ansgar Denner, Grigorios Chachamis, Bernd Jantzen, Heidi Rzehak, Karol Kampf, Stefan Kallweit, Mathias Brucherseifer, Timo Schmidt, Ryan Gavin, and in particular to Roland Rosenfelder for his support and anecdotes, to Michael Spira for all the jokes and for some of the strangest physics discussions I have ever had, to Alexander Mück and Frank Fugel for many out-of-curriculum activities and to Stefano Actis as well as to his wife Oxana.

My second home in Switzerland was the Institute for Theoretical Physics at the University of Zurich. With its endless offer of courses, seminars, colloquia, journal clubs, as well as Christmas dinners, ski trips and barbecues, I cannot imagine a better place to be a PhD student. To thank everyone who makes ITP a place where people happily spend their days and nights would take many pages. Let me at least mention Beat Tödtli and Michael Busha who have been wonderful friends to me, Doug Potter, Jonathan Coles, Rebekka Bieri and Philipp Maierhöfer who sharing my love for movies, José Zurita, my favourite flatmate, Andreas Papaefstathiou for inviting me to sleep on my own bed, Erich Weihs and Lorenzo Tancredi, the best people to get lost with in London, and all those who survived sharing an

office with me: Christian Kurz, David Noth, Tobias Motz, Pier Francesco Monni, Jaiyul Yoo and Thomas Lübbert. In addition, I would like to thank Elisabetta Furlan for her talent to turn the most ordinary things into strange and fun.

Thirdly, I would like to thank the people who have become my new family in Spain: my officemates Gregory Vulvert and Tracey Li, the Greek trio Petros Draggiotis, Panos Stamoulis and Yiannis Malamos for the countless discussions about life, physics and everything, Alejandro Celis who is an endless source of information on everyone and everything in Valencia and to Amparo Llorens who continues to help me survive in a city full of Spanish people.

Finally, I would like to give my thanks to two most important people in my life - Michal Jedinák, who has never not been there for me, and my mother, who has been there for me even longer.